DOCTORAL THESIS

Chiral Supramolecular Assemblies of Metalloporphyrins and Cyclohexanohemicucurbiturils: From Molecular Recognition to Sensing Applications

Marko Šakarašvili

TALLINNA TEHNIKAÜLIKOOL
TALLINN UNIVERSITY OF TECHNOLOGY
TALLINN 2026

TALLINN UNIVERSITY OF TECHNOLOGY
DOCTORAL THESIS
50/2026

Chiral Supramolecular Assemblies of Metalloporphyrins and Cyclohexanohemicucurbiturils: From Molecular Recognition to Sensing Applications

MARKO ŠAKARAŠVILI

TAL TECH PRESS

TALLINN UNIVERSITY OF TECHNOLOGY
School of Science
Department of Chemistry and Biotechnology
This dissertation was accepted for the defence of the degree of Doctor of Philosophy in Chemistry on 08/07/2026

Supervisor: Professor Riina Aav
School of Science
Tallinn University of Technology
Tallinn, Estonia

Co-supervisor: Dr Lukáš Ustrnul
School of Science
Tallinn University of Technology
Tallinn, Estonia

Opponents: Prof Lorenzo Di Bari
Dipartimento di Chimica e Chimica Industriale
Università di Pisa
Pisa, Italy

Prof Tomaš Fiala
Faculty of Science
Department of Chemistry
Masaryk University
Brno, Czech Republic

Defence of the thesis: 01/09/2026, Tallinn

Declaration:
Hereby I declare that this doctoral thesis, my original investigation and achievement, submitted for the doctoral degree at Tallinn University of Technology has not been submitted for doctoral or equivalent academic degree.

Marko Šakarašvili

---
signature

European Union
European Regional
Development Fund

Investing
in your future

Copyright: Marko Šakarašvili, 2026
ISSN 2585-6898 (paperback)
ISBN 978-9916-80-537-4 (paperback)
ISSN 2585-6901 (PDF)
ISBN 978-9916-80-538-1 (PDF)
https://doi.org/10.23658/taltech.50/2026

Šakarašvili, M. (2026). *Chiral Supramolecular Assemblies of Metalloporphyrins and Cyclohexanohemicucurbiturils: From Molecular Recognition to Sensing Applications* [TalTech Press]. https://doi.org/10.23658/taltech.50/2026

TALLINNA TEHNIKAÜLIKOOL
DOKTORITÖÖ
50/2026

Kiraalsed supramolekulaarsed süsteemid metalloporfüriinide ja hemikukurbituriilidega: molekulaarsest tuvastamisest sensoriteni

MARKO ŠAKARAŠVILI

TAL TECH
KIRJASTUS

Contents

List of Publications 7
Author's Contribution to the Publications 8
Introduction 9
Abbreviations 10
Symbols 12
1 Literature overview 13
1.1 Supramolecular Chemistry 13
1.1.1 Definition and evolution of supramolecular chemistry 13
1.1.2 Types of noncovalent interactions 14
1.1.3 Characterization and visualization of noncovalent interactions 16
1.1.4 Binding evaluation in supramolecular systems 18
1.2 Chirality in Supramolecular Systems 20
1.2.1 Fundamentals of molecular and supramolecular chirality 20
1.2.2 Experimental characterization methods 21
1.2.3 Induced chirality in non-chiral chromophores 23
1.3 Porphyrins and Macrocyclic Hosts in Supramolecular Chemistry 24
1.3.1 Porphyrins and Metalloporphyrins 24
1.3.2 Structural and spectroscopic features of porphyrins 26
1.3.3 Bisporphyrins 28
1.3.4 Cucurbiturils and hemicucurbiturils 29
1.4 Supramolecular Sensing and Material Design 30
1.4.1 General principles of sensor and supramolecular sensing 30
1.4.2 Quartz crystal microbalance (QMB) 32
1.4.3 The Electronic Nose Concept and Chemometric Analysis 34
2 Motivation and aims for work 35
3 Results and discussion 36
3.1 Solution and Solid-State Self-Assembly of a Library of Metalloporphyrins with Chiral Cyclohexanohemicucurbit[*n*]urils (Publication I) 36
3.1.1 Variability of binding strength in solution 36
3.1.2 Solid-state architectures from single-crystal X-ray diffraction 39
3.1.3 Noncovalent interaction analysis 42
3.1.4 Chiroptical properties in solution and the solid state 43
3.2 Self-Assembly of Bis(zinc octaethylporphyrin) with Chiral Cyclohexanohemicucurbit[*n*]urils (Publication II) 46
3.2.1 Binding properties of bis–ZnOEP with cycHC[6] and cycHC[8] 47
3.2.2 Time-dependent behaviour of the complexes 49
3.2.3 Variable-temperature NMR and fluorescence experiments 52
3.2.4 Proposed self-assembly mechanisms 52
3.3 Chiral Recognition of Volatile Enantiomers by Porphyrin·Cyclohexanohemicucurbit[8]uril-Functionalised Gravimetric Sensor Arrays (Publication III) 54
3.3.1 Film preparation and chiroptical characterisation 54
3.3.2 Gravimetric sensor responses to chiral volatile analytes 57
3.3.3 Virtual racemic sensor normalisation 59

3.3.4 Classification of analytes and their enantiomers 60
4 Conclusions 62
References 63
Acknowledgements 69
Abstract 71
Lühikokkuvõte 73
Appendix 1 75
Appendix 2 91
Appendix 3 107
Curriculum vitae 121
Elulookirjeldus 122

List of Publications

The list of author's publications, on the basis of which the thesis has been prepared:

I **Marko Šakarašvili**, Khai-Nghi Truong, Lukáš Ustrnul, Nele Konrad, Kristjan Siilak, Tatsiana Burankova, Reiko Kuroda, Mathias O. Senge, Victor Borovkov, Jas S. Ward, Kari Rissanen, Riina Aav, "Chiral Self-Assembly of Zinc and Magnesium Porphyrins with Enantiopure Cyclohexanohemicucurbiturils in Solution and in Solid State", *Inorg. Chem.* **2025**, 64, 48, 23773–23785

II **Marko Šakarašvili**, Lukas Ustrnul, Elina Suut, Jagadeesh Varma Nallaparaju, Kamini A. Mishra, Nele Konrad, Jasper Adamson, Victor Borovkov and Riina Aav, "Self-Assembly of Chiral Cyclohexanohemicucurbit[*n*]urils with Bis(Zn Porphyrin): Size, Shape, and Time-Dependent Binding", *Molecules* **2022**, 27(3), 937

III Gabriele Magna, **Marko Šakarašvili**, Manuela Stefanelli, Gabriele Giancane, Simona Bettini, Ludovico Valli, Lukas Ustrnul, Victor Borovkov, Riina Aav, Donato Monti, Corrado Di Natale and Roberto Paolesse, "Chiral Recognition by Supramolecular Porphyrin–Hemicucurbit[8]uril-Functionalized Gravimetric Sensors", *ACS Appl. Mater. Interfaces* **2023**, 15, 25, 30674–30683

Author's Contribution to the Publications

Contributions to the papers in this thesis are:

I The study was designed in collaboration with the supervisors. The author carried out a substantial part of the experimental work, including sample preparation, spectroscopic measurements, computational and data analysis. Single-crystal X-ray diffraction measurements were carried out by Dr Khai-Nghi Truong, and the crystallographic analysis was performed by Dr Khai-Nghi Truong, Dr Jas S. Ward, and Prof. Kari Rissanen (University of Jyväskylä). Vibrational circular dichroism (VCD) measurements were performed by Nele Konrad (Tallinn University of Technology), and solid-state ECD measurements were performed by Prof. Reiko Kuroda (Chubu University). The interpretation of the results and responses to the reviewers were carried out together with the supervisors. The author prepared the manuscript, figures, and supporting information.

II The study was designed in collaboration with the supervisors. The author carried out all experimental work, including sample preparation, spectroscopic measurements (NMR, UV–vis, and CD), and data analysis. The interpretation of the results and responses to the reviewers were performed together with the supervisors. The author prepared the manuscript, figures, and supporting information.

III This work was carried out in collaboration between the research groups of Prof. Riina Aav and Prof. Roberto Paolesse. The author contributed to the preparation of sensing films based on cycHC[8]–metalloporphyrin systems and their spectroscopic characterization (CD). The author participated in quartz crystal microbalance (QMB) measurements under the supervision of Dr Gabriele Magna (University of Rome Tor Vergata). The author contributed to the preparation of the supporting information, manuscript, and responses to reviewers. The main experimental design and overall coordination of the study were led by Dr Gabriele Magna and Prof. Roberto Paolesse (University of Rome Tor Vergata).

Introduction

Supramolecular chemistry exploits non-covalent interactions between modular molecular building blocks to construct functional assemblies. One area within the field is molecular recognition, in which a receptor binds a target analyte selectively through complementary non-covalent interactions. Recognition of chiral analytes (molecules that exist as non-superimposable mirror images) is among the more challenging instances, with relevance to pharmaceutical analysis[1], agrochemistry[2,3], biomedical diagnostics[4] and food safety[5], where the two enantiomers of a compound can differ substantially in biological activity and sensory properties such as taste and odour. The development of chiral receptors that are both synthetically accessible and structurally tunable is therefore an active area of research.

One approach to chiral recognition is supramolecular chirogenesis, in which chirality is transferred from one binding partner to another through non-covalent interaction. If the partner is a chromophore, the chirality transfer becomes directly detectable as an induced circular-dichroism signal, providing a sensitive optical reporter for the recognition event. Porphyrins serve this purpose well, with their intense Soret-band absorption, structural versatility, and the Lewis-acid behaviour of their central metal ion. Cyclohexanohemicucurbit[*n*]urils (cycHC[*n*]) are a family of enantiopure macrocyclic hosts whose outward-pointing carbonyl oxygens act as Lewis-base donors to the metalloporphyrin centre. The first demonstration that enantiopure cycHC[*n*] induce circular dichroism in achiral zinc porphyrins through external M···O coordination established a chirogenesis platform built from synthetically simple components.[6] The scope and limits of this platform, however, had not been systematically mapped at the start of this work. The generality of the external M···O binding mode across structurally diverse metalloporphyrins, the solid-state organisation of the resulting complexes, the behaviour of bis-porphyrin hosts capable of more complex binding modes, and the potential of these adducts as enantioselective sensing materials all remained unexplored.

This dissertation begins with a literature overview covering the supramolecular concepts on which the work is built (non-covalent interactions, binding evaluation, and the principles of induced chirality), followed by a section on porphyrins and macrocyclic hosts, with emphasis on metalloporphyrin coordination chemistry. The overview concludes with a section on supramolecular sensing, introducing quartz crystal microbalances and the use of sensor arrays for chiral analyte recognition.

The results presented in this thesis explore the scope of cycHC[*n*]·metalloporphyrin self-assembly across solution and the solid state and apply the resulting adducts as enantioselective sensing materials. The first part examines a library of nine achiral metalloporphyrins, varying in peripheral substituents, core planarity, and metal centre, and characterises their complexes with cycHC[6] and cycHC[8] by UV-vis and nuclear magnetic resonance (NMR) titrations, ECD spectroscopy in solution and the solid state, and single-crystal X-ray diffraction (Publication I). The second part extends the study to bis(zinc octaethylporphyrin), a bis-porphyrin host known to form tweezer complexes with bidentate guests, and characterises its qualitatively different binding modes with cycHC[6] and cycHC[8] by NMR, UV-vis, fluorescence, and circular dichroism spectroscopy (Publication II). The third part translates four cycHC[8]·metalloporphyrin adducts into thin-film sensing materials on quartz crystal microbalances and introduces a normalisation protocol based on virtual racemic references that enables enantiorecognition of volatile chiral analytes at unknown concentration by arrays of enantioselective sensors (Publication III).

Abbreviations

AIM	Atoms-in-molecules
BINAP	2,2′-bis(diphenylphosphino)-1,1′-binaphthalene
bis-ZnOEP	bis(Zinc(II) octaethylporphyrin)
BNSH	1,1′-binaphthalene-2,2′-dithiol
CB	Circular birefringence
CB[*n*]	Cucurbit[*n*]uril
CD	Circular dichroism
CPL	Circularly polarised luminescence
DACH	1,2-diaminocyclohexane
DCM	Dichloromethane
DMSO	Dimethyl sulfoxide
DORI	Density overlap regions indicator
Et	Ethyl
FDCD	Fluorescence-detected circular dichroism
H_2TPP	Free-base *meso*-tetraphenylporphyrin
HC[*n*]	Hemicucurbit[*n*]uril
HOMO	Highest occupied molecular orbital
HSAB	Hard–Soft Acid–Base (principle)
ICD	Induced circular dichroism
IR	Infrared (region)
IRI	Interaction region indicator
ITC	Isothermal titration calorimetry
KBr	Potassium bromide
LB	Linear birefringence
LD	Linear dichroism
LDA	Linear discriminant analysis
LUMO	Lowest unoccupied molecular orbital
MgTPP	Magnesium(II) *meso*-tetraphenylporphyrin
MOF	Metal–organic framework
NBO	Natural bond orbital
NCI	Non-covalent interaction
NMR	Nuclear Magnetic Resonance
ORD	Optical rotatory dispersion
PCA	Principal component analysis
Ph	Phenyl
QMB	Quartz crystal microbalance
RDG	Reduced density gradient
RFU	Relative Fluorescence Units
ROA	Raman optical activity

SAPT	Symmetry-adapted perturbation theory
tCB[*n*]	Twisted cucurbit[*n*]uril
THF	Tetrahydrofuran
VCD	Vibrational circular dichroism
vdW	Van der Waals
VOC	Volatile organic compound
ZnOEP	Zinc(II) octaethylporphyrin
ZnTPP	Zinc(II) *meso*-tetraphenylporphyrin

Symbols

ρ	Electron density (equation 1)
r	Coordinate vector (equation 1)
λ_2	Second largest eigenvalue of the electron-density Hessian
K_a	Association (binding) constant (equation 2)
$\Delta G°$	Standard Gibbs free energy of binding
R	Universal gas constant
T	Absolute temperature
ε	Molar absorption (extinction) coefficient
δ	Chemical shift (NMR)
P, M	Plus / Minus (Helical screw configurations)
g	Dissymmetry factor (= $\Delta A/A$ or $\Delta\varepsilon/\varepsilon$) (equation 5)
ΔA	Differential absorbance (CD signal)
A	Absorbance
g_{lum}	Luminescence dissymmetry factor
ΔT	Change in temperature (sensor transduction)
Δm	Change in mass
$\Delta\sigma$	Change in conductivity
$\Delta\Phi$	Change in work function
Δn	Change in refractive index
$\Delta\varepsilon$	Change in permittivity (sensor context)
ΔC	Change in capacitance
ΔL	Change in inductance
ΔR	Change in resistance
Δf	Change in frequency (7)
f_0	Fundamental resonance frequency of the quartz (7)
A_q	Surface area of the quartz (7)
μ_q	Shear modulus of the quartz (7)
ρ_q	Density of the quartz (7)
Δm	Adsorbed mass (7)
σ_p	Hammett substituent constant (*para*)
λ_{max}	Wavelength of absorption maximum
λ_{ex}	Excitation wavelength
θ	Ellipticity
E^R, E^L	Electric-field magnitudes of right- and left-circularly polarised light
$\bar{R}_{rac}$	Virtual racemic reference response
R_R, R_S	Responses of (*R*,*R*)- and (*S*,*S*)-sensors
$\bar{R}_{Rn}$, $\bar{R}_{Sn}$	Normalised responses of (*R*,*R*)- and (*S*,*S*)-sensors

1 Literature overview

1.1 Supramolecular Chemistry

1.1.1 Definition and evolution of supramolecular chemistry

Supramolecular chemistry is broadly defined as "chemistry beyond the molecule": a discipline that investigates how molecules organise and assemble through non-covalent interactions such as hydrogen bonding, π–π stacking, electrostatic forces, hydrophobic effects, and van der Waals forces.[7]

Jean-Marie Lehn coined the term "supramolecular chemistry" and defined it as the "chemistry of the intermolecular bond, covering the structures and functions of entities formed through the association of two or more chemical species".[8,9] However, the intellectual foundations of the field trace back much further. One of the first synthetic coordination compounds, Prussian Blue ($Fe_4[Fe(CN)_6]_3 \cdot xH_2O$), was accidentally discovered around 1706 by Diesbach and Dippel in Berlin,[10] representing an early example of extended molecular assembly. Alfred Werner's pioneering work on coordination chemistry in 1893[11] established fundamental principles of how molecules organise around metal centres. Similarly, Johannes Diderik van der Waals' description of intermolecular forces in 1873[12] provided a theoretical framework for understanding non-covalent interactions. Emil Fischer's "lock-and-key" concept introduced in 1894 articulated the principle of molecular complementarity — now recognised as the cornerstone of supramolecular recognition.[13]

The modern era of supramolecular chemistry emerged decisively in the late 1960s and early 1970s. Charles J. Pedersen's unintentional discovery of crown ethers (Figure 1 A) and their remarkable selectivity for alkali metal cations[14] demonstrated that synthetic hosts could rival biological receptors in their recognition capabilities. Jean-Marie Lehn extended these ideas through the development of three-dimensional cryptands (Figure 1 B),[8] which exhibited even greater binding selectivity due to their preorganized, three-dimensional cavities. Donald J. Cram systematically explored the principles governing host–guest chemistry, introducing concepts such as complementarity, preorganization, and the importance of cavity shape and size (Figure 1 C).[15] These foundational contributions were recognised with the 1987 Nobel Prize in Chemistry,[16] establishing supramolecular chemistry as an independent discipline spanning organic, inorganic, physical, biological, and materials chemistry.

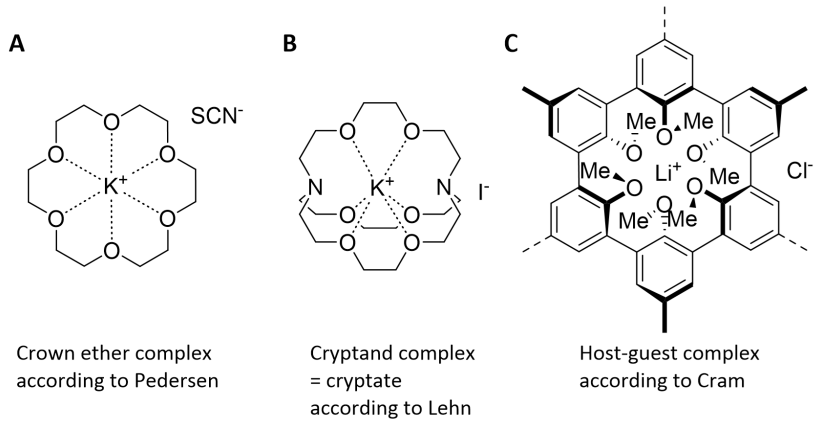

Figure 1 Structures of representative early supramolecular hosts: (A) crown ether (Pedersen), (B) cryptand (Lehn), and (C) spherand (Cram).[16]

After this recognition, the field expanded from discrete host–guest complexes to dynamic assemblies, mechanically interlocked molecules, and systems capable of controlled motion. Jean-Pierre Sauvage pioneered the template synthesis of catenanes and molecular knots,[17] J. Fraser Stoddart developed rotaxanes and molecular shuttles based on donor-acceptor interactions,[18] and Ben Feringa created light-driven molecular motors.[19] This progress toward functional molecular machines was honoured with the 2016 Nobel Prize in Chemistry.[20] More recently, the impact of supramolecular principles on materials science was recognised by the 2025 Nobel Prize in Chemistry awarded to Kitagawa, Robson, and Yaghi for their pioneering work on metal–organic frameworks (MOFs),[21–24] demonstrating how modular supramolecular design can yield functional porous materials with applications in gas storage, separation, and catalysis.

Today, supramolecular chemistry is applied in molecular sensing, drug delivery, catalysis, separation science, adaptive materials, and nanotechnology.[25]

1.1.2 Types of noncovalent interactions

Non-covalent interactions collectively define the energetic landscape of supramolecular chemistry, providing the means by which molecules recognise one another and assemble into higher-order structures. While it is convenient to categorise these interactions into distinct classes (hydrogen bonding, π–π stacking, van der Waals forces, metal–ligand coordination, ion–dipole interactions, and others), this differentiation is somewhat artificial.[26] Typical interaction types and energy ranges are listed in Table 1. In reality, supramolecular systems are governed by several interactions acting simultaneously. Their relative contributions depend on molecular geometry, electronic properties, and environmental context such as solvation and ion pairing.[26] A holistic understanding of these forces, their relative energies, and the trade-offs between them is essential for designing functional supramolecular assemblies.[27]

Table 1 Noncovalent interaction types, typical binding energies and key characteristics.[28–33]

Interaction Type	**Typical Energy Range (kJ mol^{-1})**	**Key Characteristics**
Ion–Ion	100–350	Strong, long-range; highly dependent on dielectric constant
Metal–Ligand Coordination	60–210	Directional, tunable strength; covalent/ionic character
Hydrogen Bonding	4–120	Highly directional; strength varies with D–H···A geometry
Halogen Bonding	10–150	Directional σ-hole interaction; I > Br > Cl > F
Ion–Dipole	50–200	Important in solvation and host–guest chemistry
Cation–π	5–80	Electrostatic attraction between cations and π-systems
Anion–π	20–50	Interaction with electron-deficient aromatic structures
π–π Stacking	0–50	Geometry-dependent; key in aromatic assemblies
Dipole–Dipole	4–50	Orientation-dependent electrostatic interaction
C–H···π	2–20	Weak but common in organic systems
Van der Waals (Dispersion)	0.4–4 (per contact)	Ubiquitous; cumulative over large surfaces

The interactions listed in Table 1 are predominantly attractive in nature. Exchange-repulsion (Pauli repulsion) arises at short range when molecular wavefunctions overlap: electrons become free to move over both molecules, lowering their energy, but electrons of the same spin cannot occupy the same space, which costs energy and dominates overall, resulting in a net repulsive effect.[34]

Among these diverse interaction types, metal–ligand coordination, van der Waals forces, and halogen bonding are particularly relevant to the research topics that this thesis is based on.

Metal–ligand coordination is among the strongest and most directional noncovalent interactions exploited in supramolecular chemistry, with bond energies in the range of 60–210 kJ mol^{-1}.[31] It arises from the donation of electron density from an electron-rich ligand to an electron-deficient metal centre, producing bonds with mixed ionic and covalent character that impose well-defined coordination geometries.[35,36] The selectivity and stability of these interactions are well rationalised by Pearson's Hard–Soft Acid–Base (HSAB) principle: hard metal ions (e.g., Mg^{2+}, Al^{3+}, lanthanides) preferentially bind hard donors such as oxygen and fluorine, while soft metal ions (e.g., Cu^{+}, Pd^{2+}, Pt^{2+}) favour softer donors including sulfur, phosphorus, and carbon. Borderline metals such as Zn^{2+} and Fe^{2+} bind both nitrogen and oxygen donors.[37,38] The coordination number and geometry are dictated by the metal's electronic configuration, ionic radius, and ligand field. Common geometries range from linear (coordination number 2, e.g. Au^{+}, Ag^{+}) through tetrahedral or square planar (4), trigonal bipyramidal or square pyramidal (5), to octahedral (6) and higher for lanthanides.[36]

Van der Waals forces, which include London dispersion (induced dipole–induced dipole), Debye (permanent dipole–induced dipole), and Keesom (permanent dipole–permanent dipole) interactions, are individually weak (0.4–4 kJ mol^{-1} per contact) but collectively significant when summed over extended molecular surfaces.[39] In supramolecular systems, they contribute substantially to crystal packing, inclusion complex stability, and host–guest complementarity, often acting synergistically with stronger directional interactions to fine-tune assembly geometry.[28] Their role is particularly pronounced in weakly competitive solvents such as chloroform and dichloromethane, where the absence of strong solvent–solute hydrogen bonding allows even modest dispersive contacts between host and guest to contribute meaningfully to overall binding affinity.[26,29]

Halogen bonding arises from the interaction between the σ-hole (an electropositive region on a covalently bound halogen atom along the extension of the R–X bond) and a nucleophilic site such as a lone pair, π-system, or anion.[32,35] The interaction is strongly directional, with R–X···Nu angles approaching 180°. Bond strengths follow the trend I > Br > Cl ≫ F and can be enhanced by electron-withdrawing substituents on the halogen donor.[32] Halogen bonding can coexist with hydrogen bonding without mutual interference, allowing both to be exploited simultaneously, and has found applications in crystal engineering, anion recognition, and organocatalysis.[32]

1.1.3 Characterization and visualization of noncovalent interactions

While experimental techniques such as X-ray crystallography and NMR spectroscopy reveal the geometries of supramolecular complexes, the underlying non-covalent interactions that stabilise them are not directly observable, and computational analysis is required to identify and visualise them. Several approaches are available, including atoms-in-molecules (AIM) analysis based on the topology of the electron density,[40] natural bond orbital (NBO) analysis of donor–acceptor interactions,[41] symmetry-adapted perturbation theory (SAPT) for energetic decomposition,[42] and Hirshfeld surface analysis for the visualisation of intermolecular contacts in crystal structures.[43] Among these, the non-covalent interaction (NCI) index introduced by Johnson and co-workers has become particularly widely used. It operates directly on the electron density, is computationally cheap, and produces visually intuitive maps that reveal both the location and nature of non-covalent contacts.[44] The approach relies on the reduced density gradient (RDG), a dimensionless quantity derived from the electron density and its first derivative. The RDG is defined by equation (1), where ρ is the electron density and r is the coordinate vector. Regions where the RDG approaches zero at low density correspond to non-covalent interactions.

$$\mathrm{RDG}(r) = \frac{1}{2\cdot(3\pi^2)^{1/3}} \frac{|\nabla\rho(r)|}{[\rho(r)]^{4/3}} \qquad (1)$$

The nature of these interactions is classified using the *sign* of the second largest eigenvalue (λ_2) of the electron-density Hessian. Here the Hessian is computed with respect to real-space electron density coordinates on a grid rather than atomic coordinates, making it computationally inexpensive. $\lambda_2 < 0$ indicates attractive interactions, $\lambda_2 > 0$ corresponds to steric repulsion, and values near zero represent van der Waals contacts. The second eigenvalue λ_2 changes sign between attractive and repulsive interactions, providing the most diagnostic classification, while λ_1 is negative in all bonding regions and λ_3 is always positive. Plotting the product $sign(\lambda_2)\rho$ on RDG isosurfaces produces a map that is conventionally colour-coded (blue for strong

attraction, green for weak dispersion, and red for steric clashes) to visualise the interaction landscape (Figure 2).[44]

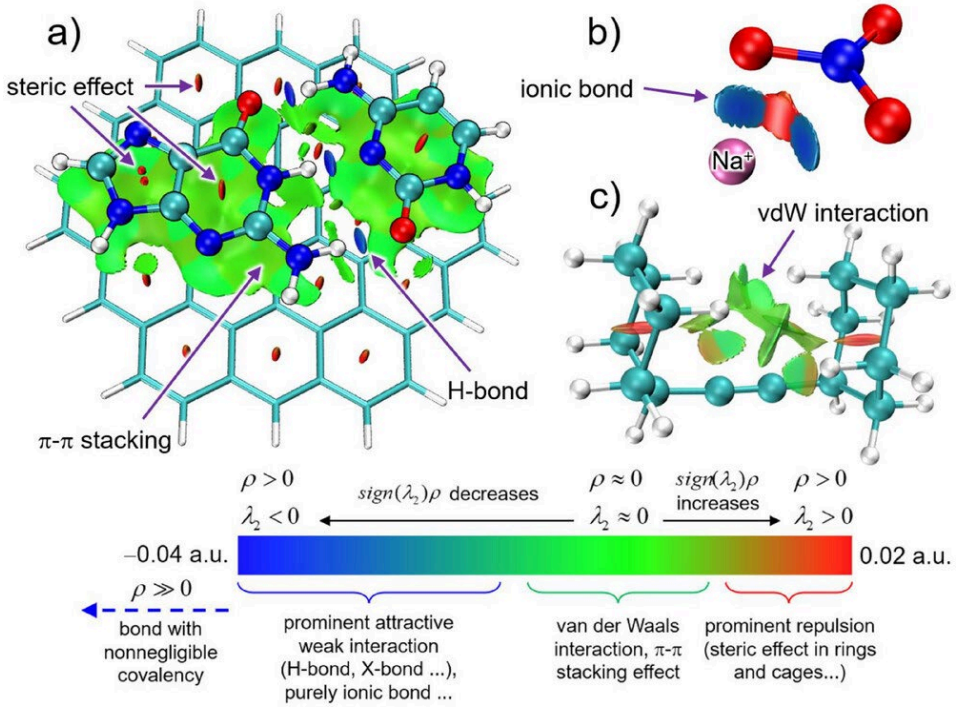

Figure 2 NCI maps of representative systems highlighting noncovalent interactions. a) Guanine-cytosine base pair adsorbed on circumcoronene, mainly showing H-bonds (blue) and π-π stacking (green). b) $NaNO_3$ molecule, illustrating ionic interactions (blue) and steric effects (red). c) axial-axial conformer of 1,2-dicyclohexylethyne molecule, primarily depicting vdW interactions (green). The colour bar indicates the sign(λ_2)ρ values, with blue representing prominent attractive interactions, red indicating prominent repulsive interactions in the regions with steric effect, and green exhibiting very weak interactions. Reproduced from reference[45].

The method can be evaluated using promolecular densities (superpositions of spherically averaged free-atom densities), making it computationally efficient and applicable to large systems including proteins. The method is implemented in the NCIPLOT program and in Multiwfn.[45,46]

A limitation of the RDG-based NCI analysis is that it cannot clearly display covalent bonding regions and weak interaction regions at the same time. Lu and Chen addressed this by proposing the interaction region indicator (IRI), which replaces the fixed 4/3 exponent in the density gradient term of RDG with an adjustable parameter *a* (2), allowing both chemical bonds and weak interactions to be visualised simultaneously on a single isosurface.[47]

$$\mathrm{IRI(r)}=\frac{|\nabla\rho(\mathrm{r})|}{[\rho(\mathrm{r})]^{a}} \qquad (2)$$

where a=1.1 is adopted as the standard value.

Compared to the density overlap regions indicator (DORI), which measures electron density overlap through a fundamentally different equation, IRI has a simpler formulation and lower computational cost. The same authors also introduced IRI-π, a

variant dedicated to revealing π-electron interactions, which can distinguish types of π-interactions and exhibit their relative strength. Both IRI and IRI-π are implemented in the freely available Multiwfn wavefunction analysis program.[47]

1.1.4 Binding evaluation in supramolecular systems

The fundamental quantity describing a host–guest interaction is the association (or binding) constant K_a, defined as the equilibrium constant for the reversible formation of the complex from its free components. For a 1:1 system:

$$\mathrm{H} + \mathrm{G} \rightleftharpoons \mathrm{HG} \qquad K_a = \frac{[\mathrm{HG}]}{[\mathrm{H}][\mathrm{G}]} \tag{3}$$

where [H], [G], and [HG] are the equilibrium concentrations of free host, free guest, and complex, respectively. For a 1:1 complex, K_a has units of M^{-1} and is related to the standard Gibbs free energy of binding through $\Delta G° = -RT \ln K_a$, providing a direct thermodynamic measure of complex stability.

When more than one host or guest can participate, higher order stoichiometries arise. The first binding step is identical to equation (3) (now denoted K_1), followed by a second step whose form depends on the stoichiometry: for 1:2 (host:guest) systems a second guest binds the existing complex:

$$\mathrm{HG} + \mathrm{G} \rightleftharpoons \mathrm{HG_2} \qquad K_2 = \frac{[\mathrm{HG_2}]}{[\mathrm{HG}][\mathrm{G}]} \tag{4}$$

while for 2:1 systems, a second host binds instead:

$$\mathrm{HG} + \mathrm{H} \rightleftharpoons \mathrm{H_2G} \qquad K_2 = \frac{[\mathrm{H_2G}]}{[\mathrm{HG}][\mathrm{H}]} \tag{5}$$

The interpretation of these stepwise constants must account for both the underlying thermodynamics and the statistical degeneracy of the binding sites. The most common approach for quantifying host–guest interactions in supramolecular chemistry is a titration experiment in which increasing amounts of a guest are added to a solution of the host while monitoring changes in a spectroscopic property such as UV-Vis absorption, fluorescence emission, or NMR chemical shift.[48] The resulting binding isotherm (a plot of the observed spectral change against guest concentration, shown in Figure 3) is then fitted to a stoichiometric binding model to extract the association constant (K_a). In addition to spectroscopic techniques, potentiometric titration can be employed when binding changes the activity of an electrode-detectable species in solution, most commonly the proton activity measured by pH electrodes. Calorimetric titration, most commonly isothermal titration calorimetry (ITC), directly measures the heat released or absorbed upon complex formation. It enables simultaneous determination of binding stoichiometry, K_a, and thermodynamic parameters such as enthalpy and entropy, without requiring an optical probe.[28]

The choice of analytical technique depends on the concentration, binding strength and the nature of the spectral response. UV-Vis and fluorescence methods are suited to micromolar host concentrations, where signal changes are often large and readily quantified, while NMR titrations operate in the millimolar range and provide atom-level information about the binding geometry through chemical shift perturbations.[48] In all cases, the selection of an appropriate binding model (1:1, 1:2, 2:1, or higher stoichiometries) is critical and should be guided by systematic comparison of residuals across models rather than by assumption. The pattern of residuals is itself diagnostic:

randomly scattered residuals indicate an appropriate model, whereas systematic, non-random trends (for example, sinusoidal deviations) signal that the chosen model fails to describe the data, regardless of the apparent quality of the isotherm fit (Figure 3). A persistent bias in the supramolecular chemistry literature toward 1:1 binding models often leads to the neglect of higher-order aggregates. Fitting a 1:2 system to a 1:1 model can yield physically meaningless apparent association constants that deviate by an order of magnitude or more from the true values.[49]

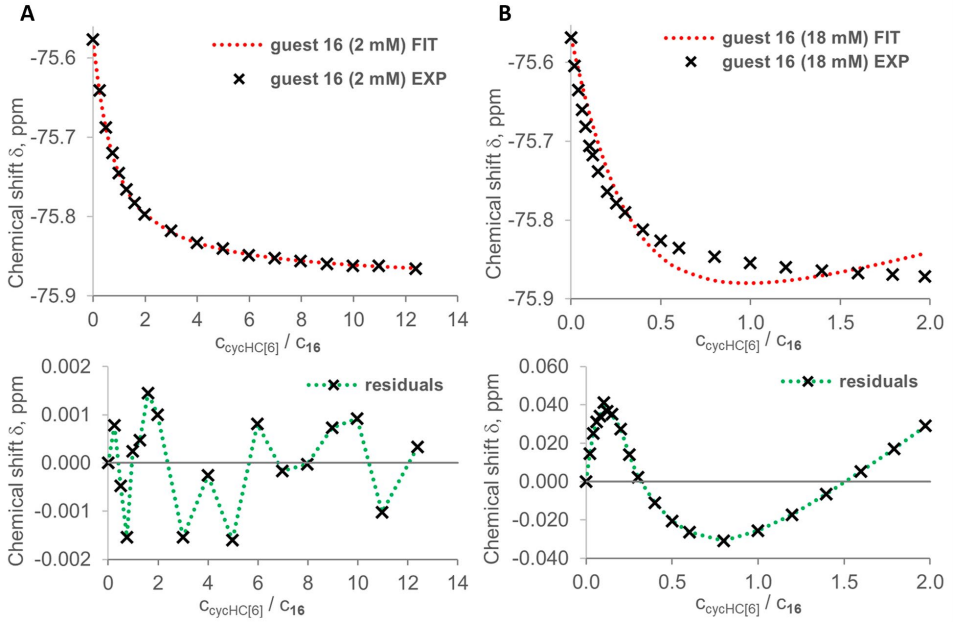

Figure 3 Examples of fitting by the online tool Bindfit (supramolecular.org) using a 2:1 binding model for trifluoroacetic acid titrated by cycHC[6] at different concentrations. Upper graphs show experimental points (black crosses) and fitted binding isotherm (red dashed line); lower graphs show residuals (distance between the experimental value and fitted isotherm). A) 2 mM trifluoroacetic acid, authors obtained a good fit and K_{1obs} = 928 ± 17 M^{-1} and K_{2obs} = 501 ± 38 M^{-1}. However, for (B) 18 mM trifluoroacetic acid, authors obtained a poor fit reflecting the inappropriate binding model (K_{1obs} = 0.04 ± 0.01 M^{-1}, K_{2obs} = 228544 ± 21727 M^{-1}). Reproduced from reference[50] under CC BY 4.0.

A key methodological requirement is the use of non-linear regression rather than linearised methods such as the Benesi–Hildebrand or Scatchard plots, which introduce distorted error distributions through data transformation and can yield unreliable constants.[28] Global analysis (the simultaneous fitting of multiple datasets from a single titration, e.g., absorbance at several wavelengths) reduces parameter uncertainty and increases the likelihood of identifying the true best-fit solution.[48]

Hibbert and Thordarson subsequently demonstrated that the Job plot (continuous variation method), long used to determine binding stoichiometry, is inappropriate for most problems in host–guest chemistry, and recommended instead the systematic fitting and testing of all reasonable binding models as the preferred approach for stoichiometry determination.[51] The same authors developed a set of best-practice protocols for data analysis in supramolecular chemistry, including rigorous uncertainty estimation and transparency in methodology, and introduced the open-access web platform

supramolecular.org (BindFit) to standardise the fitting of titration data across the community.[48,51]

When a host contains multiple binding sites, the observed binding behaviour must be interpreted in terms of cooperativity: the extent to which occupation of one site influences the affinity of subsequent sites. Hunter and Anderson provided a foundational framework for analysing cooperativity in supramolecular systems, highlighting that the chelate effect is a major origin of positive cooperativity in self-assembled structures and that its importance had often been underestimated.[52] Apparent changes in stepwise binding constants must be evaluated against a statistical (non-cooperative) reference state. In a purely statistical system with identical independent binding sites, the ratio of successive binding constants is governed solely by degeneracy factors rather than intrinsic changes in affinity. For example, a host with two identical independent sites exhibits $K_1/K_2 = 4$ for purely statistical reasons. Deviations from this ratio indicate positive cooperativity ($K_1/K_2 < 4$) or negative cooperativity ($K_1/K_2 > 4$).[52]

Von Krbek, Schalley, and Thordarson subsequently proposed a systematic classification of cooperativity in supramolecular systems into four categories: cooperative aggregation (e.g., supramolecular polymerisation), intermolecular (allosteric) cooperativity, intramolecular (chelate) cooperativity quantified via effective molarity, and interannular cooperativity in multiring or cage architectures.[53] Each type can be analysed thermodynamically by comparing experimentally determined stepwise binding constants with those predicted by the statistical model, yielding quantitative cooperativity factors. The same review emphasises that ITC remains underutilised in supramolecular chemistry despite its particular power for dissecting cooperative phenomena through direct measurement of enthalpic and entropic contributions.[53]

1.2 Chirality in Supramolecular Systems

1.2.1 Fundamentals of molecular and supramolecular chirality

Chirality, derived from the Greek word *cheir* meaning hand, describes the geometric property of an object that is non-superimposable on its mirror image. Enantiomers are identical in all scalar physical properties, yet they interact differently with polarised light and biological receptors. This distinction has practical consequences in pharmacology[1,54] and in food science, where the enantiomers of carvone, for example, are perceived as entirely different odours.[55] Similar claims have been made for limonene, although in some studies the reported differences were attributed partly to trace impurities.[56] Molecular chirality takes several distinct forms. Central chirality arises from a tetrahedral stereogenic atom bearing four distinct substituents, as in alanine (Figure 4 panel A) and ibuprofen, whose enantiomers differ significantly in pharmacological activity. Axial chirality occurs when groups on either side of a stereogenic axis cannot interconvert by rotation, as in the BINAP scaffold[57] (Figure 4 panel B) and chiral allenes[58]. Planar chirality is exhibited by molecules in which a substituent pattern on a planar unit cannot be superimposed on its mirror image due to restricted interconversion of the two faces, exemplified by cyclophanes[59] (Figure 4 panel C) and ferrocenes[60]. Helical chirality describes molecules such as [*n*]helicenes[61] (Figure 4 panel D) and chiral polyisocyanates[62] that adopt *P* or *M* screw configurations.

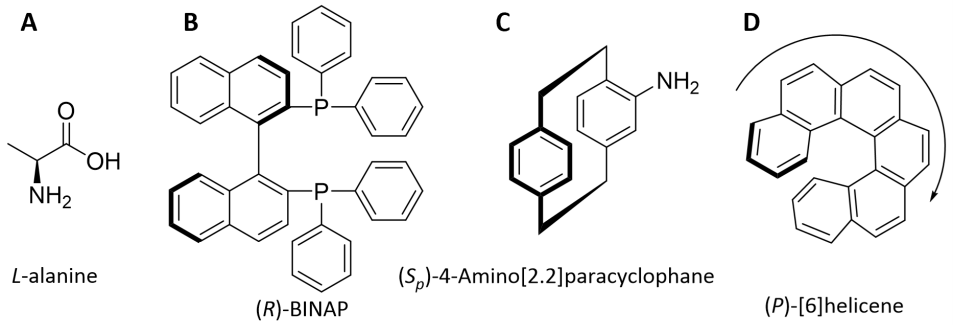

Figure 4 Representative examples of molecular chirality arising from different structural features: (A) central chirality in L-alanine, (B) axial chirality in (R)-BINAP, (C) planar chirality in (S_p)-4-amino[2.2]paracyclophane, and (D) helicity-based chirality in (P)-[6]helicene.

Supramolecular chirality arises from the non-covalent assembly of molecules into larger structures that can exhibit chirality even when the individual components are achiral. A key feature is amplification: small chiral biases, or spontaneous symmetry breaking in initially achiral systems, are reinforced through cooperative interactions, leading to strongly chiral architectures at larger length scales.[63] Helical aggregates are among the most studied manifestations. Meijer and co-workers demonstrated in oligo(phenylene vinylene) systems that small quantities of a chiral monomer bias the helical sense of an entire achiral aggregate, the "sergeant-and-soldiers" effect.[64] Chiral self-assembly encompasses larger architectures such as cages: Fujita and co-workers showed that achiral Pd(II) ions and bis-pyridine ligands self-assembled into chiral $Pd_{30}L_{60}$ spheres.[65] At the mesoscale, Feringa and co-workers demonstrated that molecular motor dopants reversibly switch the handedness of cholesteric liquid crystal phases through light-driven conformational change.[66]

1.2.2 Experimental characterization methods

Chiroptical spectroscopy comprises a family of techniques that measure how chiral molecules interact differently with right- and left-circularly polarised light, giving direct access to stereochemical information that conventional spectroscopy cannot provide. Historically, the field began with optical rotatory dispersion (ORD), which measures the wavelength dependence of optical rotation. ORD was developed into a practical structural tool for organic stereochemistry by Djerassi and co-workers in the 1950s–60s.[67] ORD was largely superseded by electronic circular dichroism (ECD), which measures the differential absorption of left- and right-circularly polarised light across electronic transitions in the UV-visible range. A chiral molecule, or an achiral molecule in a chiral environment, generates a Cotton effect (a single peak or bisignate feature) at each electronic transition.[68] When two chromophores are held in close proximity within a chiral framework, their transition dipole moments interact through space in a phenomenon called exciton coupling. This produces a characteristic bisignate Cotton effect whose zero crossing coincides with the absorption maximum of the coupled transitions. The sign of the couplet directly encodes the absolute configuration of the governing chiral element, as formalised by Harada and Nakanishi (Figure 5).[69]

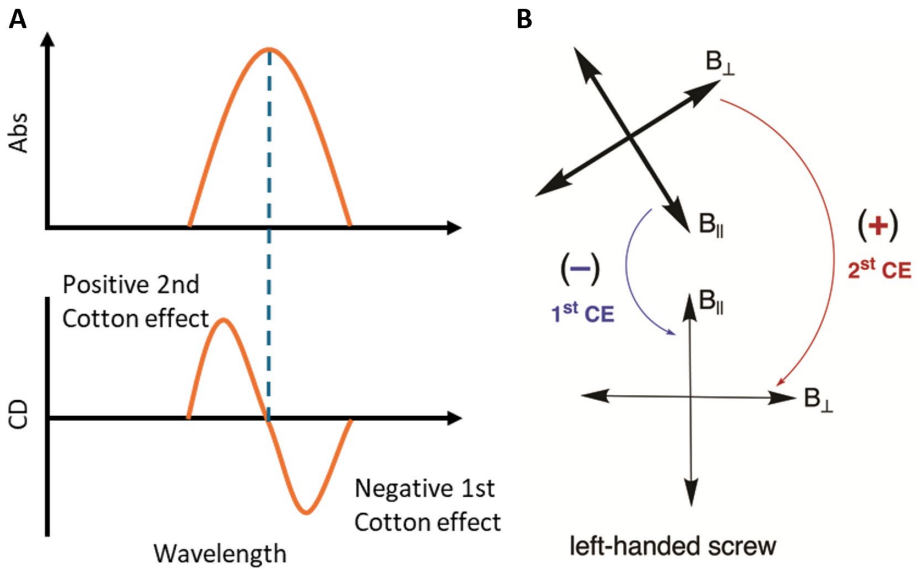

Figure 5 (A) Schematic illustration of an exciton couplet exhibiting a negative first and positive second Cotton effect (negative couplet), where the zero crossing coincides with the absorption maximum. (B) Orientation of the Soret band electronic transitions (B∥ and B⊥) in a left-handed screw arrangement, showing how the coupling of split B∥ and B⊥ transitions gives rise to the negative first and positive second Cotton effects. B panel adapted with permission from reference[70]. Copyright 2004 American Chemical Society.

The quantitative measure of chiroptical efficiency is the dissymmetry factor (equation (6), where "ΔA" is difference in absorbance between left- and right-circularly polarised light and "A" is the total absorbance) introduced by Kuhn, which is dimensionless and concentration-independent, making it the standard metric for comparing chiroptical responses across systems.[71] CD spectrometers measure ellipticity (θ) directly in millidegrees (mdeg), which is related to ΔA by ΔA = θ/32980; the two are directly proportional and interconvertible.

$$g = \frac{\Delta A}{A} = \frac{\Delta \varepsilon}{\varepsilon} \qquad (6)$$

ECD is most commonly performed in solution, although solid-state measurements on KBr pellets or thin films can enhance signals through aggregation and intermolecular exciton coupling. Solid-state ECD is particularly valuable for systems whose chiroptical properties are intrinsic to the assembled state, such as chiral aggregates, coordination polymers, and films, and that cannot be fully reconstructed from solution measurements. The KBr pellet technique, in which the sample is finely ground and pressed with potassium bromide into a transparent disc, is the most common preparation method because the resulting matrix randomises crystallite orientation and minimises macroscopic anisotropy.[72] However, solid-state samples are intrinsically anisotropic. In oriented or scattering samples, three additional optical phenomena can mix into the measured signal and mimic genuine CD (circular dichroism): linear dichroism (LD, the differential absorption along perpendicular sample axes), linear birefringence (LB, the corresponding differential refractive index), and circular birefringence (CB, equivalent to

optical rotation). Shindo and Nishio demonstrated that solid-state CD spectra of Congo red dye bound to regenerated cellulose were dominated by linear dichroism artifacts rather than genuine circular dichroism.[73] Subsequent work showed that simultaneous measurement of linear dichroism, linear birefringence, and circular birefringence is necessary to ensure artifact-free solid-state CD.[72,74,75]

Vibrational circular dichroism (VCD) is the infrared analogue of ECD. It probes local bond geometries and connectivities rather than delocalised electronic transitions, providing structural information that is highly complementary to ECD. Combined with quantum-chemical calculations, VCD is particularly powerful for determining absolute configurations.[76] In supramolecular systems, VCD can independently monitor specific functional groups within a complex, allowing the spatial extent of chirality transfer to be mapped across the assembly. VCD spectra reflect the conformational distribution of the sample, so conformationally restricted complexes give cleaner and more easily interpreted spectra than flexible molecules.[77] Raman optical activity (ROA), the Raman analogue of VCD, provides further complementary structural information though it remains less commonly applied in supramolecular chemistry.[78] Although applications of VCD to supramolecular complexes remain less developed than those of ECD, the technique has been successfully used to characterise chiral porphyrin conformers, chiral porphyrin aggregates, and host–guest assemblies based on chiral porphyrin cages. Like ECD, VCD can be measured in the solid state from KBr pellets, where rigidification of the assembly often produces sharper, more intense bands than the corresponding solution spectra.[79–81]

Circularly polarised luminescence (CPL), which probes excited-state geometry through differential emission of circularly polarised light, has found growing application in helicene-based emissive materials[82] as well as supramolecular chiroptical sensing[83]. Its quantitative metric, the luminescence dissymmetry factor g_{lum}, is the emission analogue of the ECD *g*-factor and is similarly dimensionless and concentration-independent.

1.2.3 Induced chirality in non-chiral chromophores

Induced circular dichroism (ICD) refers to the emergence of CD signals in an achiral chromophore upon interaction with a chiral entity through non-covalent forces. The phenomenon was first reported in the 1960s, when it was observed that achiral molecules dissolved in chiral solvents displayed CD signals at their achiral UV-vis absorption bands.[84,85] These early observations showed that chirality can be communicated to an achiral chromophore through its immediate molecular environment, without any covalent modification.

The theoretical framework for interpreting such signals was subsequently developed by Harada and Nakanishi through the exciton chirality method, which provided a rigorous basis for relating the sign and shape of bisignate ECD signals to the spatial arrangement of interacting chromophores and the absolute configuration of the governing chiral element.[69] Borovkov, Inoue and co-workers systematically developed ICD into a practical supramolecular tool using metalloporphyrins. They showed that enantiopure chiral guests bound to achiral zinc bisporphyrins through axial coordination induce strong, reproducible ECD signals via conformational restriction and interporphyrin exciton coupling. This work introduced the term supramolecular chirogenesis.[86] The general design principles governing such host–guest chiroptical responses were comprehensively reviewed by Hembury, Borovkov and Inoue.[87]

The scope of supramolecular chirogenesis extends well beyond porphyrin systems. Xie, Würthner and co-workers demonstrated that atropo-enantiomeric perylene bisimides form chiral J-aggregates with intense bisignate ECD signals, with the aggregate handedness templated by the axial chirality of the perylene core.[88] Matile, Berova, Nakanishi and co-workers showed that porphyrin chromophores attached to steroids as bichromophoric reporters produced reliable exciton-coupled ECD signals for absolute configuration determination at remote stereocentres.[89] They subsequently showed that porphyrins positioned at the termini of dimeric steroids and brevetoxin B can sustain exciton coupling over interchromophoric distances of up to ~50 Å.[90] More recently, Sasafuchi, Yoshizawa and co-workers demonstrated remote chirality transfer via helical polyaromatic capsules, where encapsulation of achiral guests induced ECD signals propagated through the capsule framework.[91] Similarly, Benchimol, Clever, Gunnlaugsson and co-workers reported ICD on encapsulated fullerenes C_{60} and C_{70} within chiral Pd_2L_4 cages.[92]

1.3 Porphyrins and Macrocyclic Hosts in Supramolecular Chemistry

1.3.1 Porphyrins and Metalloporphyrins

Porphyrins, often called the "pigments of life," are widespread in nature, occurring in organisms from bacteria to plants and animals. The name "porphyrin" is derived from the Greek word *porphyra*, meaning purple, a reference to the intense colour associated with these compounds. They are fundamental to life: the porphyrin ligand binds iron to form heme, the active site of haemoglobin responsible for oxygen transport in blood, and binds magnesium to form chlorophyll, the primary driver of photosynthesis in plants. The tetrapyrrolic family extends beyond heme and chlorophyll: vitamin B12 (a corrin containing cobalt, essential for carbon-skeleton rearrangements and methylation reactions) and cofactor F430 (a corphin containing nickel, the active cofactor in methanogenesis).[93–95]

From a structural perspective, porphyrins are aromatic tetrapyrrolic macrocycles composed of four pyrrole subunits linked at their α-positions by methine bridges to form a highly conjugated, planar macrocyclic framework (Figure 6). Their aromatic character arises from an 18 π-electron conjugation pathway satisfying Hückel's (4n + 2) rule (n = 4). Vogel[94,96] articulated a unifying conceptual framework recognising porphyrin as a diaza[18]annulene, which underpins the entire family of porphyrinoid macrocycles.

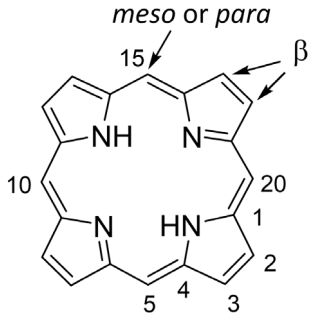

Figure 6 Structure of the free-base porphine (porphyrin) macrocycle, with the meso- and β-pyrrolic positions indicated.

The optical properties of porphyrins are governed by transitions within the delocalised π system and are well described by the four-orbital model introduced by Gouterman (see section 1.3.2).[97,98]

The porphyrin macrocycle contains four inwardly directed nitrogen atoms arranged in a square-planar N_4 cavity capable of coordinating a broad range of metal ions through displacement of the two inner N–H protons.[99] Most metals across the periodic table can be inserted into porphyrins, as illustrated by the "periodic table of metalloporphyrins" (Figure 7). Metallation preserves the aromatic character of the macrocycle whilst introducing coordination and redox properties dictated by the electronic configuration and oxidation state of the central metal, establishing metalloporphyrins as building blocks in supramolecular chemistry, catalysis, and sensing. [98–102]

Li												B		
Na	Mg											Al	Si	
K	Ca	Sc	Ti	V	Cr	Mn	Fe	Co	Ni	Cu	Zn	Ga	Ge	As
Rb	Sr	Y	Zr	Nb	Mo	Tc	Ru	Rh	Pd	Ag	Cd	In	Sn	Sb
Cs	Ba	La	Hf	Ta	W	Re	Os	Ir	Pt	Au	Hg	Tl	Pb	Bi
				Pr	Eu	Yb								
			Th											

Figure 7 The periodic table of metals that form metalloporphyrins (Metals which are inserted by Nature are coloured green). Adapted from reference[103].

This work is concerned principally with the magnesium(II) and zinc(II) complexes of *meso*-tetraphenylporphyrin, MgTPP and ZnTPP. MgTPP is the simplest fully synthetic analogue of the magnesium-centred tetrapyrrolic coordination unit found in chlorophyll. ZnTPP is not naturally occurring either, but it has become one of the most extensively studied metalloporphyrins because of its chemical stability, synthetic accessibility, and favourable photophysical and electrochemical properties.[104] Both metals have closed-shell electron configurations: Mg^{2+} has [Ne] and Zn^{2+} has $[Ar]3d^{10}$. Their complexes are therefore diamagnetic and easier to study than paramagnetic (open-shell) systems, in which the unpaired electrons cause line broadening in NMR and quench fluorescence.

Despite their differing d-electron counts, Mg^{2+} (d^0) and Zn^{2+} (d^{10}) exhibit closely related coordination behaviour in the porphyrin environment. Neither configuration carries an electronic preference for five-coordination, yet both ions are large enough to be displaced from the N_4 mean-plane, giving rise to C_{4v} square-pyramidal monoadducts with a single axial ligand; Hoard has argued that this geometry is imposed by the dimensional constraints of the porphinato core rather than favoured electronically.[105] Solution equilibrium studies are consistent with this picture: the first pyridine ligand binds with log $K_1 \approx 3.6$ to both MgTPP and ZnTPP in DCM[106,107] but binding of a second axial ligand (which would require the metal to move back into the porphyrin plane) is thermodynamically unfavourable. For ZnTPP, no six-coordinate adduct is detected with pyridine,[107] whilst for MgTPP a weak second binding is still measurable ($K_2 \approx 0.2\ M^{-1}$ for pyridine).[103,106] The five-coordinate geometry also stabilises the axial bond itself: in five-coordinate MgTPP·pyridine the Mg–N(py) distance is approximately 2.14 Å, whereas in the six-coordinate bis(pyridine) adduct the Mg moves back towards the porphyrin plane and the axial bond elongates to 2.34 Å, reflecting the geometric cost of accommodating two axial ligands simultaneously.[105]

The two metals differ markedly in their affinity for oxygen donors. Mg^{2+} ranks considerably more oxophilic than Zn^{2+} (0.6 vs 0.2 on Kepp's quantitative scale)[108], and this is confirmed experimentally — MgTPP readily coordinates water, alcohols, and carbonyl oxygens, crystallising as an aquo adduct under ambient conditions,[106] whereas ZnTPP binds methanol only weakly ($K \approx 7.3\ M^{-1}$ in chloroform[109]; $K \approx 10.7\ M^{-1}$ in DCM, Publication I).

The porphyrin ring system offers two peripheral sites for functionalisation, the *meso* positions and the β-pyrrolic positions (Figure 6), allowing systematic tuning of solubility, electronic properties, and binding affinity.[94,110] Peripheral substituents at the *meso* and β-pyrrolic positions perturb the energies of the frontier molecular orbitals, with the nature and position of the substituent governing the direction and magnitude of the resulting shifts in the Soret and Q bands.[97] Sterically demanding β-pyrrolic substituents can distort the macrocycle from planarity through nonplanar deformation modes (saddling, ruffling, and doming), each modifying the optical and redox properties in characteristic ways.[111,112]

1.3.2 Structural and spectroscopic features of porphyrins

The characteristic visible absorption of metalloporphyrins arises from their frontier molecular orbital structure, described by Gouterman's four-orbital model:[97] two nearly degenerate HOMOs of a_{1u} and a_{2u} symmetry and two degenerate LUMOs of e_g symmetry. Mixing of these configurations between the two resulting excited states produces two observable transitions of markedly different intensity: a strongly allowed transition giving rise to the intense Soret (B) band near 400 nm with molar absorption coefficients exceeding $10^5\ M^{-1}\ cm^{-1}$, and a weakly allowed transition producing the Q bands in the 500–700 nm region, whose low intensity reflects near-complete cancellation of the contributing transition dipole moments.[97] The Soret band is named after Jacques Louis Soret, who first described it in 1883; the B and Q band notation was introduced by Platt in 1949.[113]

Free-base porphyrins possess D_{2h} symmetry imposed by the two inner N–H protons, which differentiates the *x* and *y* molecular axes (the two N–H–bearing pyrroles versus the two imine pyrroles), lifts the degeneracy of the e_g LUMOs, and generates four distinct Q bands designated $Q_x(0,0)$, $Q_x(1,0)$, $Q_y(0,0)$, and $Q_y(1,0)$.[97] Upon metallation, the inner protons are displaced, all four pyrroles become equivalent, and the symmetry rises to D_{4h}. The two LUMO components become degenerate, and the Q-band manifold collapses to two transitions, Q(0,0) and Q(1,0), accompanied by a characteristic increase in Soret band intensity and a red shift in its position.[97,98] This collapse from four to two Q bands is routinely used to confirm metal insertion and to assess metalloporphyrin purity, and is well illustrated in the comparative spectra reported by Gouterman[97] and in numerous subsequent studies across the porphyrin literature.[114]

Metalloporphyrins are also fluorescent, with emission typically from the S_1 state in the 600–700 nm region. Several metalloporphyrins, including ZnTPP and MgTPP, additionally exhibit emission from the S_2 state, which is unusual as most molecules relax non-radiatively from higher excited states to S_1 before emission occurs.[114,115]

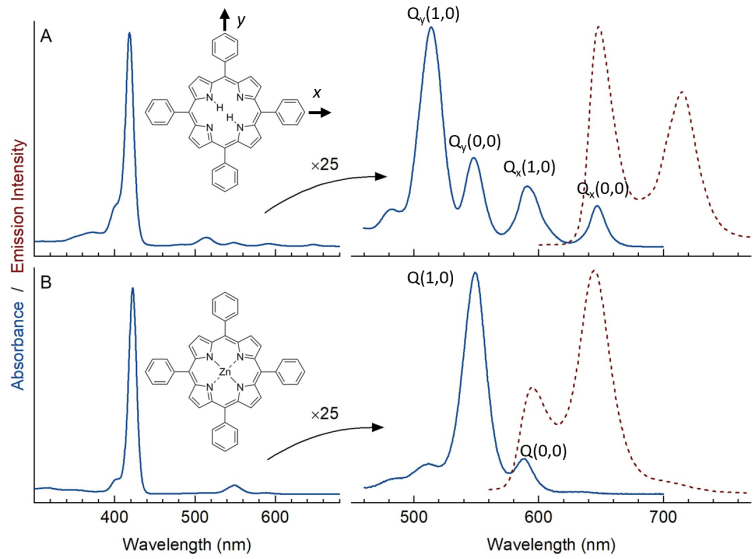

Figure 8 Room-temperature absorption (blue) and emission (red, dashed) spectra of H_2TPP (A) and ZnTPP (B) in toluene. The 450–700 nm region of the absorption spectra is shown ×25 vertically expanded; emission spectra are normalised to the strongest band. The lower (D_{2h}) symmetry of free-base H_2TPP gives rise to four Q-bands — $Q_x(0,0)$, $Q_x(1,0)$, $Q_y(0,0)$, $Q_y(1,0)$ — while the D_{4h} symmetry of ZnTPP yields only two, Q(0,0) and Q(1,0). Molecular axes (x, y) for H_2TPP are indicated. Adapted from reference[114]. Copyright (2021), with permission from Elsevier.

The Soret band position is sensitive to the identity of the coordinated metal and the nature of peripheral substituents. Electron-donating metal centres shift the Soret band bathochromically (red shift) relative to the free base, whilst strongly electron-withdrawing centres produce hypsochromic shifts (blue shift), reflecting changes in the HOMO–LUMO gap.[97] Axial ligand coordination to zinc(II) or magnesium(II) metalloporphyrins induces further red shifts of both the Soret and Q bands, typically of 2–5 nm. These shifts are routinely used to determine association constants by spectrophotometric titration in porphyrin-based host–guest chemistry.[98,99]

Porphyrins are also strong chromophores for circular dichroism (CD) spectroscopy, an area developed by Nakanishi, Berova, and co-workers.[89,98] When two porphyrin units are held in a chiral arrangement, either through covalent linkage or non-covalent host–guest assembly, the intense Soret band gives rise to a bisignate exciton-coupled CD couplet. The amplitude of this couplet scales with the square of the molar absorption coefficient and with the interchromophoric distance, making porphyrins among the most sensitive reporter groups for CD-based structural analysis; reliable measurements have been reported at concentrations as low as 10^{-8} M by conventional CD and 10^{-10} M by fluorescence-detected CD (FDCD).[98] The sign of the couplet, defined by the first Cotton effect at longer wavelength, reflects the sense of helical twist between the electric transition dipole moments of the two porphyrin chromophores and allows non-empirical assignment of absolute configuration without reference to model compounds.[98]

Finally, ^{1}H NMR spectroscopy provides complementary structural information through the large diamagnetic ring current of the aromatic porphyrin macrocycle. This shifts protons located above or below the macrocycle plane strongly to lower frequency (typically –2 to –4 ppm for the inner NH protons of free-base porphyrins) and peripheral

β-pyrrolic and *meso* protons to higher frequency (typically 8–10 ppm).[99,103] This effect is diagnostically sensitive to π–π stacking interactions between porphyrin units and to the binding of guests within porphyrin cavities, and has been used to confirm intramolecular porphyrin–porphyrin stacking in bis-porphyrin derivatives through the characteristic splitting of aromatic ^{1}H NMR signals.[70]

1.3.3 Bisporphyrins

Bisporphyrins (also called diporphyrins) consist of two porphyrin macrocycles held within a single molecular entity, and are commonly classified by how the two cores are connected. In directly linked systems the two macrocycles share one or more covalent bonds between their peripheral atoms: *meso*–*meso* singly-linked, doubly (*meso*–β), or fully fused "porphyrin tape" arrays, an area studied by Osuka and co-workers.[70,116] In linker-connected systems the two porphyrins are tethered through an external spacer. Rigid aromatic scaffolds such as anthracene, xanthene, dibenzofuran, or biphenyl enforce cofacial "face-to-face" or "Pacman" geometries, while flexible aliphatic tethers and alkyne/butadiyne bridges allow conformational freedom.[70,117,118] In supramolecular bisporphyrins the two units are not covalently joined but held together by non-covalent forces such as hydrogen bonding, π-stacking, or metal–ligand coordination.[118,119] Bisporphyrins are also useful reporters for the exciton chirality method.[69] The intense Soret (B) transition of each porphyrin (ε ≈ 10^5 M^{-1} cm^{-1}) gives strong through-space exciton coupling whenever the two macrocycles adopt a non-coplanar, chiral arrangement.[89,118] The classic system here is the ethane-linked bis(zinc(II) octaethylporphyrin), hereafter bis-ZnOEP, developed by Borovkov, Inoue and co-workers as a flexible "tweezer" host whose two zinc centres bind guest ligands and translate their point chirality into a CD-active twist between the two porphyrin planes.[70,86]

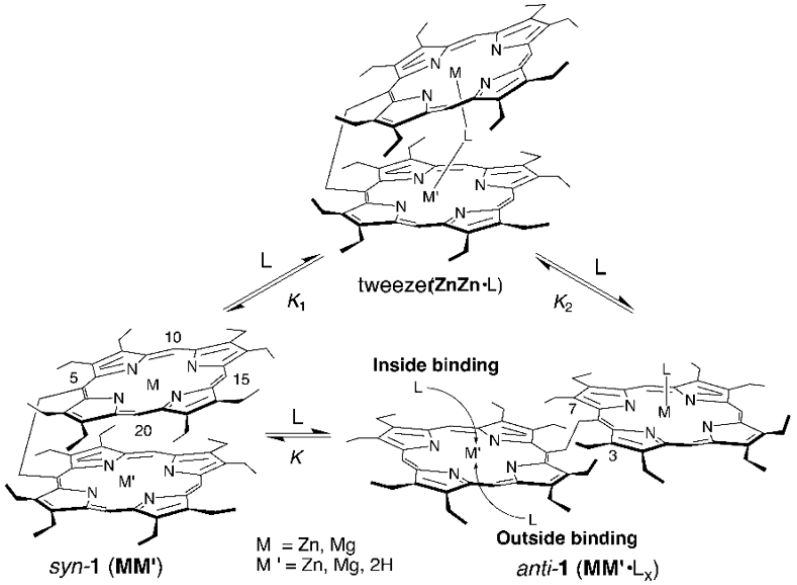

Figure 9 Conformations of the bis(zinc octaethylporphyrin) (bis-ZnOEP) host: the syn (closed) form, the tweezer form induced by coordination of a binodentate ligand (L), and the fully opened anti form stabilised by binding of two ligands (2L). Adapted with permission from reference[70]. Copyright 2004 American Chemical Society.

1.3.4 Cucurbiturils and hemicucurbiturils

Cucurbit[*n*]urils (CB[*n*]) are a family of barrel-shaped macrocyclic hosts composed of glycoluril units linked by pairs of methylene bridges, with two identical carbonyl-lined portals and a hydrophobic inner cavity. The parent CB[6] (Figure 10) was first obtained by Behrend in 1905,[120] but its structure remained unresolved until Mock's reinvestigation in 1981,[121] and the homologous series CB[5]–CB[8] was reported by Kim et al. around the turn of the millennium.[122] The family has since been extended to CB[10] and to the larger twisted homologues tCB[13], tCB[14], and tCB[15], which adopt figure-of-eight geometries rather than the conventional barrel.[123–125] CB[*n*]s bind cations and neutral guests with high affinities in aqueous media, with association constants reaching 10^{15} M^{-1} for CB[7] complexes,[126] through a combination of ion–dipole interactions at the carbonyl portals and hydrophobic encapsulation inside the cavity. CB[*n*]s have since become central to supramolecular catalysis, drug delivery, and sensing.[127]

Hemicucurbit[*n*]urils (HC[*n*]) differ from CB[*n*]s in a single but consequential structural feature: only one methylene bridge connects adjacent urea moieties instead of two. As a result, neighbouring urea units are forced into opposite orientations around the macrocyclic belt, with their carbonyl groups pointing alternately up and down. The first hemicucurbituril, HC[6] (Figure 10), was reported by Miyahara in 2004,[128] and the family has since been extended by Sindelar's bambus[*n*]urils[129] and related single-belt architectures. Unlike CB[*n*]s, hemicucurbiturils bind anions rather than cations, with selectivity governed by anion size, shape, and charge distribution rather than simple hydrophobic fit.[130]

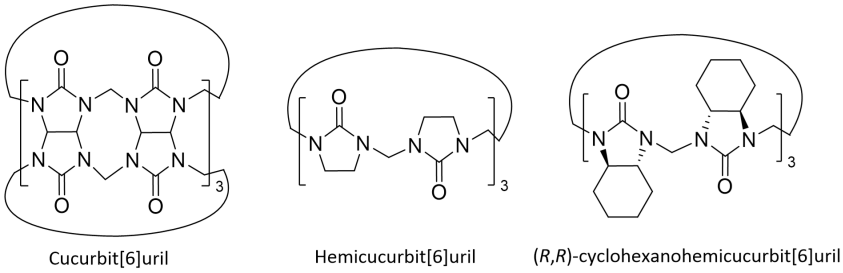

Figure 10 Structures of cucurbit[6]uril, hemicucurbit[6]uril, and (R,R)-cyclohexanohemicucurbit[6]uril, illustrating the structural relationship between the parent and its analogues.

A limitation of the parent CB[*n*] and HC[*n*] families is that they are achiral. Introducing inherent chirality has proved challenging. Enantiopure variants remained rare until Aav and co-workers developed the template-controlled synthesis of cyclohexanohemicucurbit[*n*]urils (cycHC[*n*]), in which each urea-based monomer is fused to a (*R*,*R*)- or (*S*,*S*)-cyclohexane ring. The ring size is controlled by the templating anion employed during macrocyclisation: chloride templates favour cycHC[6] (Figure 10),[131] larger anions such as hexafluorophosphate direct the assembly towards cycHC[8].[132] Both cycHC[6] and cycHC[8] have a height of approximately 1 nm, with outer diameters of 1.4 and 1.7 nm respectively, and present six or eight outward-pointing carbonyl oxygens in the equatorial region that can participate in external binding.

The binding behaviour of cycHC[*n*]s is strongly solvent-dependent. In protic media such as water and methanol, cycHC[6] and cycHC[8] act as anion receptors, encapsulating halides, oxoanions, and related species inside the hydrophobic cavity with selectivity governed by size and charge complementarity.[133] They also form inclusion complexes

with polar organic guests[50] and electron-rich heterocycles, the latter enabling selective extraction of sulfur compounds from water.[134] In non-protic solvents such as dichloromethane, however, the cavity remains unoccupied and the outward-facing carbonyl oxygens become the dominant binding sites, forming external interactions with Brønsted and Lewis acids.[50,135] This external binding mode is directly relevant to the present work: the electron-rich carbonyl groups of cycHC[*n*]s are well positioned to coordinate to the Lewis acidic metal centres of metalloporphyrins, enabling supramolecular self-assembly in which chirality is transferred from the enantiopure host to the inherently achiral porphyrin guest.[6] Ustrnul and co-workers demonstrated this principle in 2019, showing that (*R*,*R*)- and (*S*,*S*)-cycHC[*n*]s induce mirror-image ECD signals in the Soret region of ZnOEP and ZnTPP through Zn···O=C coordination,[6] and subsequent work extended the concept. These porphyrin–cycHC[*n*] systems form the supramolecular platform explored throughout this thesis.

1.4 Supramolecular Sensing and Material Design

1.4.1 General principles of sensor and supramolecular sensing

Chemical sensors are analytical devices that detect and quantify chemical species by converting chemical information into a measurable signal. They consist of a sensing material (receptor), which interacts with the analyte, and a transducer that converts this interaction into an electrical or optical output.[102] These devices enable rapid, real-time, and on-site monitoring of chemical compounds in applications such as environmental control, healthcare, and food safety.[136] The sensing mechanism relies on changes in physical properties of the sensing material upon analyte interaction. In optical sensors, these include variations in absorbance, fluorescence or emission, as well as other optical parameters such as refractive index and reflectivity, while other sensor types may measure changes in conductivity, mass, or electrochemical properties.[137,138] An additional advantage of optical sensing is that the transducer and sensing element can be physically separated.

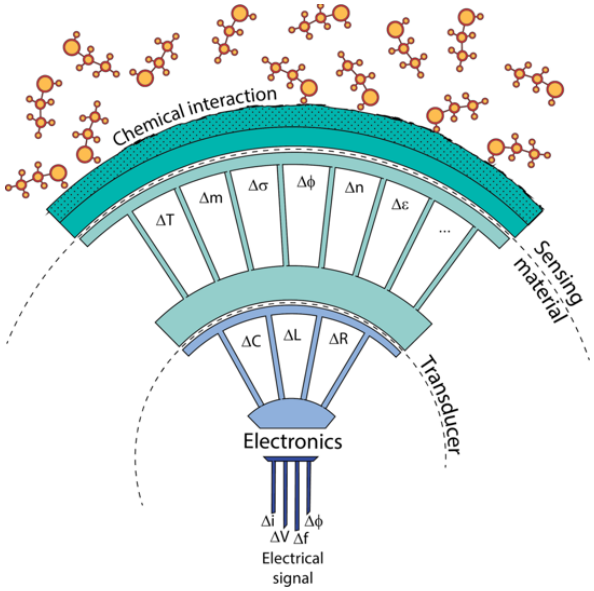

Figure 11 Logical structure of a chemical sensor. Analytes interact with the sensing material and change one or more of its physical properties (such as temperature ΔT, mass Δm, conductivity Δσ, work function ΔΦ, refractive index Δn, or permittivity Δε). The transducer is an electronic device that converts the changed property into a variation of one of its electrical parameters (here capacitance ΔC, inductance ΔL, or resistance ΔR). The connected electronics then produce the final electrical signal, which can be measured as a current or voltage in terms of magnitude, frequency, or phase. Reproduced with permission from reference[102]. Copyright © 2016 American Chemical Society.

Two key performance parameters are sensitivity and selectivity. Sensitivity refers to how strongly the sensor signal changes with analyte concentration, determining the detection limit, while selectivity describes the ability to distinguish a target analyte from interfering species in complex mixtures.[102] For quantitative applications, a well-defined and reproducible relationship between signal and concentration is additionally required. Achieving high sensitivity and selectivity depends on the properties of the sensing material. Among these, porphyrins are widely used in chemical sensors because of their structural and optical properties. They possess a large π-conjugated aromatic system and can undergo reversible binding interactions, catalytic processes, and optical or electrochemical changes upon analyte interaction.[102] Their optical properties, including intense, spectrally narrow light absorption and fluorescence, enable high sensitivity, while their chemical structure can be easily modified to tune selectivity toward specific analytes.[137] Furthermore, porphyrins can coordinate metal ions and interact with analytes through various mechanisms such as π–π interactions or axial coordination, enhancing their versatility in sensing applications.[102,137]

An advanced extension of chemical sensing is chiral sensing, which focuses on the discrimination of enantiomers. Because enantiomers have nearly identical physical properties in achiral environments, their differentiation requires a chiral recognition element that forms distinct interactions with each enantiomer, often through non-covalent forces, creating different binding affinities.[139] This molecular recognition must be coupled to a transduction mechanism that converts these differences into measurable signals. Several transduction approaches, including optical, electrochemical, and mass-

sensitive techniques such as quartz crystal microbalance (QMB), have been developed for this purpose.[139]

1.4.2 Quartz crystal microbalance (QMB)

Quartz crystal microbalances (QMBs) are highly sensitive mass-based sensors that operate on the principle of piezoelectricity, enabling the detection of extremely small mass changes at surfaces. A typical QMB consists of an AT-cut quartz crystal disc placed between two metal electrodes (commonly gold). When an alternating electric field is applied, the quartz crystal itself oscillates at a fundamental resonance frequency f_o.[140] In practice the crystal forms the frequency-determining element of an oscillator circuit, and its resonance frequency is read continuously with a frequency counter. The fundamental frequency f_o is a fixed property of the crystal and is not calibrated against an external mass standard; instead, the bare crystal is measured before coating to establish a baseline, and the analytically meaningful quantity is the shift Δf relative to that baseline.

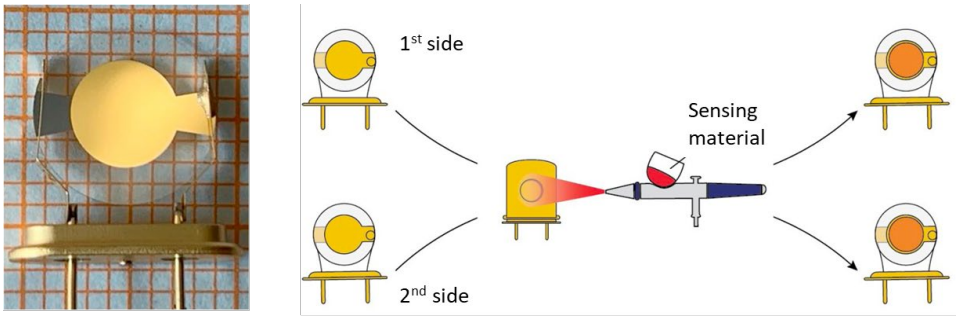

Figure 12 Left: typical quartz crystal microbalance (QMB) used in chemical and biosensing applications. Right: schematic of the procedure for estimating the amount of porphyrin deposited on the QMB. Adapted from reference[141]. Copyright (2020), with permission from Elsevier.

Adsorption of molecules onto the sensor surface increases the oscillating mass, causing a proportional decrease in the resonance frequency, a relationship described by the Sauerbrey equation (7), forming the basis for quantitative sensing.[140,142]

$$\Delta f = -\frac{2f_0^2}{A_q \cdot \sqrt{\mu_q \rho_q}} \cdot \Delta m \qquad (7)$$

where, Δf is the frequency shift, f_0 is the fundamental resonance frequency of the quartz, A_q is the quartz surface area, μ_q is the quartz shear modulus, and ρ_q is the quartz density. The Sauerbrey relation holds if the deposited film is thin, rigid and evenly distributed, with a mass small compared with that of the crystal. This direct relationship between mass loading and frequency shift allows QMBs to detect nanogram or even sub-nanogram changes in real time, making them powerful tools for chemical and biological sensing.[140] The sensing performance is determined by the functional coating applied to the electrode surface, which interacts selectively with analytes and translates molecular recognition events into measurable frequency shifts. In operation, exposure to an analyte vapour shifts the frequency away from baseline; when the analyte flow is replaced by clean carrier gas the adsorbed molecules desorb and the frequency returns to its pre-exposure baseline. The shift between the baseline and the exposure plateau is recorded as the sensor signal.

The functional coating can be deposited by several established techniques, described in detail by Zhou et al.[143] Solvent-based methods dissolve the sensing material in a volatile solvent and apply it to the electrode before the solvent evaporates, and include drop-casting, dip-coating, spray-coating and spin-coating. Self-assembly approaches such as layer-by-layer deposition, chemical vapour deposition and electrochemical deposition instead build the film through specific interactions at the surface. In each case the deposited mass is small enough to be followed directly from the frequency shift through the Sauerbrey relation. The films in this work were prepared by drop-casting and spin-coating. In drop-casting the solution is applied to the electrode with a micropipette and left to dry, which needs no specialised equipment but lets the solvent evaporate unevenly, leaving clustered material and coffee-ring deposits at the droplet edge. In spin-coating the substrate is mounted on the rotating plate of a spin-coater and the solution is dispensed onto it while the plate spins at a set speed, spreading the solution into a thin, uniform layer of a thickness governed by the rotation speed. This produces films free of the drop-casting artefacts, so spin-coating was preferred where film homogeneity mattered for the optical measurements.

The application of QMBs to chiral sensing dates back to the mid-1990s. One of the earliest demonstrations was reported by Ide et al. (1995)[144], who showed that quartz-resonator gas sensors coated with cyclodextrins could discriminate between optical isomers of aromatic compounds through differences in frequency shifts arising from enantioselective adsorption. Shortly thereafter, May et al. (1997)[145] demonstrated statistically significant discrimination of monoterpene enantiomers (e.g., α- and β-pinene) using cyclodextrin-coated QMBs, confirming that preferential host–guest interactions lead to measurable differences in frequency response. In the same period, Bodenhöfer et al. (1997)[146] further advanced the concept by combining mass-sensitive quartz resonators with chiral polymer coatings, showing that enantioselective sorption leads to distinct and reversible frequency shifts, enabling real-time monitoring of enantiomeric composition. Later work, such as that by Fietzek et al. (2001)[147], refined these approaches by employing sensor arrays and advanced data analysis methods (e.g., artificial neural networks) to improve the discrimination of enantiomers like limonene in the gas phase. These early studies demonstrated the fundamental principle that chiral recognition at the sensor surface can be directly transduced into a measurable mass signal.

A major conceptual advance in QMB-based chiral sensing was the introduction of enantiomeric sensor materials, where both enantiomers of the sensing layer are employed to form a mirror-symmetric sensing system. As already demonstrated by Bodenhöfer et al. (1997)[146], the use of enantiomeric polymer coatings ((*R*)- and (*S*)-octyl-Chirasil-Val) enables preferential sorption of matching analyte enantiomers, with switching of the analyte leading to a characteristic cross-wise inversion of the sensor signals. This dual-sensor strategy improves reliability by enabling differential comparison of responses rather than relying solely on absolute signal magnitude. Later work moved from polymers to structurally well-defined molecular systems. Self-assembled monolayers of the atropisomeric compound 1,1′-binaphthalene-2,2′-dithiol (BNSH) were immobilised on gold-coated QMB crystals, forming ordered mirror-image chiral surfaces for the (*R*)- and (*S*)-enantiomers.[148] These monolayers showed enantioselective adsorption of amino acids such as phenylalanine, with the QMB response falling into two distinct kinetic classes depending on whether analyte and surface chirality matched.[148] Monolayers gave finer control over surface chirality than polymers and more

reproducible host–guest interactions. Modern chiral QMB sensors build directly on this enantiomeric-pair principle.

1.4.3 The Electronic Nose Concept and Chemometric Analysis

Achieving high selectivity with a single chemical sensor is intrinsically difficult, because most receptors respond to a range of analytes rather than to one specific target. Biological olfaction overcomes this limitation through combinatorial coding: many olfactory receptors respond to multiple odorants with different affinities, and discrimination among thousands of distinct odorants emerges from the global pattern of activation across many receptors rather than from individual receptor specificity.[149] Artificial olfaction systems (commonly called electronic noses) apply the same principle. They use arrays of partially selective sensors whose combined responses constitute a chemical fingerprint for each analyte.[150]

The response patterns produced by sensor arrays are multidimensional and therefore require chemometric methods for interpretation. Linear discriminant analysis (LDA) is a supervised dimensionality-reduction and classification method that uses samples with known class labels to construct linear discriminant functions. The basic function of LDA is to reduce the distances present within-class while increasing the distances between different classes. In this way, the original sensor responses are projected into a lower-dimensional discriminant space where class separation is maximised and within-class spread is minimised. In a problem with k classes, LDA can reduce the data to at most k − 1 discriminant dimensions, and the resulting discriminant functions or canonical variables can be visualised in scatter plots to assess class separation. The trained model can then be used to classify unknown samples. LDA formally assumes approximately normal class distributions and comparable covariance structures, so its performance should be evaluated by validation rather than by visual separation alone.[151–153]

Porphyrin-based sensor arrays have been widely used to discriminate complex volatile organic compound (VOC) mixtures, exploiting the structural tunability of the porphyrin macrocycle to generate partially overlapping selectivity profiles.[102] Extending this approach to chiral analytes is more demanding, because individual sensors show only a small difference in response between enantiomers. The array approach, combined with suitable normalisation, can recover chiral information from these small differences; this is the idea developed in Publication III.

2 Motivation and aims for work

Cyclohexanohemicucurbit[*n*]urils (cycHC[*n*]) are a family of enantiopure macrocycles whose outward-pointing carbonyl oxygens act as Lewis-base donors to the metalloporphyrin centre. Enantiopure cycHC[*n*] were first shown to transfer chirality to achiral zinc porphyrins through external M···O coordination, producing induced circular dichroism in the porphyrin Soret region. This established a chirogenesis platform built from synthetically simple, modular components. The scope of the chirogenesis, however, remains insufficiently mapped. It is not known how robustly the external M···O binding mode survives variation of the porphyrin periphery, core planarity, or metal centre, nor how the resulting complexes organise in the solid state. The interaction of cycHC[*n*] with bis-porphyrin hosts capable of tweezer-type encapsulation is even less explored. Finally, although solid-state chiroptical enhancement makes cycHC[*n*]·metalloporphyrin films an appealing class of functional materials, no chiral sensor based on these adducts had been reported at the start of this work. Enantioselective sensing is relevant across pharmaceutical quality control, food and fragrance analysis, and environmental monitoring, yet existing chiral sensors typically require lengthy synthesis of highly specific receptors. The modular cycHC[*n*]·metalloporphyrin platform offers a low-effort route to practical and portable chiral detection devices.

The specific aims of the current work were:

- to investigate the scope of cycHC[*n*]·metalloporphyrin self-assembly across a library of nine achiral metalloporphyrins varying in peripheral substituents, core planarity, and metal centre, by measuring association constants in solution and obtaining single-crystal X-ray structures of the resulting complexes
- to characterise the chiroptical response of the complexes by electronic circular dichroism in solution and in the solid state, and to rationalise the differences in binding strength and solid-state architecture observed across the porphyrin library
- to extend the study to bis(zinc octaethylporphyrin) (a bis-porphyrin host known for its strong chirogenic response upon forming tweezer complexes with bidentate guests), and to determine the binding mode, stoichiometry, and induced CD signal with cycHC[6] and cycHC[8]
- to exploit cycHC[8]·metalloporphyrin adducts as chiral coatings on quartz crystal microbalances, and to develop a normalisation protocol based on virtual racemic references that enables enantiorecognition of volatile chiral analytes by arrays of enantioselective sensors at unknown concentration

3 Results and discussion

This section presents the results of three interconnected studies. Section 3.1 (publication I) maps the scope of cycHC[*n*]·metalloporphyrin self-assembly across a library of porphyrins, establishing the binding modes, crystal structures, and chiroptical properties of 1:1 complexes. Section 3.2 (publication II) extends this to bis-ZnOEP, a tweezer-type host capable of encapsulating chiral guests, revealing time-dependent and size-selective binding behaviour. Section 3.3 (publication III) translates the solid-state chiroptical properties of cycHC[*n*]·metalloporphyrin films into a functional enantioselective sensor array, demonstrating chiral recognition of volatile analytes through a novel virtual racemic normalisation strategy.

3.1 Solution and Solid-State Self-Assembly of a Library of Metalloporphyrins with Chiral Cyclohexanohemicucurbit[*n*]urils (Publication I)

Mapping the scope of a supramolecular chirogenesis platform requires systematic variation of both binding partners across a deliberately broad range of structures. In 2019 Ustrnul et al. showed that enantiopure cycHC[*n*] macrocycles bind achiral zinc porphyrins externally through Lewis acid–base interactions between the porphyrin metal centre and the cycHC[*n*] urea oxygens, and that this interaction induces detectable circular dichroism in the porphyrin Soret band.[6] Two questions left open by this earlier report motivated the broader study presented in this section. First, how general is this binding mode and can it be extended across the metalloporphyrin family with variations in peripheral electronic character, core planarity, and the metal cation itself? Second, what supramolecular assemblies does it produce in the solid state, and how do those architectures relate to the observed chirogenic behaviour?

To address these questions, nine metalloporphyrins were studied: five Zn-porphyrins differing in the electron-donating or -withdrawing character of their peripheral substituents, a more extreme octahalogenated Zn-porphyrin in which the core is also significantly distorted from planarity, and three direct analogues to Zn-porphyrins in which the central Zn^{2+} was replaced by Mg^{2+}, Fe^{3+}, or Pd^{2+}. Their interaction with both cycHC[6] and cycHC[8] was characterised in dichloromethane (DCM) solution and in the solid state, and the chiroptical response of the resulting complexes was probed in both phases. Single-crystal X-ray diffraction data were collected and refined by Dr Khai-Nghi Truong, Dr Jas S. Ward and Prof. Kari Rissanen (University of Jyväskylä); solid-state ECD measurements on KBr pellets were performed by Prof. Reiko Kuroda (Chubu University); and VCD measurements were performed by Nele Konrad (Tallinn University of Technology).

3.1.1 Variability of binding strength in solution

The structures of the nine metalloporphyrins examined are shown in Figure 13, together with those of (*R*,*R*)- and (*S*,*S*)-cycHC[6] and cycHC[8]. Five of the porphyrins (**1**–**5**) sample peripheral electronic variation in the Zn^{2+} series: zinc 2,3,7,8,12,13,17,18-octaethylporphyrin, commonly known as ZnOEP (**1**) bearing weakly electron-donating ethyl groups at the β-positions; zinc 5,10,15,20-tetraphenylporphyrin, commonly known as ZnTPP (**2**); and three *para*-substituted Zn-tetraarylporphyrins (**3**, **4**, **5**) carrying fluoro, chloro, or trifluoromethyl groups, respectively. Porphyrin **6** combines β-octabromo

substitution with *meso*-pentafluorophenyl groups, producing both a strongly electron-deficient metal centre and a non-planar core distorted by the β-halogenation.[111,154] The remaining three (**7**, **8**, **9**) are direct **1** or **2** analogues in which Zn^{2+} has been replaced by Mg^{2+}, Fe^{3+}, or Pd^{2+}, respectively.

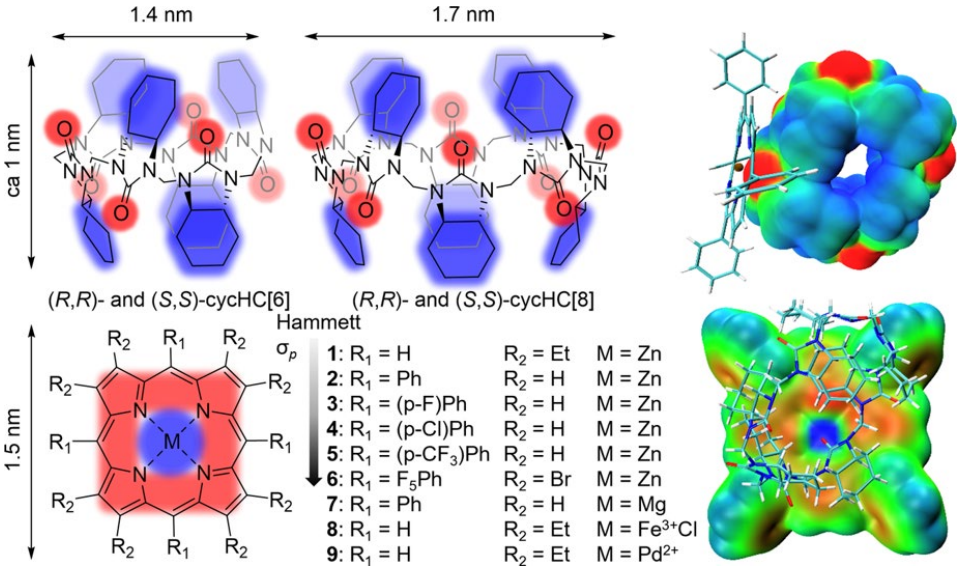

*Figure 13 Structures of hemicucurbiturils and metalloporphyrins studied on the left, and electrostatic-potential-coloured molecular van der Waals surface of (S,S)-cycHC[8]·**7** on the right. Blue corresponds to electron-donating and red to electron-accepting regions. The Hammett constant σ_p for para-substituents increases from porphyrins **1** to **6**. Reproduced from Publication I under CC BY 4.0.*

Screening of various solvents was performed to explore influence of media on the binding, confirming that nonpolar aprotic media support external M···O complexation in this family. All UV-vis titrations were performed by global fitting of absorbance changes at the $Q_{(1,0)}$ band of the uncomplexed porphyrin and the $Q_{(1,0)}$ and $Q_{(0,0)}$ bands of the complexed form. Titrations of **2** with (*R*,*R*)-cycHC[8] in toluene and chloroform gave first-step association constants of K_1 = 1110 ± 40 M^{-1} and K_1 = 1080 ± 40 M^{-1}, respectively, both lower than the K_1 = 2070 ± 40 M^{-1} reported by Ustrnul et al. for the same complex in DCM.[6] Oxygen-containing solvents capable of competing for the porphyrin metal, namely methanol, THF, and DMSO, suppressed the interaction entirely, and no binding was detectable for **2**·cycHC[8] in either neat methanol or a 1:1 methanol/dichloromethane mixture. Direct titration of **2** with methanol in dichloromethane gave a 1:1 association constant of K = 10.7 ± 0.5 M^{-1} for ZnTPP–methanol binding. This value is comparable to the K = 7.32 ± 0.21 M^{-1} reported by Andreev et al. in chloroform for the same interaction,[109] but differs by more than three orders of magnitude from the K = 0.002 M^{-1} reported by Olsson et al.[155] under similar conditions. The present result therefore supports the higher of the two literature values and explains the loss of cycHC[*n*] binding in protic media as direct competition by methanol at the porphyrin metal centre. DCM was used throughout the remainder of the study. Titrations were performed with both (*R*,*R*)- and (*S*,*S*)-enantiomers of cycHC[6] and cycHC[8] as parallel experiments, since binding strength is independent of host chirality

in achiral spectroscopy; the values reported in Table 2 are the means of the two corresponding measurements. Association constants were extracted using the Bindfit online tool (https://supramolecular.org)[48,51] with a 2:1 statistical model for porphyrins **1**–**6**, and a 2:1 full model for the more strongly binding Mg-porphyrin **7**, using the Soret band maximum of the uncomplexed porphyrin and the shifted Soret band maximum of the complex for fitting. The first-step association constant K_1, which corresponds to the formation of the 1:1 complex, is the most informative single measure across the series and is summarised in Table 2.

Table 2 Association constants of the first step K_1 for metalloporphyrin and cycHC[n] complexes obtained with Bindfit 2:1 statistical model (2:1 full model in case of **7***) are listed in the table (choice of binding models and acquiring of constants is elaborated in the supporting information of publication I).*

Metallo-porphyrin	$\boldsymbol{K_1}$ with cycHC[6], $\times 10^3$ M^{-1}	$\boldsymbol{K_1}$ with cycHC[8], $\times 10^3$ M^{-1}
1	2.9 ± 0.2	0.69 ± 0.01
2	5.34 ± 0.06[a]	2.07 ± 0.02[a]
3	4.8 ± 0.3	2.1 ± 0.3
4	6.01 ± 0.07	2.87 ± 0.05
5	7.4 ± 0.5	3.34 ± 0.02
6	409 ± 4	n.d.
7	1840 ± 70[b]	1040 ± 40[b]

a – constants from reference,[6] b – apparent K in the presence of 10 equivalents of water. All constants were determined from at least two independent measurements with enantiomeric cycHC[n]s, uncomplexed porphyrin Soret band Maxima and complex maxima were used for fitting, deviations are standard deviation from independently measured K values. n.d. – not determined (No satisfactory fit could be obtained). Reproduced from Publication I under CC BY 4.0.

For the planar core Zn-tetraarylporphyrins **2**–**5**, K_1 with cycHC[8] increased consistently from 2.07 × 10^3 M^{-1} for the unsubstituted **2** to 3.34 × 10^3 M^{-1} for the trifluoromethyl-substituted **5**, mirroring the order of Hammett σ_p values of the para-substituents (H: 0.00, F: +0.06, Cl: +0.23, CF_3: +0.54),[156] a measure of their electron-withdrawing character. With cycHC[6], the same overall trend was followed, with the strongly electron-withdrawing **4** (*p*-Cl) and **5** (*p*-CF_3) again giving higher K_1 values than the unsubstituted **2**, but the *p*-fluoro analogue **3** appeared as a small outlier with K_1 = 4.80 × 10^3 M^{-1}, slightly below the value of **2**. Such deviations are not uncommon in Hammett correlations involving fluorine, where the small σ_p value and the comparable magnitudes of the inductive and resonance contributions can disrupt this trend in sensitive systems.[157] The octaethyl-substituted **1**, with weakly electron-donating peripheral groups, gave the lowest K_1 values across the Zn series (2.9 × 10^3 M^{-1} for cycHC[6], 0.69 × 10^3 M^{-1} for cycHC[8]), consistent with the lower electrophilicity at the zinc centre. The β-octabromo, pentafluorophenyl-substituted **6** behaved as an extreme limit of the same

trend: K_1 with cycHC[6] reached 4.09×10^5 M^{-1}, two orders of magnitude above the rest of the Zn series. The strong binding of **6** was directly visible in the titration; complete complexation was achieved with a 1000-fold lower excess of cycHC[*n*] than for **1**–**5**.

Variation of the metal cation produced larger effects than peripheral substitution. The Mg^{2+} porphyrin **7** bound cycHC[6] with $K_1 = 1.84 \times 10^6$ M^{-1}, three orders of magnitude stronger than the structurally identical Zn-porphyrin **2**, and the strongest binding observed in the entire study. The corresponding K_1 with cycHC[8] was 1.04×10^6 M^{-1}. This binding was determined as an apparent constant in the presence of approximately 10 equivalents of water, since Mg^{2+}-porphyrins are intrinsically oxophilic and retain coordinated water under ambient conditions. The high observed K_1 values indicate that cycHC[*n*] binds more strongly to Mg^{2+} than water does and is able to displace it from the coordination sphere. By contrast, the Fe^{3+} (**8**) and Pd^{2+} (**9**) analogues showed no measurable binding to cycHC[8]. For Pd^{2+}, a soft metal centre with low affinity for hard oxygen donors such as urea carbonyls, this is consistent with the HSAB principle discussed in section 1.1.2. The absence of binding for Fe^{3+} is less straightforwardly rationalised and was not investigated further. The combination of peripheral electronic effects and metal-centre choice therefore spans the full association-constant range from 690 M^{-1} (***1***·cycHC[8]) to 1.84×10^6 M^{-1} (***7***·cycHC[6]), more than three orders of magnitude across a single supramolecular platform. Across all cases where binding was measurable, cycHC[6] consistently bound more strongly than cycHC[8], a trend that recurred in the solid-state structures discussed below.

3.1.2 Solid-state architectures from single-crystal X-ray diffraction

Crystallisation of equimolar mixtures of seven of the achiral metalloporphyrins (**1**–**7**) with both enantiomers of cycHC[6] and cycHC[8] in DCM/MeOH or chlorobenzene/MeOH yielded 31 novel single-crystal structures (six with (*R*,*R*)-cycHC[6], seven with (*S*,*S*)-cycHC[6], ten with (*R*,*R*)-cycHC[8], and eight with (*S*,*S*)-cycHC[8]), all featuring direct M···O coordination between the porphyrin metal and a cycHC[*n*] urea oxygen as the dominant interaction. Crystal structures were deposited in the CCDC (deposition numbers 2444098–2444118, 2444120, 2444122–2444124, 2444126–2444131). Crystallisation experiments were not pursued for the Fe^{3+} porphyrin **8**, for which no binding was detected by titration, or for the Pd^{2+} porphyrin **9**, for which the binding was too weak to be quantified. Polymorphism was observed for cycHC[6] complexes with porphyrins **1**, **2**, and **3**, and for cycHC[8] complexes with porphyrins **1**, **2**, **3**, and **4**, arising from both stoichiometric differences and connectivity variations under different crystallisation conditions. Across the structures characterised, the assembly topology varied systematically with the host, the porphyrin, the crystallisation temperature, and the solvent additive, ranging from discrete penta- or hexa-coordinated complexes through 1D coordination polymers to a 2D square-grid network and a chiral 1D helical polymer. The cycHC[6] complexes are illustrated in Figure 14 and the cycHC[8] complexes in Figure 15.

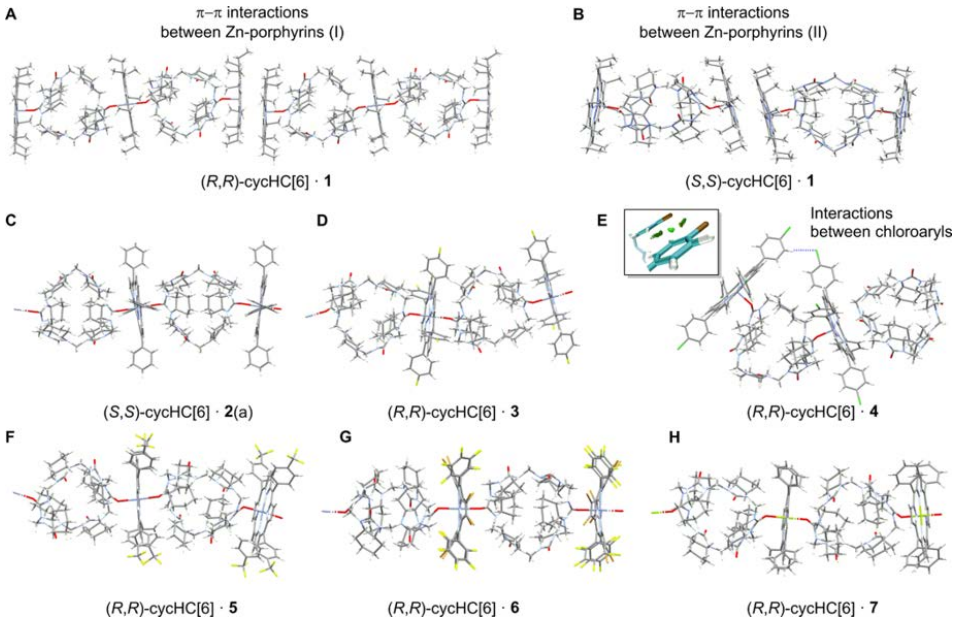

*Figure 14 Molecular structures of cycHC[6] complexes with porphyrins **1** (A, B), **2** (C), **3** (D), **4** (E), **5** (F), **6** (G), and **7** (H). Where multiple crystal forms were obtained for the same complex, letters in parentheses denote distinct polymorphic forms. In panels C, D, F, G, and H the crystals are 1D coordination polymers; the remaining structures are complexes with discrete host-guest ratios. The inset in panel E shows an NCI isosurface highlighting intermolecular C–H···Cl interactions between neighbouring porphyrins. Atom sites with minor occupancies and co-crystallised solvent molecules have been omitted for clarity. Atoms are coloured according to the CPK (Corey–Pauling–Koltun) code. Reproduced from Publication I under CC BY 4.0.*

The cycHC[6] complexes (Figure 14) split broadly into two architectural families. Discrete complexes were obtained with the octaethyl porphyrin **1** and, in some polymorphs, with **3** and **4**, often featuring direct π–π stacking between adjacent porphyrin cores at distances of 3.3–3.4 Å. The remaining porphyrins (**2**, **5**, **6**, **7**) gave 1D coordination polymers in which each cycHC[6] bridges two metalloporphyrins through opposite urea carbonyls, with the internal metal centres hexa-coordinated. Although solution equilibria disfavour extended coordination geometries, crystal packing forces can stabilise polymeric architectures in the solid state that would not persist in solution. Several complexes were polymorphic, with the discrete-complex/polymer outcome sensitive to crystallisation conditions: porphyrin **3** gave a 1D-chain polymer at ambient temperature with (*R*,*R*)-cycHC[6] but a discrete 2:2 complex with (*S*,*S*)-cycHC[6] at 3 °C, and porphyrin **4** formed a discrete 1:2 complex stabilised by intermolecular C–H···Cl contacts between neighbouring chloroaryl groups, which prevented polymerisation despite the otherwise comparable coordination geometry. The cycHC[8] complexes (Figure 15) showed greater architectural diversity: predominantly discrete 1:1 and 1:2 complexes for porphyrins **1**–**5**, but also a 2D square-grid coordination polymer for one polymorph of cycHC[8]·**1** in which each cycHC[8] binds four porphyrins via alternating urea pairs.

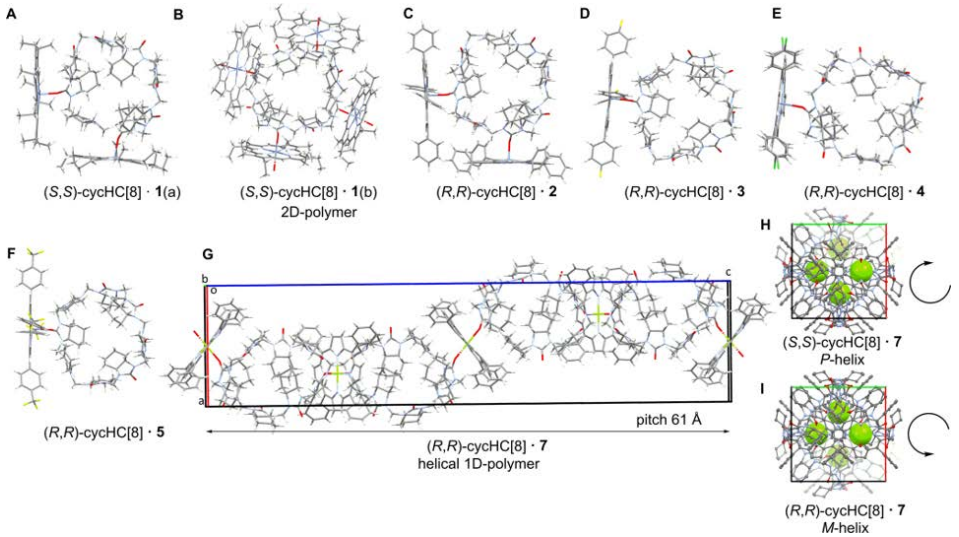

*Figure 15 Crystal structures of cycHC[8] complexes with porphyrins **1**(a) (A), **1**(b) (B), **2**(a) (C), **3**(a) (D), **4**(a) (E), **5** (F), and **7** (G, H, I). Panel B is a 2D square-grid coordination polymer; panels G–I show a 1D helical coordination polymer, with H presenting the P-helix formed by (S,S)-cycHC[8] and I the M-helix formed by (R,R)-cycHC[8]. The structures in panels D and E are isostructural with one another; the (S,S)-cycHC[8]·**3** enantiomer (not shown) is also isostructural with D and E. The remaining panels show discrete complexes. Atom sites with minor occupancies and co-crystallised solvent molecules have been omitted for clarity. Atoms are coloured according to the CPK code. Reproduced from Publication I under CC BY 4.0.*

The most unusual structural outcome was for the Mg-porphyrin **7**, which crystallised exclusively as a 1D-chain polymer with cycHC[8]. The non-aligned arrangement of cycHC[8] urea carbonyls forces the polymer to adopt a helical conformation, with a pitch of approximately 61 Å containing four porphyrin and four cycHC[8] units per turn. The handedness of the helix is determined by the chirality of the macrocycle: (*R*,*R*)-cycHC[8] produces a *P*-helix and (*S*,*S*)-cycHC[8] an *M*-helix (Figure 15, panels H and I). This is the only example in the entire structure set in which the chirality of the host is transferred into a long-range chiral architecture, rather than only into the local geometry around each porphyrin.

Across porphyrins **1**–**6**, the M···O distances clustered tightly around 2.38 Å for hexa-coordinated Zn^{2+} centres and 2.18 Å for penta-coordinated Zn^{2+} centres, in agreement with literature values for analogous complexes. Mg···O distances in the **7** complexes were 0.1–0.2 Å shorter than the corresponding hexa-coordinated Zn···O distances, consistent with the stronger Mg–O interaction shown by solution titrations. A general structural pattern emerged from the combined data: cycHC[6] preferentially gives 1D coordination polymers across most porphyrins, with discrete complexes appearing only when temperature, intermolecular C–H···X contacts, or other secondary interactions disfavour polymerisation. cycHC[8] shows the opposite tendency, predominantly giving discrete 1:1 or 1:2 complexes and forming extended networks only under specific conditions: a 2D square grid templated by chlorobenzene inclusion in cycHC[8]·**1**, and a 1D helical polymer driven by the strong oxophilicity and hexa-coordination preference of Mg^{2+} in cycHC[8]·**7**.

3.1.3 Noncovalent interaction analysis

To rationalise the contrasting binding strengths and crystallisation behaviours observed between the Zn and Mg porphyrins, the noncovalent contributions to complex stabilisation were examined by NCI and IRI analyses on the crystallographic geometries. Two complexes were compared in detail: (*S*,*S*)-cycHC[8]·**2** as the Zn-tetraarylporphyrin reference, and (*S*,*S*)-cycHC[8]·**7** as the Mg analogue (Figure 16).

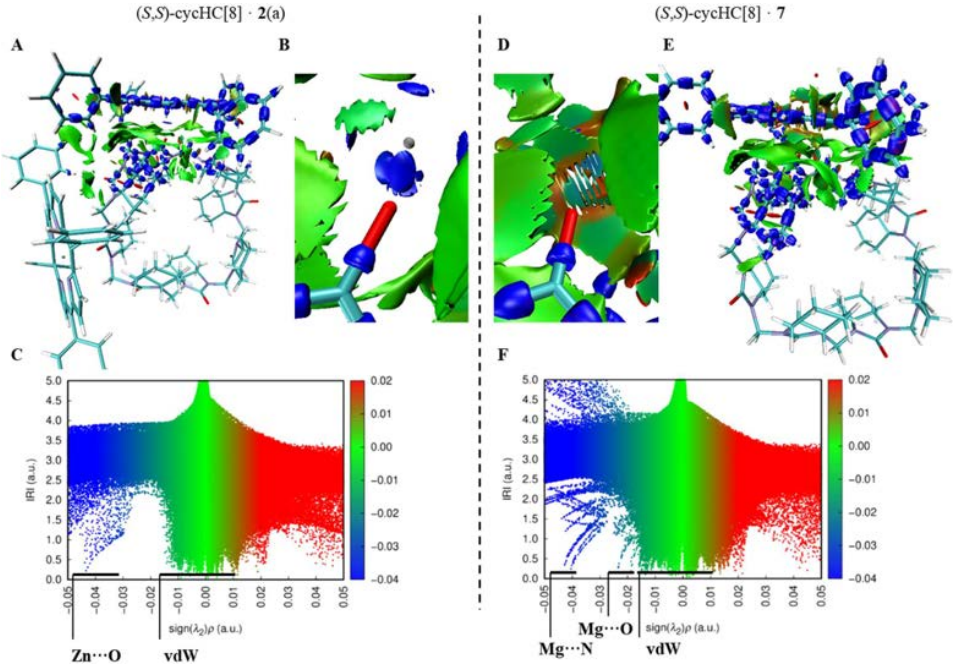

*Figure 16 IRI isosurfaces and corresponding scatter graphs for the porphyrin–cycHC[8] interaction region in (S,S)-cycHC[8]·**2** (A–C) and (S,S)-cycHC[8]·**7** (D–F). Isosurfaces were calculated using a = 1.1 (2). The grid was selected between one porphyrin and the cycHC[8] face directly opposite to it. Panels A and E show the full IRI isosurfaces; B and D show enlarged views of the Zn···O and Mg···O coordination regions, respectively; C and F show the corresponding scatter graphs of IRI versus sign(λ₂)ρ. Colour scale: blue, attractive interactions; green, van der Waals contacts; red, repulsive forces. Reproduced from Publication I under CC BY 4.0.*

In both complexes, the dominant attractive feature corresponds to coordination between the porphyrin metal and a cycHC[8] urea oxygen, but the two metals organise this coordination differently. In the Zn complex (Figure 16 panel B), the attraction appears as a discrete blue disc localised between the Zn and O atoms, consistent with a strongly directional Zn–O coordination bond. In the Mg complex (Figure 16 panel D), the contact is more spatially extended and predominantly green with a blue tint, indicating a genuine attractive interaction layered on a broader van der Waals contact rather than a single sharp coordination. This diffuse character is consistent with the additional weak Mg···O contacts previously reported in magnesium–carboxylate complexes.[158] This bluish-green Mg···O signature is clearly distinguishable from the pure-green halos elsewhere in the panels, which mark dispersion-only contacts between the porphyrin face and the cycHC[8] exterior. The corresponding IRI scatter plots (Figure 16) place the M···O bond-critical-point feature at sign(λ₂)ρ ≈ −0.033 a.u. for Zn but at the less attractive sign(λ₂)ρ ≈ −0.023 a.u. for Mg. The further-left feature at sign(λ₂)ρ ≈ −0.042 a.u. visible

only in the Mg plot corresponds to Mg···N coordination within the porphyrin core and is intrinsic to the Mg-porphyrin scaffold rather than to the cycHC[*n*] binding event.

This contrast helps to rationalise the much stronger solution binding of **7** relative to **2**, which exceeds two orders of magnitude across both cycHC[*n*] hosts. Although the per-contact Lewis acidities of Zn^{2+} and Mg^{2+} are comparable (Zn^{2+} = 0.33–0.50, Mg^{2+} = 0.334) on the bond-valence scale,[159,160] the Mg complex draws on a more spatially extended interaction with the urea oxygen, supplemented by the broader vdW contribution visible in the IRI map. The IRI alone does not fully account for the magnitude of the difference, which likely also involves solvation effects and the strong oxophilicity of Mg^{2+} noted in 3.1.1. The pure-green vdW regions, while individually weaker than the metal–oxygen coordination, span a substantial surface area and contribute meaningfully to the overall stabilisation.

3.1.4 Chiroptical properties in solution and the solid state

The chiroptical response of the cycHC[*n*]·metalloporphyrin complexes was examined by electronic circular dichroism (ECD) in DCM solution and in KBr pellets (made from crushed crystals of the discrete 1:2 complexes of cycHC[8]·**2** and the helical 1D polymers of cycHC[8]·**7**), and by vibrational circular dichroism (VCD) in the IR region. The dissymmetry factor $g = \Delta\varepsilon/\varepsilon$ was used to quantify the chirogenic intensity in a manner comparable across phases and concentrations.

In DCM solution, all 1:1 complexes of porphyrins **1**–**7** with either cycHC[6] or cycHC[8] gave mirror-image ECD signals in the Soret region between (*R*,*R*)- and (*S*,*S*)-cycHC[*n*] enantiomers (Figure 17 and Table 3), confirming chirality transfer from the cycHC macrocycle to the achiral porphyrin chromophore. Free metalloporphyrins are CD silent, and cycHC[*n*] macrocycles are transparent in the visible range, confirming that all observed signals arise from the chiral complex. The shape of the induced ECD differed across the porphyrin library according to the orientational freedom of the *meso*-aryl substituents. Porphyrin **1**, which carries no *meso*-aryl groups, gave a monosignate ICD with λ_{max} near 409 nm. The planar tetraarylporphyrins **2**–**5**, in which the *meso*-aryls are free to rotate, produced bisignate signals near 418 nm. The chirally biased aryl orientation splits the otherwise-degenerate Soret transitions, and the two split components with opposite CD signs give rise to the bisignate Cotton effect.[161,162] The β-halogenated porphyrin **6** displays a red-shifted, broader Soret band compared to **2**–**5**, both features intrinsic to the free porphyrin arising from β-halogenation-induced core distortion. Upon complexation, **6** gave a monosignate ICD profile rather than the bisignate signature of **2**–**5**: the bulky pentafluorophenyl groups are sterically locked in place by the surrounding β-octabromo substituents, eliminating the rotational freedom that gives rise to the bisignate signal in the unrestricted tetraarylporphyrins. Despite these differences in spectral shape, the *g*-factors (average of absolute values at the ECD maximum for complexes with both cycHC[*n*] enantiomers, calculated according to Equation 6) of the planar Zn-tetraarylporphyrins **2**–**5** clustered tightly around 3.5×10^{-5}, the β-halogenated **6** gave roughly twofold this value, and the strongly binding Mg-porphyrin **7** gave a *g*-factor of 4.5×10^{-5}, only marginally larger than the Zn analogues. Across three orders of magnitude in K_1, the chirogenic intensity varies only modestly. Binding strength and the magnitude of induced CD are therefore decoupled in solution, and the spectral shape (mono- vs bisignate) is determined by porphyrin substituent geometry rather than by the strength of the host–guest interaction.

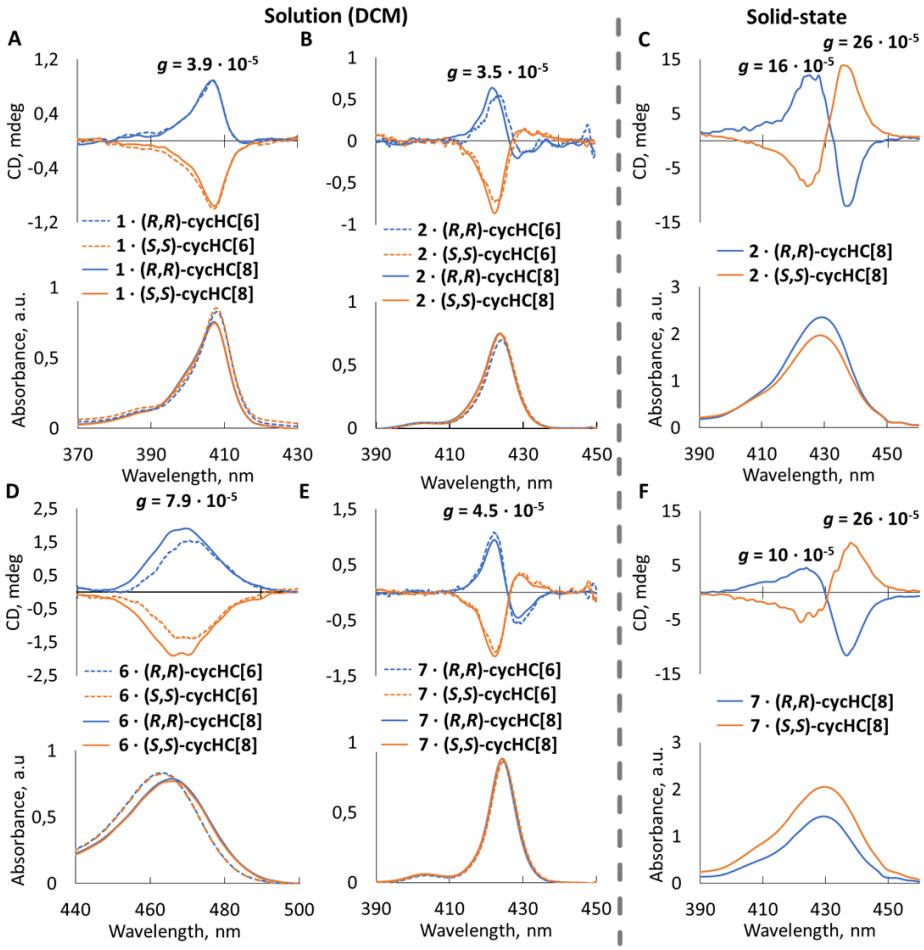

*Figure 17 ECD spectra of enantiomeric 1:1 complexes of cycHC[6] (dashed lines) and cycHC[8] (solid lines) with **1** (A), **2** (B), **6** (D), and **7** (E) in DCM. ECD spectra of porphyrins **3**, **4**, and **5** which were analogous to **2** can be found in SI of publication I. Panels C and F show solid-state ECD spectra of KBr pellets prepared from microcrystals of cycHC[8]·2 (C) and cycHC[8]·7 (F) together with their corresponding UV-vis absorption spectra. Blue lines: complexes with (R,R)-cycHC[n]; orange lines: complexes with (S,S)-cycHC[n]. Reproduced from Publication I under CC BY 4.0.*

Table 3 The UV-vis λ_{max}, ECD λ_{max} and g-factors at ECD λ_{max} values for porphyrin-cycHC[n] 1:1 complexes in DCM. + and – Cotton effects are assigned for complexes with (R,R)-cycHC[n] while g-factor is average of porphyrin complexes with both enantiomers of cycHC[n]. Reproduced from Publication I under CC BY 4.0.

No	Complex	free porphyrin/complex UV-vis λ_{max}, nm	ECD λ_{max} of complex, nm	$\lvert g \rvert$-factor, 10^{-5}
1	**1**·cycHC[8]	401/408	407 (+)	3.9
2	**1**·cycHC[6]	401/409	407 (+)	3.8
3	**2**·cycHC[8]	418/424	422 (+)/429 (-)	3.5/2.3
4	**2**·cycHC[6]	418/425	423 (+)/430 (-)	2.8/2.3
5	**3**·cycHC[8]	418/424	422 (+)/429 (-)	3.5/3.6
6	**3**·cycHC[6]	418/425	422 (+)/429 (-)	3.8/3.1
7	**4**·cycHC[8]	420/426	424 (+)/433 (-)	3.4/3.8
8	**4**·cycHC[6]	420/426	424 (+)/432 (-)	3.3/3.6
9	**5**·cycHC[8]	418/425	422 (+)/429 (-)	3.7/3.4
10	**5**·cycHC[6]	418/425	422 (+)/429 (-)	3.7/3.3
11	**6**·cycHC[8]	456/467	468 (+)	7.9
12	**6**·cycHC[6]	456/464	469 (+)	6.4
13	**7**·cycHC[8]	424/425	422 (+)/429 (-)	4.5/3.0
14	**7**·cycHC[6]	424/426	422 (+)/429 (-)	4.8/3.9

The solid-state ECD spectra showed substantial enhancement (Figure 17 C, F) of lowest energy band. For both cycHC[8]·**2** and cycHC[8]·**7** in KBr pellets, the *g*-factor reached 26×10^{-5}, approximately tenfold larger than in solution, accompanied by a 4–5 nm red shift of the Soret maximum and a clear bisignate Cotton effect whose zero-crossing closely matched the absorption maximum. The latter feature is a sign of exciton coupling between neighbouring porphyrin chromophores, which is suppressed in dilute solution but becomes operative when porphyrins are brought into proximity in the solid state. A pellet prepared from a precipitate of cycHC[8]·**2** obtained by rotary evaporation of the same DCM/MeOH solution, which yields an amorphous or partially microcrystalline solid, gave a qualitatively identical bisignate Cotton effect with the same band positions and sign pattern but with a magnitude approximately half that of the crystalline sample (Figure 18, *g*-factor up to 16.9×10^{-5} at 437 nm versus 26×10^{-5} for the crystals). The enhancement is therefore reproducible across different solid forms of the same complex and is not specific to one crystalline phase. Linear dichroism, linear birefringence, and circular birefringence measurements on the same pellets confirmed that optical anisotropies remained at negligible levels and did not contribute to the observed signals.

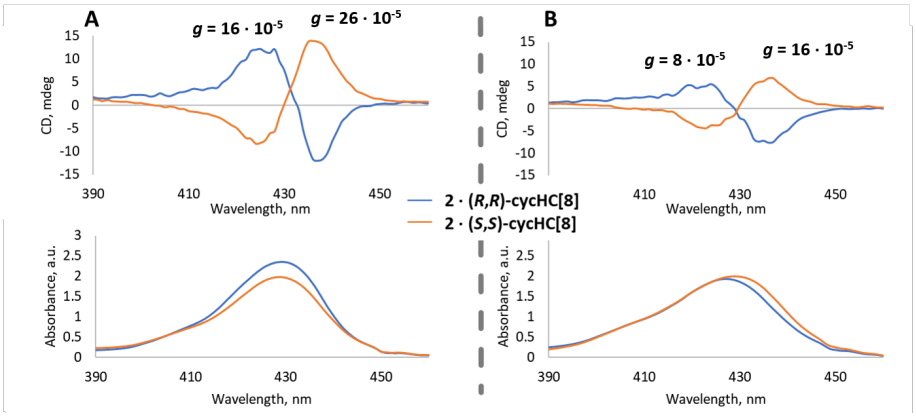

*Figure 18 Solid-state ECD spectra (top) and corresponding UV-vis absorption spectra (bottom) of cycHC[8]·**2** in KBr pellets, prepared from crushed crystals (A) and from a precipitate obtained by rotary evaporation of a DCM/MeOH solution (B). Blue lines: complexes with (R,R)-cycHC[8]; orange lines: complexes with (S,S)-cycHC[8]. Adapted from Publication I under CC BY 4.0.*

A second observation was the near-independence of the enhancement from the underlying solid-state architecture. CycHC[8]·**7** forms a chiral 1D helical polymer in which the porphyrins are positioned in a unidirectional helical array (chapter 3.1.2), which on geometric grounds would be expected to amplify exciton coupling more strongly than a discrete 1:2 complex of cycHC[8]·**2**. Yet both gave *g*-factors of 26 × 10^{-5}, with similar Cotton-effect signs and only minor differences in band positions. This also implies that exciton coupling does not extend through the cycHC[*n*] macrocycle itself. Together with the precipitate observation above, this points to a dominant amplification mechanism operating at the level of nearest-neighbour porphyrin pairs rather than at the level of long-range crystallographic or helical order: the macrocyclic host serves primarily to bring porphyrins into chiral proximity at short range, and once that proximity is established, neither the crystalline phase nor the helical organisation of the assembly significantly modifies the chiroptical response. This matters for sensor design: the solid-state ECD enhancement does not require a specific architecture, which would be hard to control in a working sensor film.

3.2 Self-Assembly of Bis(zinc octaethylporphyrin) with Chiral Cyclohexanohemicucurbit[*n*]urils (Publication II)

Section 3.1 showed that mono-porphyrins of the cycHC[*n*]·metalloporphyrin family share a common external M···O binding mode across a wide range of peripheral substitutions and metal cations, with cycHC[6] consistently binding more strongly than cycHC[8], but with no qualitative difference in the binding mechanism between the two homologues. The work described in this section addresses a structurally distinct case within the same family: bis(zinc octaethylporphyrin) (bis–ZnOEP), a flexible bis-porphyrin in which two ZnOEP units are tethered by an ethane bridge (Figure 19). The presence of two porphyrin faces on a single molecule opens the possibility of binding modes inaccessible to mono-porphyrins. The following subchapters utilise the sensitivity of the bis-porphyrin to report on the size, shape, and binding kinetics of cycHC[*n*] guests. All measurements were performed in DCM or its deuterated equivalent.

3.2.1 Binding properties of bis–ZnOEP with cycHC[6] and cycHC[8]

In the absence of a guest, bis–ZnOEP adopts a stable face-to-face *syn* conformation (Figure 19). Upon ligand coordination to the Zn centres, the host can rearrange into different conformational states depending on the denticity and geometry of the guest.[70]

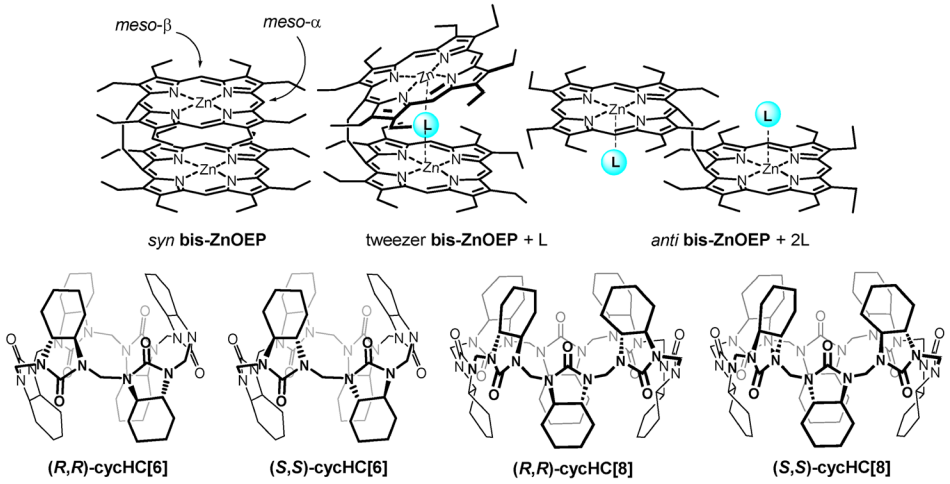

Figure 19 Top: structures of bis–ZnOEP in syn, tweezer, and anti-conformations, with the meso-α and meso-β proton positions indicated; L denotes a coordinating ligand. Bottom: structures of (R,R)- and (S,S)-enantiomers of cycHC[6] and cycHC[8]. Reproduced from Publication II under CC BY 4.0.

Monodentate ligands induce formation of extended anti 1:2 complexes in which the two porphyrin rings are spatially separated. Chiral monodentate guests can induce a screw distortion, producing induced CD signals that reflect both the guest chirality and the conformational response of the bis-porphyrin. Bidentate ligands, in contrast, can coordinate simultaneously to both Zn centres to form a 1:1 tweezer complex (Figure 19), in which the guest is held between the two porphyrin faces in a pincer-like geometry. The defined non-parallel arrangement of the porphyrin rings in the tweezer structure produces strong exciton coupling and intense bisignate CD signals. At higher ligand concentrations, the equilibrium may shift toward the *anti* 1:2 complex, although the tweezer complex is more stable ($K_1 > K_2$). The different conformational states therefore possess characteristic chiroptical signatures: tweezer complexes display the largest CD amplitudes, whereas *anti* complexes generally exhibit weaker and more ligand-dependent optical activity. These conformational changes are also reflected in the UV–vis spectra and in the chemical shifts of characteristic porphyrin proton resonances observed by NMR spectroscopy, providing complementary diagnostic handles for identifying the bound state of the host.[86,163–165]

Stepwise addition of cycHC[*n*] (*n*=6,8) in DCM showed that bis–ZnOEP loses its symmetric *syn* arrangement on addition of either cycHC macrocycle. CycHC[6] produced much larger *meso*-β and *meso*-α ^{1}H NMR shifts than cycHC[8] (0.69 vs. 0.17 ppm), and additionally reversed the *meso*-α shielding direction beyond ~2 equivalents, consistent with weaker association of the larger homologue (Figure 20). The splitting of the meso-β signal upon cycHC[*n*] addition arises from the opening of bis-ZnOEP from the symmetric *syn* conformation, in which both porphyrin units are equivalent, to an unsymmetric form in which they become inequivalent.[166]

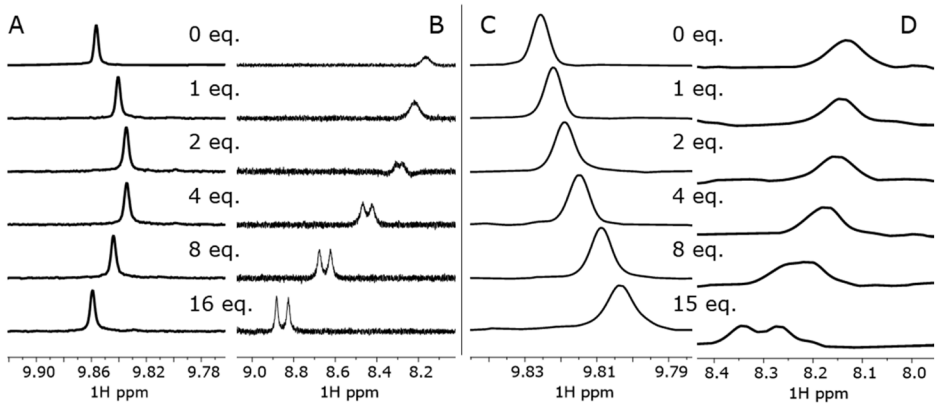

Figure 20 ^{1}H NMR titrations of bis–ZnOEP. Meso-α (A,C) and meso-β (B,D) proton signals upon addition of (R,R)-cycHC[6] in CD_2Cl_2 (A, B) and upon addition of (R,R)-cycHC[8] in CH_2Cl_2 with 10% $CDCl_3$ (C, D). Equivalents of cycHC[n] added are shown beside each spectrum. Reproduced from Publication II under CC BY 4.0.

UV-vis titrations confirmed and extended this picture (Figure 21 Panels A and B). The Soret band of bis–ZnOEP shifted bathochromically from 397 to 402 nm in the presence of cycHC[6], and additional red-shifted absorption bands appeared at 418 and 437 nm, the three-band pattern characteristic of a tweezer-type bis–ZnOEP complex previously reported for 1,2-diaminocyclohexane (Figure 21 panel C).[167] With cycHC[8], by contrast, the band at 397 nm decreased in intensity and a single new transition emerged at 424 nm, producing a spectrum of an entirely different shape at the same equivalents of guest. Apparent saturation was reached at approximately 1500 equivalents of cycHC[8], whereas more than 2000 equivalents of cycHC[6] were required; the interpretation of this difference is discussed in sections 3.2.2 and 3.2.4. The clean isosbestic point reflects the spectral similarity of the 1:1 and 1:2 complexes, which can produce essentially identical UV-vis profiles.[163]

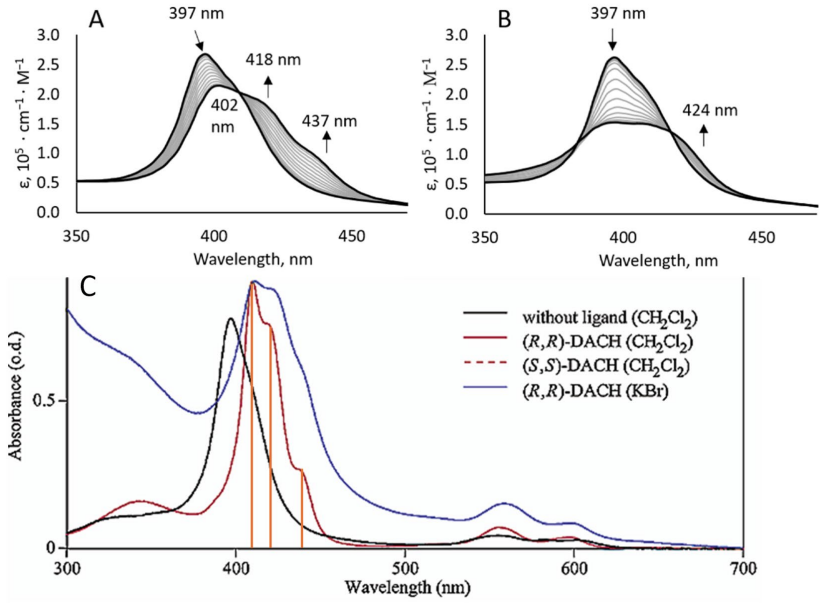

Figure 21 UV-vis titration of bis–ZnOEP ($3.2 \cdot 10^{-6}$ M in CH_2Cl_2, 296 K) with (A) (R,R)-cycHC[6] and (B) (R,R)-cycHC[8], both from 0 to 2000 equivalents. (C) Reference absorption spectra of bis–ZnOEP and its 1:1 tweezer complex with (R,R)- and (S,S)-1,2-diaminocyclohexane (DACH) in CH_2Cl_2 and in KBr, reported by Borovkov et al.[167] Orange bars mark the band positions of the tweezer. Panels A and B reproduced from Publication II under CC BY 4.0.; panel C adapted with permission from reference[167]. Copyright 2002 American Chemical Society.

Fitting of both NMR and UV-vis titration data using Bindfit gave a consistent picture for the cycHC[6] complex. Only a 1:2 binding model produced a satisfactory fit, yielding K_1 = 1650 ± 180 M^{-1} and K_2 = 183 ± 2 M^{-1} from NMR and K_1 = 4550 ± 470 M^{-1} and K_2 = 92 ± 1 M^{-1} from UV-vis. Although the K_1 values from NMR and UV-vis differ approximately threefold, both methods independently support the same 1:2 binding model with pronounced negative cooperativity.[48] The negative cooperativity, with K_2 one to two orders of magnitude lower than K_1, is consistent with bis–ZnOEP first forming a 1:1 tweezer-like complex that is subsequently driven by excess of guest into a 1:2 *anti* complex with the 1:2 form reaching only ~35% mole fraction even at 2000 equivalents of cycHC[6].[163] The same fitting strategy did not work for cycHC[8]: the 1:2 model failed, and only a 1:1 model fitted to the millimolar-concentration NMR data gave a reasonable result (K_1 = 198 ± 5 M^{-1}). During subsequent ECD measurements of the same titration samples, the UV-vis spectra had visibly changed from those recorded at titration, pointing to a slow kinetic process accompanying the cycHC[8] interaction. This prompted a closer look at the time evolution of the complex.

3.2.2 Time-dependent behaviour of the complexes

To characterise the time-dependent behaviour of the cycHC[8] complex more systematically, UV-vis spectra were recorded immediately after a single addition of 2000–3000 equivalents of cycHC macrocycle and compared with the final point of the corresponding titration, which was recorded approximately one hour after the first addition (Figure 21 and Figure 22). For cycHC[6], the two spectra were essentially identical, confirming that equilibrium was reached well within the timeframe of a

conventional titration. For cycHC[8], the single-addition spectrum at t = 0 was clearly different from the spectrum at 25 h (Figure 22). The spectral evolution proceeded in two regimes: a rapid initial change followed by a slower approach to the final shape, completed after 25 hours. The simultaneous failure of the 1:2 binding model and the time dependence of the spectra together pointed to two sequential processes: a primary binding event followed by a secondary, kinetically slower transformation.

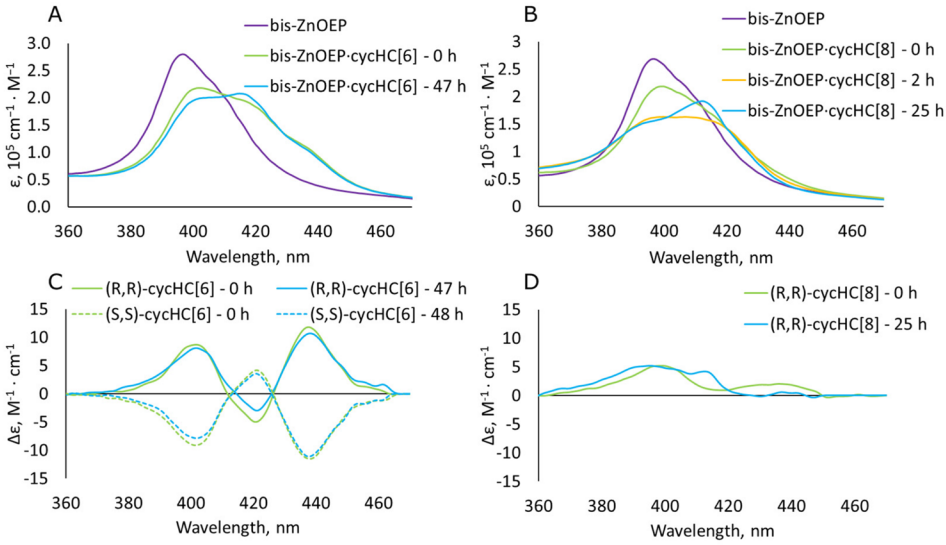

Figure 22 Time-dependent UV–vis absorption and CD spectra of bis–ZnOEP·cycHC[n] complexes in CH_2Cl_2 at 296 K. (A) UV–vis absorption spectra of free bis–ZnOEP ($2.2 \cdot 10^{-6}$ M) and after single addition of 3000 equiv of (R,R)-cycHC[6] ((C) corresponding CD spectra). (B) UV–vis absorption spectra of free bis–ZnOEP ($3.0 \cdot 10^{-6}$ M) and after single addition of 2200 equiv of (R,R)-cycHC[8] ((D) corresponding CD spectra). Reproduced from Publication II under CC BY 4.0.

CD and fluorescence spectra clarified the nature of these processes (Figure 22 and Figure 23). The cycHC[6] complex displayed three Cotton effects in the Soret region, mirroring the three-band UV-vis absorption pattern characteristic of the bis-ZnOEP tweezer complex and arising from exciton coupling between the split B‖ and B⊥ porphyrin transitions upon host opening.[168] . The cycHC[8] complex showed weak monosignate ICD resembling that of monomeric ZnOEP·cycHC[*n*] reported earlier, indicating two nearly parallel porphyrin cores with chiral induction arising from local distortion of each porphyrin rather than from a unidirectional helical arrangement of the dimer. The fluorescence of the cycHC[8] complex was nearly unchanged immediately after mixing but transformed drastically over 25 h: the Q(0,0) band emerged at 585 nm and the Q(0,1) at 632 nm, producing an emission profile closely resembling that of monomeric ZnOEP (Figure 23 panel C) and consistent with the spatial separation of the two porphyrin cores in the *anti*-conformation.

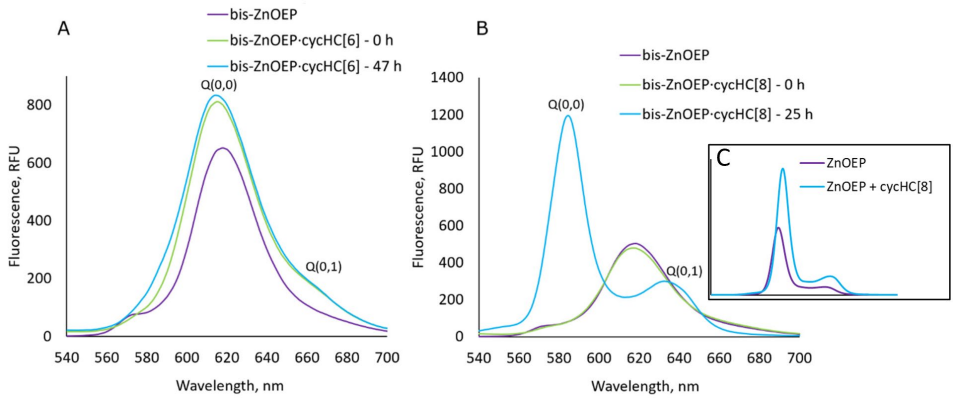

Figure 23 Time-dependent fluorescence response of (A) (λ_{ex} = 399 nm) of free bis–ZnOEP (2.2 · 10^{-6} M, DCM, 296 K) and after single addition of 3000 eq. of (R,R)-cycHC[6] (λ_{ex} = 404 nm) recorded immediately after mixing (0 h) and after 47 h. (B) Fluorescence spectra of free bis–ZnOEP (3.0 · 10^{-6} M, DCM, 296 K) and after single addition of 2200 eq. of (R,R)-cycHC[8] (λ_{ex} = 413 nm) recorded at 0 h and after 25 h. (C) Fluorescence emission of monomeric ZnOEP (2.4 × 10^{-6} M, DCM, λ_{ex} = 408 nm; purple) and after a single addition of 2167 eq. of (S,S)-cycHC[8], shown as a comparison. Adapted from Publication II under CC BY 4.0.

Time-dependent ^{1}H NMR at higher (mM) concentration told a different story (Figure 24). Spectra of bis–ZnOEP·cycHC[8] recorded immediately after mixing and after 21 hours (8 equivalents of guest) or 17 days (1 equivalent) showed no significant changes. The *meso*-β splitting indicating *syn*-opening was already complete at the first time point. The slow transformation observed at µM concentration by UV-vis, CD, and fluorescence was therefore not a consequence of slow conformational switching alone, since that step was fast on the NMR timescale. Instead, it pointed to a concentration-dependent secondary process.

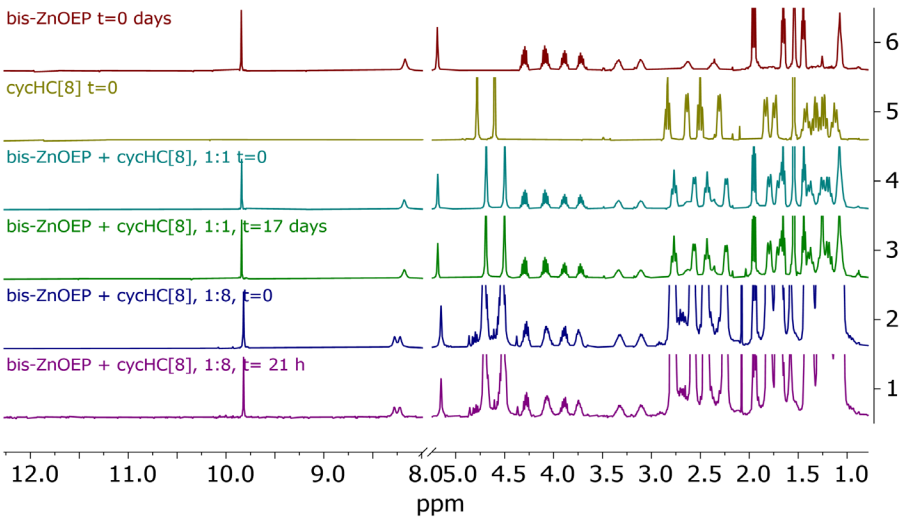

Figure 24 Spectrum of 1.0 · 10^{-3} M bis-ZnOEP at time zero; spectrum of 1.0 · 10^{-3} M (R,R)-cycHC[8] at time zero; spectrum of 1:1 ratio mixture of 1.0 · 10^{-3} M bis-ZnOEP and (R,R)-cycHC[8] measured at time zero and re-measured after 17 days; spectrum of 1:8 ratio mixture of 1.0 · 10^{-3} M bis-ZnOEP

and (R,R)-cycHC[8] measured at time zero and re-measured after 21 h. Samples were kept at room temperature. No changes in time were observed. Reproduced from supporting information of Publication II under CC BY 4.0.

3.2.3 Variable-temperature NMR and fluorescence experiments

Variable-temperature ^{1}H NMR (1.0 mM, 298 → 253 K) of 1:1 bis–ZnOEP·cycHC[*n*] mixtures showed reversible chemical-shift changes and progressive line broadening of the *meso*-β proton at 8.2 ppm, but no signals attributable to discrete aggregates. At µM concentration, by contrast, holding bis–ZnOEP·cycHC[8] samples at 248, 295, or 308 K for 5 h and then re-measuring fluorescence at 295 K showed that higher hold temperatures accelerated the slow transformation of the emission profile (Figure 25). Together, the two experiments locate the detectable slow process at µM concentration and identify it as temperature-dependent aggregation rather than a conformational change on the bis-ZnOEP itself, which is fast on the NMR timescale.

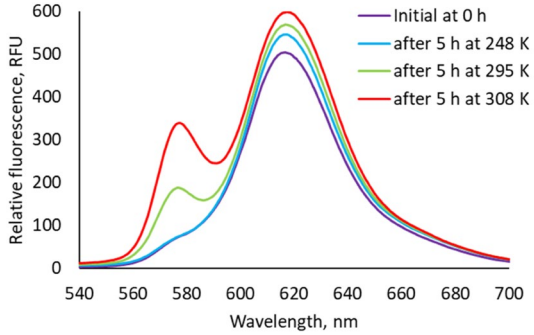

Figure 25 Emission spectra (excited at 397 nm) of bis–ZnOEP (3 · 10−6 M) samples with 2000 equivalents of cycHC[8] measured at 295 K immediately after preparation and then again after being kept for 5 h at different temperatures. Reproduced from Publication II under CC BY 4.0.

3.2.4 Proposed self-assembly mechanisms

The combined data support two distinct binding scenarios for the two homologous hosts (Figure 26). The interaction of bis–ZnOEP with cycHC[6] resembles that of small bidentate guests: a 1:1 tweezer complex is formed, in which the cycHC[6] is sandwiched between the two porphyrin rings and held by two Zn···O coordination bonds. Negative cooperativity disfavours binding of a second cycHC[6], but an excess of guest eventually drives the equilibrium to the 1:2 *anti* complex in which each porphyrin core coordinates one cycHC[6]. The strong, exciton-coupled bisignate ICD reflects the helical distortion of the bis-porphyrin imposed by this geometry.

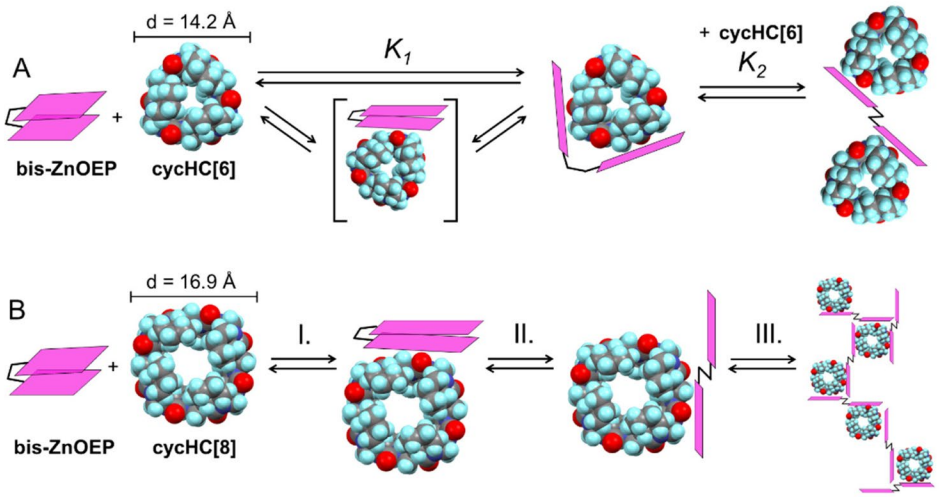

Figure 26 The proposed binding mechanisms of bis–ZnOEP with (A) cycHC[6] described by obtained association constants and with (B) cycHC[8]. The 3D structures and diameters of cycHC[n]s are based on previously reported crystal structures.[6] Colour coding: C—gray, H—light blue, O—red, and N—dark blue. Reproduced from Publication II under CC BY 4.0.

The interaction with cycHC[8] proceeds along a different pathway. The first binding event is weak, and bis–ZnOEP appears to retain its *syn* conformation initially, as judged from the small spectroscopic changes immediately after mixing. Subsequent opening to the *anti*-conformation occurs via a kinetically slow process at µM concentration, after which the two porphyrin rings adopt a nearly parallel orientation, consistent with the absence of significant exciton coupling in the ICD spectra. At µM concentration this *anti* complex undergoes further aggregation, accounting for the slow time evolution observed in UV-vis, CD, and fluorescence but not in NMR, where the higher concentration and small (8 eq.) excess of cycHC[8] disfavour formation of the assembled species.

The differing behaviour can be rationalised on geometric grounds. Measurements on the published crystal structures of bis–ZnOEP[168–170] gave two characteristic diameters of the porphyrin face: 12.0 ± 0.1 Å measured between the β-carbons of the porphyrin core, and 14.7 ± 0.1 Å measured between the methylene carbons of the peripheral ethyl substituents that lie in the porphyrin mean plane. The two cycHC[*n*] hosts are similar in height (12.4 Å for cycHC[6] and 11.9 Å for cycHC[8]) but differ in diameter (14.2 Å for cycHC[6] and 16.9 Å for cycHC[8]).[6] The cycHC[6] diameter is therefore an almost exact match to the ethyl-decorated face of bis–ZnOEP, and the cycHC[6] macrocycle can be accommodated cleanly between the two porphyrin cores in a tweezer geometry. The 16.9 Å diameter of cycHC[8] exceeds the outer ethyl-defined diameter of a single porphyrin face by more than 2 Å, making the same tweezer arrangement sterically unfavourable. Coordination is therefore forced to proceed externally, and the additional binding sites available on the larger cycHC[8] macrocycle further enable the inter-complex contacts that lead to aggregation.

The qualitatively different binding behaviour of bis–ZnOEP with cycHC[6] and cycHC[8] thus stands in clear contrast to the smooth structural variation observed across the mono-porphyrin library in section 3.1, where both cycHC macrocycles produced architecturally similar M···O coordination modes that differed only in connectivity.

Adding a second porphyrin face to the receptor introduces a new binding regime, tweezer encapsulation, that is accessible only to one of the two cycHC macrocycles; the geometric mismatch with the larger cycHC[8] reroutes the interaction toward external coordination and aggregation. Whether bis-porphyrins with longer linkers could accommodate cycHC[8] in a proper tweezer geometry remains an open question for future work. This is useful for sensor design: bis–ZnOEP can in principle distinguish between cycHC[6] and cycHC[8] by their distinct chiroptical signatures (intense bisignate ICD versus weak monosignate ICD), a discrimination that is not available with mono-porphyrins.

3.3 Chiral Recognition of Volatile Enantiomers by Porphyrin·Cyclohexanohemicucurbit[8]uril-Functionalised Gravimetric Sensor Arrays (Publication III)

Sections 3.1 and 3.2 demonstrated that cycHC[*n*] macrocycles transfer chirality to achiral metalloporphyrins through external M···O coordination, which operates across a broad range of mono-porphyrins and the bis-porphyrin host. Chirogenesis was shown to outlast the transition from solution to the solid state, and in the case of the mono-porphyrin·cycHC[8] complexes the ECD dissymmetry factor is amplified roughly tenfold in the microcrystalline solid state relative to dilute solution (section 3.1.4). These observations suggested that thin films of cycHC[*n*]·metalloporphyrin adducts could be used as functional materials for chiral sensing. This section describes such an implementation. Four achiral metalloporphyrins (ZnOEP (**1**), ZnTPP (**2**), MgTPP (**7**), and bis-ZnOEP) were each combined with both enantiomers of cycHC[8] to produce eight chiral films, deposited on quartz crystal microbalances (QMB), and used to construct an enantioselective electronic nose array. A new normalisation protocol, based on virtual racemic references (introduced in section 3.3.3), is introduced to extract the enantioselective component of the sensor response from concentration-dominated raw data.

3.3.1 Film preparation and chiroptical characterisation

Sensing films were obtained by drop-casting or spin-coating DCM solutions of metalloporphyrin and cycHC[8] in a 2:1 molar ratio (0.4 mM porphyrin, 0.2 mM cycHC[8]) onto glass slides or gold QMB electrodes. In drop-casting, 50 µL of solution was deposited with a syringe onto the substrate and the solvent allowed to evaporate under ambient conditions; this is operationally simple but can produce inhomogeneous films with coffee-ring artefacts due to solvent flow during drying. In spin-coating, 10 µL aliquots of solution were repeatedly applied to a substrate rotating at 1500 rpm, where centrifugal force spreads the solution into a thin uniform layer as the solvent evaporates rapidly, giving more reproducible film morphology. Both methods gave essentially identical UV-vis and ECD profiles, confirming that the chiroptical response is intrinsic to the adduct rather than a deposition artefact. Spin-coated films were preferred for chiroptical characterisation due to their greater uniformity, while drop-casting was retained for QMB sensor fabrication as it allows precise control of the deposited mass through iterative casting steps. The 2:1 stoichiometry was selected on the basis of the crystal structures reported in section 3.1.2, where one cycHC[8] molecule binds two porphyrins through external M···O coordination.

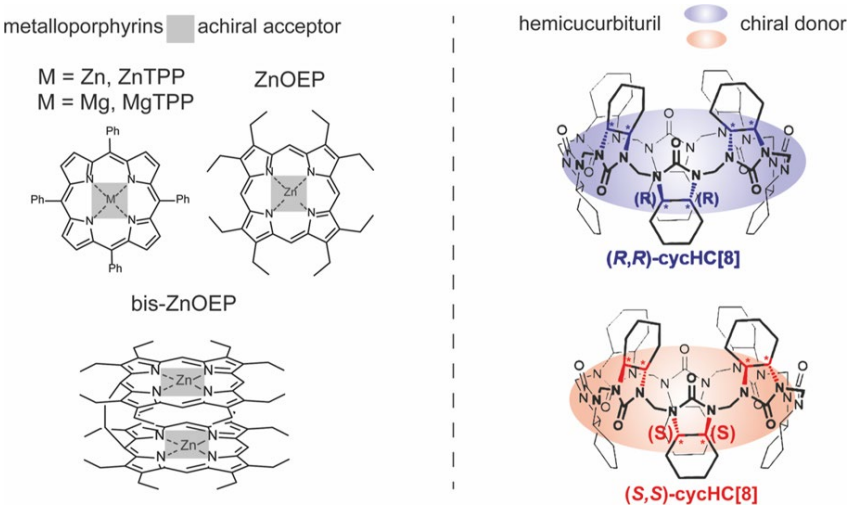

*Figure 27 Structures of the four metalloporphyrins (**1**, **2**, **7**, bis-ZnOEP) and (R,R)- and (S,S)-cycHC[8] used to prepare the sensing films. Reproduced from Publication III under CC BY 4.0.*

In DCM solution at the concentrations used for film deposition (0.4 mM porphyrin, 0.2 mM cycHC[8]), none of the eight mixtures showed any detectable ECD signal in the porphyrin absorption region. As discussed in section 3.1.4, an excess of cycHC[*n*] is normally required to populate the complex sufficiently for solution ECD detection at micromolar porphyrin concentrations. Upon solvent evaporation, however, all four porphyrin·cycHC[8] systems gave films with clear bisignate Cotton effects in the Soret region, with mirror-image profiles between (*R*,*R*)- and (*S*,*S*)-cycHC[8] (Figure 28). ECD signals appear in the solid state where the solutions were ECD silent. This is similar to the enhancement seen in section 3.1.4 for KBr pellets of cycHC[8]·**2** and cycHC[8]·**7**. In both cases, solvent removal drives the equilibrium towards the complexation and brings the porphyrin chromophores close enough for exciton coupling to become observable.

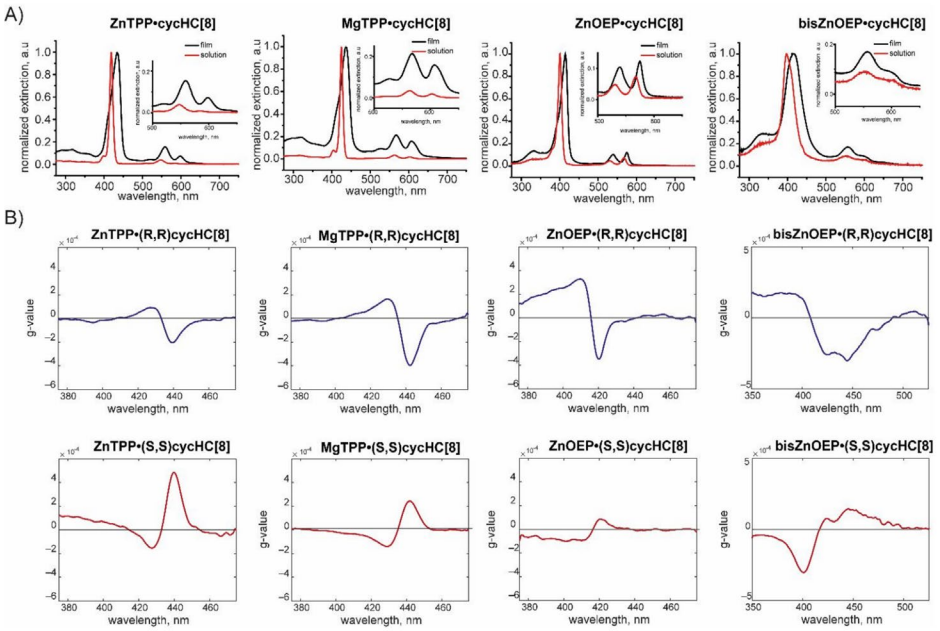

Figure 28 UV-vis spectra of metalloporphyrin·cycHC[8] systems in DCM solution (red) and as spin-coated films (black), with the Q-band region magnified. (B) ECD spectra of the films prepared with (R,R)- (blue) and (S,S)-cycHC[8] (red) enantiomers, CD intensities are expressed as dissymmetry factor g (×10⁻⁴); the corresponding solutions are ECD-silent. Reproduced from the Supporting Information of Publication III under CC BY 4.0.

The UV-vis spectra of all four porphyrin·cycHC[8] films showed broadening and a bathochromic shift of both the Soret and Q-bands of 5–20 nm relative to DCM solution (Table 4), consistent with the formation of porphyrin aggregates on solvent evaporation.[171] The ECD response of bis-ZnOEP·cycHC[8] was more complex than those of the mono-porphyrin films, reflecting the *syn*/*anti* conformational equilibrium discussed in section 3.2.4 and the resulting superposition of intra- and intermolecular exciton couplings. The chiroptical signature of the adduct is preserved across substrates and deposition geometries, unlike films of intrinsically chiral porphyrins, whose response is often highly sensitive to solvent, substrate, and deposition method.[172]

Table 4 UV-vis absorption and ECD maxima of metalloporphyrin·cycHC[8] systems in DCM solution and in spin-coated films, with ECD crossover wavelengths. Reproduced from Publication III under CC BY 4.0.

DCM solution			Film on glass	
No	Metalloporphyrine ·cycHC[8]	UV-Vis bands (nm)	UV-Vis bands (nm)	CD bands (nm), (crossover)
1	ZnTPP	417, 547, 587	434, 558, 596	427, 440, (433)
2	MgTPP	425, 563, 602	437, 567, 609	428, 441, (435)
3	ZnOEP	410, 531, 568	415, 539, 575	409, 419, (416)
4	bis–ZnOEP	398, 534	419, 562	446

3.3.2 Gravimetric sensor responses to chiral volatile analytes

Films were deposited onto AT-cut quartz resonators oscillating at approximately 20 MHz, for which the theoretical mass sensitivity is 7.2 Hz ng^{-1}. QMBs were chosen for three reasons. First, they are chemically non-selective transducers whose response depends only on the mass adsorbed, so the enantioselectivity observed in the array can be attributed entirely to the chiral film. Second, the frequency shift between bare and coated QMB quantifies the amount of sensing material deposited, which is essential for the normalisation procedure introduced in section 3.3.3. Third, multiple QMB elements can be measured simultaneously as an array, enabling the combinatorial pattern recognition approach that underpins the enantioselective electronic nose concept. The complete array consisted of ten elements: eight chiral sensors from four metalloporphyrins combined with both cycHC[8] enantiomers, and two achiral reference sensors based on **2** and bis-ZnOEP. Each sensor was a separate piezoelectric device connected to a dedicated oscillator circuit, allowing all ten elements to be measured simultaneously under identical analyte exposure conditions. Each measurement consisted of a 5-minute gas exposure followed by a 20-minute carrier gas purge; responses were fully reversible.

The array was exposed to vapours of three pairs of chiral analytes (Figure 29) representing different sorption regimes: (*R*)- and (*S*)-limonene, whose flexible linear structure and extra C=C bond facilitate diffusion into internal sites of the porphyrin aggregate matrix through π-interactions; (*R*)- and (*S*)-1-phenylethylamine, an aromatic amine capable of π-stacking with NH_2 coordination to the porphyrin metal centre; and (1*R*,5*R*)- and (1*S*,5*S*)-α-pinene, whose bicyclic structure and dimethylmethylene bridge create greater steric bulk, confining adsorption to accessible surface sites of the film.[173,174]

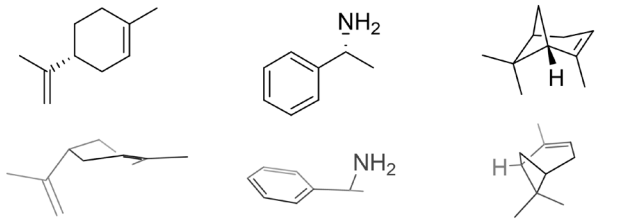

Figure 29 Structures of the three chiral analytes used in sensor array evaluation, shown as (R)-enantiomers in 2D (top) and 3D (bottom) representations. Both enantiomers of each analyte were tested.

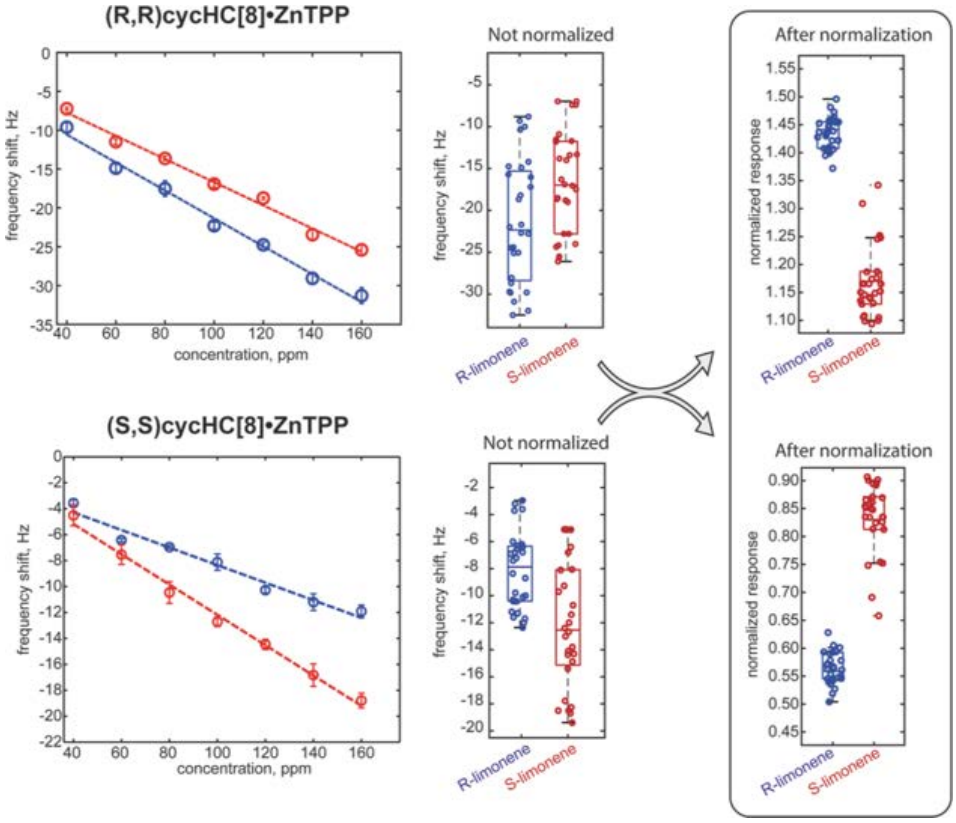

*Figure 30 Characteristic response curves of (R,R)- and (S,S)-cycHC[8]·**2** sensor pairs (sensors 1 and 2 of the 10-element array) to (R)- and (S)-limonene vapour at varying concentrations (left), with data distributions before (centre) and after normalisation (right). Reproduced from Publication III under CC BY 4.0.*

Sensor responses were linear in concentration over the ranges tested (40–160 ppm for limonene, 76–139 ppm for 1-phenylethylamine, 39–234 ppm for α-pinene). For limonene, almost all chiral sensors showed a systematic preference for one enantiomer. All Zn-porphyrin·(*R*,*R*)-cycHC[8] films preferred (*R*)-limonene, whereas the MgTPP·(*R*,*R*)-cycHC[8] film preferred (*S*)-limonene. The (*S*,*S*)-cycHC[8] sensors gave mirror-image selectivities. The Zn/Mg inversion is consistent with the qualitative difference in coordination geometry identified by NCI analysis in section 3.1.3 between the more localised Zn···O and more spatially extended Mg···O interactions. For 1-phenylethylamine, clear enantio-discrimination emerged only on the ZnOEP- and bis-ZnOEP-based sensors and grew at higher concentrations. This concentration-dependent growth indicates that the amine penetrates into the film bulk rather than adsorbing only at the surface, presumably due to the axial coordination of its NH_2-group to the porphyrin metal. For α-pinene, no sensor gave statistically significant discrimination and overall responses were low, supporting the view that enantioselectivity requires diffusion of the analyte into the film bulk. As expected, the two achiral reference sensors gave no enantio-distinction towards any analyte.

Control experiments on pure (*R*,*R*)- and (*S*,*S*)-cycHC[8] films, without porphyrin, gave no enantio-discrimination. Their response to water vapour, however, was approximately

fifty times higher than that of the porphyrin·cycHC[8] adducts. Together, these observations indicate that chiral recognition arises from the porphyrin·cycHC[8] adduct as a whole, rather than from either component alone, with the cycHC[8] enantiomer providing the chiral environment. Complexation also suppresses the water sensitivity of free cycHC[8], which is essential for stable operation in ambient atmosphere.

Although the regression lines for the two enantiomers were clearly displaced for several sensor–analyte pairs, the response distributions across the full concentration range overlapped substantially (Figure 30, middle panels). A given frequency shift can equally be produced by a higher concentration of the less-preferred enantiomer or a lower concentration of the preferred one. Single-sensor discrimination is therefore impossible at unknown concentration, motivating the normalisation procedure described in the next section.

3.3.3 Virtual racemic sensor normalisation

A normalisation procedure was developed to extract the enantioselective component of the sensor response from the concentration-dominated raw signal. The procedure draws on an analogy with the ellipticity θ used to express CD signals in spectroscopy, defined by:

$$\tan(\theta)=\frac{(E_{\mathrm{R}}-E_{\mathrm{L}})}{(E_{\mathrm{R}}+E_{\mathrm{L}})} \tag{8}$$

where E_{R} and E_{L} are the electric-field magnitudes of right- and left-circularly polarised light. Here, the two enantiomeric receptors play the role of the two polarisations: their mean response represents the achiral, non-enantioselective component of mass uptake, while their difference reflects the chiral discrimination.

For each metalloporphyrin·cycHC[8] enantiomer pair, a virtual racemic reference $\overline{R}_{rac}$ is defined as the arithmetic mean of the responses of the (*R*,*R*)- and (*S*,*S*)-sensors:

$$\overline{R}_{rac}=\frac{(R_R+R_S)}{2} \tag{9}$$

and the normalised responses are obtained by division:

$$\overline{R}_{\mathrm{Rn}}=\frac{R_R}{\overline{R}_{rac}} \tag{10}$$

$$\overline{R}_{\mathrm{Sn}}=\frac{R_S}{\overline{R}_{rac}} \tag{11}$$

Within a linear-response approximation, the normalised responses become independent of analyte concentration and depend only on ratios of sensitivities (full derivation in Publication III, Supporting Information). The mass-calibration capability of QMB is essential here: it allows the amount of sensing material on each electrode to be matched between the two members of an enantiomeric pair, ensuring that the reference accurately represents the non-enantioselective baseline.

Applied to the experimental data, the normalisation collapsed the broad concentration-dependent distributions of raw responses into narrow, well-separated distributions for the two enantiomers wherever an underlying enantio-distinction was present (Figure 30, right panels). The separation between enantiomers was also enhanced relative to the raw data, since compensation for the common achiral component removed both concentration spread and ancillary fluctuations from non-chiral sources such as humidity. For α-pinene, where no underlying enantio-distinction was present, the normalised distributions remained overlapping, as expected.

A generic normalisation using one of the achiral reference sensors (**2** or bis-ZnOEP) as the denominator was also tested. This partially separated the enantiomer distributions but performed visibly worse than the virtual racemic procedure. The achiral reference compensates only partially for concentration because it does not share the same chemical structure as the chiral sensors. The virtual racemic reference, built from sensors that differ only in the absolute configuration of cycHC[8], captures the achiral component far more faithfully and rejects concentration variability almost entirely.

3.3.4 Classification of analytes and their enantiomers

To evaluate the array as an enantioselective electronic nose, the normalised responses were used as inputs to a two-step linear discriminant analysis (LDA), as illustrated in Figure 31. The first step classified samples by chemical identity (limonene, 1-phenylethylamine, or α-pinene) using the ten non-normalised sensor responses; normalisation was deliberately withheld at this stage since it removes concentration information needed for compound identification. The second step further classified samples by enantiomer using only the normalised responses of the chiral sensors; the achiral reference sensors, which lack enantiomeric pairs, were excluded from this step. Performance was evaluated over 100 random training/test splits in which test concentrations were absent from the training set, providing a stringent test of generalisation.

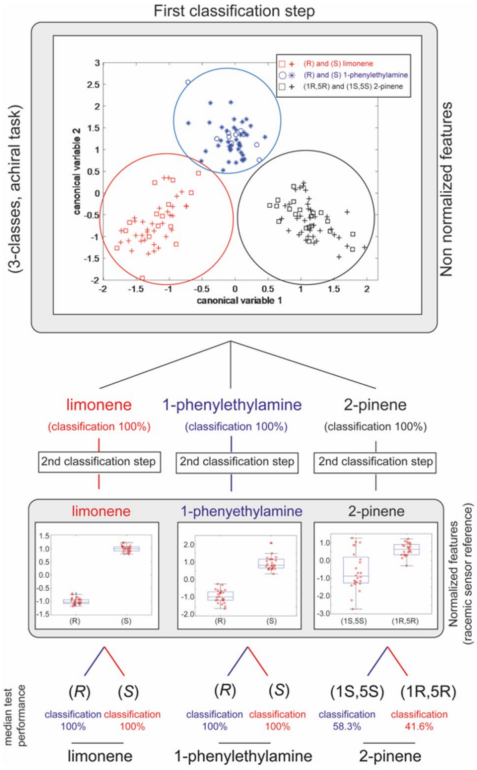

	training	test
enantiomers	concentrations [ppm]	concentrations [ppm]
limonene	All the samples belonging to 4 random concentrations selected among [40, 60, 80, 100, 120, 140, 160].	The samples belonging to the 3 remaining concentrations not included in the training
1-phenyl-ethylamine	All the samples belonging to 3 random concentrations selected among [76, 88, 101, 113, 126, 139]	The samples belonging to the 3 remaining concentrations not included in the training
2-pinene	All the samples belonging to 3 random concentrations selected among [39, 78, 117, 156, 195, 234]	The samples belonging to the 3 remaining concentrations not included in the training
	Total samples = 80	**Total samples = 72**

Figure 31 Two-step classification protocol used to recognise the chemical identity and absolute configuration of volatile chiral analytes. Top-Left: the first step classifies samples by compound class (limonene, 1-phenylethylamine, α-pinene) using the non-normalised responses of all ten

sensors (top, canonical-variable plot); Bottom-Left: the second step classifies samples within each compound class by enantiomer, using the normalised responses of the chiral sensors against their virtual racemic references (bottom, box plots). Right: subdivision of the dataset into training and test concentrations for each analyte, with the training set always restricted to a subset of the available concentrations so that the test set contains concentrations not present during training. Adapted from Publication III and its Supporting Information under CC BY 4.0.

The three chemical classes were separated with median accuracy of 100% in the first step, confirming that combinatorial selectivity across the ten-element array is sufficient to identify the analyte class regardless of concentration. In the second step, normalised responses correctly identified both enantiomers of limonene and 1-phenylethylamine with median accuracy of 100%, even when test concentrations had not been seen during training. Classification of α-pinene enantiomers remained near chance level (58.3% / 41.6%), as expected from the absence of underlying discrimination. The high classification rates achieved with a small array of structurally simple, enantioselective sensors validate the central premise of Publication III: chemical specificity and chiral discrimination can be addressed independently, provided that each chiral receptor is available in both enantiomeric forms and that the transducer permits accurate mass calibration.

4 Conclusions

The objectives of this thesis were to map the scope of cycHC[*n*]·metalloporphyrin self-assembly across solution and the solid state, to extend the study to bis-porphyrin hosts, and to translate the resulting adducts into a functional sensor array.

Nine achiral metalloporphyrins, differing in peripheral substituents, core planarity, and metal centre, were investigated for self-assembly with cycHC[6] and cycHC[8]. Seven formed external M···O complexes in solution (six Zn^{2+} and one Mg^{2+} porphyrin), while the Fe^{3+} and Pd^{2+} analogues showed no quantifiable binding. For the Zn-tetraarylporphyrin series, association constants followed a Hammett correlation with the para-substituents, and cycHC[6] bound more strongly than cycHC[8] across the entire library. Replacement of Zn^{2+} by Mg^{2+} enhanced the association by approximately three orders of magnitude, identifying the metal centre as the main determinant of binding strength. Crystallisation yielded 31 novel single-crystal structures, all built on direct M···O coordination with architectures ranging from discrete complexes to 1D and 2D coordination polymers. The complexes were ECD-active across the porphyrin library, with mirror-image Cotton effects between (*R*,*R*)- and (*S*,*S*)-cycHC[*n*] confirming chirality transfer. In KBr pellets prepared from microcrystals, the dissymmetry factor reached values about tenfold larger than in solution. The enhancement was independent of the higher-order solid-state architecture and instead tracked the local porphyrin·cycHC[*n*] coordination geometry, indicating that the close M···O contact, rather than long-range packing, is the principal source of chirality transfer.

Bis(zinc octaethylporphyrin) interacted with cycHC[6] and cycHC[8] through qualitatively different binding modes. CycHC[6] acted as a bidentate guest and formed a 1:1 tweezer complex on the timescale of mixing, while cycHC[8] was too large to encapsulate and instead drove slow self-assembly into an anti 1:2 complex over several hours, consistent with a concentration-dependent secondary aggregation process.

Exploiting the established cycHC[8]·metalloporphyrin coordination chemistry and the solid-state chiroptical enhancement of the resulting adducts, four metalloporphyrins were each combined with both enantiomers of cycHC[8] and deposited as thin films onto quartz crystal microbalances, giving eight chiroptically active sensors. Porphyrin complexation was essential for enantioselective recognition and also suppressed the strong water sensitivity of free cycHC[8], giving stable operation in ambient atmosphere. A normalisation protocol based on virtual racemic references was developed to extract enantioselective information at unknown analyte concentration. Without normalisation, the array first classified all three analytes by chemical identity; after normalisation, it further discriminated the enantiomers of limonene and 1-phenylethylamine with median accuracy of 100%, while α-pinene enantiomers were not discriminated.

Combining achiral metalloporphyrins with enantiopure cycHC[*n*] macrocycles offers a modular and synthetically efficient route to libraries of chiral sensing materials, without the multi-step synthesis traditionally required for intrinsically chiral porphyrin scaffolds. Variation of the porphyrin alone tunes the chemical selectivity, while the choice of cycHC[*n*] enantiomer dictates the handedness of recognition. This decoupling provides a practical route to expanding chiral sensor libraries from a small set of commercially or synthetically accessible components, with potential applications in pharmaceutical quality control, food and fragrance analysis, and environmental monitoring of chiral pollutants. Future work could extend the approach to other macrocyclic hosts, larger porphyrin libraries, or optical transduction platforms.

References

1 L. A. Nguyen, H. He and C. Pham-Huy, *Int. J. Biomed. Sci. IJBS*, 2006, **2**, 85–100.
2 A. W. Garrison, in *Chiral Pesticides: Stereoselectivity and Its Consequences*, American Chemical Society, 2011, vol. 1085, pp. 1–7.
3 A. A. Basheer, *Chirality*, 2018, **30**, 402–406.
4 Y. Liu, Z. Wu, D. W. Armstrong, H. Wolosker and Y. Zheng, *Nat. Rev. Chem.*, 2023, **7**, 355–373.
5 G. Alvarez-Rivera, M. Bueno, D. Ballesteros-Vivas and A. Cifuentes, *TrAC Trends Anal. Chem.*, 2020, **123**, 115761.
6 L. Ustrnul, S. Kaabel, T. Burankova, J. Martõnova, J. Adamson, N. Konrad, P. Burk, V. Borovkov and R. Aav, *Chem. Commun.*, 2019, **55**, 14434–14437.
7 IUPAC, IUPAC - supramolecular chemistry (ST07111), https://goldbook.iupac.org/terms/view/ST07111, (accessed November 4, 2025).
8 J. M. Lehn, *Pure Appl. Chem.*, 1978, **50**, 871–892.
9 J.-M. Lehn, *Angew. Chem. Int. Ed. Engl.*, 1988, **27**, 89–112.
10 A. Kraft, *Bull. Hist. Chem.*, 2008, **33**, 61–67.
11 K. Bowman-James, *Acc. Chem. Res.*, 2005, **38**, 671–678.
12 K.-T. Tang and J. P. Toennies, *Angew. Chem. Int. Ed.*, 2010, **49**, 9574–9579.
13 F. Cramer, in *Perspectives in Supramolecular Chemistry*, John Wiley & Sons, Ltd, 1994, pp. 1–23.
14 C. J. Pedersen, *J. Am. Chem. Soc.*, 1967, **89**, 7017–7036.
15 D. J. Cram and J. M. Cram, *Science*, 1974, **183**, 803–809.
16 Nobel Prize in Chemistry 1987, https://www.nobelprize.org/prizes/chemistry/1987/press-release/, (accessed November 21, 2025).
17 C. O. Dietrich-Buchecker, J. P. Sauvage and J. M. Kern, *J. Am. Chem. Soc.*, 1984, **106**, 3043–3045.
18 P. L. Anelli, N. Spencer and J. F. Stoddart, *J. Am. Chem. Soc.*, 1991, **113**, 5131–5133.
19 N. Koumura, R. W. J. Zijlstra, R. A. van Delden, N. Harada and B. L. Feringa, *Nature*, 1999, **401**, 152–155.
20 Nobel Prize in Chemistry 2016, https://www.nobelprize.org/prizes/chemistry/2016/press-release/, (accessed February 6, 2026).
21 Nobel Prize in Chemistry 2025, https://www.nobelprize.org/prizes/chemistry/2025/press-release/, (accessed November 21, 2025).
22 M. Kondo, T. Yoshitomi, H. Matsuzaka, S. Kitagawa and K. Seki, *Angew. Chem. Int. Ed. Engl.*, 1997, **36**, 1725–1727.
23 B. F. Hoskins and R. Robson, *J. Am. Chem. Soc.*, 1989, **111**, 5962–5964.
24 H. Li, M. Eddaoudi, M. O'Keeffe and O. M. Yaghi, *Nature*, 1999, **402**, 276–279.
25 D. E. Balderston, E. Feo, A. Leonescu, M. Stevens, A. M. Wilmshurst, P. A. Gale, C. J. E. Haynes, G. T. Williams and J. R. Hiscock, *Chem. Soc. Rev.*, 2025, **54**, 8888–8924.
26 C. A. Hunter, *Angew. Chem. Int. Ed.*, 2004, **43**, 5310–5324.
27 M. C. Storer and C. A. Hunter, *Chem. Soc. Rev.*, 2022, **51**, 10064–10082.
28 J. W. Steed and J. L. Atwood, *Supramolecular Chemistry*, John Wiley & Sons, Hoboken, NJ, 3rd edn., 2022.
29 H.-J. Schneider, *Angew. Chem. Int. Ed.*, 2009, **48**, 3924–3977.
30 F. Biedermann and H.-J. Schneider, *Chem. Rev.*, 2016, **116**, 5216–5300.
31 R. Chakrabarty, P. S. Mukherjee and P. J. Stang, *Chem. Rev.*, 2011, **111**, 6810–6918.

32 G. Cavallo, P. Metrangolo, R. Milani, T. Pilati, A. Priimagi, G. Resnati and G. Terraneo, *Chem. Rev.*, 2016, **116**, 2478–2601.
33 B. L. Schottel, H. T. Chifotides and K. R. Dunbar, *Chem. Soc. Rev.*, 2007, **37**, 68–83.
34 A. J. Stone, *The theory of intermolecular forces*, Oxford University Press, Oxford, Second edition., 2013.
35 P. Atkins, *Inorganic Chemistry*, OUP Oxford, 2010.
36 C. E. Housecroft and A. G. Sharpe, *Inorganic Chemistry (5th Edition)*, Pearson, 2018.
37 R. G. Pearson, *J. Am. Chem. Soc.*, 1963, **85**, 3533–3539.
38 R. G. Parr and R. G. Pearson, *J. Am. Chem. Soc.*, 1983, **105**, 7512–7516.
39 J. N. Israelachvili, *Intermolecular and Surface Forces*, Academic Press (Elsevier), Waltham, MA, 3rd edn., 2011.
40 R. F. W. Bader, *Chem. Rev.*, 1991, **91**, 893–928.
41 A. E. Reed, L. A. Curtiss and F. Weinhold, *Chem. Rev.*, 1988, **88**, 899–926.
42 K. Szalewicz, *WIREs Comput. Mol. Sci.*, 2012, **2**, 254–272.
43 M. A. Spackman and D. Jayatilaka, *CrystEngComm*, 2009, **11**, 19–32.
44 E. R. Johnson, S. Keinan, P. Mori-Sánchez, J. Contreras-García, A. J. Cohen and W. Yang, *J. Am. Chem. Soc.*, 2010, **132**, 6498–6506.
45 T. Lu, *Angew. Chem. Int. Ed.*, 2025, **64**, e202504895.
46 J. Contreras-García, E. R. Johnson, S. Keinan, R. Chaudret, J.-P. Piquemal, D. N. Beratan and W. Yang, *J. Chem. Theory Comput.*, 2011, **7**, 625–632.
47 T. Lu and Q. Chen, *Chemistry–Methods*, 2021, **1**, 231–239.
48 P. Thordarson, *Chem. Soc. Rev.*, 2011, **40**, 1305–1323.
49 F. Ulatowski, K. Dąbrowa, T. Bałakier and J. Jurczak, *J. Org. Chem.*, 2016, **81**, 1746–1756.
50 L. Ustrnul, T. Burankova, M. Öeren, K. Juhhimenko, J. Ilmarinen, K. Siilak, K. A. Mishra and R. Aav, *Front. Chem.*, 2021, **9**, 701028.
51 D. B. Hibbert and P. Thordarson, *Chem. Commun.*, 2016, **52**, 12792–12805.
52 C. A. Hunter and H. L. Anderson, *Angew. Chem. Int. Ed.*, 2009, **48**, 7488–7499.
53 L. K. S. von Krbek, C. A. Schalley and P. Thordarson, *Chem. Soc. Rev.*, 2017, **46**, 2622–2637.
54 I. Agranat, H. Caner and J. Caldwell, *Nat. Rev. Drug Discov.*, 2002, **1**, 753–768.
55 M. Laska, A. Wieser, R. M. Rivas Bautista and L. T. Hernandez Salazar, *Chem. Senses*, 2004, **29**, 101–109.
56 K. Roth, H. Bauer, B. J. Sjursnes, L. Kvittingen and R. Schmid, *ChemBioChem*, 2025, **26**, e202401085.
57 Y. Kono, K. Nakabayashi, S. Kitamura, R. Kuroda, M. Fujiki and Y. Imai, *Tetrahedron*, 2015, **71**, 3985–3989.
58 T. Taniguchi, *Synlett*, 2023, **34**, 1839–1844.
59 C. Rosini, R. Ruzziconi, S. Superchi, F. Fringuelli and O. Piermatti, *Tetrahedron Asymmetry*, 1998, **9**, 55–62.
60 G. Mazzeo, S. Pedotti, G. Longhi, A. Patti and S. Abbate, *Spectrochim. Acta. A. Mol. Biomol. Spectrosc.*, 2022, **272**, 121010.
61 W. S. Brickell, A. Brown, C. M. Kemp and S. F. Mason, *J. Chem. Soc. Inorg. Phys. Theor.*, 1971, 756–760.
62 M. Goodman and S. Chen, *Macromolecules*, 1971, **4**, 625–629.
63 E. Yashima, N. Ousaka, D. Taura, K. Shimomura, T. Ikai and K. Maeda, *Chem. Rev.*, 2016, **116**, 13752–13990.
64 A. R. A. Palmans and E. W. Meijer, *Angew. Chem. Int. Ed.*, 2007, **46**, 8948–8968.

65 D. Fujita, Y. Ueda, S. Sato, N. Mizuno, T. Kumasaka and M. Fujita, *Nature*, 2016, **540**, 563–566.
66 B. L. Feringa, *Angew. Chem. Int. Ed.*, 2017, **56**, 11060–11078.
67 C. Djerassi, *Science*, 1961, **134**, 649–655.
68 P. Laur, in *Comprehensive Chiroptical Spectroscopy*, John Wiley & Sons, Ltd, 2012, pp. 1–35.
69 N. Harada and K. Nakanishi, *Acc. Chem. Res.*, 1972, **5**, 257–263.
70 V. V. Borovkov, G. A. Hembury and Y. Inoue, *Acc. Chem. Res.*, 2004, **37**, 449–459.
71 W. Kuhn, *Trans. Faraday Soc.*, 1930, **26**, 293–308.
72 E. Castiglioni, P. Biscarini and S. Abbate, *Chirality*, 2009, **21**, E28–E36.
73 Y. Shindo and M. Nishio, *Biopolymers*, 1990, **30**, 25–31.
74 R. Kuroda, T. Harada and Y. Shindo, *Rev. Sci. Instrum.*, 2001, **72**, 3802–3810.
75 R. Kuroda and T. Honma, *Chirality*, 2000, **12**, 269–277.
76 P. J. Stephens, F. J. Devlin and J. R. Cheeseman, *VCD Spectroscopy for Organic Chemists*, CRC Press, Boca Raton, 2012.
77 M. Urbanová and P. Maloň, in *Analytical Methods in Supramolecular Chemistry*, John Wiley & Sons, Ltd, 2012, pp. 337–369.
78 F. Zhu, N. W. Isaacs, L. Hecht and L. D. Barron, *Structure*, 2005, **13**, 1409–1419.
79 A. Castaings, J.-C. Marchon, D. Cavagnat and T. Buffeteau, *Chirality*, 2013, **25**, 480–486.
80 J. Ouyang, A. Swartjes, M. Geerts, P. J. Gilissen, D. Wang, P. C. P. Teeuwen, P. Tinnemans, N. Vanthuyne, S. Chentouf, F. P. J. T. Rutjes, J.-V. Naubron, J. Crassous, J. A. A. W. Elemans and R. J. M. Nolte, *Nat. Commun.*, 2020, **11**, 4776.
81 J. P. J. Bruekers, M. A. Hellinghuizen, N. Vanthuyne, P. Tinnemans, P. J. Gilissen, W. J. Buma, J.-V. Naubron, J. Crassous, J. A. A. W. Elemans and R. J. M. Nolte, *Eur. J. Org. Chem.*, 2021, **2021**, 607–617.
82 J. Wade, J. R. Brandt, D. Reger, F. Zinna, K. Y. Amsharov, N. Jux, D. L. Andrews and M. J. Fuchter, *Angew. Chem. Int. Ed.*, 2021, **60**, 222–227.
83 P. Chen, H. Fan, S. Du, X. Wen, L. Zhang and M. Liu, *Soft Matter*, 2024, **20**, 8937–8946.
84 B. Bosnich, *J. Am. Chem. Soc.*, 1966, **88**, 2606–2606.
85 L. D. Hayward and R. N. Totty, *J. Chem. Soc. Chem. Commun.*, 1969, 676–677.
86 V. V. Borovkov, J. M. Lintuluoto and Y. Inoue, *J. Am. Chem. Soc.*, 2001, **123**, 2979–2989.
87 G. A. Hembury, V. V. Borovkov and Y. Inoue, *Chem. Rev.*, 2008, **108**, 1–73.
88 Z. Xie, V. Stepanenko, K. Radacki and F. Würthner, *Chem. – Eur. J.*, 2012, **18**, 7060–7070.
89 S. Matile, N. Berova, K. Nakanishi, S. Novkova, I. Philipova and B. Blagoev, *J. Am. Chem. Soc.*, 1995, **117**, 7021–7022.
90 S. Matile, N. Berova, K. Nakanishi, J. Fleischhauer and R. W. Woody, *J. Am. Chem. Soc.*, 1996, **118**, 5198–5206.
91 H. Sasafuchi, M. Ueda, N. Kishida, T. Sawada, S. Suzuki, Y. Imai and M. Yoshizawa, *Chem*, 2025, **11**, 102332.
92 E. Benchimol, H. M. O'Connor, B. Schmidt, N. Bogo, J. J. Holstein, J. I. Lovitt, S. Shanmugaraju, C. J. Stein, T. Gunnlaugsson and G. H. Clever, *Angew. Chem. Int. Ed.*, 2025, **64**, e202421137.
93 P. J. Brothers and M. O. Senge, in *Fundamentals of Porphyrin Chemistry*, eds. P. J. Brothers and M. O. Senge, Wiley, 1st edn., 2022, pp. 1–8.

94 M. O. Senge, N. N. Sergeeva and K. J. Hale, *Chem. Soc. Rev.*, 2021, **50**, 4730–4789.
95 V. Nikolaou, E. Nikoloudakis, K. Ladomenou, G. Charalambidis and A. G. Coutsolelos, *Front. Chem. Biol.*, 2024, **2**, 1346465.
96 E. Vogel, *J. Heterocycl. Chem.*, 1996, **33**, 1461–1487.
97 M. Gouterman, *J. Mol. Spectrosc.*, 1961, **6**, 138–163.
98 X. Huang, K. Nakanishi and N. Berova, *Chirality*, 2000, **12**, 237–255.
99 I. Beletskaya, V. S. Tyurin, A. Yu. Tsivadze, R. Guilard and C. Stern, *Chem. Rev.*, 2009, **109**, 1659–1713.
100 C. M. Drain, A. Varotto and I. Radivojevic, *Chem. Rev.*, 2009, **109**, 1630–1658.
101 H. Lee, H. Park, D. Y. Ryu and W.-D. Jang, *Chem. Soc. Rev.*, 2023, **52**, 1947–1974.
102 R. Paolesse, S. Nardis, D. Monti, M. Stefanelli and C. Di Natale, *Chem. Rev.*, 2017, **117**, 2517–2583.
103 K. M. Smith, *Porphyrins and Metalloporphyrins: A New Edition Based on the Original Volume by J. E. Falk*, Elsevier Scientific Publishing Company, 1975.
104 U. Tripathy, D. Kowalska, X. Liu, S. Velate and R. P. Steer, *J. Phys. Chem. A*, 2008, **112**, 5824–5833.
105 J. L. Hoard, *Science*, 1971, **174**, 1295–1302.
106 K. M. Kadish and L. R. Shiue, *Inorg. Chem.*, 1982, **21**, 1112–1115.
107 K. M. Kadish, L. R. Shiue, R. K. Rhodes and L. A. Bottomley, *Inorg. Chem.*, 1981, **20**, 1274–1277.
108 K. P. Kepp, *Inorg. Chem.*, 2016, **55**, 9461–9470.
109 V. P. Andreev, P. S. Sobolev, D. O. Zaitsev and V. A. Tafeenko, *Russ. J. Gen. Chem.*, 2014, **84**, 320–325.
110 S. Hiroto, Y. Miyake and H. Shinokubo, *Chem. Rev.*, 2017, **117**, 2910–3043.
111 C. J. Kingsbury and M. O. Senge, *Coord. Chem. Rev.*, 2021, **431**, 213760.
112 C. J. Medforth, M. O. Senge, K. M. Smith, L. D. Sparks and J. A. Shelnutt, *J. Am. Chem. Soc.*, 1992, **114**, 9859–9869.
113 J. R. Platt, *J. Chem. Phys.*, 1949, **17**, 484–495.
114 M. Taniguchi, J. S. Lindsey, D. F. Bocian and D. Holten, *J. Photochem. Photobiol. C Photochem. Rev.*, 2021, **46**, 100401.
115 W. Zheng, N. Shan, L. Yu and X. Wang, *Dyes Pigments*, 2008, **77**, 153–157.
116 T. Tanaka and A. Osuka, *Chem. Soc. Rev.*, 2015, **44**, 943–969.
117 P. D. Harvey, C. Stern, C. P. Gros and R. Guilard, *Coord. Chem. Rev.*, 2007, **251**, 401–428.
118 V. Borovkov and Y. Inoue, *Eur. J. Org. Chem.*, 2009, **2009**, 189–197.
119 V. Borovkov, *Symmetry*, 2014, **6**, 256–294.
120 R. Behrend, E. Meyer and F. Rusche, *Justus Liebigs Ann. Chem.*, 1905, **339**, 1–37.
121 W. A. Freeman, W. L. Mock and N. Y. Shih, *J. Am. Chem. Soc.*, 1981, **103**, 7367–7368.
122 J. Kim, I.-S. Jung, S.-Y. Kim, E. Lee, J.-K. Kang, S. Sakamoto, K. Yamaguchi and K. Kim, *J. Am. Chem. Soc.*, 2000, **122**, 540–541.
123 S. Liu, P. Y. Zavalij and L. Isaacs, *J. Am. Chem. Soc.*, 2005, **127**, 16798–16799.
124 Q. Li, S.-C. Qiu, J. Zhang, K. Chen, Y. Huang, X. Xiao, Y. Zhang, F. Li, Y.-Q. Zhang, S.-F. Xue, Q.-J. Zhu, Z. Tao, L. F. Lindoy and G. Wei, *Org. Lett.*, 2016, **18**, 4020–4023.
125 X. Cheng, L. Liang, K. Chen, N. Ji, X. Xiao, J. Zhang, Y. Zhang, S. Xue, Q. Zhu, X. Ni and Z. Tao, *Angew. Chem. Int. Ed.*, 2013, **52**, 7252–7255.
126 M. V. Rekharsky, T. Mori, C. Yang, Y. H. Ko, N. Selvapalam, H. Kim, D. Sobransingh, A. E. Kaifer, S. Liu, L. Isaacs, W. Chen, S. Moghaddam, M. K. Gilson, K. Kim and Y. Inoue, *Proc. Natl. Acad. Sci.*, 2007, **104**, 20737–20742.

127 N. Barooah, J. Mohanty and A. C. Bhasikuttan, *Langmuir*, 2022, **38**, 6249–6264.
128 Y. Miyahara, K. Goto, M. Oka and T. Inazu, *Angew. Chem. Int. Ed.*, 2004, **43**, 5019–5022.
129 J. Svec, M. Necas and V. Sindelar, *Angew. Chem. Int. Ed.*, 2010, **49**, 2378–2381.
130 F. Ali Mohammed, T. Xiao, L. Wang and R. B. P. Elmes, *Chem. Commun.*, 2024, **60**, 11812–11836.
131 R. Aav, E. Shmatova, I. Reile, M. Borissova, F. Topić and K. Rissanen, *Org. Lett.*, 2013, **15**, 3786–3789.
132 E. Prigorchenko, M. Öeren, S. Kaabel, M. Fomitšenko, I. Reile, I. Järving, T. Tamm, F. Topić, K. Rissanen and R. Aav, *Chem. Commun.*, 2015, **51**, 10921–10924.
133 S. Kaabel, J. Adamson, F. Topić, A. Kiesilä, E. Kalenius, M. Öeren, M. Reimund, E. Prigorchenko, A. Lõokene, H. J. Reich, K. Rissanen and R. Aav, *Chem. Sci.*, 2017, **8**, 2184–2190.
134 T. Shalima, K. A. Mishra, S. Kaabel, L. Ustrnul, S. Bartkova, K. Tõnsuaadu, I. Heinmaa and R. Aav, *Front. Chem.*, 2021, **9**, 786746.
135 E. Prigorchenko, S. Kaabel, T. Narva, A. Baškir, M. Fomitšenko, J. Adamson, I. Järving, K. Rissanen, T. Tamm and R. Aav, *Chem. Commun.*, 2019, **55**, 9307–9310.
136 G. Magna, F. Mandoj, M. Stefanelli, G. Pomarico, D. Monti, C. Di Natale, R. Paolesse and S. Nardis, *Nanomaterials*, 2021, **11**, 997.
137 E. V. Ermakova and A. Bessmertnykh-Lemeune, *Chemosensors*, 2024, **12**, 253.
138 M. Penza, *Sensors*, 2025, **25**, 5422.
139 E. Zor, H. Bingol and M. Ersoz, *TrAC Trends Anal. Chem.*, 2019, **121**, 115662.
140 N. Alanazi, M. Almutairi and A. N. Alodhayb, *Sens. Imaging*, 2023, **24**, 10.
141 G. Magna, R. Belugina, F. Mandoj, A. Catini, A. V. Legin, R. Paolesse and C. Di Natale, *Sens. Actuators B Chem.*, 2020, **320**, 128373.
142 R. Bhushan, *Sep. Purif. Rev.*, 2025, 1–20.
143 Q. Zhou, C. Zheng, L. Zhu and J. Wang, *TrAC Trends Anal. Chem.*, 2022, **157**, 116805.
144 J. Ide, T. Nakamoto and T. Moriizumi, *Sens. Actuators Phys.*, 1995, **49**, 73–78.
145 I. P. May, M. P. Byfield, M. Lindström and L. F. Wünsche, *Chirality*, 1997, **9**, 225–232.
146 K. Bodenhöfer, A. Hierlemann, J. Seemann, G. Gauglitz, B. Koppenhoefer and W. Göpel, *Nature*, 1997, **387**, 577–580.
147 C. Fietzek, T. Hermle, W. Rosenstiel and V. Schurig, *Fresenius J. Anal. Chem.*, 2001, **371**, 58–63.
148 T. Nakanishi, N. Yamakawa, T. Asahi, T. Osaka, B. Ohtani and K. Uosaki, *J. Am. Chem. Soc.*, 2002, **124**, 740–741.
149 I. Manzini, D. Schild and C. Di Natale, *Physiol. Rev.*, 2022, **102**, 61–154.
150 F. Röck, N. Barsan and U. Weimar, *Chem. Rev.*, 2008, **108**, 705–725.
151 M. A. Akbar, A. Ait Si Ali, A. Amira, F. Bensaali, M. Benammar, M. Hassan and A. Bermak, *IEEE Sens. J.*, 2016, **16**, 5734–5746.
152 M. Śliwińska, P. Wiśniewska, T. Dymerski, J. Namieśnik and W. Wardencki, *J. Agric. Food Chem.*, 2014, **62**, 1423–1448.
153 H. Sun, F. Tian, Z. Liang, T. Sun, B. Yu, S. X. Yang, Q. He, L. Zhang and X. Liu, *IEEE Trans. Ind. Electron.*, 2017, **64**, 7350–7358.
154 C. J. Kingsbury and M. O. Senge, *Angew. Chem. Int. Ed.*, 2024, **63**, e202403754.
155 S. Olsson, C. Dahlstrand and A. Gogoll, *Dalton Trans.*, 2018, **47**, 11572–11585.
156 C. Hansch, A. Leo and R. W. Taft, *Chem. Rev.*, 1991, **91**, 165–195.
157 C. G. Swain and E. C. Lupton, *J. Am. Chem. Soc.*, 1968, **90**, 4328–4337.

158 S. Kavitha, P. Deepa, M. Karthika and R. Kanakaraju, *J. Mol. Graph. Model.*, 2018, **85**, 13–24.
159 F. C. Hawthorne, *Phys. Chem. Miner.*, 2012, **39**, 841–874.
160 I. D. Brown, *The Chemical Bond in Inorganic Chemistry: The Bond Valence Model*, Oxford University Press, 2006.
161 I. Osadchuk, R. Aav, V. Borovkov and E. Clot, *ChemPhysChem*, 2021, **22**, 1817–1833.
162 I. Osadchuk, H.-E. Luts, A. Zahharova, T. Tamm and V. Borovkov, *ChemPhysChem*, 2024, **25**, e202400104.
163 V. V. Borovkov, J. M. Lintuluoto, G. A. Hembury, M. Sugiura, R. Arakawa and Y. Inoue, *J. Org. Chem.*, 2003, **68**, 7176–7192.
164 V. V. Borovkov, J. M. Lintuluoto and Y. Inoue, *J. Phys. Chem. B*, 1999, **103**, 5151–5156.
165 V. V. Borovkov, J. M. Lintuluoto and Y. Inoue, *Tetrahedron Lett.*, 1999, **40**, 5051–5054.
166 K. Sugiura, G. Ponomarev, S. Okubo, A. Tajiri and Y. Sakata, *Bull. Chem. Soc. Jpn.*, 1997, **70**, 1115–1123.
167 V. V. Borovkov, J. M. Lintuluoto, M. Sugiura, Y. Inoue and R. Kuroda, *J. Am. Chem. Soc.*, 2002, **124**, 11282–11283.
168 V. V. Borovkov, I. Fujii, A. Muranaka, G. A. Hembury, T. Tanaka, A. Ceulemans, N. Kobayashi and Y. Inoue, *Angew. Chem. Int. Ed.*, 2004, **43**, 5481–5485.
169 S. Safran, T. Hökelek, S. Bilge, S. Demiriz, A. Natsagdorj and Z. Kiliç, *Anal. Sci. X-Ray Struct. Anal. Online*, 2005, **21**, x77–x78.
170 I. Osadchuk, N. Konrad, K.-N. Truong, K. Rissanen, E. Clot, R. Aav, D. Kananovich and V. Borovkov, *Symmetry*, 2021, **13**, 275.
171 G. Albano, G. Pescitelli and L. Di Bari, *Chem. Rev.*, 2020, **120**, 10145–10243.
172 G. Magna, T. Traini, M. L. Naitana, G. Bussetti, F. Domenici, G. Paradossi, M. Venanzi, C. Di Natale, R. Paolesse, D. Monti and M. Stefanelli, *Front. Chem.*, 2022, **9**, 804893.
173 Y. Fang, P. S. J. Lakey, S. Riahi, A. T. McDonald, M. Shrestha, D. J. Tobias, M. Shiraiwa and V. H. Grassian, *Chem. Sci.*, 2019, **10**, 2906–2914.
174 S. E. Hale, S. Endo, H. P. H. Arp, A. R. Zimmerman and G. Cornelissen, *Chemosphere*, 2015, **119**, 881–888.

Acknowledgements

The work presented in this dissertation was carried out at the Department of Chemistry and Biotechnology, School of Science, Tallinn University of Technology. It was financially supported by the Estonian Research Council (grant PRG399 "Adaptable supramolecular chirality sensors"), the European Union's Horizon 2020 FET-OPEN programme (project INITIO, grant agreement no. 828779), the European Union's Horizon Europe Pathfinder programme (project CHIRALFORCE, grant agreement no. 101046961), and the Estonian Centre of Excellence in Circular Economy for Strategic Mineral and Carbon Resources (SOURCES, TK228). This support is gratefully acknowledged.

I am grateful to my supervisor, Professor Riina Aav, for accepting me into her group and for her patience and trust throughout these years. I was probably not always the easiest student. She made sure we had a real group culture: regular events, honest feedback, and opportunities to present our work at conferences. Her support went well beyond science, and I think everyone in the group would agree she has a way of pushing you to grow as a person, not just as a researcher. I am equally grateful to my co-supervisor, Dr Lukáš Ustrnul, for his time, patience, and day-to-day involvement in this work. We built a good friendship along the way, which made the harder parts of the PhD considerably easier. I also owe a great deal to Dr Victor Borovkov, whose deep expertise in porphyrin chemistry and chiroptical spectroscopy was invaluable throughout this work, and whose discussions and help with rationalising the results shaped my understanding of the field.

I would like to thank all of the co-authors of the publications on which this thesis is based. The single-crystal X-ray diffraction work that underpins much of Publication I was carried out by Dr Khai-Nghi Truong, Dr Jas S. Ward, and Professor Kari Rissanen at the University of Jyväskylä, and I am very grateful for their crystallographic expertise and willingness to make sense of often difficult datasets. Solid-state ECD measurements on KBr pellets were performed by Professor Reiko Kuroda at Chubu University, whose contribution was essential to one of the central findings of this thesis. Vibrational circular dichroism measurements were performed by Nele Konrad at TalTech, whom I thank for her care and rigour. I also thank Professor Mathias O. Senge and Professor Victor Borovkov for their valuable input on porphyrin chemistry, and my TalTech co-authors Kristjan Siilak, Tatsiana Burankova, Elina Suut, Jagadeesh Varma Nallaparaju, Kamini A. Mishra, and Dr Jasper Adamson for their respective contributions to Publications I and II.

The sensor work in Publication III would not have been possible without the hospitality and scientific support of Professor Roberto Paolesse and his group at the University of Rome Tor Vergata. I particularly thank Dr Gabriele Magna for his patient introduction to quartz crystal microbalance measurements and his close involvement in the design and analysis of the sensor experiments, and Dr Manuela Stefanelli for her expertise in porphyrin thin films. I am also grateful to Professor Donato Monti (Sapienza University of Rome), Professor Corrado Di Natale (University of Rome Tor Vergata), and Professor Ludovico Valli, Dr Gabriele Giancane, and Dr Simona Bettini (University of Salento) for their contributions to the same study.

I would also like to thank the internal pre-reviewer, Dr Charles William Stark, for a thorough and constructive review of the thesis and for agreeing to do so on short notice.

Beyond the work presented here, I would like to thank Professor Ott Scheler for the opportunity to contribute to his project and for the support, both scientific and financial,

that this collaboration has provided. Working with him has broadened my chemistry experience considerably.

My thanks go to the entire Supramolecular Chemistry group at TalTech, both its present and former members, and to my many co-workers across the department, for the everyday companionship, the scientific discussions, and the friendly atmosphere that made the department a place I enjoyed coming back to.

I am deeply thankful to my parents, Zaza and Ragne, and to my sisters Salome and Elene and their families, for standing by me, believing in me, supporting me through the difficult moments, letting me vent when I needed to, and asking how things were going even when I had little new to say. I thank my friends for the same. I am also grateful to my coach, Mongkon Kongpan, for looking after my physical health and, through that, my mental health as well.

Finally, and most of all, I want to thank my partner and co-worker, Nele, who has been beside me through every part of this journey. She has helped me in the lab and in life, through good times and bad, at every conference we attended together, and through the writing of every article and of this thesis. I am very lucky.

Abstract

Chiral Supramolecular Assemblies of Metalloporphyrins and Cyclohexanohemicucurbiturils: From Molecular Recognition to Sensing Applications

The two enantiomers of a chiral compound can differ markedly in biological activity, taste, or odour, which makes their selective recognition relevant to pharmaceutical analysis, agrochemistry, biomedical diagnostics and food safety. Developing receptors that distinguish enantiomers and that are at the same time synthetically accessible and structurally tunable therefore remains an active area of supramolecular chemistry.

A widely used approach is supramolecular chirogenesis, in which chirality is transferred from one binding partner to another through non-covalent interaction. When the receiving partner is a chromophore, the transfer becomes detectable as induced circular dichroism (ICD). Cyclohexanohemicucurbit[*n*]urils (cycHC[*n*]) are a family of enantiopure macrocycles whose carbonyl oxygens act as Lewis-base donors and are well-matched to the Lewis-acidic metal centres of metalloporphyrins. The first demonstration that enantiopure cycHC[*n*] induce circular dichroism in achiral zinc porphyrins through external M···O coordination established a chirogenesis platform built from synthetically simple, modular components. The scope of this platform, however, had not been systematically mapped at the start of this work. In particular, the influence of porphyrin substituents, core planarity, and metal centre on the binding interaction remained unclear, as did the solid-state organisation of the resulting complexes, the behaviour of a bis-porphyrin host, and the translation of these adducts into functional sensing materials.

The literature overview introduces the relevant supramolecular chemistry concepts (non-covalent interactions, binding evaluation methods, and the principles of induced chirality), followed by a section on porphyrins and macrocyclic hosts with particular emphasis on metalloporphyrin coordination chemistry. It concludes with an introduction to supramolecular sensing, focusing on quartz crystal microbalances (QMB) and the use of sensor arrays combined with chemometric analysis for the recognition of chiral analytes.

The first results chapter examines a library of nine achiral metalloporphyrins differing in peripheral substituents, core planarity, and metal centre, in their interaction with both enantiomers of cycHC[6] and cycHC[8] (Publication I). UV-vis and nuclear magnetic resonance (NMR) titrations in dichloromethane showed that seven of the nine porphyrins (six Zn^{2+} and one Mg^{2+}) bind through external M···O coordination, while the Fe^{3+} and Pd^{2+} analogues showed no quantifiable binding. For the *para*-substituted Zn-tetraarylporphyrin series, the association constants followed a Hammett correlation. Across the series, cycHC[6] bound more strongly than cycHC[8], while replacement of Zn^{2+} by Mg^{2+} enhanced binding by approximately three orders of magnitude. These results identify the metal centre as the principal determinant of affinity. Thirty-one new single-crystal X-ray structures showed a range of supramolecular architectures, all built on direct M···O coordination. Solid-state CD on KBr pellets showed dissymmetry factors approximately tenfold larger than in solution; this chiroptical enhancement was found to track the local porphyrin·cycHC[*n*] coordination geometry rather than long-range crystal packing, identifying the close M···O contact as the dominant source of chirality transfer.

The second results chapter extends the study to bis(zinc octaethylporphyrin), a tweezer host known to encapsulate small bidentate guests (Publication II). NMR, UV-vis, fluorescence, and CD spectroscopy showed that the two cycHC sizes interact through qualitatively different binding modes: cycHC[6] is small enough to act as a bidentate guest and forms a 1:1 tweezer complex on the timescale of mixing, whereas cycHC[8] is too large to encapsulate and instead drives slow self-assembly of bis-ZnOEP into an *anti* 1:2 complex over several hours, as revealed by time-resolved spectroscopic monitoring and variable-temperature experiments.

The third results chapter translates the cycHC[8]·metalloporphyrin coordination chemistry into chiral sensing materials (Publication III). Four metalloporphyrins were combined with both enantiomers of cycHC[8] and deposited as thin films onto QMBs, yielding eight chiroptically active sensors assembled into an enantioselective array. A novel normalisation protocol based on virtual racemic references was developed to extract enantioselective information at unknown analyte concentration. Without normalisation, the array classified limonene, α-pinene, and 1-phenylethylamine by chemical identity; after normalisation, it further discriminated the enantiomers of limonene and 1-phenylethylamine with median accuracy of 100%, while α-pinene enantiomers were not discriminated.

Overall, the work maps cycHC[*n*]·metalloporphyrin self-assembly across a broad metalloporphyrin scope in both solution and the solid state, and demonstrates its first application as a functional enantioselective sensor. The results support the rational design of chiral supramolecular materials and show how enantioselective sensor arrays can be used to recognise volatile chiral analytes.

Lühikokkuvõte

Kiraalsed Metalloporfüriinide ja Tsükloheksanohemikukurbituriilide Supramolekulaarsed Süsteemid: Molekulaarsest Äratundmisest Sensortehnoloogiani

Kiraalse ühendi kaks enantiomeeri võivad bioloogilise aktiivsuse, maitse või lõhna poolest märgatavalt erineda, mistõttu on nende eristamine oluline ravimitööstuse , põllumajanduskemikaalide, biomeditsiinilise diagnostika ja toiduohutuse valdkonnas. Selliste retseptorite väljatöötamine, mis on võimelised enantiomeere eristama, olles samal ajal sünteetiliselt kättesaadavad ja struktuurselt häälestatavad, on supramolekulaarse keemia aktiivne uurimissuund.

Supramolekulaarne kirogenees, mille käigus enantiopuhas võõrustaja-molekul kannab kiraalsuse mittekovalentse interaktsiooni kaudu üle akiraalsele kromofoorsele partnerile, on oluline suund supramolekulaarsete retseptorite arenduses. Kiraalsuse ülekanne on tuvastatav indutseeritud ringdikroismi (ICD) kaudu. Tsükloheksanohemikukurbit[*n*]uriilid (cycHC[*n*]) on enantiopuhaste makrotsüklite perekond, mille karbonüülsed hapnikud käituvad Lewise aluseliste doonoritena ja sobivad hästi metalloporfüriinide Lewise happeliste metallitsentritega. Enantiopuhtad cycHC[*n*] indutseerivad akiraalsetes tsinkporfüriinides ringdikroismi M···O koordinatsiooni kaudu, luues seega mitmekülgse kirogeneesi platvormi, mis põhineb sünteetiliselt lihtsatest, modulaarsetest komponentidest. Käesoleva töö alguses ei olnud selle platvormi ulatust süstemaatiliselt uuritud. Eelkõige oli ebaselge, kuidas mõjutavad porfüriini perifeersed asendajad, tsentraalne metall ja porfüriini tuuma geomeetria sidumisinteraktsiooni. Samuti olid kaardistamata tekkivate komplekside organiseerumine tahkes faasis, bisporfüriinsete võõrustaja-molekulide käitumine ning nende komplekside rakendamine funktsionaalsete sensormaterjalidena. Käesolev doktoritöö käsitleb järjest kõiki neid aspekte.

Doktoritöö kirjanduse ülevaade tutvustab asjakohaseid supramolekulaarse keemia mõisteid (mittekovalentsed interaktsioonid, sidumise hindamise meetodid ning indutseeritud kiraalsuse põhimõtted), millele järgneb peatükk porfüriinidest ja makrotsüklilistest võõrustaja-molekulidest, kus pööratakse erilist tähelepanu metalloporfüriinide koordinatsioonikeemiale. Ülevaade lõppeb sissejuhatusega supramolekulaarsesse sensoorikasse, keskendudes kvartskristall-mikrokaaludele (QMB) ja kemomeetrilise analüüsiga toetatud sensorimassiivide kasutamisele kiraalsete analüütide tuvastamisel.

Tulemuste esimene peatükk uurib üheksa akiraalse metalloporfüriini interaktsioone nii cycHC[6] kui ka cycHC[8] mõlema enantiomeeriga. Uuritavate kromofooride struktuurid erinesid perifeersete asendajate, porfüriinide tuuma geomeetria ja sellega seotud metalli poolest ning cycHC-d erinesid oma suuruse ja kiraalsuse poolest. (Publikatsioon I). UV-vis- ja tuumamagnetresonants-spektroskoopial põhinevad tiitrimised diklorometaanis näitasid, et seitse üheksast porfüriinist (kuus Zn^{2+} ja üks Mg^{2+}), kuid Fe^{3+} ja Pd^{2+} analoogidega sidumist ei tuvastatud. Sidumine leiab aset M···O koordinatsiooni kaudu, kusjuures sidumiskonstandid järgivad Hammeti korrelatsiooni Zn-tetraarüülporfüriinide *para*-asendajate reas. cycHC[6] sidus porfüriine järjepidevalt tugevamini kui cycHC[8]. Peamiseks sidumistugevuse määrajaks osutus tsentraalse

metalli muutmine. Zn^{2+} asendamine Mg^{2+}-iga suurendas sidumistugevust ligikaudu kolme suurusjärgu võrra, kuid Pd^{2+} ja Fe^{3+} katioonide puhul ei olnud sidumine tuvastatav. Töö käigus saadi 31 uut monokristallstruktuuri, mis avasid mitmekesiste supramolekulaarsete arhitektuuride olemuse, kusjuures kõik need struktuurid põhinevad otsesel M···O koordinatsioonil. KBr-tablettides mõõdetud tahkefaasi elektrooniline ringdikroism näitas, et tahkes faasis on kompleksite dissümmeetriategurid ligikaudu kümme korda suuremad kui lahuses. Töös järeldati, et kiroptiline võimendus järgis pigem lokaalset porfüriin·cycHC[*n*] koordinatsioonigeomeetriat kui kaugulatusega kristallpakkimist, identifitseerides lähedase M···O kontakti kui peamise kiraalsuse ülekande allika.

Tulemuste teine peatükk laiendab uurimist bis(tsink-oktaetüülporfüriinile) (bis-ZnOEP), pintsett-tüüpi võõrustaja-molekulile, mis on tuntud väikeste bidentaatsete külaliste sidumisvõime poolest (Publikatsioon II). Tuumamagnetresonants-, UV-vis-, fluorestsents- ja ringdikroismi-spektroskoopia näitasid, et erineva suurusega cycHC molekulid interakteeruvad bis-ZnOEP-iga kvalitatiivselt erinevate sidumisrežiimide kaudu. CycHC[6] on piisavalt väike, et mahtuda bidentaatse külalisena ja moodustab 1:1 pintsett-kompleksi, samas kui cycHC[8] on liiga suur sellise geomeetriaga kompleksi tekkeks. Spektroskoopiliste mõõtmiste ja muutuva temperatuuriga eksperimendid näitasid, et cycHC[8] sidumisel bis-ZnOEP-le toimub iseorganiseerumine *anti* 1:2 kompleksiks mitme tunni jooksul.

Tulemuste kolmas peatükk rakendab uuritud cycHC[8]·metalloporfüriini komplekse kiraalsete sensormaterjalide loomiseks (Publikatsioon III). Neli metalloporfüriini kombineeriti cycHC[8] mõlema enantiomeeriga ja sadestati õhukeste kiledena kvartskristall-mikrokaaludele, saades kaheksa kiroptiliselt aktiivset sensorit. Töö käigus loodi esmakordselt virtuaalsel ratseemilisel referentsil põhinev normaliseerimisprotokoll, mis võimaldab enantioselektiivse info eraldamist ka teadmata analüüdi kontsentratsiooni korral. Enantiomeersete komplekside kiledest moodustatud sensorimassiivi abil sai klassifitseerida aurufaasis limoneeni, α-pineeni ja 1-fenüületüülamiini ning pärast normaliseermist tuvastada limoneeni ja 1-fenüületüülamiini vastasenantiomeere 100 % täpsusega.

Kokkuvõtvalt, käesoleva tööga kinnitati, et cycHC[*n*]·metalloporfüriini iseorganiseerumisega saab luua usaldusväärse kirogeneesi platvormi, mis toimib laiaulatusliku metalloporfüriinide kogule nii lahuse- kui ka tahkefaasi süsteemides. Ühtlasi näidati selle esimest rakendust toimivas enantioselektiivses sensorseadmes. Saadud tulemused loovad aluse kiraalsete supramolekulaarsete materjalide ratsionaalseks disainiks ja näitavad teed, kuidas enantioselektiivseid sensoreid saab rakendada lenduvate kiraalsete analüütide äratundmiseks.

Appendix 1

Publication I

Marko Šakarašvili, Khai-Nghi Truong, Lukáš Ustrnul, Nele Konrad, Kristjan Siilak, Tatsiana Burankova, Reiko Kuroda, Mathias O. Senge, Victor Borovkov, Jas S. Ward, Kari Rissanen, Riina Aav. Chiral Self-Assembly of Zinc and Magnesium Porphyrins with Enantiopure Cyclohexanohemicucurbiturils in Solution and in Solid State. *Inorganic Chemistry* **2025**, 64, 48, 23773–23785.

Reproduced under CC-BY 4.0

Inorganic Chemistry

Open Access
This article is licensed under CC-BY 4.0

pubs.acs.org/IC
Article

Chiral Self-Assembly of Zinc and Magnesium Porphyrins with Enantiopure Cyclohexanohemicucurbiturils in Solution and in Solid State

Marko Šakarašvili, Khai-Nghi Truong, Lukáš Ustrnul, Nele Konrad, Kristjan Siilak, Tatsiana Burankova, Reiko Kuroda, Mathias O. Senge, Victor Borovkov, Jas S. Ward, Kari Rissanen, and Riina Aav*

Cite This: *Inorg. Chem.* 2025, 64, 23773−23785

Read Online

ACCESS | Metrics & More | Article Recommendations | Supporting Information

ABSTRACT: Chiral self-assembled supramolecular networks offer great potential for new chiral materials. We report the predictable self-assembly of metalloporphyrins with chiral cyclohexanohemicucurbit[*n*]urils (cycHC[6] and cycHC[8]), where cycHC[*n*] chirality is transferred to achiral porphyrins in solution and the solid state. Solvent and porphyrin substituents directed the formation of 31 novel complexes characterized by single-crystal X-ray diffraction. All complexes feature metal−urea coordination centers, with architectures ranging from discrete complexes to 1D, helical 1D, and 2D square-grid coordination polymers, governed by the shape and binding strength of cycHC[*n*]s. Noncovalent interaction analysis highlighted van der Waals interactions alongside metal−oxygen coordination. In solution, binding strengths ranged from 690 to 1,840,000 M^{-1}, while electronic circular dichroism (ECD) *g*-factors remained consistent. Solid-state measurements revealed a 10-fold increase in induced ECD intensity in the Soret region, attributed to chiral aggregation and interporphyrin exciton coupling. Vibrational circular dichroism showed chirality induction in the infrared range, with the *g*-factor of cycHC[6] carbonyl signals increasing 10-fold upon complexation. These results demonstrate the robustness of hemicucurbituril−metalloporphyrin supramolecular systems for developing advanced chiral sensing materials.

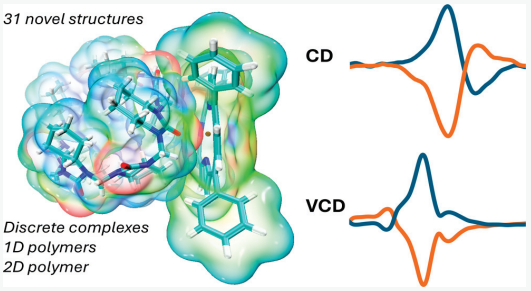

INTRODUCTION

Porphyrins, with their highly tunable ring systems and metal centers,[1,2] offer remarkable structural and electronic versatility, enabling diverse applications in catalysis,[3,4] photodynamic therapy,[5,6] solar energy conversion,[7] and, notably, chemical sensing.[8−12] Their conjugated core gives rise to distinctive UV−vis absorption properties, while the chelated metal ion often governs the chemical reactivity. Inducing chirality in porphyrins through supramolecular complexation expands their utility to include the recognition of chiral molecules—such as pharmaceuticals,[13] environmental pollutants,[14,15] and food ingredients,[16] as well as absolute configuration determination.[17−19] Recently, the induction of chirality in supramolecular host−guest systems has gained significant attention, with studies demonstrating efficient chiroptical responses through the encapsulation of achiral guests such as fullerenes and fluorescent dyes in chiral nanocapsules.[20,21] Supramolecular control over the self-assembly of metalloporphyrins with a chiral molecular entity enables the efficient formation of tunable chemical and chiroptical sensors. This requires the presence of complementary interaction sites and steric compatibility between the individual molecules. Porphyrins and cyclohexanohemicucurbit[*n*]urils[22−24] (cycHC[*n*]s) possess these features (Figure 1). The size of the porphyrin core unit is 0.84 nm, and in the case of 5,10,15,20-tetraphenylporphyrin, the distance between phenyl *meso*-substituents is about 1.5 nm. CycHC[6] and cycHC[8] have comparable dimensions, with a height of roughly 1 nm and diameters of 1.4−1.7 nm.

Metalloporphyrins and cycHC[*n*]s also feature complementary apolar organic regions and Lewis acid−base interaction sites. This can be seen on the electrostatic potential surfaces of the (*S*,*S*)-cycHC[8]·7 complex (Figure 1, SI Figures S116 and S117), where the main interaction between the electron-rich carbonyl oxygen (red) and the electron-deficient central metal (blue) is accompanied by a secondary interaction between the cycHC[*n*]'s hydrophobic parts (blue) and the porphyrin's π-ring (red). We have reported that the urea groups of

Received: October 22, 2025
Revised: November 10, 2025
Accepted: November 13, 2025
Published: November 24, 2025

Downloaded via 89.235.205.39 on May 19, 2026 at 11:12:37 (UTC).
See https://pubs.acs.org/sharingguidelines for options on how to legitimately share published articles.

ACS Publications
© 2025 The Authors. Published by American Chemical Society

https://doi.org/10.1021/acs.inorgchem.5c04969
Inorg. Chem. 2025, 64, 23773−23785

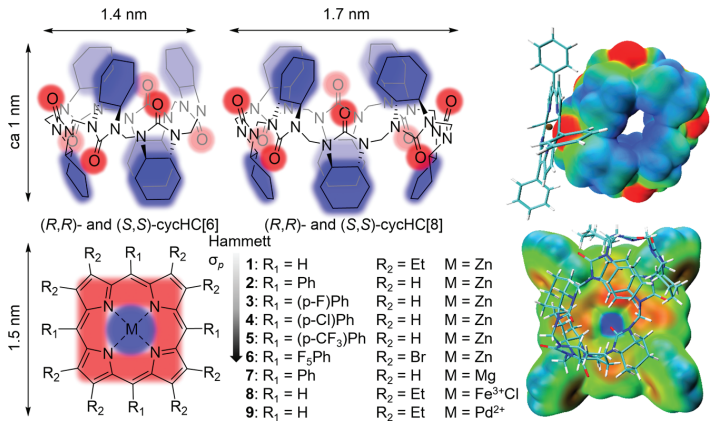

Figure 1. Structures of hemicucurbiturils and metalloporphyrins studied on the left and electrostatic potential colored molecular van der Waals surfaces of (*S*,*S*)-cycHC[8]·**7** on the right. Blue color corresponds to electron-donating and red color corresponds to electron-accepting capabilities. The Hammett constant σ_p for *para*-substituents increases from porphyrins **1** to **6**.

enantiomeric cycHC[*n*]s can externally bind zinc porphyrins through Lewis acid−base interactions, inducing chirality at both mono- and bis-porphyrin cores.[25,26] This induces electronic circular dichroism (ECD) signals in the Soret region of inherently achiral (ECD-silent) zinc 2,3,7,8,12,13,17,18-octaethylporphyrin (**1**), zinc 5,10,15,20-tetraphenylporphyrin (**2**), and bis(zinc 2,3,7,8,12,13,17,18-octaethylporphyrin).[25,26] Furthermore, the first successful application of cycHC[*n*] and metalloporphyrin complexes for chiral sensing of volatile organic compounds was demonstrated using an enantioselective electronic nose with a quartz crystal microbalance detector array.[27]

To develop a versatile sensing system and uncover new supramolecular architectures, we investigated how substituents at the Zn-porphyrin ring (**1**−**6**) and variations in metal cations (Mg^{2+}, Fe^{3+}, and Pd^{2+}; **7**−**9**) affect their binding with cycHC[6] and cycHC [8], as well as their chiroptical properties. The choice of Mg- and Fe-porphyrins was motivated by their previously reported complexes with oxygen-bearing ligands, while the Pd-porphyrin was recently shown to sense oxygen gas.[12,17,28−33] However, no information was available regarding their interactions with urea macrocycles. Exploration of new complexes for supramolecular chirogenesis in both solution and solid-state using ECD and vibrational circular dichroism (VCD) spectroscopies is essential for the further development of optical chiral sensing applications. Furthermore, single-crystal X-ray diffraction (SC-XRD) analysis of 31 novel crystal structures revealed the high structural versatility of cycHC[*n*]−porphyrin complexes. The obtained results demonstrate coherent binding motifs and a broad range of chiral supramolecular architectures, offering a robust platform for next-generation sensing arrays driven by specific cycHC[*n*]-porphyrin interactions.

Experimental Section. Unless otherwise stated, all reagents and solvents were purchased from commercial suppliers of the highest grade available and used as received. Compounds prepared in our laboratories were cycHC[*n*]s[22,24] and porphyrins **3**−**7**.[34−37] All solutions were prepared using Hamilton Gastight syringes; those syringes were also used for all additions during UV−vis and NMR titrations. To ensure precise measurement in sample preparation, the mass of solvent and its density were used along with volumetric glassware. Samples were weighed on a microbalance with an accuracy of 6 μg (Radwag MYA 11.4Y, Poland). The online tool Bindfit (supramolecular.org)[38,39] was used for evaluating the binding constants. See additionally SI p. S2−S36.

^{1}H NMR Measurements. All the ^{1}H NMR experiments were measured on a Bruker Avance III 400 MHz or a Bruker Avance III 800 MHz spectrometer at a temperature of 298 K. All NMR titrations used deuterium solvent to lock. Chemical shifts in ^{1}H NMR were referenced to the deuterated solvent residual peak. The data was analyzed using the program MNova (Mestrelab) and MS excel. See additionally SI p. S7 and S33−S36.

UV−Vis and CD Measurements. The UV−vis absorption spectra were recorded with a Jasco V-730 spectrophotometer or with a Varian Cary 50 UV−vis spectrophotometer. The CD spectra were recorded with a Jasco J-1500 circular dichroism spectrophotometer in the 370−430 nm range for **1**, the 420−520 nm range for **6**, and the 390−450 nm range for other metalloporphyrins. Measurement parameters were as follows: scanning speed 20 nm/min; data pitch 0.1 nm; digital integration time 4 s; bandwidth 2.00 nm. A total of 6 scans were recorded for each metalloporphyrin cycHC[*n*] complex, and the average of them was taken; DCM spectra were subtracted for baseline correction. The thermostat (PTC-510) was used to keep the cell holder temperature at 20 °C. See additionally SI p. S37−S51.

Solid-state ECD, LD UV−vis, LB and CB spectra were recorded by a solid-state dedicated circular dichroism (CD) spectrophotometer (J-800 KCM) by mixing the sample with KBr and pressing into a pellet. See additionally SI p. S52−S56.

IR and VCD Measurements. IR and VCD measurements were carried out with a Bruker Tensor27 spectrometer equipped with a VCD module PMA 50. For VCD measurement, a linear polarizer and a 50 kHz ZnSe photoelastic modulator (PEM) were used. The absorption signals were detected with a liquid nitrogen cooled MCT infrared detector from a sample of a KBr pellet with a resolution of 4 cm^{-1}. Data collection time was set at 6 h using six blocks of 60 min. For the demodulation of the signals, a lock-in amplifier (Stanford Research Systems 830) was used. The PEM was adjusted for a

https://doi.org/10.1021/acs.inorgchem.5c04969
Inorg. Chem. 2025, 64, 23773−23785

maximum efficiency at 1600 or 900 cm^{-1}, depending on the region under investigation. A multiple wavelength plate (CdS) combined with a wire grid linear polarizer was used to calibrate the phase of the lock-in amplifier. For the baseline of VCD, a pure KBr pellet was used. The baseline signal was subtracted from the original sample signal. See additionally SI p. S57−S62.

Single-Crystal X-ray Diffraction. Single-crystal X-ray diffraction data were collected on Rigaku SuperNova and Bruker-Nonius Kappa CCD diffractometers using Cu K_α (λ = 1.54184 Å) and Mo K_α (λ = 0.71073 Å) radiation, respectively. Data collection and reduction employed CrysAlis^{Pro},[40] COLLECT,[41] and HKL DENZO/SCALEPACK,[42] with absorption corrections applied via Gaussian and SADABS[43] methods. Structures were solved by direct methods (SHELXS) and refined by full-matrix least-squares on F^2 using SHELXL-2015.[44−46] Non-hydrogen atoms were refined anisotropically; hydrogen atoms were positioned geometrically or refined with restraints. Rigid-bond,[47,48] distance (DFIX), and SIMU restraints were applied as needed. If no sensible disordered model could be formulated for the unknown solvates, the program SQUEEZE[49] within PLATON[50] was used to account for the residual electron density. Crystallographic and refinement details, including CCDC numbers, are provided below and in the Supporting Information. See additionally SI p. S63−S103.

Computational Methods. For all the computations in this work, single-point energy calculations were performed with the ORCA[51−54] program package using the B3LYP functional and the def2-SVP basis set. The crystallographic coordinates were used as input geometries without further optimization. Tight SCF convergence criteria and ORCA's Grid5 integration grid were employed.

Multiwfn[55,56] was used to perform quantitative molecular surface analysis for electrostatic potential surface coloring, noncovalent interactions (NCI, a.k.a reduced density gradient) analysis[57] and Interaction region indicator (IRI) analysis.[58] VMD[59] software was used for visualization of the NCI and IRI color-filled isosurface graphs. The Gnuplot program (http://www.gnuplot.info) was used for generating color mapped NCI and IRI scatter maps. See additionally SI p. S104−S123.

RESULTS AND DISCUSSION

Variability of Binding Strength of Metalloporphyrins to Hemicucurbiturils. CycHC[*n*]s have been shown to form inclusion complexes with anions and electron-rich heterocycles only in protic media, such as methanol and water, whereas Lewis and Brønsted acids form external interactions in nonprotic solvents, such as dichloromethane (DCM).[25,60−62] In the present work, it was found that nonpolar solvents (toluene, chloroform, and DCM) facilitate the formation of the **2**·cycHC[*n*] complex with minor differences in affinity, the strongest being observed in DCM (SI Table S1). In contrast, oxygen-containing solvents (e.g., MeOH, THF, and DMSO) suppressed the formation of complexes with cycHC[8] due to competition with abundant solvent molecules (SI p. S3−S8).[63,64]

The influence of substituents on the porphyrin core **1**−**9** was explored by conducting UV−vis titrations in DCM with cycHC[*n*]s (*n* = 6, 8), and corresponding affinity constants *K* were determined by evaluating the data with a 2:1 statistical binding model from the online tool BindFit,[38,39] where K_1 indicates 1:1 and subsequently K_2 2:1 complex formation equilibria (Table 1 and Table S1, SI p. S8−S36). To highlight the differences in binding strengths of the studied complexes, the K_1 values are compared in Table 1.

Table 1. Association Constants of the First Step K_1 for Metalloporphyrin and cycHC[*n*] Complexes Obtained with Bindfit[38,39] 2:1 Statistical Model (2:1 Full Model in Case of 7) Are Listed in the Table (Choice of Binding Models and Acquiring of Constants Is Elaborated in SI)

metallo-porphyrin	K_1 with cycHC[6], $\times 10^3$ M^{-1}	K_1 with cycHC[8], $\times 10^3$ M^{-1}
1	2.9 ± 0.2	0.69 ± 0.01
2	5.34 ± 0.06[a]	2.07 ± 0.02[a]
3	4.8 ± 0.3	2.1 ± 0.3
4	6.01 ± 0.07	2.87 ± 0.05
5	7.4 ± 0.5	3.34 ± 0.02
6	409 ± 4	n.d.
7	1840 ± 70[b]	1040 ± 40[b]

[a]Constants from ref 25. [b]Apparent *K* in the presence of 10 equiv of water. All constants were determined from at least two independent measurements with enantiomeric cycHC[*n*]s, deviations are standard deviation from independently measured *K* values. n.d., not determined (No satisfactory fit could be obtained, SI p. S26−S29).

In agreement with our previous studies on the binding of Lewis basic thioureas,[65] the binding strength of porphyrins **1**−**6** to cycHC[*n*]s correlates with the electron deficiency at the central metal. Porphyrin **1** bearing weak electron-donating ethyl substituents showed the weakest binding, whereas for Zn^{2+} tetraarylporphyrins decorated with chloro-, fluoro-, or trifluoromethyl groups at *para*-position **2**−**5** (Table 1, lines 1−5) the binding strength increases along with the Hammett σ_p values[66] of these substituents. A two-order-of-magnitude larger K_1 was obtained for a more extreme example of the electron-deficient Zn-porphyrin **6**, bearing four pentafluorophenyl groups and eight bromine substituents (Table 1, line 6). Strong affinity between cycHC[*n*]s and **6** was manifested by full complexation and a 1000-fold lower excess of cycHC[*n*], compared to titrations of porphyrins **1**−**5** in the same conditions (SI p. S26−S29).

Variation in the metal cations Mg^{2+} **7**, Fe^{3+} **8**, and Pd^{2+} **9** in the porphyrin coordination center demonstrated that Mg^{2+} is an outstanding alternative to the previously known Zn-porphyrin-cycHC[*n*] complexes.[25] No binding to cycHC[8] was observed with **8** and **9** (SI Figures S55 and S56), probably due to an unfavorable interaction between the metal and urea oxygen of cycHC[*n*]s. Complexation of **7** with various ligands via nitrogen and oxygen coordination with magnesium cation has been previously described.[33,67−69] However, the interaction between cycHC[*n*]s and Mg-porphyrin **7** uncovered in this study prevailed even in the presence of competing water molecules. It was found that **7** binds cycHC[*n*] by 2−3 orders of magnitude more strongly than the structurally equivalent zinc porphyrin **2** (Table 1, lines 2 and 7). The binding of **7** with cycHC[*n*]s was evaluated as an apparent association constant, as roughly 10 equiv of water per **7** was in the titration solution due to the high oxophilicity of Mg-porphyrin at ambient conditions (SI Figure S60).

Overall, binding constants for porphyrins **1**−**7** cover the range from 690 to 1,840,000 M^{-1} in DCM and follow the Lewis acidity of porphyrins. The results revealed that the smaller cycHC[6], compared to the larger cycHC[8] macro-

https://doi.org/10.1021/acs.inorgchem.5c04969
Inorg. Chem. 2025, 64, 23773−23785

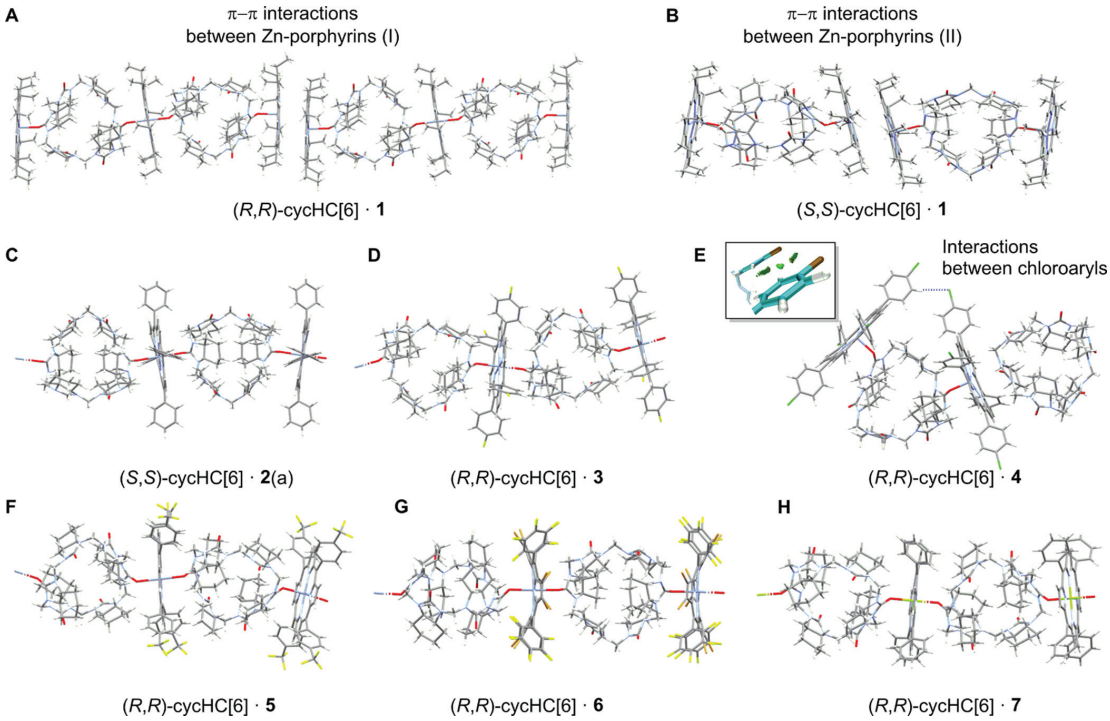

Figure 2. View of the molecular structures of cycHC[6] complexes with porphyrins **1** (A and SI p. S73; B and SI p. S74), **2** (C and SI p. S75), **3** (D and SI p. S77), **4** (E and SI p. S79 and C–H···Cl noncovalent interaction isosurface SI p. S110), **5** (F and Si p. S81), **6** (G and SI p. S83), and **7** (H and SI p. S84). In C, D, F, G, and H, crystals are 1D coordination polymers; see additional details in SI. Atom sites with minor occupancies as well as cocrystallized solvent molecules have been omitted for clarity. Atoms are colored according to the CPK code.

cycle, has slightly stronger binding for all of the studied Zn^{2+} and Mg^{2+} porphyrins.

Versatility of Solid-State Supramolecular Architectures. Self-assembly of cycHC[*n*]s and metalloporphyrins is affected by the solvent, crystallization temperature, and additives. Crystallization experiments with equimolar mixtures of seven achiral metalloporphyrins (**1**–**7**) and four chiral cycHC[*n*]s produced 31 novel structures: six with (*R*,*R*)-cycHC[6], seven with (*S*,*S*)-cycHC[6], ten with (*R*,*R*)-cycHC[8], and eight with (*S*,*S*)-cycHC[8]. All structures display electrostatic M···O interactions, with assemblies ranging from discrete penta- or hexa-coordinated complexes to coordination polymers (Figures 2 and 3, Table S6 and Figures S85–S115).

Assembly of (*R*,*R*)-cycHC[6] with porphyrin **1** at −20 °C in DCM/MeOH yielded a discrete 2:3 complex in which cycHC[6] links two terminal porphyrins in a double-metalloporphyrin sandwich. While the bridging porphyrin coordinates two cycHC[6] molecules via hexa-coordinated Zn···O interactions, terminal Zn centers are penta-coordinated and stabilized by π–π stacking between two porphyrins. This interaction is evidenced by the close proximity (3.3 Å) of planes passing through the porphyrin cores, resulting in a Zn—Zn distance of 4.83 Å (Figure 2A, SI p. S73).

Porphyrin-porphyrin interaction with a distance of 3.4 Å between the porphyrin cores and the Zn—Zn distance of 4.87 Å was also seen in the (*S*,*S*)-cycHC[6]·**1** polymorph (Figure 2B), the latter was crystallized under the same conditions as its enantiomeric congener; however, in this case a discrete 1:2 complex with solely penta-coordinated Zn centers was formed.

Porphyrin **2** was reported to form a 1D-chain polymer with (*R*,*R*)-cycHC[6].[25] In this study, using (*S*,*S*)-cycHC[6], crystallization at 3 °C also yielded a 1D-chain polymer (Figure 2C, (*S*,*S*)-cycHC[6]·**2**(a), SI p. S75), that was isomorphous and isostructural to complexes forming with the Mg-porphyrin **7** (Figure 2H, SI p. S84–S85). Crystallization at ambient temperature produces a discrete 1:1 complex with an uncoordinated cycHC[6] molecule ((*S*,*S*)-cycHC[6]·**2**(b), SI p. S76). This change from a polymer to a discrete complex is accompanied by a 0.2 Å decrease in the Zn···O distance (SI Table S7).

Porphyrin **3** exhibits a strong temperature-dependent behavior: (*R*,*R*)-cycHC[6]·**3** forms a 1D-chain polymer at ambient temperature (Figure 2D, SI p. S77), whereas crystallization of (*S*,*S*)-cycHC[6]·**3** at 3 °C yields a discrete 2:2 complex in which the porphyrins coordinate to two carbonyl oxygens of the one (*S*,*S*)-cycHC[6] (SI p. S78 while only a single Zn-porphyrin is attached to the second (*S*,*S*)-cycHC[6]. A similar binding pattern is observed for porphyrin **4**, which bears *p*-chlorophenyl substituents. Intermolecular C–H···Cl interactions (Figure 2 inset shows NCI isosurface, further details SI p. S110) link neighboring porphyrins, resulting in a 1:2 (*R*,*R*)-cycHC[6]·**4** complex along with an uncoordinated, cocrystallized (*R*,*R*)-cycHC[6]. These interactions do not perturb Zn···O coordination but bring the porphyrins closer together, preventing formation of a 1D

https://doi.org/10.1021/acs.inorgchem.5c04969
Inorg. Chem. 2025, 64, 23773−23785

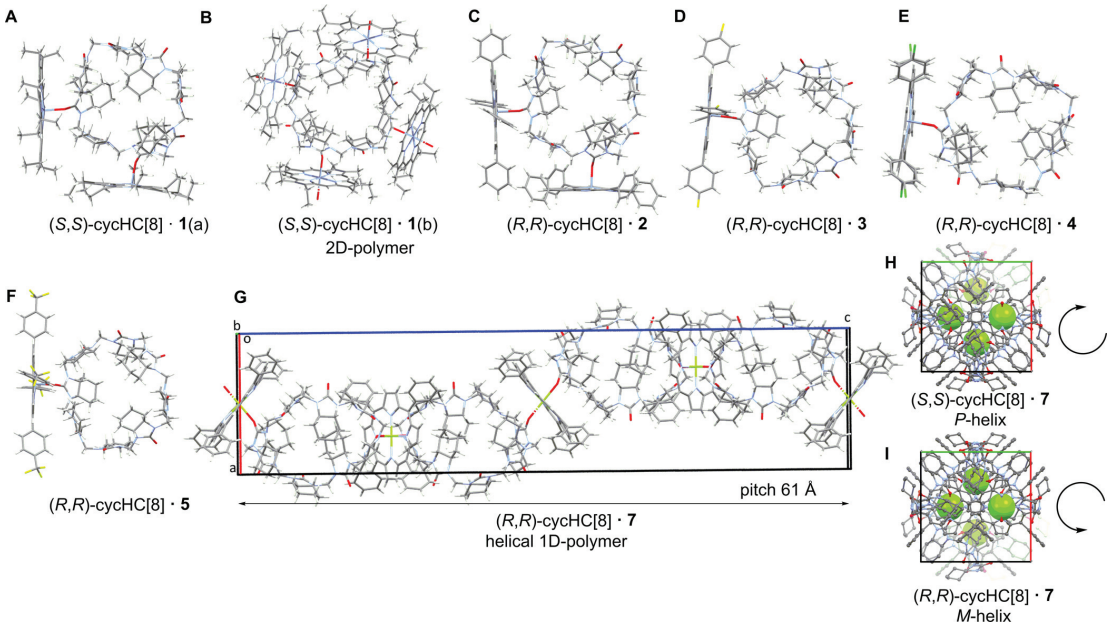

Figure 3. View of the crystal structures in the cycHC[8] complexes with porphyrins **1**(a) (A and SI p. S86), **1**(b) (B and SI p. S87), **2**(a) (C and SI p. S88), and **3**(a) (D and SI p. S94; the enantiomer complex is isostructural SI p. S96, also isostructural to E, SI p. S97), **4**(a) (E and SI p. S97; isostructural to D), **5** (F and SI p. S100), and **7** (G, H, I, and SI p. S102–S103), where B is a 2D square-grid coordination polymer and G is a 1D helical coordination polymer of which H shows a *P*-helix formed with (*S*,*S*)-cycHC[8] and I shows an *M*-helix with (*R*,*R*)-cycHC[8], see additional details in SI p. S102–S103. Atom sites with minor occupancies as well as cocrystallized solvent molecules have been omitted for clarity. Atoms are colored according to the CPK code.

polymer. Despite different crystallization temperatures—ambient for (*R*,*R*)-cycHC[6]·**4** (Figure 2 E, SI p. S79) and 3 °C for (*S*,*S*)-cycHC[6]·**4** (SI p. S80)—both enantiomers form isomorphous and isostructural crystals.

Other metalloporphyrins (**5**, **6**, **7**) form 1D-chain polymers with cycHC[6], in which the Zn^{2+} and Mg^{2+} centers are exclusively hexa-coordinated (Figure 2F–H, SI p. S81–S85). For porphyrins **5** and **7**, isomorphous and isostructural complexes are obtained even with varying crystallization temperatures, whereas for porphyrin **6**, only a single enantiomer was crystallized.

Crystallization of the larger macrocycle, cycHC[8], under conditions analogous to those used for cycHC[6], produced a distinct set of single crystals containing porphyrins **1**–**5** and **7**, highlighting the structural adaptability and polymorphism of the host. For porphyrin **1**, two polymorphs were obtained: (*S*,*S*)-cycHC[8]·**1**(a), crystallized from DCM/MeOH at 3 °C over 8 days, represents a discrete 1:2 complex with two porphyrins bound in a pincer-like fashion to alternating urea subunits of cycHC[8] (Figure 3A and SI p. S86). The Zn···O distances between the porphyrin **1** and the (*S*,*S*)-cycHC[8] moieties are 0.1 Å shorter than in the (*R*,*R*)-cycHC[6] crystals (Figure 2A), showing a larger overlap of van der Waals radii due to the lower coordination number at the zinc ion. In the second form, (*S*,*S*)-cycHC[8]·**1**(b), crystallized from chlorobenzene/MeOH at 3 °C over 2 weeks, chlorobenzene is included in some of the cycHC[8]s cavities, forming a 2D-square-grid coordination polymer where each (*S*,*S*)-cycHC[8] binds four porphyrins via alternating urea subunits (Figure 3B, SI p. S87). This structure demonstrates the host's ability to organize multiple metal centers into an extended 2D network, stabilized by both Zn···O interactions and solvent inclusion. The average Zn···O distance is the same as for a hexa-coordinated Zn^{2+} cation in the 2:3 complex of (*R*,*R*)-cycHC[6]·**1**.

For porphyrin **2**, the crystallization yielded multiple polymorphs, illustrating the myriad of solid-state structures that could be accommodated by the system under different crystallization conditions. Using (*R*,*R*)-cycHC[8], the following polymorphs were obtained: (*R*,*R*)-cycHC[8]·**2**(a) (Figure 3 C and SI p. S88), crystallized from DCM/MeOH at ambient temperature over 2 days, forms a discrete 1:2 complex stabilized by solvate molecules. The other polymorphs—(*R*,*R*)-cycHC[8]·**2**(c) (SI p. S89), obtained from DCM/MeOH with 1,4-thioxane, (*R*,*R*)-cycHC[8]·**2**(d) (SI p. S90), from DCM/MeOH with tetrahydrofuran, and (*R*,*R*)-cycHC[8]·**2**(e) (SI p. S91), from MeOH with (*R*)-(+)-limonene—all produced discrete complexes without incorporation of the additive into the porphyrin–cycHC assembly. For (*S*,*S*)-cycHC[8], two polymorphs were observed: (*S*,*S*)-cycHC[8]·**2**(a) (SI p. S92) (DCM/MeOH, 3 °C, 3 days) forms a 1:2 complex analogous to (*R*,*R*)-cycHC[8]·**2**(a), and (*S*,*S*)-cycHC[8]·**2**(b) (SI p. S93) (chlorobenzene/MeOH, ambient temperature, 2.5 weeks) includes chlorobenzene in the cavity.

The use of different additives (chlorobenzene, thioxane, tetrahydrofuran, and (*R*)-(+)-limonene) was intended to probe whether ternary complexes could form, i.e., host–porphyrin–additive assemblies. Only in chlorobenzene was a ternary complex formed with inclusion of the aromatic guest to

https://doi.org/10.1021/acs.inorgchem.5c04969
Inorg. Chem. 2025, 64, 23773–23785

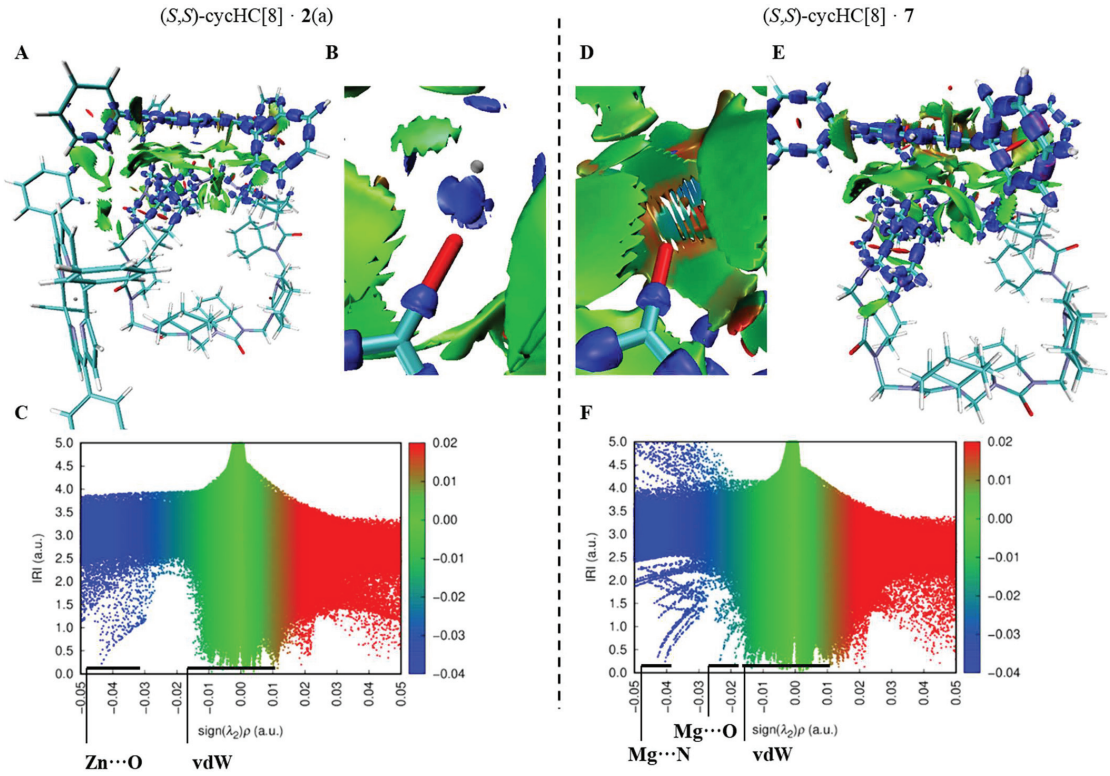

Figure 4. IRI isosurfaces and scatter graphs of porphyrin-cycHC[8] interactions, where grid area is taken between one porphyrin and the porphyrin facing part of cycHC[8], (A) (*S*,*S*)-cycHC[8]·**2**(a); (B) inset of Zn···O interaction; (C) corresponding scatter graph; (D) inset of Mg···O interaction in (*S*,*S*)-cycHC[8]·7; (E) (*S*,*S*)-cycHC[8]·7; and (F) corresponding scatter graph. Coloring: blue—attractive forces, green—van der Waals interactions, and red—repulsive forces (SI Figure S118).

cycHC[8], while maintaining the porphyrin external interaction, demonstrating that cycHC[8] strongly favors direct porphyrin coordination.

Porphyrins **3**−**5** crystallized as discrete 1:1 complexes with both enantiomers of cycHC[8] (Figure 3D−F and SI p. S94−S101). For porphyrin **3**, (*R*,*R*)-cycHC[8]·**3**(a) and (*S*,*S*)-cycHC[8]·**3** are isomorphous and isostructural with (*R*,*R*)-cycHC[8]·**4**(a), forming a family of crystals with essentially identical packing and coordination environments. In contrast, (*R*,*R*)-cycHC[8]·**3**(b) represents an alternative, nonisomorphous arrangement under slightly different crystallization conditions (with quinine as the additive). Porphyrin **4** also forms two families of crystals: (*R*,*R*)-cycHC[8]·**4**(b) and (*S*,*S*)-cycHC[8]·**4** are isomorphous and isostructural with one another, but distinct from the **3**(a)/**3**/**4**(a) set. Porphyrin **5** crystallizes as discrete 1:1 complexes with both (*R*,*R*)-cycHC[8] crystallized from chlorobenzene/MeOH (chlorobenzene inside) and (*S*,*S*)-cycHC[8] crystallized from DCM/MeOH, but these do not belong to any previously observed isomorphous families. Across all of these structures, peripheral substituents (fluoro, chloro, or CF_3) slightly affect packing but do not alter the Zn···O coordination motif, which remains consistent in all cases.

Finally, the only porphyrin forming a 1D-chain polymer with cycHC[8] was **7** (Figure 3G). A preference of **7** to form exclusively polymeric complexes could be expected because Mg^{2+} is typically hexa-coordinated.[70,71] The nonlinearity of carbonyl groups in cycHC[*n*]s leads to a helical polymer with a pitch length of approximately 61 Å including four porphyrins with four cycHC[*n*]s. Helix handedness is dictated by host chirality: (*R*,*R*)-cycHC[8] induces a *P*-helix (Figure 3H), while (*S*,*S*)-cycHC[8] forms an *M*-helix (Figure 3I).

Across porphyrins **1**−**6**, the Zn···O distances are primarily determined by coordination number: 2.38 Å for hexa-coordinated and 2.18 Å for penta-coordinated cations, in agreement with the literature values, with the only exception being ∼0.1 Å longer distances in cycHC[6]·**1** due to different substituents (ethyl vs phenyl). Mg···O distances in porphyrin **7** are 0.1−0.2 Å shorter than for comparable hexa-coordinated Zn^{2+}. A general trend emerges: cycHC[6] preferentially forms 1D polymers when competing hydrogen bonding is absent, whereas cycHC[8] can form extended networks when metal binding is sufficiently strong. This combination of robust host−metal coordination and solvent-sensitive assembly provides a versatile framework for tuning solid-state chirality transfer and material properties, consistent with variations in sensing behavior observed for different porphyrin−cycHC[*n*] complexes.[27]

Analysis of NCIs of Complexes. NCI[57,72] analysis (SI p. S105−S122) and IRI[58] analysis (SI p. S123) were carried out

https://doi.org/10.1021/acs.inorgchem.5c04969
Inorg. Chem. 2025, 64, 23773−23785

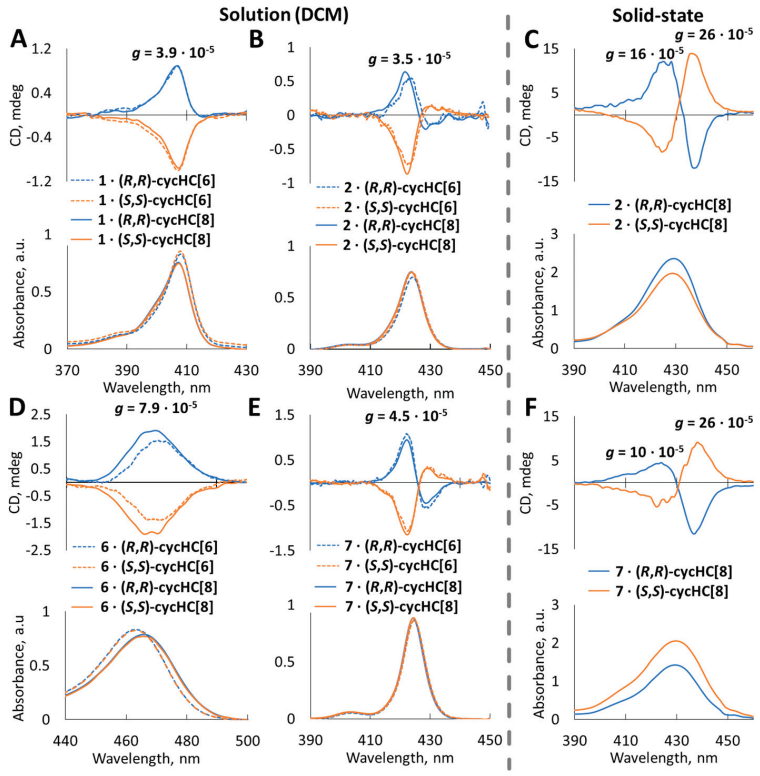

Figure 5. ECD spectra of enantiomeric 1:1 complexes of cycHC[6] (dashed line) and cycHC[8] (solid line) with **1** (A), **2** (B), **6** (D), and **7** (E) in DCM; ECD spectra with other porphyrins and cycHC[*n*] complexes can be found in SI (p. S37–S51), and the values of λ_{max} and *g*-factors are listed in SI Table S3. ECD spectra of KBr pellets ground with microcrystals of cycHC[8]·**2** (C) and cycHC[8]·**7** (F) and their corresponding absorption spectra. In all the spectra, blue lines correspond to complexes with (*R*,*R*)-cycHC[*n*], and orange lines correspond to complexes with (*S*,*S*)-cycHC[*n*].

to gain deeper insight into the interaction modes between cycHC[*n*]s and porphyrins. The key difference between approaches is that NCI is primarily used to visualize weak NCIs, whereas IRI allows simultaneous visualization of both covalent and NCI regions.[58,72] The *x*-axis in the IRI scatter plots (Figure 4C,F) reflects electron density in the interaction regions, which correlates with the strength and nature of the interactions.

The IRI isosurfaces and scatter plots for (*S*,*S*)-cycHC[8]·**2**(a) (Figure 4A–C) and (*S*,*S*)-cycHC[8]·**7** (Figure 4D–F) reveal clear differences in the distribution of attractive interactions. In (*S*,*S*)-cycHC[8]·**2**(a), the strongest contributions correspond to Zn···O coordination between the porphyrin metal center and carbonyl groups of cycHC[8] (Figure 4C, Zn···O region), indicating localized and strong metal–oxygen interactions. In contrast, in (*S*,*S*)-cycHC[8]·**7**, the corresponding Mg···O interactions are more delocalized (Figure 4F, Mg···O region). This can be attributed to the stronger Lewis acidity[73] of Zn^{2+} compared to Mg^{2+} and differences in their electron configuration. To further disentangle contributions from different interactions, region masking (by setting RDG to 100 in specific areas) was applied (SI p. S119–S122). This analysis confirmed that one of the dominant high-electron-density regions in (*S*,*S*)-cycHC[8]·**7** corresponds to Mg···N coordination within the porphyrin core (Figure 4F, Mg···N region).

In addition to metal–oxygen coordination, secondary hydrophobic interactions were detected between the porphyrin and the hydrophobic exterior of cycHC[8] (Figure 4, **2**···cycHC[8] and **7**···cycHC[8]). Although weaker than the metal–O coordination, these interactions contribute to the overall stabilization of the supramolecular assembly. Furthermore, Mg^{2+} exhibits additional weak contacts with the carbonyl oxygen atoms of cycHC[8], consistent with previously observed Mg···O interactions in magnesium–carboxylate complexes.[74]

Chiroptical Properties in Solution and the Solid State. The wide range of association constants determined in solution offers a unique opportunity to investigate the relationship between the binding strength and the chirogenic properties of porphyrins. The chirality induction is evidenced by the emergence of ECD signals in the Soret band region (λ_{max} was in the range of 408–467 nm). The absolute dissymmetry factor—the *g*-factor—was used to describe the intensity of induced circular dichroism (ICD) in order to appropriately compare solution and solid-state chiroptical properties.[75] The values of the *g*-factors of the studied complexes are shown in Figure 5 with the corresponding ECD spectra (SI Tables S3 and S4). Among the porphyrins

https://doi.org/10.1021/acs.inorgchem.5c04969
Inorg. Chem. 2025, 64, 23773–23785

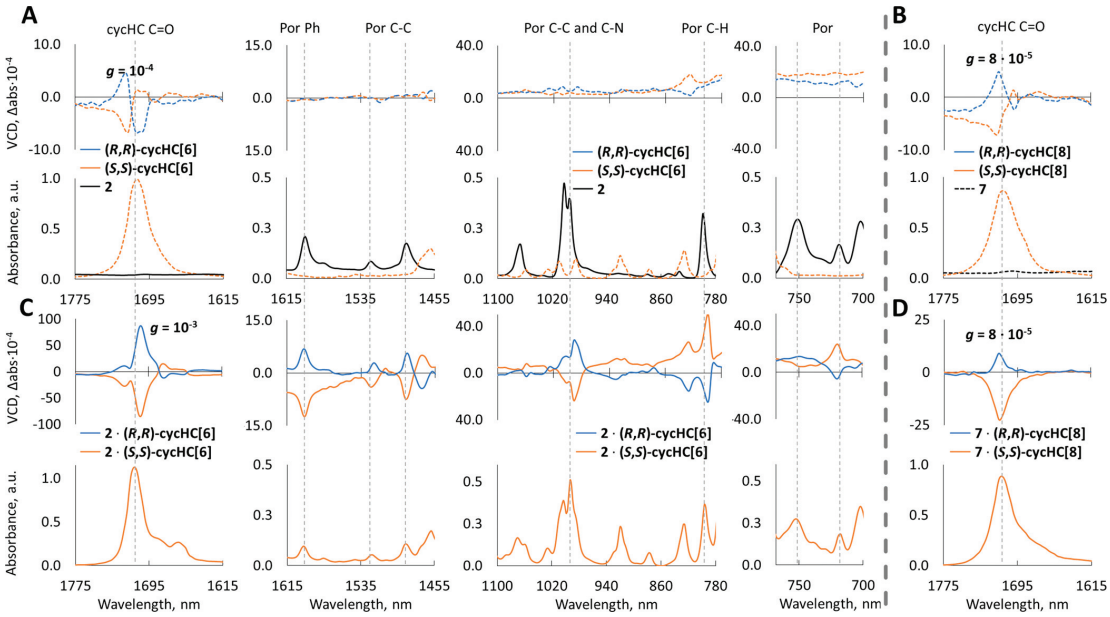

Figure 6. IR and VCD spectra of cycHC[n] complexes measured from KBr pellet: (A) spectral fragments of uncomplexed cycHC[6] and **2**; (B) spectral fragment of uncomplexed cycHC[8] and **7** spectra; (C) spectral fragments of cycHC[6]·**2** enantiomeric complexes; (D) fragment of cycHC[8]·**7** enantiomeric complexes. On all the spectra, blue lines correspond to (*R*,*R*)-cycHC[n] and orange lines to (*S*,*S*)-cycHC[n].

studied, the weakest binder, porphyrin **1** with ethyl groups, exhibited only a monosignate ICD in the Soret band region (λ_{max} = 409 nm, Figure 5A). In contrast, the tetraphenylporphyrin derivatives **2**−**5** demonstrated bisignate ICD (λ_{max} = 418 nm, Figure 5C and SI); this is apparently due to exciton coupling and the orientation of *meso*-phenyls.[76−79] Even though the porphyrins are far apart, the exciton coupling effect has been observed over interchromophoric distances up to 50 Å.[80] Despite the differences in the ICD shape, the *g*-factors for porphyrins **1**−**5** remained comparable, at around 3.5 × 10^{-5}. Notably, the significantly stronger binding magnesium tetraphenylporphyrin 7 displayed a similar ICD shape and position (Figure 5E), with only a slightly larger *g*-factor (4.5 × 10^{-5}) compared to the Zn-porphyrins **2**-**5** (Figure 5B and SI Table S3).

In contrast to other metalloporphyrins, the geometry of porphyrin **6** is significantly distorted due to *β*-halogenation, resulting in a red shift of its Soret band.[36,81,82] It was anticipated that the nonplanar conformation[83,84] of porphyrin **6** would enhance chiral induction upon complexation, thereby increasing the ICD signal. However, despite the binding strength of complex with **6** being several orders of magnitude greater (Table 1, line 6), its *g*-factor was only about twice that of the other zinc porphyrins **1**−**5** (SI Table S3).

Interestingly, the absorption band of complex **6**·cycHC[n]s was significantly broader (up to 40 nm, compared to 20 nm for the others) (Figure 5B and SI p. S38−S51). It is known that distortion of the porphyrin core geometry leads to a larger split in the energy gap of electronic transitions, and this agrees with the broader signal of **6**·cycHC[n]s, compared to other complexes.[78] Notably, both *β*-substituted porphyrin **1** and distorted porphyrin **6** exhibited monosignate ICD bands, in contrast to the bisignate signals observed for the planar tetraphenylmetalloporphyrins (**2**−**5** and **7**). A bisignate pattern can be rationalized by the influence of phenyl group orientations in planar porphyrins,[78,79] while in the case of monosignate porphyrin **6**, the rotation angle and symmetry of the pentafluoro-groups position in the complex deviate strongly from other phenyl-substituted porphyrins.

In conclusion, the *g*-factor is not significantly affected by the binding strength in solution. The 1:1 complexes of metalloporphyrins **1**−**7** with the corresponding enantiomers of cycHC[n]s generate specular ECD signals with patterns that reflect substantial changes in porphyrin geometry.

Although the solution measurements of 1:1 complexes indicated weak ICD, it is known that porphyrins may form aggregates with strong ICD, which can be directed by chiral guests.[85,86] Given the formation of coordination polymers in single crystals, we anticipated differences in solid-state ICD signals compared with those in solution, particularly in the context of the chiral helical coordination polymer of cycHC[8]·**7**. To investigate chirality induction in these complexes in solid-state, we measured the CD of solids using KBr as a pellet matrix in both the UV−vis (ECD) and IR (VCD) regions.[87] Careful measures were taken to minimize the influence of optical anisotropies, including thorough grinding of the sample using a mortar to achieve a homogeneous pellet. In addition to ECD, linear dichroism as well as linear and circular birefringence were measured, confirming that optical anisotropies remained at negligible levels (SI p. S53−S56). The ECD spectra obtained in the Soret band region for (*R*,*R*)-cycHC[8]·**2** and (*S*,*S*)-cycHC[8]·**2** (Figure 5E) showed corresponding mirror images, and the overall shape exhibited a bisignate feature. In contrast to the solution spectra, the UV−vis absorption maxima closely matched the zero point of the ECD spectra, indicating that

https://doi.org/10.1021/acs.inorgchem.5c04969
Inorg. Chem. 2025, 64, 23773−23785

the major contribution to the chirogenic effect in the solid state is exciton coupling between the neighboring porphyrin chromophores. This phenomenon was previously described in **1** upon the development of chiral aggregates.[86] However, the Soret band was red-shifted by 5 nm, the intensity of ICD increased, and the relative proportion of the Cotton effect changed in the solid-state in comparison to the solution. Compared to the solution, the *g*-factor increased 7-fold, up to 26×10^{-5} in solid-state (Figure 5C). As previously mentioned, porphyrin aggregation can enhance ECD intensity; thus, we anticipated a significant increase in the ECD intensity for cycHC[8]·**7** complexes, driven by their unidirectional helical shape and the corresponding amplification of interporphyrin exciton coupling. Surprisingly, the differences between ECD in solution and solid-state for cycHC[8]·**7** were remarkably similar to those observed for the cycHC[8]·**2** complexes. The Soret band underwent a 4 nm red shift, the signs of Cotton effects remained consistent, and the *g*-factor increased up to 26×10^{-5} as in the complex with **2** in solid-state. This increase in ICD intensity in the solid-state compared to the solution can be attributed to chiral aggregation.

Surprisingly, the crystals of the 1:2 discrete complex (cycHC[8]·**2**) and the 1D helical polymer (cycHC[8]·**7**) displayed similar ICD signal intensities, indicating that the organization of porphyrins and cycHC[*n*]s within the crystal does not significantly impact ICD. We can only speculate that spatial separation of porphyrins by cycHC[*n*] macrocycles in the crystal structure allows weak exciton-coupling interactions between the nearest porphyrins. The ECD from powder and crystal of cycHC[8]·**2** were similar in terms of the shape and position of the signals, with the *g*-factors deviating slightly (SI Tables S3 and S4).

While ECD analyzes the molecule as a whole and provides chiral information through chromophore properties, VCD focuses on localized phenomena, offering detailed insights into molecular structures.[88] Despite limited research on VCD in supramolecular systems, notable examples include chiral porphyrins,[89,90] porphyrin aggregates,[91,92] and host–guest complexes involving chiral porphyrins.[19,93] When it comes to achiral porphyrins complexing with chiral guests, most examples include simple porphyrins and biomolecules such as DNA, oligonucleotides, and peptides—with tripeptides being the smallest example.[94,95]

We were able to explore chirality induction in the IR absorption range and recorded distinct features in VCD spectra of cycHC[6] and cycHC[8] as well as their complexes with **2** and **7** in the KBr matrix (Figure 6 and SI p. S57–S62). The cycHC[*n*]s exhibit a relatively strong and characteristic VCD signal in the carbonyl region, and their highest *g*-factors are shown in Figure 6 and SI Table S5.

Upon complexation of cycHC[6] with porphyrin **2**, the *g*-factor of the VCD carbonyl signal is increased 10-fold for cycHC[6]·**2**, compared to unbound cycHC[6] (Figure 6A,C). Additionally, several induced VCD signals appeared in the porphyrin **2** vibration regions due to the chiral cycHC[6]·**2** complex formation, the most prominent ones being around 800, 990, 1490, 1530, and 1600 cm^{-1}, which are characteristic for pyrrole C–H, C–C, and C–N bonds and phenyl groups in **2**. Moreover, new induced VCD signals at 748 cm^{-1} on Ph and 717 cm^{-1} on C(beta)H were observed for the cycHC[6]·**2** complex (Figure 6). In cycHC[8]·**2** and cycHC[6]·**7**, the *g*-factors of carbonyl signals were increased 2- to 3-fold compared to unbound cycHC[*n*]s. Contrary to cycHC[6]·**2**, the larger homologue cycHC[8] did not induce strong and distinct VCD signals outside of the cycHC[8] carbonyl region (SI p. S57–S62). Interestingly, the only complex that showed a monosignate VCD carbonyl signal and no new apparent shoulder around 1660 cm^{-1} was cycHC[8]·**7** (Figure 6D), which produces a helical 1D-chain polymer in solid-state (Figure 3G–I). CycHC[8]·**7** is also the only complex where the *g*-factor in the carbonyl region did not increase upon complexation (Figure 6C,D). It is known from the literature that the structures of host and guest are rigidified upon complexation, which can lead to a more limited conformational space and more intense VCD signals.[19] However, induction of the VCD signal in the cycHC[*n*]–porphyrin complexes cannot be generalized, due to strong induced VCD for cycHC[6]·**2** but only modest changes in signals for other complexes. This phenomenon warrants separate investigation in the future.

CONCLUSIONS

This comprehensive study investigated the complexation of various porphyrins **1**–**9** with enantiomers of cycHC[*n*]s, focusing on the influence of the electron-withdrawing groups, metal coordination centers, and solvent media on binding affinity and chirality induction. Our findings reveal that the binding strength of various zinc tetraarylporphyrins **2**–**5** slightly increases with the growth of Lewis acidity; however, this increase does not significantly affect the induced CD. In contrast, the nonplanar porphyrin **6** and magnesium tetraphenylporphyrin **7** exhibited markedly stronger binding, yet only a modest increase in ICD. Iron and palladium porphyrins showed no binding to cycHC[*n*]s. In general, the cycHC[6] exhibited slightly stronger binding than its eight-membered counterpart.

Analysis of SC-XRD data indicated that the Zn···O distances for zinc porphyrins **1**–**6** are primarily influenced by the coordination number, ranging from 2.38 Å for hexacoordinated zinc cations and 2.18 Å for penta-coordinated zinc cations. Analysis of NCIs pointed to clear differences between Zn- and Mg-porphyrin binding. A particularly interesting finding is that Zn-porphyrins tend to form 1D chain polymers with cycHC[6], and Mg-porphyrin **7** gave a helical 1D-chain polymer with cycHC[8]. The handedness of the helix was determined by the chirality of cycHC[8]. This structural feature was not observed with porphyrin **2**, prompting further investigation into solid-state chirality, as no discernible differences in ICD were noted between **2** and **7** in solution. In the solid state, we observed a red shift of the Soret band and a significant increase in ICD intensity—up to 10-fold compared to solution—suggesting the formation of aggregates. However, no substantial differences were found between the ICD of complexes **2** and **7**, indicating that the helical structure had no significant influence. VCD studies revealed distinct chiral features, with cycHC[6]·**2** exhibiting the most pronounced VCD spectrum, where the *g*-factor of the carbonyl signal increased 10-fold upon complexation. Specular induced VCD signals were also observed for porphyrins complexed with opposite-handed cycHC[*n*]s. In summary, the *g*-factor values were notably larger in the solid state compared to the solution.

A large pool of new supramolecular chiral systems with characteristic spectroscopic and structural features was uncovered, motivating further exploration of their potential in optical sensing or other supramolecular applications.

https://doi.org/10.1021/acs.inorgchem.5c04969
Inorg. Chem. 2025, 64, 23773–23785

■ ASSOCIATED CONTENT

Supporting Information

The Supporting Information is available free of charge at https://pubs.acs.org/doi/10.1021/acs.inorgchem.5c04969.

Experimental details and data on titrations, binding constants and characterization of complexes by ^{1}H NMR, UV−vis, ECD, VCD, SC-XRD, and computational analysis methods (PDF)

Accession Codes

Deposition numbers 2444098−2444118, 2444120, 2444122−2444124, 2444126−2444131 contain the supplementary crystallographic data for this paper. These data can be obtained free of charge via the joint Cambridge Crystallographic Data Centre (CCDC) and Fachinformationszentrum Karlsruhe Access Structures service.

■ AUTHOR INFORMATION

Corresponding Author

Riina Aav − *Department of Chemistry and Biotechnology, Tallinn University of Technology, 12618 Tallinn, Estonia;* orcid.org/0000-0001-6571-7596; Email: riina.aav@taltech.ee

Authors

Marko Šakarašvili − *Department of Chemistry and Biotechnology, Tallinn University of Technology, 12618 Tallinn, Estonia*

Khai-Nghi Truong − *Department of Chemistry, University of Jyväskylä, 40014 Jyväskylä, Finland*

Lukáš Ustrnul − *Department of Chemistry and Biotechnology, Tallinn University of Technology, 12618 Tallinn, Estonia;* orcid.org/0000-0003-4170-2132

Nele Konrad − *Department of Chemistry and Biotechnology, Tallinn University of Technology, 12618 Tallinn, Estonia*

Kristjan Siilak − *Department of Chemistry and Biotechnology, Tallinn University of Technology, 12618 Tallinn, Estonia*

Tatsiana Burankova − *Process Analytics, Hamilton Bonaduz AG, 7402 Bonaduz, Switzerland*

Reiko Kuroda − *Chubu University, Kasugai-shi, Aichi 487-8501, Japan*

Mathias O. Senge − *School of Chemistry, Trinity Biomedical Sciences Institute, Trinity College Dublin, The University of Dublin, Dublin D02 R590, Ireland; Institute for Advanced Study (TUM-IAS), Focus Group—Molecular and Interfacial Engineering of Organic Nanosystems, Technical University of Munich, 85748 Garching, Germany;* orcid.org/0000-0002-7467-1654

Victor Borovkov − *Department of Chemistry and Biotechnology, Tallinn University of Technology, 12618 Tallinn, Estonia;* orcid.org/0000-0001-7898-0457

Jas S. Ward − *Department of Chemistry, University of Jyväskylä, 40014 Jyväskylä, Finland;* orcid.org/0000-0001-9089-9643

Kari Rissanen − *Department of Chemistry, University of Jyväskylä, 40014 Jyväskylä, Finland;* orcid.org/0000-0002-7282-8419

Complete contact information is available at: https://pubs.acs.org/10.1021/acs.inorgchem.5c04969

Author Contributions

M.Š.: Investigation (experiments in titration and UV−vis, ECD in solid and solution phase, computational analysis), methodology, writing—original draft, visualization, analysis; K.-N.T.: Investigation (SC-XRD), methodology; L.U.: Conceptualization, formal analysis, data curation, supervision; N.K.: Investigation (VCD), methodology; K.S.: Investigation (titration); T.B.: formal analysis, data curation (association constants determination); R.K.: Investigation (solid-state ECD), methodology, formal analysis, data curation; M.O.S.: methodology, resources; V.B.: conceptualization, methodology (spectroscopic investigations), supervision; J.S.W.: Investigation (SC-XRD), methodology (SC-XRD); K.R.: methodology (SC-XRD), supervision, resources; and R.A.: overall conceptualization, methodology, supervision, resources. All authors contributed to writing—review and editing.

Notes

This work was published as a preprint in ChemRxiv.[96]
The authors declare no competing financial interest.

■ ACKNOWLEDGMENTS

The authors would like to thank Dzmitry Kananovich for the synthesis of MgTPP, Thi Thanh Ngân Nguyen for the synthesis of cycHCs, and Dzmitry Kananovich and Irina Osadchuk for fruitful discussions and European Union's H2020- FET OPEN grant 828779 (INITIO), HORIZON EUROPE European Innovation Council (101046961), Estonian Research Council grants PRG2169, the Ministry of Education and Research through the Centre of Excellence in Circular Economy for Strategic Mineral and Carbon Resources SOURCES (01.01.2024−31.12.2030, TK228), Technical University of Munich − Institute for Advanced Study (Hans Fischer Senior Fellowship), and Taighde Éireann − Research Ireland (21/FFP-A/9469)

■ REFERENCES

(1) Senge, M. O.; Sergeeva, N. N.; Hale, K. J. Classic Highlights in Porphyrin and Porphyrinoid Total Synthesis and Biosynthesis. *Chem. Soc. Rev.* **2021**, *50* (7), 4730−4789.

(2) Senge, M. O.; Brothers, P. J. *Fundamentals of Porphyrin Chemistry: A 21st Century Approach*; John Wiley & Sons, Ltd: NJ, 2022.

(3) Barona-Castaño, J. C.; Carmona-Vargas, C. C.; Brocksom, T. J.; de Oliveira, K. T. Porphyrins as Catalysts in Scalable Organic Reactions. *Molecules* **2016**, *21* (3), 310.

(4) Liu, Y.; Han, Y.; Zhang, Z.; Zhang, W.; Lai, W.; Wang, Y.; Cao, R. Low Overpotential Water Oxidation at Neutral pH Catalyzed by a Copper(Ii) Porphyrin. *Chem. Sci.* **2019**, *10* (9), 2613−2622.

(5) Zhu, S.; Yao, S.; Wu, F.; Jiang, L.; Wong, K.-L.; Zhou, J.; Wang, K. Platinated Porphyrin as a New Organelle and Nucleus Dual-Targeted Photosensitizer for Photodynamic Therapy. *Org. Biomol. Chem.* **2017**, *15* (27), 5764−5771.

(6) Qiu, H.; Kim, M. M.; Penjweini, R.; Finlay, J. C.; Busch, T. M.; Wang, T.; Guo, W.; Cengel, K. A.; Simone, C. B.; Glatstein, E.; Zhu, T. C. A Comparison of Dose Metrics to Predict Local Tumor Control for Photofrin-Mediated Photodynamic Therapy. *Photochem. Photobiol.* **2017**, *93* (4), 1115−1122.

(7) Spoerke, E. D.; Small, L. J.; Foster, M. E.; Wheeler, J.; Ullman, A. M.; Stavila, V.; Rodriguez, M.; Allendorf, M. D. MOF-Sensitized Solar Cells Enabled by a Pillared Porphyrin Framework. *J. Phys. Chem. C* **2017**, *121* (9), 4816−4824.

(8) Intrieri, D.; Damiano, C.; Rizzato, S.; Paolesse, R.; Venanzi, M.; Monti, D.; Savioli, M.; Stefanelli, M.; Gallo, E. Sensing of Diclofenac by a Porphyrin-Based Artificial Receptor. *New J. Chem.* **2018**, *42* (19), 15778−15783.

(9) Penza, M.; Rossi, R.; Alvisi, M.; Signore, M. A.; Serra, E.; Paolesse, R.; D'Amico, A.; Di Natale, C. Metalloporphyrins-Modified

Carbon Nanotubes Networked Films-Based Chemical Sensors for Enhanced Gas Sensitivity. *Sens. Actuators, B* **2010**, *144* (2), 387−394.
(10) Labuta, J.; Hill, J. P.; Ishihara, S.; Hanyková, L.; Ariga, K. Chiral Sensing by Nonchiral Tetrapyrroles. *Acc. Chem. Res.* **2015**, *48* (3), 521−529.
(11) Hembury, G. A.; Borovkov, V. V.; Inoue, Y. Chirality-Sensing Supramolecular Systems. *Chem. Rev.* **2008**, *108* (1), 1−73.
(12) Paolesse, R.; Nardis, S.; Monti, D.; Stefanelli, M.; Di Natale, C. Porphyrinoids for Chemical Sensor Applications. *Chem. Rev.* **2017**, *117* (4), 2517−2583.
(13) Nguyen, L. A.; He, H.; Pham-Huy, C. Chiral Drugs: An Overview. *Int. J. Biomed. Sci.* **2006**, *2* (2), 85−100.
(14) Basheer, A. A. Chemical Chiral Pollution: Impact on the Society and Science and Need of the Regulations in the 21 st Century. *Chirality* **2018**, *30* (4), 402−406.
(15) Garrison, A. W. An Introduction to Pesticide Chirality and the Consequences of Stereoselectivity. In *ACS Symp. Ser.*; Garrison, A. W.; Gan, J.; Liu, W., Eds.; ACS: Washington, DC, 2011; *1085*.
(16) Fanali, C.; D'Orazio, G.; Gentili, A.; Fanali, S. Analysis of Enantiomers in Products of Food Interest. *Molecules* **2019**, *24* (6), 1119.
(17) Lintuluoto, J. M.; Borovkov, V. V.; Inoue, Y. Direct Determination of Absolute Configuration of Monoalcohols by Bis(Magnesium Porphyrin). *J. Am. Chem. Soc.* **2002**, *124* (46), 13676−13677.
(18) Borovkov, V. V.; Lintuluoto, J. M.; Inoue, Y. Supramolecular Chirogenesis in Zinc Porphyrins: Mechanism, Role of Guest Structure, and Application for the Absolute Configuration Determination. *J. Am. Chem. Soc.* **2001**, *123* (13), 2979−2989.
(19) Ouyang, J.; Swartjes, A.; Geerts, M.; Gilissen, P. J.; Wang, D.; Teeuwen, P. C. P.; Tinnemans, P.; Vanthuyne, N.; Chentouf, S.; Rutjes, F. P. J. T.; Naubron, J.-V.; Crassous, J.; Elemans, J. A. A. W.; Nolte, R. J. M. Absolute Configuration and Host-Guest Binding of Chiral Porphyrin-Cages by a Combined Chiroptical and Theoretical Approach. *Nat. Commun.* **2020**, *11* (1), 4776.
(20) Sasafuchi, H.; Ueda, M.; Kishida, N.; Sawada, T.; Suzuki, S.; Imai, Y.; Yoshizawa, M. Remote Optical Chirality Transfer via Helical Polyaromatic Capsules upon Encapsulation. *Chem.* **2025**, *11* (3), 102332.
(21) Benchimol, E.; O'Connor, H. M.; Schmidt, B.; Bogo, N.; Holstein, J. J.; Lovitt, J. I.; Shanmugaraju, S.; Stein, C. J.; Gunnlaugsson, T.; Clever, G. H. Chiral Pd2L4 Capsules from Readily Accessible Tröger's Base Ligands Inducing Circular Dichroism on Fullerenes C60 and C70. *Angew. Chem., Int. Ed.* **2025**, *64* (10), No. e202421137.
(22) Aav, R.; Shmatova, E.; Reile, I.; Borissova, M.; Topić, F.; Rissanen, K. New Chiral Cyclohexylhemicucurbit[6]Uril. *Org. Lett.* **2013**, *15* (14), 3786−3789.
(23) Öeren, M.; Shmatova, E.; Tamm, T.; Aav, R. Computational and Ion Mobility MS Study of (All-S)-Cyclohexylhemicucurbit[6]Uril Structure and Complexes. *Phys. Chem. Chem. Phys.* **2014**, *16* (36), 19198−19205.
(24) Prigorchenko, E.; Öeren, M.; Kaabel, S.; Fomitšenko, M.; Reile, I.; Järving, I.; Tamm, T.; Topić, F.; Rissanen, K.; Aav, R. Template-Controlled Synthesis of Chiral Cyclohexylhemicucurbit[8]Uril. *Chem. Commun.* **2015**, *51* (54), 10921−10924.
(25) Ustrnul, L.; Kaabel, S.; Burankova, T.; Martõnova, J.; Adamson, J.; Konrad, N.; Burk, P.; Borovkov, V.; Aav, R. Supramolecular Chirogenesis in Zinc Porphyrins by Enantiopure Hemicucurbit[*n*]Urils (n = 6, 8). *Chem. Commun.* **2019**, *55* (96), 14434−14437.
(26) Šakarašvili, M.; Ustrnul, L.; Suut, E.; Nallaparaju, J. V.; Mishra, K. A.; Konrad, N.; Adamson, J.; Borovkov, V.; Aav, R. Self-Assembly of Chiral Cyclohexanohemicucurbit[n]Urils with Bis(Zn Porphyrin): Size, Shape, and Time-Dependent Binding. *Molecules* **2022**, *27* (3), 937.
(27) Magna, G.; Šakarašvili, M.; Stefanelli, M.; Giancane, G.; Bettini, S.; Valli, L.; Ustrnul, L.; Borovkov, V.; Aav, R.; Monti, D.; Di Natale, C.; Paolesse, R. Chiral Recognition by Supramolecular Porphyrin−Hemicucurbit[8]Uril-Functionalized Gravimetric Sensors. *ACS Appl. Mater. Interfaces* **2023**, *15* (25), 30674−30683.
(28) Chaudhary, A.; Patra, R.; Rath, S. P. Binding of Catechols to Iron(III)−Octaethylporphyrin: An Experimental and DFT Investigation. *Eur. J. Inorg. Chem.* **2010**, *2010* (33), 5211−5221.
(29) Reddy, C. V. B.; Khaderbad, M. A.; Gandhi, S.; Kandpal, M.; Patil, S.; Chetty, K. N.; Rajulu, K. G.; Chary, P. C. K.; Ravikanth, M.; Rao, V. R. Piezoresistive SU-8 Cantilever With Fe(III)Porphyrin Coating for CO Sensing. *IEEE Trans. Nanotechnol.* **2012**, *11*, 701−706.
(30) Borisov, S. M.; Lehner, P.; Klimant, I. Novel Optical Trace Oxygen Sensors Based on Platinum(II) and Palladium(II) Complexes with 5,10,15,20-*Meso*-Tetrakis-(2,3,4,5,6-Pentafluorphenyl)-Porphyrin Covalently Immobilized on Silica-Gel Particles. *Anal. Chim. Acta* **2011**, *690* (1), 108−115.
(31) Amao, Y.; Tabuchi, Y.; Yamashita, Y.; Kimura, K. Novel Optical Oxygen Sensing Material: Metalloporphyrin Dispersed in Fluorinated Poly(Aryl Ether Ketone) Films. *Eur. J. Inorg. Chem.* **2002**, *38* (4), 675−681.
(32) Wang, Y.; Qin, F.; Zhang, H.; Kou, M.; Zhang, Z. A High-Performance Optical Trace Oxygen Sensor Based on the Room-Temperature Phosphorescence from Palladium (II) Octaethylporphyrin. *Measurement* **2023**, *206*, No. 112275.
(33) Alanazi, A. N.; Ezzayani, K.; Ben Khelifa, A.; Mansour, A.; Alanazi, R. Eltoom Abdalla Hussein, I.; Hajlaoui, K.; Abdelbasit Nory Salih, M. Bioactive Porphyrin Magnesium (II) Complex. Synthesis, Molecular Structure and Spectroscopic Characterization. Biological Activity and Molecular Docking Studies. *Polyhedron* **2024**, *250*, No. 116815.
(34) Borovkov, V. V.; Lintuluoto, J. M.; Inoue, Y. Synthesis of Zn-, Mn-, and Fe-Containing Mono- and Heterometallated Ethanediyl-Bridged Porphyrin Dimers. *Helv. Chim. Acta* **1999**, *82* (6), 919−934.
(35) Kojima, T.; Nakanishi, T.; Honda, T.; Harada, R.; Shiro, M.; Fukuzumi, S. Impact of Distortion of Porphyrins on Axial Coordination in (Porphyrinato)Zinc(II) Complexes with Aminopyridines as Axial Ligands. *Eur. J. Inorg. Chem.* **2009**, *2009* (6), 727−734.
(36) Mandon, D.; Ochenbein, P.; Fischer, J.; Weiss, R.; Jayaraj, K.; Austin, R. N.; Gold, A.; White, P. S.; Brigaud, O. Beta.-Halogenated-Pyrrole Porphyrins. Molecular Structures of 2,3,7,8,12,13,17,18-Octabromo-5,10,15,20-Tetramesitylporphyrin, Nickel(II) 2,3,7,8,12,13,17,18-Octabromo-5,10,15,20-Tetramesitylporphyrin, and Nickel(II) 2,3,7,8,12,13,17,18-Octabromo-5,10,15,20-Tetrakis-(Pentafluorophenyl)Porphyrin. *Inorg. Chem.* **1992**, *31* (11), 2044−2049.
(37) Lindsey, J. S.; Woodford, J. N. A Simple Method for Preparing Magnesium Porphyrins. *Inorg. Chem.* **1995**, *34* (5), 1063−1069.
(38) Thordarson, P. Determining Association Constants from Titration Experiments in Supramolecular Chemistry. *Chem. Soc. Rev.* **2011**, *40* (3), 1305−1323.
(39) Brynn Hibbert, D.; Thordarson, P. The Death of the Job Plot, Transparency, Open Science and Online Tools, Uncertainty Estimation Methods and Other Developments in Supramolecular Chemistry Data Analysis. *Chem. Commun.* **2016**, *52* (87), 12792−12805.
(40) *CrysAlisPro Software System*, **2017**.
(41) Hooft, R. W. W. *COLLECT*, 1998.
(42) Otwinowski, Z.; Minor, W. Processing of X-Ray Diffraction Data Collected in Oscillation Mode. In *Methods in Enzymology; Macromolecular Crystallography Part A*; Academic Press, 1997; *276*, 307−326.
(43) Sheldrick, G. M. *SADABS*, 1996.
(44) Sheldrick, G. M. A Short History of *SHELX*. *Acta Crystallogr. A Found Crystallogr.* **2008**, *64* (1), 112−122.
(45) Sheldrick, G. M. *SHELXL13. Program Package for Crystal Structure Determination from Single Crystal Diffraction Data*, 2013.
(46) Sheldrick, G. M. Crystal Structure Refinement with *SHELXL*. *Acta Crystallogr. C Struct Chem.* **2015**, *71* (1), 3−8.

https://doi.org/10.1021/acs.inorgchem.5c04969
Inorg. Chem. 2025, 64, 23773−23785

(47) Hirshfeld, F. L. Can. X-Ray Data Distinguish Bonding Effects from Vibrational Smearing? *Acta Cryst. A* **1976**, *32* (2), 239−244.
(48) Thorn, A.; Dittrich, B.; Sheldrick, G. M. Enhanced Rigid-Bond Restraints. *Acta Crystallogr. A Found Crystallogr.* **2012**, *68* (4), 448−451.
(49) van der Sluis, P.; Spek, A. L. BYPASS: An Effective Method for the Refinement of Crystal Structures Containing Disordered Solvent Regions. *Acta Crystallogr.* **1990**, *A46*, 194−201.
(50) Spek, A. L. Structure Validation in Chemical Crystallography. *Acta Crystallogr. D Biol. Crystallogr.* **2009**, *65* (2), 148−155.
(51) Neese, F. Software Update: The ORCA Program System—Version 5.0. *Wiley Interdiscip. Rev. Comput. Mol. Sci.* **2022**, *12* (5), No. e1606.
(52) Neese, F. An Improvement of the Resolution of the Identity Approximation for the Formation of the Coulomb Matrix. *J. Comput. Chem.* **2003**, *24* (11), 1740−1747.
(53) Neese, F. The SHARK Integral Generation and Digestion System. *J. Comput. Chem.* **2023**, *44* (3), 381−396.
(54) Garcia-Ratés, M.; Neese, F. Effect of the Solute Cavity on the Solvation Energy and Its Derivatives within the Framework of the Gaussian Charge Scheme. *J. Comput. Chem.* **2020**, *41* (9), 922−939.
(55) Lu, T.; Chen, F. Multiwfn: A Multifunctional Wavefunction Analyzer. *J. Comput. Chem.* **2012**, *33* (5), 580−592.
(56) Lu, T. A Comprehensive Electron Wavefunction Analysis Toolbox for Chemists, Multiwfn. *J. Chem. Phys.* **2024**, *161* (8), No. 082503.
(57) Johnson, E. R.; Keinan, S.; Mori-Sánchez, P.; Contreras-García, J.; Cohen, A. J.; Yang, W. Revealing Noncovalent Interactions. *J. Am. Chem. Soc.* **2010**, *132* (18), 6498−6506.
(58) Lu, T.; Chen, Q. Interaction Region Indicator: A Simple Real Space Function Clearly Revealing Both Chemical Bonds and Weak Interactions. *Chem.−Methods* **2021**, *1* (5), 231−239.
(59) Humphrey, W.; Dalke, A.; Schulten, K. VMD: Visual Molecular Dynamics. *J. Mol. Graphics* **1996**, *14* (1), 33−38.
(60) Kaabel, S.; Adamson, J.; Topić, F.; Kiesilä, A.; Kalenius, E.; Öeren, M.; Reimund, M.; Prigorchenko, E.; Lõokene, A.; Reich, H. J.; Rissanen, K.; Aav, R. Chiral Hemicucurbit[8]Uril as an Anion Receptor: Selectivity to Size. *Shape and Charge Distribution. Chem. Sci.* **2017**, *8* (3), 2184−2190.
(61) Ustrnul, L.; Burankova, T.; Öeren, M.; Juhhimenko, K.; Ilmarinen, J.; Siilak, K.; Mishra, K. A.; Aav, R. Binding Between Cyclohexanohemicucurbit[n]Urils and Polar Organic Guests. *Front. Chem.* **2021**, *9*, No. 701028.
(62) Shalima, T.; Mishra, K. A.; Kaabel, S.; Ustrnul, L.; Bartkova, S.; Tõnsuaadu, K.; Heinmaa, I.; Aav, R. Cyclohexanohemicucurbit[8]Uril Inclusion Complexes With Heterocycles and Selective Extraction of Sulfur Compounds From Water. *Front. Chem.* **2021**, *9*, No. 786746.
(63) Andreev, V. P.; Sobolev, P. S.; Zaitsev, D. O.; Tafeenko, V. A. Complex Formation between Zinc(II) Tetraphenylporphyrinate and Alkylamines. *Russ. J. Gen. Chem.* **2014**, *84* (2), 320−325.
(64) Olsson, S.; Dahlstrand, C.; Gogoll, A. Design of Oxophilic Metalloporphyrins: An Experimental and DFT Study of Methanol Binding. *Dalton Trans.* **2018**, *47* (33), 11572−11585.
(65) Konrad, N.; Horetski, M.; Sihtmäe, M.; Truong, K.-N.; Osadchuk, I.; Burankova, T.; Kielmann, M.; Adamson, J.; Kahru, A.; Rissanen, K.; Senge, M. O.; Borovkov, V.; Aav, R.; Kananovich, D. Thiourea Organocatalysts as Emerging Chiral Pollutants: En Route to Porphyrin-Based (Chir)Optical Sensing. *Chemosensors* **2021**, *9* (10), 278.
(66) Hansch, C.; Leo, A.; Taft, R. W. A Survey of Hammett Substituent Constants and Resonance and Field Parameters. *Chem. Rev.* **1991**, *91* (2), 165−195.
(67) Ezzayani, K.; Ben Khelifa, A.; Saint-Aman, E.; Loiseau, F.; Nasri, H. Synthesis, Spectroscopic Characterizations, Cyclic Voltammetry Investigation and Molecular Structure of the Di-μ-Cyanato-*N*-Bis(μ-1,4,7,10,13,16-Hexaoxacyclooctadecane)Bis(5,10,15,20-Tetraphenylporphyrinato)Dimagnesiumdipotassium Complex. *Polyhedron* **2016**, *117*, 817−825.
(68) Ezzayani, K.; Denden, Z.; Najmudin, S.; Bonifácio, C.; Saint-Aman, E.; Loiseau, F.; Nasri, H. Exploring the Effects of Axial Pseudohalide Ligands on the Photophysical and Cyclic Voltammetry Properties and Molecular Structures of MgII Tetraphenyl/Porphyrin Complexes. *Eur. J. Inorg. Chem.* **2014**, *2014* (31), 5348−5361.
(69) Ghosh, A.; Mobin, S. M.; Fröhlich, R.; Butcher, R. J.; Maity, D. K.; Ravikanth, M. Effect of Five Membered Versus Six Membered Meso-Substituents on Structure and Electronic Properties of Mg(II) Porphyrins: A Combined Experimental and Theoretical Study. *Inorg. Chem.* **2010**, *49* (18), 8287−8297.
(70) Ezzayani, K.; Ben Khelifa, A.; Saint-Aman, E.; Loiseau, F.; Nasri, H. Complex of Hexamethylenetetramine with Magnesium-Tetraphenylporphyrin: Synthesis, Structure, Spectroscopic Characterizations and Electrochemical Properties. *J. Mol. Struct.* **2017**, *1137*, 412−418.
(71) Amiri, N.; Hajji, M.; Taheur, F. B.; Chevreux, S.; Roisnel, T.; Lemercier, G.; Nasri, H. Two Novel Magnesium(II) *Meso*-Tetraphenylporphyrin-Based Coordination Complexes: Syntheses, Combined Experimental and Theoretical Structures Elucidation, Spectroscopy, Photophysical Properties and Antibacterial Activity. *J. Solid State Chem.* **2018**, *258*, 477−484.
(72) Lu, T. Visualization Analysis of Covalent and Noncovalent Interactions in Real Space. *Angew. Chem., Int. Ed.* **2025**, *64* (29), No. e202504895.
(73) Hawthorne, F. C. A Bond-Topological Approach to Theoretical Mineralogy: Crystal Structure, Chemical Composition and Chemical Reactions. *Phys. Chem. Minerals* **2012**, *39* (10), 841−874.
(74) Kavitha, S.; Deepa, P.; Karthika, M.; Kanakaraju, R. Hybrid DFT Study on Non-Covalent Interactions and Their Influence on p*Ka*'s of Magnesium-Carboxylate Complexes. *Journal of Molecular Graphics and Modelling* **2018**, *85*, 13−24.
(75) Kuhn, W. The Physical Significance of Optical Rotatory Power. *Trans. Faraday Soc.* **1930**, *26*, 293.
(76) Matile, S.; Berova, N.; Nakanishi, K.; Novkova, S.; Philipova, I.; Blagoev, B. Porphyrins: Powerful Chromophores for Structural Studies by Exciton-Coupled Circular Dichroism. *J. Am. Chem. Soc.* **1995**, *117* (26), 7021−7022.
(77) Pescitelli, G.; Gabriel, S.; Wang, Y.; Fleischhauer, J.; Woody, R. W.; Berova, N. Theoretical Analysis of the Porphyrin−Porphyrin Exciton Interaction in Circular Dichroism Spectra of Dimeric Tetraarylporphyrins. *J. Am. Chem. Soc.* **2003**, *125* (25), 7613−7628.
(78) Osadchuk, I.; Aav, R.; Borovkov, V.; Clot, E. Chirogenesis in Zinc Porphyrins: Theoretical Evaluation of Electronic Transitions, Controlling Structural Factors and Axial Ligation. *ChemPhysChem* **2021**, *22* (17), 1817−1833.
(79) Osadchuk, I.; Luts, H.; Zahharova, A.; Tamm, T.; Borovkov, V. Controlling Chirogenic Effects in Porphyrin Based Supramolecular Systems: Theoretical Analysis Versus Experimental Observations. *ChemPhysChem* **2024**, *25* (11), No. e202400104.
(80) Matile, S.; Berova, N.; Nakanishi, K.; Fleischhauer, J.; Woody, R. W. Structural Studies by Exciton Coupled Circular Dichroism over a Large Distance: Porphyrin Derivatives of Steroids, Dimeric Steroids, and Brevetoxin B. *J. Am. Chem. Soc.* **1996**, *118* (22), 5198−5206.
(81) Nguyen, K. A.; Day, P. N.; Pachter, R.; Tretiak, S.; Chernyak, V.; Mukamel, S. Analysis of Absorption Spectra of Zinc Porphyrin, Zinc Meso-Tetraphenylporphyrin, and Halogenated Derivatives. *J. Phys. Chem. A* **2002**, *106* (43), 10285−10293.
(82) Nguyen, K. A.; Day, P. N.; Pachter, R. Effects of Halogenation on the Ionized and Excited States of Free-Base and Zinc Porphyrins. *J. Chem. Phys.* **1999**, *110* (18), 9135−9144.
(83) Kingsbury, C. J.; Senge, M. O. Molecular Symmetry and Art: Visualizing the Near-Symmetry of Molecules in Piet Mondrian's De Stijl. *Angew. Chem., Int. Ed.* **2024**, *63* (25), No. e202403754.
(84) Kingsbury, C. J.; Senge, M. O. The Shape of Porphyrins. *Coord. Chem. Rev.* **2021**, *431*, No. 213760.
(85) Borovkov, V. V.; Harada, T.; Inoue, Y.; Kuroda, R. Phase-Sensitive Supramolecular Chirogenesis in Bisporphyrin Systems. *Angew. Chem., Int. Ed.* **2002**, *41* (8), 1378−1381.

https://doi.org/10.1021/acs.inorgchem.5c04969
Inorg. Chem. 2025, 64, 23773−23785

(86) Borovkov, V. V.; Harada, T.; Hembury, G. A.; Inoue, Y.; Kuroda, R. Solid-State Supramolecular Chirogenesis: High Optical Activity and Gradual Development of Zinc Octaethylporphyrin Aggregates. *Angew. Chem., Int. Ed.* **2003**, *42* (15), 1746−1749.
(87) Castiglioni, E.; Biscarini, P.; Abbate, S. Experimental Aspects of Solid State Circular Dichroism. *Chirality* **2009**, *21* (1E), E28−E36.
(88) Urbanová, M.; Maloň, P. Circular Dichroism Spectroscopy. In *Analytical Methods in Supramolecular Chemistry*; John Wiley & Sons, Ltd, 2006; 265−304.
(89) Castaings, A.; Marchon, J.-C.; Cavagnat, D.; Buffeteau, T. Conformational Equilibria of Bridled Chiroporphyrins in Solution Investigated by Vibrational Circular Dichroism. *Chirality* **2013**, *25* (8), 480−486.
(90) Kobayashi, N.; Fukuda, T. First Observation of the Vibrational Circular Dichroism Spectra of Synthetic Chiral Porphyrazines. *Chem. Lett.* **2004**, *33* (1), 32−33.
(91) Nieto-Ortega, B.; Ramírez, F. J.; Amabilino, D. B.; Linares, M.; Beljonne, D.; Navarrete, J. T. L.; Casado, J. Electronic and Vibrational Circular Dichroism Spectroscopies for the Understanding of Chiral Organization in Porphyrin Aggregates. *Chem. Commun.* **2012**, *48* (73), 9147−9149.
(92) Nagahara, T.; Kisoda, K.; Harima, H.; Aida, M.; Ishibashi, T. Chiral Sum Frequency Spectroscopy of Thin Films of Porphyrin J-Aggregates. *J. Phys. Chem. B* **2009**, *113* (15), 5098−5103.
(93) Bruekers, J. P. J.; Hellinghuizen, M. A.; Vanthuyne, N.; Tinnemans, P.; Gilissen, P. J.; Buma, W. J.; Naubron, J.-V.; Crassous, J.; Elemans, J. A. A. W.; Nolte, R. J. M. Allosteric Guest Binding in Chiral Zirconium(IV) Double Decker Porphyrin Cages. *Eur. J. Org. Chem.* **2021**, *2021* (4), 607−617.
(94) Urbanová, M. Bioinspired Interactions Studied by Vibrational Circular Dichroism. *Chirality* **2009**, *21* (1E), E215−E230.
(95) Mölzer, C.; Huber, H.; Steyrer, A.; Ziesel, G. V.; Wallner, M.; Goncharova, I.; Orlov, S.; Urbanová, M.; Ahlfors, C. E.; Vítek, L.; Bulmer, A. C.; Wagner, K.-H. Interaction between TNFone and Tetrapyrroles May Account for Their Anti-Genotoxic Effects — a Novel Mechanism for DNA-Protection. *J. Porphyrins Phthalocyanines* **2013**, *17* (12), 1157−1166.
(96) Šakarašvili, M.; Truong, K.-N.; Ustrnul, L.; Konrad, N.; Siilak, K.; Burankova, T.; Kuroda, R.; Senge, M. O.; Borovkov, V.; Ward, J. S.; Rissanen, K.; Aav, R. Chiral Self-Assembly of Zinc and Magnesium Porphyrins with Enantiopure Cyclohexanohemicucurbiturils in Solution and in Solid-State. *ChemRxiv* **2025**

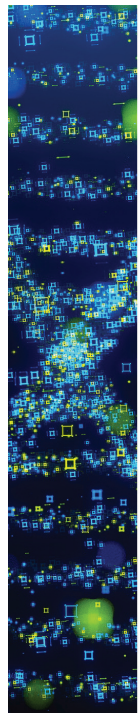
CAS BIOFINDER DISCOVERY PLATFORM™
STOP DIGGING THROUGH DATA —START MAKING DISCOVERIES
CAS BioFinder helps you find the right biological insights in seconds
Start your search
CAS
A division of the American Chemical Society

https://doi.org/10.1021/acs.inorgchem.5c04969
Inorg. Chem. 2025, 64, 23773−23785

Appendix 2

Publication II

Marko Šakarašvili, Lukas Ustrnul, Elina Suut, Jagadeesh Varma Nallaparaju, Kamini A. Mishra, Nele Konrad, Jasper Adamson, Victor Borovkov, Riina Aav. Self-Assembly of Chiral Cyclohexanohemicucurbit[n]urils with Bis(Zn Porphyrin): Size, Shape, and Time-Dependent Binding. *Molecules,* **2022**, *27*(3), 937

Reproduced under CC-BY 4.0

molecules

MDPI

Article

Self-Assembly of Chiral Cyclohexanohemicucurbit[*n*]urils with Bis(Zn Porphyrin): Size, Shape, and Time-Dependent Binding

Marko Šakarašvili [1,†], Lukas Ustrnul [1,†], Elina Suut [1], Jagadeesh Varma Nallaparaju [1], Kamini A. Mishra [1], Nele Konrad [1], Jasper Adamson [2], Victor Borovkov [1,*] and Riina Aav [1,*]

[1] Department of Chemistry and Biotechnology, School of Science, Tallinn University of Technology, 12618 Tallinn, Estonia; marko.sakarasvili@taltech.ee (M.Š.); lukas.ustrnul@taltech.ee (L.U.); elina.suut@taltech.ee (E.S.); jagadeesh.varma@taltech.ee (J.V.N.); kamini.mishra@taltech.ee (K.A.M.); nele.konrad@taltech.ee (N.K.)

[2] Laboratory of Chemical Physics, National Institute of Chemical Physics and Biophysics, 12618 Tallinn, Estonia; jasper.adamson@kbfi.ee

* Correspondence: victor.borovkov@taltech.ee (V.B.); riina.aav@taltech.ee (R.A.)

† These authors contributed equally to this work.

Abstract: In order to investigate the ability of bis(zinc octaethylporphyrin) (**bis–ZnOEP**) to discriminate cyclohexanohemicucurbit[n]urils (**cycHC[*n*]**) of different shapes and sizes, the self-assembly of barrel-shaped chiral **cycHC[*n*]** with **bis–ZnOEP** was studied by various spectroscopic methods (absorption, fluorescence, circular dichroism (CD), and NMR). While the binding of 6-membered **cycHC[6]** induced a tweezer-like conformation followed by the formation of *anti*-form of **bis–ZnOEP** upon further addition of **cycHC[6]**, the interaction of 8-membered **cycHC[8]** is more complex and proceeds through the featured *syn*-to-*anti* conformational change of **bis–ZnOEP** and further intermolecular self-assembly via multiple noncovalent associations between **cycHC[8]** and **bis–ZnOEP**. Whilst bis–porphyrins are known to be effective chemical sensors able to differentiate various guests based on their chirality via induced CD, their ability to sense small differences in the shape and size of relatively large macrocycles, such as chiral **cycHC[6]** and **cycHC[8]**, is scarcely examined. Both studied complexes exhibited characteristic induced CD signals in the region of porphyrin absorption upon complexation.

Keywords: supramolecular chemistry; noncovalent interaction; hemicucurbituril; bis–porphyrin; metalloporphyrin; chirogenesis; induced chirality; chiral recognition; circular dichroism; self-assembly; sensing

check for updates

Citation: Šakarašvili, M.; Ustrnul, L.; Suut, E.; Nallaparaju, J.V.; Mishra, K.A.; Konrad, N.; Adamson, J.; Borovkov, V.; Aav, R. Self-Assembly of Chiral Cyclohexanohemicucurbit [*n*]urils with Bis(Zn Porphyrin): Size, Shape, and Time-Dependent Binding. *Molecules* **2022**, *27*, 937. https://doi.org/10.3390/molecules27030937

Academic Editors: Alessandro D'Urso and Maria Elena Fragala

Received: 12 November 2021
Accepted: 25 January 2022
Published: 29 January 2022

Publisher's Note: MDPI stays neutral with regard to jurisdictional claims in published maps and institutional affiliations.

Copyright: © 2022 by the authors. Licensee MDPI, Basel, Switzerland. This article is an open access article distributed under the terms and conditions of the Creative Commons Attribution (CC BY) license (https://creativecommons.org/licenses/by/4.0/).

1. Introduction

Porphyrins and their derivatives are one of the cornerstones of life; they are responsible for storing and transporting oxygen [1], photosynthesis [2], and enzyme-catalyzed reactions [3,4]. Synthetic derivatives have a wide range of applications, e.g., catalysis, photodynamic therapy, and sensing [5–9]. The versatility of porphyrin application can be significantly improved by metal insertion and/or covalently linking two porphyrin rings into a bis–porphyrin structure. The corresponding linker(s) may provide conformational flexibility or rigidity and thus make it possible to vary the distance between corresponding cores [10–16]. The most exciting aspect of bis–metalloporphyrins is their ability to recognize enantiomers of various monodentate and bidentate chiral molecules [11,17–22] related to the general phenomenon of chiral information transfer from guest to host, which is also employed by other sensing systems [23–26]. Typically, upon the host–guest interaction, a noticeably strong circular dichroism (CD) signal in the region of porphyrin absorption is induced. This is because the bis–porphyrin molecule must accommodate its conformation to the guest's chiral structure, hence resulting in chirality transfer from a chiral guest to achiral bis–porphyrin [18]. Moreover, the intensity of the signal can be further enhanced

by exciton coupling (EC) caused by the through space interaction between corresponding electronic transitions of a bis–porphyrin [10,27]. As a result, bis–metalloporphyrins can be sensitive not only to the stereochemistry of a guest but also to the bulkiness and shape of its substituents. Such properties were well described on the widely studied bis–porphyrin structure with a simple flexible ethane link between two porphyrin rings: bis(zinc(II) octaethylporphyrin) (**bis–ZnOEP**) [18,28,29].

In a noncoordinating solvent, **bis–ZnOEP** favors a remarkably stable *syn* face-to-face conformation (Figure 1) due to strong π–π interactions between the porphyrin rings [18]. Upon the binding of an external guest, the π–π interactions are disrupted, and **bis–ZnOEP** can be rearranged into two major conformations: (1) tweezer-like conformation with a guest positioned between two porphyrin rings, a conformation especially favored in the complexes with bidentate guests, and (2) opened *anti* conformation with two porphyrin rings separated from each other in an almost parallel arrangement, a conformation typical for complexation with monodentate guests. If the guest is chiral, induced CD (ICD) can be observed with an intensity related to EC. In turn, EC exhibits a parabola-like dependence on the dihedral angle between the porphyrin cores with no EC for the dihedral angles of 0° and 180° [28,30–32]. The tweezer conformation with a chiral guest conventionally provides strong EC and intense ICD, due to the exceptional rigidity and unidirectional helicity of the formed supramolecular complex. However, in the case of a more flexible *anti* conformation, ICD may strongly depend upon the corresponding complex geometry, which can be parallel (no EC) or slightly distorted to form a screw structure (relatively weak EC) [31,33–35].

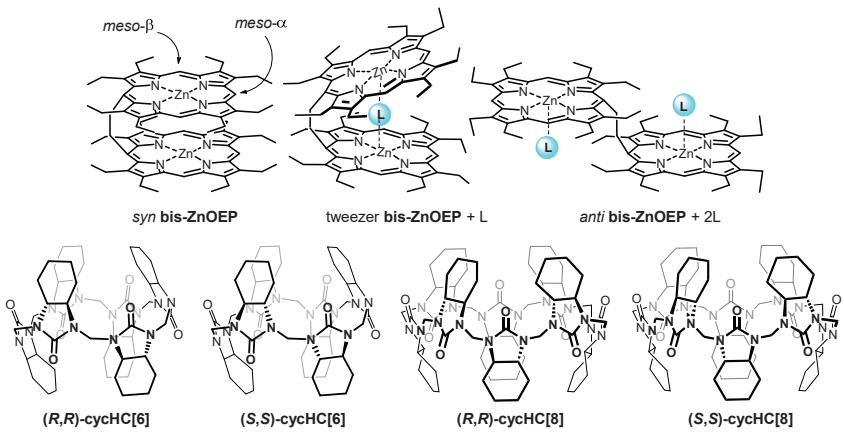

Figure 1. On top: structure of **bis–ZnOEP** in *syn*, tweezer, and *anti* conformations, and beneath: structures of (*R*,*R*)- and (*S*,*S*)-**cycHC[*n*]**.

Recently, we reported that carbonyl groups of (*R*,*R*)- and (*S*,*S*)-enantiomers of barrel-shaped macrocycles, cyclohexanohemicucurbit[*n*]urils (**cycHC[*n*]**, *n* = 6, 8) (Figure 1), can externally bind multiple zinc porphyrins through the Lewis acid-base interactions and subsequently induce chirality at the porphyrin core [36]. A family of **cycHC[*n*]**s consists of chiral and nonchiral (*n* = 6, 8, 12) members [37–40] and features, analogous to all single bridged cucurbiturils [41,42], binding anions inside the macrocycle cavity. Additionally, **cycHC[*n*]**s bind hydrogen bond donors and electron-rich organic molecules [43,44]. Upon complexation of chiral **cycHC[*n*]**s with achiral and CD silent zinc octaethylporphyrin (**ZnOEP**) and zinc tetraphenylporphyrin (**ZnTPP**) in CH_2Cl_2, an ICD signal is observed in the region of the porphyrin Soret band [36]. This inspired us to explore further complexation and chirogenesis with **bis–ZnOEP** due to its aforementioned binding and chirality sensing abilities. Moreover, the complexation of **bis–ZnOEP** with relatively large multidentate molecules, such as **cycHC[*n*]**s, has not yet been studied. Thus, we present a binding

study employing various spectroscopic techniques (UV-vis absorption, fluorescence (FS), CD, NMR), including variable temperature (VT) and time-dependent measurements to characterize the corresponding supramolecular complexes of **bis–ZnOEP** with enantiomerically pure **cycHC[6]** and **cycHC[8]**, which have six and eight available urea binding sites, respectively.

2. Results and Discussion

2.1. Binding of **Bis–ZnOEP** *with* **CycHC[6]** *and* **CycHC[8]**

The binding properties of **bis–ZnOEP** with **cycHC[*n*]**s were evaluated by ^{1}H-NMR and UV-vis titrations using only (*R*,*R*)- enantiomers of chiral macrocycles. A stepwise addition of **cycHC[6]** to the *syn* form of **bis–ZnOEP** in CD_2Cl_2 shows the shielding of the *meso*-α protons of **bis–ZnOEP** (Figures 1 and 2A). However, the addition of two equivalents of macrocycle was followed by the deshielding of the same signal in the presence of higher equivalency, which clearly indicates the presence of more than one structural transformation. The change in chemical shifts of signals is influenced by **cycHC[6]** binding and subsequent conformational switching of **bis–ZnOEP**. The conformational changes of **bis–ZnOEP** are generally evaluated by ^{1}H-NMR signals from the *meso*-β protons (Figures 1 and 2B). In *syn* conformation, the *meso*-β protons experience a strong ring-current effect from the neighboring porphyrin ring and, due to the symmetry-related magnetic equivalency, provide a shielded broad singlet. Upon binding an external guest, the geometry of **bis–ZnOEP** changes; the influence of the ring-current effect of the porphyrin core causes deshielding, and due to symmetry loss, the signal is split [29,45]. These trends were observed in the case of **cycHC[6]**, where chemical shifts of *meso*-β protons split and are deshielded by 0.69 ppm (Figure 2B), which clearly indicates that the **bis–ZnOEP** *syn* form opens upon complexation with **cycHC[6]**. Similar behavior was found for the complex formation of **cycHC[8]** with **bis–ZnOEP**, namely that the porphyrin *meso*-protons exhibited deshielding and splitting in the case of *meso*-β protons (Figure 2D) and shielding in the case of *meso*-α protons (Figure 2C). However, for **cycHC[8]**, the changes of chemical shifts were to a lesser extent, and the reverse deshielding of the chemical shift of the *meso*-α proton was not observed (Figure 2C).

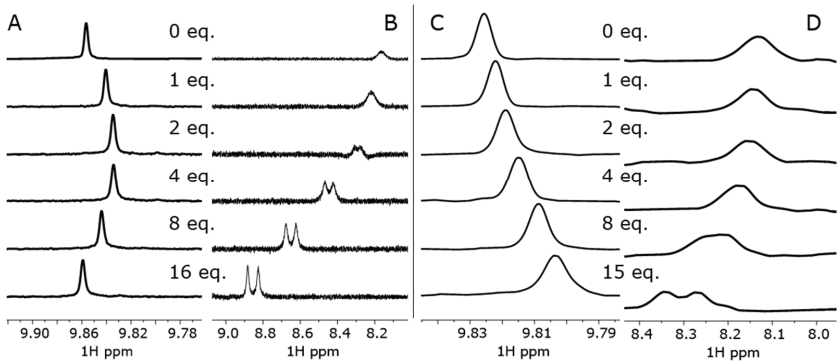

Figure 2. ^{1}H-NMR spectra of **bis–ZnOEP** upon addition of **cycHC[6]** in CD_2Cl_2: signals of (**A**) *meso*-α protons and (**B**) *meso*-β protons; and upon addition of **cycHC[8]** in CH_2Cl_2 and 10% $CDCl_3$: signals of (**C**) *meso*-α and (**D**) *meso*-β protons.

Titration experiments revealed that the maximum observed shift of *meso*-β protons were 0.17 ppm with **cycHC[8]** and 0.69 ppm with **cycHC[6]**, whilst the signal of the *meso*-α proton shifted by 0.02 ppm in the presence of 15 equivalents of **cycHC[8]** and only 2 equivalents of **cycHC[6]**. Assuming that the extent of chemical shift change is caused by the abundance of complexed species, a seemingly weaker binding of **cycHC[8]** compared to that of **cycHC[6]** can be deduced. This is in line with our previously published study [36],

wherein mono **ZnOEP** interacted with both **cycHC[*n*]**s through the same supramolecular mechanism; **cycHC[6]** was bound approximately five times stronger than **cycHC[8]**.

The UV-vis titrations of **bis–ZnOEP** with **cycHC[6]** show bathochromic shifting of the porphyrin B band λ_{max} from 397 to 402 nm upon complexation. Additionally, further red-shifted absorptions appear at 418 and 437 nm (Figure 3A). These electronic transitions indicate the formation of a tweezer-like complex; they appear closely similar to the previously published complexation study for **bis–ZnOEP** with amino alcohols [35], where three well-resolved transitions were exhibited at 407 nm, as the main band, and at 418 and 435 nm, as corresponding shoulders.

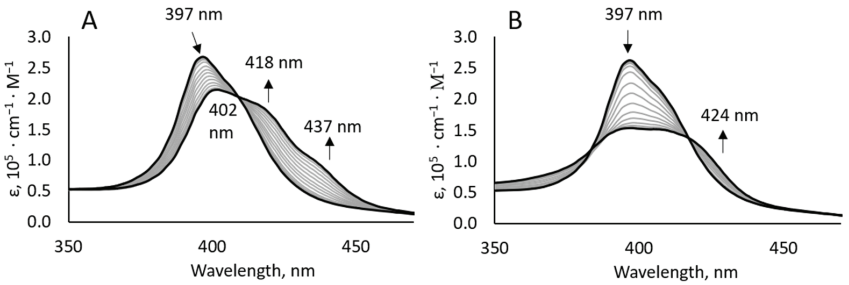

Figure 3. Absorption spectra of titration of **bis–ZnOEP** (3.2×10^{-6} M, CH_2Cl_2, 296 K) with (**A**) (*R*,*R*)-**cycHC[6]** from 0 to 2000 equivalents and with (**B**) (*R*,*R*)-**cycHC[8]** from 0 to 2000 equivalents.

Surprisingly, UV-vis titration of **bis–ZnOEP** with **cycHC[8]** showed a clear difference between the binding of two homologous macrocycles (Figure 3A,B). In particular, the complexation with **cycHC[8]** induced a decrease in the B band at λ_{max} 397 nm and appearance of the transition at 424 nm. This gave the absorption spectra of a contrastingly different shape at the same equivalents of **cycHC[8]**, as compared to **cycHC[6]**. Moreover, the saturation of the complex formation with **cycHC[8]** was seemingly reached at 1500 equivalents, while for **cycHC[6]**, more than 2000 equivalents were needed (Supplementary Materials pages S11–S15).

The ^{1}H-NMR and UV-vis titration data of **bis–ZnOEP** with **cycHC[6]** were evaluated using the Bindfit online tool [46,47]. Only the 1:2 binding model gave a reasonable correlation between the experimental data and fitted the binding isotherm for both titration methods. The fitting of the ^{1}H-NMR titration data (Supplementary Materials pages S3–S5) provided the corresponding association constants $K_1 = 1650 \pm 180$ M^{-1} and $K_2 = 183 \pm 2$ M^{-1}, and the fitting of UV-vis titration data showed the binding strength of the same magnitude with $K_1 = 4550 \pm 470$ M^{-1} and $K_2 = 92 \pm 1$ M^{-1} (Supplementary Materials pages S11–S13). The association constants obtained by both methods clearly indicate a negative cooperativity of the binding process, meaning that the binding of the first **cycHC[6]** molecule diminishes the binding of the second one. Such behavior is also typical for **bis–ZnOEP** forming a 1:1 tweezer-like complex with bidentate guests [35]. However, an excess of the bidentate guest forces **bis–ZnOEP** to adopt a 1:2 *anti* conformation. Apparently, the second guest binding is less favorable due to additional energy needed to break interactions with the first guest molecule and also the conformational change of **bis–ZnOEP**. It should be noted that in the case of the guests that give 1:1 complex in *anti* conformation, the binding of the second guest has positive cooperativity. This is because the intramolecular interactions in **bis–ZnOEP** are destroyed, and the subsequent *syn*-to-*anti* conformational change occurs upon the binding of the first guest. Therefore, the second guest molecule can be freely bound to the second porphyrin core and has no additional constraints. Hence, as the negative cooperativity was observed, and on the basis of spectral data obtained, we can assume that the 1:1 complex with **cycHC[6]** has a tweezer-like conformation. Moreover, with K_1 in the 10^3 M^{-1} range and K_2 being roughly 2–3 orders of magnitude smaller, the values correspond well with the previously described binding of smaller bidentate chiral guests, which formed the corresponding tweezer structure [35].

However, the evaluation of the ^{1}H-NMR and UV-vis titration data for the **bis–ZnOEP** and **cycHC[8]** complex was unsuccessful with 1:2 binding models, and a reasonable fit was achieved only in the NMR concertation range (mM) for 1:1 binding with $K_1 = 198 \pm 5\ M^{-1}$. Therefore, a different mechanism of the binding of **cycHC[8]**, as compared to **cycHC[6]**, should be considered. Additionally, certain time-dependent changes during the UV-vis titration experiments with **cycHC[8]** were noted.

2.2. Time-Dependent Behavior of Complexes

The evaluation of the stability of **cycHC[*n*]** complexes in time was checked by measuring the UV-vis spectra of **bis–ZnOEP** immediately after the single addition of 2000 (or more) equivalents of **cycHC[8]** and **cycHC[6]** to provide sufficient abundance of the complex (see mole fractions on page S11) and compared with the data from the UV-vis titration first (pure **bis–ZnOEP)** and last points (complexed **bis–ZnOEP**) for the same macrocycles. The titration last points were measured approximately 1 h after the first addition and had the same equivalents of a guest as in the comparative single addition experiment (Figure 4A,B). In the case of **cycHC[6]**, the binding outcome was the same in both experiments (titration and single addition). As less pronounced changes in time were observed for the complex of **bis–ZnOEP** with **cycHC[6]**, we can conclude that the complex formation equilibrium is relatively fast within the measurement timeframe.

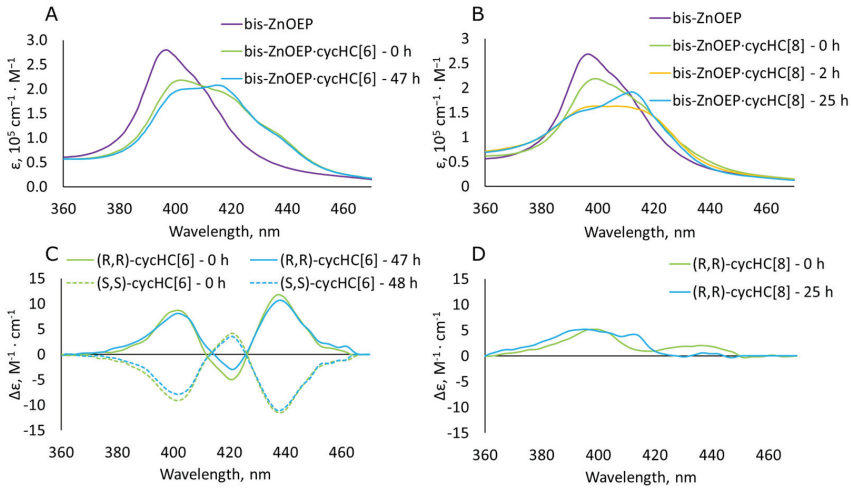

Figure 4. (**A**) Absorption spectra of free **bis–ZnOEP** (2.2×10^{-6} M, CH_2Cl_2, 296 K) and after single addition of 3000 eq of (*R*,*R*)-**cycHC[6]** in time. (**B**) Absorption spectra of free **bis–ZnOEP** (3.0×10^{-6} M, CH_2Cl_2, 296 K) and after single addition of 2200 eq of (*R*,*R*)-**cycHC[8]** in time. (**C**) Change of CD spectra in time corresponding to the sample of **bis–ZnOEP·cycHC[6]** from absorption spectra A and for the complex with (*S*,*S*)-**cycHC[6]** measured at the same conditions. (**D**) Change of CD spectra in time corresponding to the sample of **bis–ZnOEP·cycHC[8]** from absorption spectra B immediately after single addition and after 25 h.

Conversely, in the case of the **cycHC[8]** complex, the distinct differences were spotted between the final spectrum of titration and single addition of the same equivalents of **cycHC[8]** (Figures 3B and 4B, 0 h). The single addition (Figure 4B, 0 h) caused a lesser initial change in the spectrum, and noticeable spectral changes occurred in time (Figure 4B, 25 h), indicating a kinetically slow process. After 2 h, the spectra from a single addition experiment became similar to the last titration point (Figures 3B and 4B, 2 h). After 24 h, further changes in the UV-vis spectra became negligible. Therefore, one can conclude that a relatively slow and concurrent kinetics of the complexation of **cycHC[8]** with **bis–ZnOEP** prevents the successful evaluation of association constants by the standard procedure.

To further study the kinetic process, additional CD and fluorescence spectra of **bis–ZnOEP** after a single addition of **cycHC[*n*]** were measured. In the case of **cycHC[6]**, minor changes in the spectra were noted. The ICD spectra (Figure 4C) exhibit a complex spectral profile consisting of three Cotton effects as a result of EC between two pairs of the porphyrin electronic transitions in **bis–ZnOEP**. The latter observation proves interaction with chiral **cycHC[6]** and corresponding helical distortion of **bis–ZnOEP**. The fluorescence spectrum in the presence of **cycHC[6]** showed the emissions of the complex at 611 nm, the Q(0,0) band, and at 660 nm, the Q(0,1) band (Figure 5A), which also support the formation of a tweezer-like complex as was suggested based on the UV absorption spectra. There are apparent similarities to the previously published complexes with small molecules that form tweezer-like structures [29].

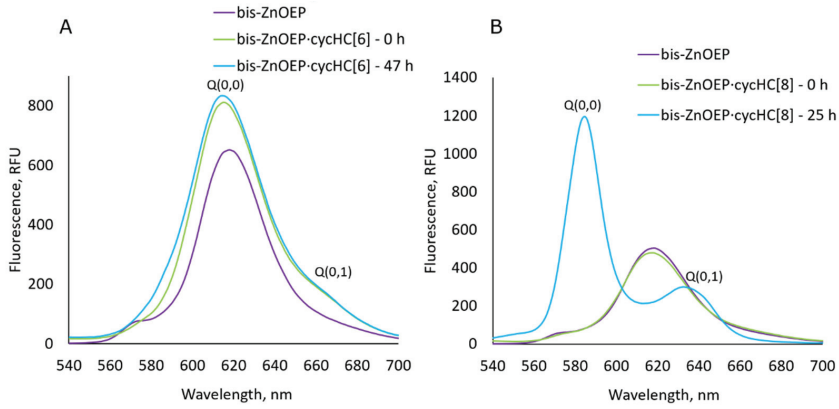

Figure 5. (**A**) Fluorescence spectra (λ_{ex} = 399 nm) of free **bis–ZnOEP** (2.2×10^{-6} M, CH_2Cl_2, 296 K) and after single addition of 3000 eq of (*R*,*R*)-**cycHC[6]** in time (λ_{ex} = 404 nm). (**B**) Fluorescence spectra of free **bis–ZnOEP** ($3.0 \cdot 10^{-6}$ M, CH_2Cl_2, 296 K) and after single addition of 2200 eq of (*R*,*R*)-**cycHC[8]** in time (λ_{ex} = 413 nm).

Analogous to UV-vis data, a distinct complexation character of **bis–ZnOEP** with **cycHC[8]** was also observed in CD and fluorescence spectral data (Figures 4B,D and 5B). The presence of the ICD signal of **bis–ZnOEP** upon mixing with **cycHC[8]** at the starting point (0 h) proves the formation of a chiral complex (Figure 4D). Although the shape of ICD is changed in time, all recorded spectra lack strong EC, resembling monosignate ICD of previously studied monomeric **ZnOEP** in complexes with **cycHC[*n*]** [36]. This along with the fact that the intensity of ICD remains low in time clearly indicates that chiral induction is apparently caused by unsymmetrical deformation of the individual porphyrin moieties at the nearly parallel-oriented porphyrin cores rather than by a unidirectional helical arrangement of the whole **bis–ZnOEP** molecule [48]. Moreover, a distinct contrast in the intensity and shape of the CD spectra of corresponding **cycHC[6]** and **cycHC[8]** complexes is additional evidence of the specific chiroptical selectivity of **bis–ZnOEP** as a chirality sensor for large chiral macrocycles (Figure 4C,D). Notably, further UV-vis kinetic experiments at higher concentration (3.4×10^{-5} M) of **bis–ZnOEP** also fully support this conclusion (see Supplementary Materials pages S16–S18 and S23).

Interestingly, the emission spectrum exhibited a negligible change directly after adding **cycHC[8]** to **bis–ZnOEP** (Figure 5B). However, the emission spectrum drastically changed after 25 h when the complex stabilized; it exhibited two distinct bands with the smaller Q(0,1) band at 632 nm and main Q(0,0) band at 585 nm of a higher intensity as compared to that at 0 h. These observations also suggest that the *syn*-to-*anti* conformational switching of **bis–ZnOEP** leads to fluorescence firing as the porphyrin cores become more spatially separated and hence less interactive. Similar changes have been also evidenced in previous studies [35]. This assumption is additionally supported by the similarity of the

emission spectra shapes of monomeric **ZnOEP** and **bis–ZnOEP·cycHC[8]** with the Q(0,0) and Q(0,1) bands of **ZnOEP** appearing at 577 and 628 nm, respectively (Figure 5B and Supplementary Material pages S24–S26). Moreover, upon the binding of **cycHC[8]**, the shape of the **ZnOEP** emission spectrum remained the same (Supplementary Material page S26).

The substantial change in time of **bis–ZnOEP·cycHC[8]** UV-vis, CD, and FS spectra should arise either from slow *syn*-to-*anti* conformational change of **bis–ZnOEP** or aggregation of the host–guest complex. The time-dependent ^{1}H-NMR measurements of the **bis–ZnOEP·cycHC[8]** complex were performed in the 1:1 ratio and in excess of **cycHC[8]** to follow the conformational changes of **bis–ZnOEP** upon complexation. In addition, similar analysis of the **bis–ZnOEP·cycHC[6]** complex was performed for comparison (see Supplementary Material page S28). Spectra were collected immediately after mixing and then 20 days later for solutions containing 1 equivalent of **cycHC[*n*]** and after 24 h for solutions containing excess of 8 equivalent of **cycHC[*n*]**. Time-dependent changes in the chemical shifts and signal shapes were not observed in neither of the complexes; however, the split in *meso*-β proton signals in excess of **cycHC[*n*]** clearly indicated opening of the *syn*-conformation of **bis–ZnOEP** in both **cycHC[*n*]** complexes (Figure 2 and Supplementary Material pages S3–S6 and S28) with comparably fast rate.

The observed difference in time-dependent behavior of the **bis–ZnOEP·cycHC[8]** supramolecular system in the UV-vis, CD, and FS measurements, as compared to the NMR measurements, can be related to a substantial difference in the sample concentrations (μM and mM, respectively) and in excess of **cycHC[8]** (2000 and 8 equivalents, respectively). The low binding constant of **bis–ZnOEP** to **cycHC[8]** and relatively small excess of **cycHC[8]** in the NMR study might hinder the formation of the assembled species, as indicated by other methods.

2.3. Variable Temperature ^{1}H-NMR and Fluorescence Experiments

To find a process responsible for the time-dependent changes, two VT experiments were performed.

Firstly, a stability and reversibility of the aggregate formation together with the thermodynamic parameters of the complex formation were studied by VT ^{1}H-NMR of a samples containing 1:1 ratio of **bis–ZnOEP** and **cycHC[*n*]** (Figure 6 and Supplementary Materials pages S29–S30). Upon cooling down to 253 K, all the signals of **bis–ZnOEP** and both **cycHC[*n*]**s exhibited changes in chemical shifts, which can be related to the increased abundance of complexes due to a stronger binding at lower temperature. However, larger changes were observed in the presence of **cycHC[6]** complex in comparison to **cycHC[8]** (Figure 6A,B, respectively). The line broadening, caused by the slow exchange between complexed and noncomplexed species or aggregates, was most prominent in the shift of *meso*-β proton at 8.2 ppm in both samples; nevertheless, the coalescence point was not passed, and therefore, thermodynamic parameters could not be evaluated in this study.

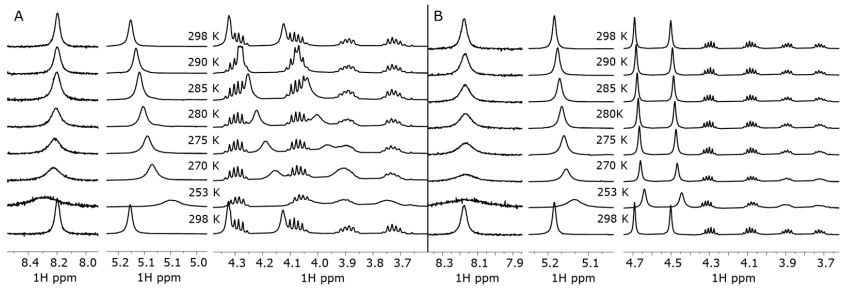

Figure 6. The selected areas of ^{1}H-NMR spectrum of 1:1 ratio mixture of 1.0×10^{-3} M **bis-ZnOEP** and (**A**) (*R*,*R*)-**cycHC[6]** and (**B**) (*R*,*R*)-**cycHC[8]** at (from top to bottom): 298 (before cooling), 290, 285, 280, 275, 270, 253, and 298 K (after heating back to initial temperature).

Upon heating the samples from 253 back to 298 K, the observed changes were immediately reversed and resulted in the same ^{1}H-NMR spectrum as observed prior to cooling (Figure 6). Therefore, the formation of new species that could be clearly identified as aggregates were not proven at mM concentration.

Secondly, the influence of temperature on the *syn*-to-*anti* conformational change was studied by fluorescence spectroscopy, as a method used for a μM concentration region. Samples containing mixtures of **bis–ZnOEP** and **cycHC[8]** were brought and kept at the temperature of 248, 295, and 308 K immediately after the samples preparation and then measured at 295 K (Figure 7). Based on the previous UV-vis experiments, it was estimated that maintaining the samples at different temperatures for 2–8 h should be sufficient to observe their differences; hence, samples were measured 5 h after the mixing of compounds. Importantly, the emission spectra were measured at 295 K; therefore, the observed differences can be attributed only to the time spent at different temperatures. The obtained results thus clearly show that at higher temperatures, the expected transformation of emission spectra progressed faster. This means that the conformational change from *syn*-to-*anti* form contributes in the kinetically slow process, stabilizing after approximately 24 h at room temperature. However, as noted above, the changes in emission spectra cannot be simply attributed only to the conformational change as opening of the *syn* conformation was relatively fast according to the NMR studies. Therefore, the aggregation of the complexes where **bis–ZnOEP** is in the *anti* conformation can be proposed at μM concentration range.

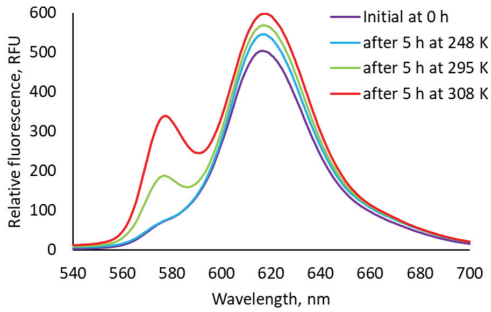

Figure 7. Emission spectra (excited at 397 nm) of **bis–ZnOEP** (3×10^{-6} M) samples with 2000 equivalents of **cycHC[8]** measured at 295 K immediately after preparation and then again after being kept for 5 h at different temperatures.

2.4. Proposed Self-Assembly Mechanism

The following binding and self-assembly mechanisms for the **bis–ZnOEP·cycHC[*n*]** complexes were proposed based on the above-discussed experimental results (Figure 8).

The interaction of **bis–ZnOEP** and **cycHC[6]** resembles the complexation of **bis–ZnOEP** with small bidentate guests [35]. Furthermore, the observed negative cooperativity is in line with the formation of a tweezer-like 1:1 complex, in which a molecule of **cycHC[6]** is placed between two porphyrin moieties and fixed by two coordination bonds. The further addition of **cycHC[6]** leads to the formation of 1:2 complex, which is in the *anti* form (Figure 8A). In the case of **cycHC[8]**, the self-assembly process is more complicated due to the presence of a slow kinetic process at μM concentration. Minor changes in absorption and fluorescence maximum wavelength and intensity shortly after mixing (Figures 4B and 5B) suggest that the first binding (process I. at Figure 8B) is relatively weak and **bis–ZnOEP** is likely to preserve the *syn* conformation. Further time evolution in fluorescence proves the opening of **bis–ZnOEP** (II. and III.) via the kinetically slow process into the *anti* conformation, in which two porphyrin moieties are apart from each other, and as no EC was observed in CD, the angle between them is close to 180°. In addition, an aggregation (III.) of the complex would be the more probable explanation [49] for the slow process as opening

of the *syn* conformation was proven to be fast by NMR studies. Nevertheless, *syn*-to-*anti* interconversion kinetics can be influenced by the concentration.

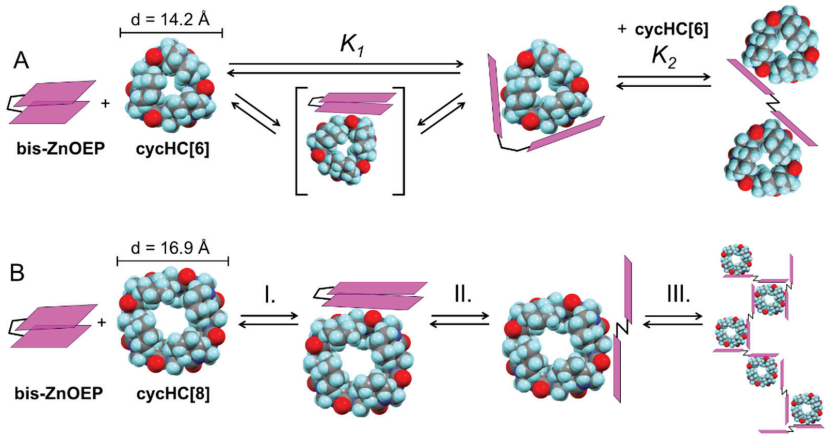

Figure 8. The proposed binding mechanisms of **bis–ZnOEP** with (**A**) **cycHC[6]** described by obtained association constants and with (**B**) **cycHC[8]**. The 3D structures and diameters of **cycHC[*n*]**s are based on previously reported crystal structures [36]. Color coding: C—gray, H—light blue, O—red, and N—dark blue.

As both macrocycles are chemically analogous, the observed differences in binding mechanisms must be related to structural inequalities, such as bulkiness, shapes, and the number of binding sites. While the heights of **cycHC[6]** (12.4 Å) and **cycHC[8]** (11.9 Å) are similar, the diameters (d) and shapes obviously differ as a consequence of a differing number of monomers in **cycHC[*n*]** (Figure 8, Supplementary Material pages S31–S32). However, the diameter of **bis–ZnOEP** aromatic rings (12 Å) is comparable in size to measures of **cycHC[*n*]** (see Supplementary Material pages S31–S32). Clearly, a larger volume of **cycHC[8]** may lead to increased steric hindrance and preference for the opened *anti* conformation. Hence, it is reasonable to assume that the interaction between **bis–ZnOEP** and **cycHC[8]** is directed by the macrocycle size and steric hindrance caused by the ethyl groups of **bis–ZnOEP**.

Nevertheless, a probable relation between the guest's bulkiness and kinetics of bis–porphyrin's spectral changes at μM concentrations cannot explicitly explain why **cycHC[8]** could exhibit further aggregation while **cycHC[6]** does not. Although the binding of **cycHC[6]** proceeds through the tweezer-like complex—which is unsuitable for aggregation—an excess of both **cycHC[*n*]** leads to the final *anti* conformation, where both porphyrin rings of **bis–ZnOEP** are bound to the guests. This situation is essentially the same in the 1:2 *anti* complex and in the aggregate. Hence, the probable ability to aggregate with **cycHC[8]** but not with **cycHC[6]** can arise from the difference in shape and position of additional binding sites. As one can deduce from the ICD spectra, the specific geometry of **bis–ZnOEP·cycHC[8]** complexes is close to parallel, while **bis–ZnOEP·cycHC[6]** exhibits a helical distortion. Therefore, it is reasonable to assume that the geometry of one complex is suitable for aggregate formation, whereas the other is not. However, we are currently undertaking further study to elucidate the detailed structure of observed complexes, mechanism of self-association, and chirogenic processes and will report our findings in due course.

3. Materials and Methods

3.1. General

Unless otherwise stated, all reagents and solvents were purchased from commercial suppliers and used as received. Compounds prepared in our laboratories were **bis–ZnOEP** [50], (*S*,*S*) and (*R*,*R*)-**cycHC[8]** [38], (*S*,*S*) and (*R*,*R*)-**cycHC[6]** [37] and were prepared in all cases according to the procedures described in the literature. All solutions were prepared using Hamilton® Gastight syringes (Hamilton Company, Reno, NV, USA); those syringes were also used for all additions during UV-VIS and NMR titrations. To ensure precise measurement in sample preparation, the mass of solvent and its density were used along with volumetric glassware. Samples were weighed on a microbalance with an accuracy of 6 µg (Radwag® MYA 11.4Y, Radom, Poland). The NMR and UV-vis titrations, as well as other experiments using methods nonsensitive to chirality of complexes, were performed only with enantiopure (*R*,*R*)-**cycHC[*n*]** since the same binding for (*S*,*S*)-enantiomers is expected. Titration data were fitted using Bindfit software [46,47]. All the UV-vis, CD, and fluorescence spectra are presented in the range of wavelengths corresponding to absorption or emission of **bis–ZnOEP**, while **cycHC[*n*]**s have no bands in the same range (see Supplementary Materials page S27). The excess of 2000 or more equivalents of **cycHC[*n*]** used in single-addition experiments was necessary to secure sufficient abundance of complex in solution. The amount was rationalized based on the shape of UV-vis titration binding isotherms (seeming saturation in the case of **cycHC[8]**) and mole fractions based on the obtained association constants for **cycHC[6]**. We examined previously obtained crystal structures of **bis–ZnOEP** [51–53] and of **cycHC[*n*]** with ZnTPP [36] for their similarity to herein presented complexes. All distances were measured between the centers of corresponding atoms, and the van der Waals radius was then added.

3.2. Spectroscopic Measurements

^{1}H-NMR experiments were measured using a QCI CryoProbe and DUL probe on a Bruker AVANCE III 800 MHz (Bruker Corporation, Billerica, MA, USA) spectrometer at a temperature of 298.15 K, except that time-dependent ^{1}H-NMR and VT-NMR (253–298 K) were measured using 5 mm ID probe (Inverse Detect probe) on Agilent DD2 500 MHz spectrometer (Agilent Technologies, Inc., Santa Clara, CA, USA). All NMR titrations were performed in either CD_2Cl_2 or CH_2Cl_2 containing 10% $CDCl_3$ to lock. Data was processed with MestreNova (Version 14.1.2) software. The UV-vis absorption spectra were recorded with Varian Cary® 50 UV-vis spectrophotometer (Agilent Technologies, Inc., Santa Clara, CA, USA). The CD spectra were recorded with a Jasco J-1500 circular dichroism spectrophotometer (JASCO International Co., Ltd., Tokyo, Japan). All the fluorescence measurements were recorded by Hitachi F-7000 fluorescence spectrophotometer (Hitachi, Ltd., Tokyo, Japan). All spectroscopic measurements were performed in CH_2Cl_2, and concentrations and spectral data are available in further detail in Supplementary Materials.

4. Conclusions

In summary, the complex formation of **bis–ZnOEP** with bulky chiral multidentate **cycHC[*n*]** macrocycles was studied using UV–vis, CD, fluorescence, and ^{1}H-NMR spectroscopy methods. Although **cycHC[6]** and **cycHC[8]** are chemically analogous and differ only in the number of binding sites, shape, and volume, **bis–ZnOEP** is able to differentiate between the two macrocycles by exhibiting a different behavior related to the self-assembly mechanism. **Bis–ZnOEP** forms a tweezer-like 1:1 complex with **cycHC[6]**, which subsequently transforms into the opened 1:2 *anti* complex upon further addition of **cycHC[6]**. The evaluation of ^{1}H-NMR and UV-vis titration data showed a negative cooperativity with the average association constants for both methods: K_1 = 3200 M^{-1}; K_2 = 140 M^{-1}. In contrast to **cycHC[6]**, the interaction between **bis–ZnOEP** and **cycHC[8]** exhibited obscure host–guest interaction. This included the intermolecular binding itself and further time-dependent self-association, which prevented the evaluation of the corresponding association constants. This host–guest interaction includes the formation of the 1:1 *syn* complex

between **bis–ZnOEP** and **cycHC[8]** followed by slow opening to the *anti* conformation, which is apparently driven by subsequent aggregate generation. Moreover, the specific **cycHC[8]**'s shape and larger number of binding sites leading to a different geometry of the complexes are associated with the presumed aggregate formation, which was not observed in the case of **cycHC[6]** complexes. Finally, this paper confirms that **bis–ZnOEP** is able to recognize **cycHC[*n*]**s and their enantiomers. Chiral **cycHC[6]** induces noticeably intense CD employing exciton coupling, therefore indicating a helical distortion of the whole **bis–ZnOEP** molecule, whilst chiral **cycHC[8]** induces only weak and monosignate CD, with exciton coupling absent apparently due to nearly parallel orientation of the porphyrin cores of **bis–ZnOEP**. In conclusion, this work clearly demonstrated an advanced sensory ability of **bis–ZnOEP** to recognize large macrocyclic systems, such as **cycHC[*n*]**s, and that the complexation-induced aggregation of porphyrins can lead to the formation of new chiral materials.

Supplementary Materials: The following supporting information can be downloaded online. General information; ^{1}H NMR titrations: Figures S1–S7, Tables S1–S3; UV-Vis titrations: Figures S8–S12, Tables S4 and S5; Spectroscopic UV-Vis and fluorescence kinetics: Figures S13–S31; UV-Vis and CD of pure cycHC[n]: The highest intensity UV-Vis maxima for cycHC[n] in CH3CN are reported previously in literature [54] and are following: for cycHC[6] λmax = 196 nm and for cycHC[8] λmax = 197 nm. Figure S32; ^{1}H NMR time dependent change: Figures S33 and S34; Variable temperature in 1H NMR: Figures S35 and S36; Structural analysis of cycHC and bis–ZnOEP: Figures S37 and S38.

Author Contributions: Conceptualization, L.U., R.A. and V.B.; methodology, M.Š, L.U., R.A. and V.B.; formal analysis, M.Š., L.U., R.A. and V.B.; investigation, M.Š., N.K. and J.A.; resources, K.A.M., J.V.N. and E.S.; data curation, M.Š.; writing—original draft preparation, M.Š. and L.U.; writing—review and editing, M.Š., L.U., K.A.M., J.V.N., E.S., N.K., J.A., V.B. and R.A.; visualization, M.Š. and L.U.; supervision, R.A., V.B. and L.U.; funding acquisition, R.A. and L.U. All authors have read and agreed to the published version of the manuscript.

Funding: This research was funded by the Estonian Research Council Grants (PRG399, PSG400, and MOBJD592); the European Regional Development Fund (CoE 2014-2020.4.01.15-0013, and CoE TK134); Estonian Research Council (TT4); and H2020-FETOPEN 828779 (INITIO).

Institutional Review Board Statement: Not available.

Informed Consent Statement: Not available.

Data Availability Statement: Data will be available on reasonable request from the corresponding author.

Acknowledgments: The authors would like to thank Vitālijs Rjabovs and Indrek Reile for their help on setting up the NMR experiments.

Conflicts of Interest: The authors declare no conflict of interest.

Sample Availability: Samples of the compounds are available from the corresponding authors.

References

1. Barona-Castaño, J.C.; Carmona-Vargas, C.C.; Brocksom, T.J.; de Oliveira, K.T. Porphyrins as Catalysts in Scalable Organic Reactions. *Molecules* **2016**, *21*, 310. [CrossRef] [PubMed]
2. Borah, K.D.; Bhuyan, J. Magnesium Porphyrins with Relevance to Chlorophylls. *Dalton Trans.* **2017**, *46*, 6497–6509. [CrossRef] [PubMed]
3. Moore, S.J.; Sowa, S.T.; Schuchardt, C.; Deery, E.; Lawrence, A.D.; Ramos, J.V.; Billig, S.; Birkemeyer, C.; Chivers, P.T.; Howard, M.J.; et al. Elucidation of the Biosynthesis of the Methane Catalyst Coenzyme F 430. *Nature* **2017**, *543*, 78–82. [CrossRef] [PubMed]
4. Karlberg, T.; Hansson, M.D.; Yengo, R.K.; Johansson, R.; Thorvaldsen, H.O.; Ferreira, G.C.; Hansson, M.; Al-Karadaghi, S. Porphyrin Binding and Distortion and Substrate Specificity in the Ferrochelatase Reaction: The Role of Active Site Residues. *J. Mol. Biol.* **2008**, *378*, 1074–1083. [CrossRef] [PubMed]
5. Strianese, M.; Pappalardo, D.; Mazzeo, M.; Lamberti, M.; Pellecchia, C. The Contribution of Metalloporphyrin Complexes in Molecular Sensing and in Sustainable Polymerization Processes: A New and Unique Perspective. *Dalton Trans.* **2021**, *50*, 7898–7916. [CrossRef]
6. Aykanat, A.; Meng, Z.; Benedetto, G.; Mirica, K.A. Molecular Engineering of Multifunctional Metallophthalocyanine-Containing Framework Materials. *Chem. Mater.* **2020**, *32*, 5372–5409. [CrossRef]

7. Norvaiša, K.; Kielmann, M.; Senge, M.O. Porphyrins as Colorimetric and Photometric Biosensors in Modern Bioanalytical Systems. *ChemBioChem* **2020**, *21*, 1793–1807. [CrossRef]
8. Melissari, Z.; Williams, R.; Senge, M. Porphyrinoids for Photodynamic Therapy. In *Applications of Porphyrinoids as Functional Materials*; Lang, H., Rueffer, T., Eds.; R. Soc. Chem.: Croydon, UK, 2021; pp. 252–291.
9. Paolesse, R.; Nardis, S.; Monti, D.; Stefanelli, M.; Di Natale, C. Porphyrinoids for Chemical Sensor Applications. *Chem. Rev.* **2017**, *117*, 2517–2583. [CrossRef]
10. Matile, S.; Berova, N.; Nakanishi, K.; Novkova, S.; Philipova, I.; Blagoev, B. Porphyrins: Powerful Chromophores for Structural Studies by Exciton-Coupled Circular Dichroism. *J. Am. Chem. Soc.* **1995**, *117*, 7021–7022. [CrossRef]
11. Lu, H.; Kobayashi, N. Optically Active Porphyrin and Phthalocyanine Systems. *Chem. Rev.* **2016**, *116*, 6184–6261. [CrossRef]
12. Lu, W.; Yang, H.; Li, X.; Wang, C.; Zhan, X.; Qi, D.; Bian, Y.; Jiang, J. Chiral Discrimination of Diamines by a Binaphthalene-Bridged Porphyrin Dimer. *Inorg. Chem.* **2017**, *56*, 8223–8231. [CrossRef] [PubMed]
13. Saha, B.; Ikbal, S.A.; Petrovic, A.G.; Berova, N.; Rath, S.P. Complexation of Chiral Zinc-Porphyrin Tweezer with Achiral Diamines: Induction and Two-Step Inversion of Interporphyrin Helicity Monitored by ECD. *Inorg. Chem.* **2017**, *56*, 3849–3860. [CrossRef] [PubMed]
14. Miyake, Y.; López-Moreno, A.; Yang, J.; Xu, H.-J.; Desbois, N.; Gros, C.P.; Komatsu, N. Synthesis of Flexible Nanotweezers with Various Metals and Their Application in Carbon Nanotube Extraction. *New J. Chem.* **2018**, *42*, 7592–7594. [CrossRef]
15. Saha, B.; Petrovic, A.G.; Dhamija, A.; Berova, N.; Rath, S.P. Complexation of Chiral Zinc(II) Porphyrin Tweezer with Achiral Aliphatic Diamines Revisited: Molecular Dynamics, Electronic CD, and ^{1}H-NMR Analysis. *Inorg. Chem.* **2019**, *58*, 11420–11438. [CrossRef]
16. Mondal, P.; Rath, S.P. Cyclic Metalloporphyrin Dimers: Conformational Flexibility, Applications and Future Prospects. *Coord. Chem. Rev.* **2020**, *405*, 213117. [CrossRef]
17. Huang, X.; Rickman, B.H.; Borhan, B.; Berova, N.; Nakanishi, K. Zinc Porphyrin Tweezer in Host−Guest Complexation: Determination of Absolute Configurations of Diamines, Amino Acids, and Amino Alcohols by Circular Dichroism. *J. Am. Chem. Soc.* **1998**, *120*, 6185–6186. [CrossRef]
18. Borovkov, V.V.; Hembury, G.A.; Inoue, Y. Origin, Control, and Application of Supramolecular Chirogenesis in Bisporphyrin-Based Systems. *Acc. Chem. Res.* **2004**, *37*, 449–459. [CrossRef]
19. Tanasova, M.; Anyika, M.; Borhan, B. Sensing Remote Chirality: Stereochemical Determination of β-, γ-, and δ-Chiral Carboxylic Acids. *Angew. Chem. Int. Ed.* **2015**, *54*, 4274–4278. [CrossRef]
20. Hayashi, S.; Yotsukura, M.; Noji, M.; Takanami, T. Bis(Zinc Porphyrin) as a CD-Sensitive Bidentate Host Molecule: Direct Determination of Absolute Configuration of Mono-Alcohols. *Chem. Commun.* **2015**, *51*, 11068–11071. [CrossRef]
21. Dhamija, A.; Saha, B.; Rath, S.P. Metal-Center-Driven Supramolecular Chirogenesis in Tweezer Amino Alcohol Complexes: Structural, Spectroscopic, and Theoretical Investigations. *Inorg. Chem.* **2017**, *56*, 15203–15215. [CrossRef]
22. Gholami, H.; Chakraborty, D.; Zhang, J.; Borhan, B. Absolute Stereochemical Determination of Organic Molecules through Induction of Helicity in Host–Guest Complexes. *Acc. Chem. Res.* **2021**, *54*, 654–667. [CrossRef] [PubMed]
23. Balaz, M.; Napoli, M.D.; Holmes, A.E.; Mammana, A.; Nakanishi, K.; Berova, N.; Purrello, R. A Cationic Zinc Porphyrin as a Chiroptical Probe for Z-DNA. *Angew. Chem. Int. Ed.* **2005**, *44*, 4006–4009. [CrossRef] [PubMed]
24. Wolf, C.; Bentley, K.W. Chirality Sensing Using Stereodynamic Probes with Distinct Electronic Circular Dichroism Output. *Chem. Soc. Rev.* **2013**, *42*, 5408–5424. [CrossRef] [PubMed]
25. Chen, Z.; Wang, Q.; Wu, X.; Li, Z.; Jiang, Y.-B. Optical Chirality Sensing Using Macrocycles, Synthetic and Supramolecular Oligomers/Polymers, and Nanoparticle Based Sensors. *Chem. Soc. Rev.* **2015**, *44*, 4249–4263. [CrossRef] [PubMed]
26. Labuta, J.; Hill, J.P.; Ishihara, S.; Hanyková, L.; Ariga, K. Chiral Sensing by Nonchiral Tetrapyrroles. *Acc. Chem. Res.* **2015**, *48*, 521–529. [CrossRef] [PubMed]
27. Pescitelli, G.; Bari, L.D.; Berova, N. Application of Electronic Circular Dichroism in the Study of Supramolecular Systems. *Chem. Soc. Rev.* **2014**, *43*, 5211–5233. [CrossRef]
28. Borovkov, V.V.; Harada, T.; Inoue, Y.; Kuroda, R. Phase-Sensitive Supramolecular Chirogenesis in Bisporphyrin Systems. *Angew. Chem. Int. Ed.* **2002**, *114*, 1436–1439. [CrossRef]
29. Borovkov, V.V.; Lintuluoto, J.M.; Sugiura, M.; Inoue, Y.; Kuroda, R. Remarkable Stability and Enhanced Optical Activity of a Chiral Supramolecular Bis-Porphyrin Tweezer in Both Solution and Solid State. *J. Am. Chem. Soc.* **2002**, *124*, 11282–11283. [CrossRef]
30. Harada, N.; Nakanishi, K. *Circular Dichroic Spectroscopy: Exciton Coupling in Organic Stereochemistry*; University Science Books: Mill Valley, CA, USA, 1983; ISBN 978-0-935702-09-5.
31. Borovkov, V.V.; Lintuluoto, J.M.; Inoue, Y. Supramolecular Chirogenesis in Zinc Porphyrins: Mechanism, Role of Guest Structure, and Application for the Absolute Configuration Determination. *J. Am. Chem. Soc.* **2001**, *123*, 2979–2989. [CrossRef]
32. Harada, N.; Nakanishi, K. Exciton Chirality Method and Its Application to Configurational and Conformational Studies of Natural Products. *Acc. Chem. Res.* **1972**, *5*, 257–263. [CrossRef]
33. Borovkov, V.V.; Lintuluoto, J.M.; Inoue, Y. Temperature Controlled Syn-Anti Conformational Switching in Zinc Containing Porphyrin Dimers via Ligand Assistance. *Tetrahedron Lett.* **1999**, *40*, 5051–5054. [CrossRef]
34. Borovkov, V.V.; Lintuluoto, J.M.; Inoue, Y. Syn-Anti Conformational Changes in Zinc Porphyrin Dimers Induced by Temperature-Controlled Alcohol Ligation. *J. Phys. Chem. B* **1999**, *103*, 5151–5156. [CrossRef]

35. Borovkov, V.V.; Lintuluoto, J.M.; Hembury, G.A.; Sugiura, M.; Arakawa, R.; Inoue, Y. Supramolecular Chirogenesis in Zinc Porphyrins: Interaction with Bidentate Ligands, Formation of Tweezer Structures, and the Origin of Enhanced Optical Activity. *J. Org. Chem.* **2003**, *68*, 7176–7192. [CrossRef] [PubMed]
36. Ustrnul, L.; Kaabel, S.; Burankova, T.; Martõnova, J.; Adamson, J.; Konrad, N.; Burk, P.; Borovkov, V.; Aav, R. Supramolecular Chirogenesis in Zinc Porphyrins by Enantiopure Hemicucurbit[*n*]urils (*n* = 6, 8). *Chem. Commun.* **2019**, *55*, 14434–14437. [CrossRef] [PubMed]
37. Aav, R.; Shmatova, E.; Reile, I.; Borissova, M.; Topić, F.; Rissanen, K. New Chiral Cyclohexylhemicucurbit[6]uril. *Org. Lett.* **2013**, *15*, 3786–3789. [CrossRef] [PubMed]
38. Prigorchenko, E.; Öeren, M.; Kaabel, S.; Fomitšenko, M.; Reile, I.; Järving, I.; Tamm, T.; Topić, F.; Rissanen, K.; Aav, R. Template-Controlled Synthesis of Chiral Cyclohexylhemicucurbit[8]uril. *Chem. Commun.* **2015**, *51*, 10921–10924. [CrossRef] [PubMed]
39. Prigorchenko, E.; Kaabel, S.; Narva, T.; Baškir, A.; Fomitšenko, M.; Adamson, J.; Järving, I.; Rissanen, K.; Tamm, T.; Aav, R. Formation and Trapping of the Thermodynamically Unfavoured Inverted-Hemicucurbit[6]uril. *Chem. Commun.* **2019**, *55*, 9307–9310. [CrossRef]
40. Mishra, K.A.; Adamson, J.; Öeren, M.; Kaabel, S.; Fomitšenko, M.; Aav, R. Dynamic Chiral Cyclohexanohemicucurbit[12]uril. *Chem. Commun.* **2020**, *56*, 14645–14648. [CrossRef]
41. Andersen, N.N.; Lisbjerg, M.; Eriksen, K.; Pittelkow, M. Hemicucurbit[n]urils and Their Derivatives—Synthesis and Applications. *Isr. J. Chem.* **2018**, *58*, 435–448. [CrossRef]
42. Lizal, T.; Sindelar, V. Bambusuril Anion Receptors. *Isr. J. Chem.* **2018**, *58*, 326–333. [CrossRef]
43. Ustrnul, L.; Burankova, T.; Öeren, M.; Juhhimenko, K.; Ilmarinen, J.; Siilak, K.; Mishra, K.A.; Aav, R. Binding Between Cyclohexanohemicucurbit[n]urils and Polar Organic Guests. *Front. Chem.* **2021**, *9*, 468. [CrossRef] [PubMed]
44. Shalima, T.; Mishra, K.A.; Kaabel, S.; Ustrnul, L.; Bartkova, S.; Tõnsuaadu, K.; Heinmaa, I.; Aav, R. Binding of Heterocycles by Cyclohexanohemicucurbit[8]uril Inclusion Complexes With Heterocycles and Selective Extraction of Sulfur Compounds From Water. *Front. Chem.* **2021**, *9*, 786746. [CrossRef] [PubMed]
45. Sugiura, K.; Ponomarev, G.; Okubo, S.; Tajiri, A.; Sakata, Y. Interactions of Two Porphyrin Rings: Metal-Induced Structural Change of 5,5′-Ethylenebis(Porphyrin). *Bull. Chem. Soc. Jpn.* **1997**, *70*, 1115–1123. [CrossRef]
46. Brynn Hibbert, D.; Thordarson, P. The Death of the Job Plot, Transparency, Open Science and Online Tools, Uncertainty Estimation Methods and Other Developments in Supramolecular Chemistry Data Analysis. *Chem. Commun.* **2016**, *52*, 12792–12805. [CrossRef]
47. Thordarson, P. Determining Association Constants from Titration Experiments in Supramolecular Chemistry. *Chem. Soc. Rev.* **2011**, *40*, 1305–1323. [CrossRef] [PubMed]
48. Liu, P.; Neuhaus, P.; Kondratuk, D.V.; Balaban, T.S.; Anderson, H.L. Cyclodextrin-Templated Porphyrin Nanorings. *Angew. Chem. Int. Ed.* **2014**, *53*, 7770–7773. [CrossRef]
49. Magna, G.; Monti, D.; Di Natale, C.; Paolesse, R.; Stefanelli, M. The Assembly of Porphyrin Systems in Well-Defined Nanostructures: An Update. *Molecules* **2019**, *24*, 4307. [CrossRef]
50. Borovkov, V.V.; Lintuluoto, J.M.; Inoue, Y. Synthesis of Zn-, Mn-, and Fe-Containing Mono- and Heterometallated Ethanediyl-Bridged Porphyrin Dimers. *Helv. Chim. Acta* **1999**, *82*, 919. [CrossRef]
51. Borovkov, V.V.; Fujii, I.; Muranaka, A.; Hembury, G.A.; Tanaka, T.; Ceulemans, A.; Kobayashi, N.; Inoue, Y. Rationalization of Supramolecular Chirality in a Bisporphyrin System. *Angew. Chem. Int. Ed.* **2004**, *43*, 5481–5485. [CrossRef]
52. Fujii, I.; Borovkov, V.V.; Inoue, Y. Crystal Structure of Bis-Zn-Porphyrin. *X-ray Struct. Anal. Online* **2006**, *22*, x77–x78. [CrossRef]
53. Osadchuk, I.; Konrad, N.; Truong, K.-N.; Rissanen, K.; Clot, E.; Aav, R.; Kananovich, D.; Borovkov, V. Supramolecular Chirogenesis in Bis-Porphyrin: Crystallographic Structure and CD Spectra for a Complex with a Chiral Guanidine Derivative. *Symmetry* **2021**, *13*, 275. [CrossRef]
54. Fomitšenko, M.; Peterson, A.; Reile, I.; Cong, H.; Kaabel, S.; Prigorchenko, E.; Järving, I.; Aav, R. A Quantitative Method for Analysis of Mixtures of Homologues and Stereoisomers of Hemicucurbiturils That Allows Us to Follow Their Formation and Stability. *New J. Chem.* **2017**, *41*, 2490–2497. [CrossRef]

Appendix 3

Publication III

Gabriele Magna, Marko Šakarašvili, Manuela Stefanelli, Gabriele Giancane, Simona Bettini, Ludovico Valli, Lukas Ustrnul, Victor Borovkov, Riina Aav, Donato Monti, Corrado Di Natale, Roberto Paolesse. Chiral Recognition by Supramolecular Porphyrin-Hemicucurbit[8]uril-Functionalized Gravimetric Sensors. *ACS Appl Mater Interfaces,* **2023**, *15*, 25, 30674–30683

Reproduced under CC-BY 4.0

ACS APPLIED MATERIALS & INTERFACES

www.acsami.org

Research Article

Chiral Recognition by Supramolecular Porphyrin−Hemicucurbit[8]uril-Functionalized Gravimetric Sensors

Gabriele Magna, Marko Šakarašvili, Manuela Stefanelli, Gabriele Giancane, Simona Bettini, Ludovico Valli, Lukas Ustrnul, Victor Borovkov, Riina Aav, Donato Monti, Corrado Di Natale, and Roberto Paolesse*

Cite This: *ACS Appl. Mater. Interfaces* 2023, 15, 30674−30683

Read Online

ACCESS | Metrics & More | Article Recommendations | Supporting Information

ABSTRACT: Enantiorecognition of a chiral analyte usually requires the ability to respond with high specificity to one of the two enantiomers of a chiral compound. However, in most cases, chiral sensors have chemical sensitivity toward both enantiomers, showing differences only in the intensity of responses. Furthermore, specific chiral receptors are obtained with high synthetic efforts and have limited structural versatility. These facts hinder the implementation of chiral sensors in many potential applications. Here, we utilize the presence of both enantiomers of each receptor to introduce a novel normalization that allows the enantio-recognition of compounds even when single sensors are not specific for one enantiomer of a target analyte. For this purpose, a novel protocol that permits the fabrication of a large set of enantiomeric receptor pairs with low synthetic efforts by combining metalloporphyrins with (*R*,*R*)- and (*S*,*S*)-cyclohexanohemicucurbit[8]uril is developed. The potentialities of this approach are investigated by an array of four pairs of enantiomeric sensors fabricated using quartz microbalances since gravimetric sensors are intrinsically non-selective toward the mechanism of interaction of analytes and receptors. Albeit the weak enantioselectivity of single sensors toward limonene and 1-phenylethylamine, the normalization allows the correct identification of these enantiomers in the vapor phase indifferent to their concentration. Remarkably, the achiral metalloporphyrin choice influences the enantioselective properties, opening the way to easily obtain a large library of chiral receptors that can be implemented in actual sensor arrays. These enantioselective electronic noses and tongues may have a potential striking impact in many medical, agrochemical, and environmental fields.

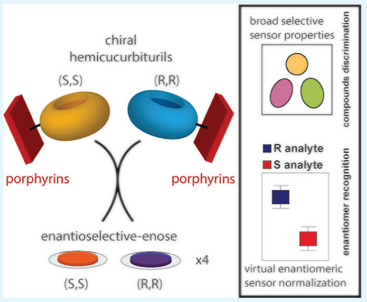

KEYWORDS: *porphyrin, hemicucurbituril, chiral recognition, quartz crystal microbalances, chemical sensors*

Downloaded via 89.235.205.39 on May 19, 2026 at 11:37:03 (UTC).
See https://pubs.acs.org/sharingguidelines for options on how to legitimately share published articles.

1. INTRODUCTION

Molecular systems endowed with chiral receptors are continuously developed, aiming to satisfy the challenging task of chiral recognition.[1−3] Ideally, a single sensor can correctly detect a compound only when it is highly selective versus the target enantiomer, meaning that it must have negligible interactions with any other molecular species. Unfortunately, nearly all the receptors are commonly only partial or broadly selective to a target analyte; therefore, the recognition of target molecular species is unreliable since a single sensor response cannot be univocally correlated to the concentration of just one analyte. This behavior in sensors resembles the properties of olfactory sensory cells observed in mammals, where each receptor is sensitive to a group of volatile compounds rather than a single molecule. Albeit this limitation, olfaction may discriminate many thousands of odors, even for chiral species, relying on the differences between the sensitivity patterns of each receptor. The principle of combinatorial selectivity has been widely exploited in gas sensing to produce artificial olfaction systems,[4] usually named electronic noses (enoses), which achieve chemical specificity, thanks to the high selectivity of global patterns of array responses, overcoming the problem of individual sensor selectivity and facilitating the design of the recognition unit.[5]

In this study, we explore the possibility of utilizing sensing films having weak selectivity for the two enantiomers of compounds into a sensor array to develop an enantioselective enose (e-enose). An e-enose should then include sensors with complementary selectivity and enantio-selectivity patterns to be able to recognize both a single compound from other ones and an enantiomer from its mirrored image, respectively. However, producing a set of chiral receptors with distinct sensing behaviors is difficult and requires a considerable synthetic effort because of the high number of reaction steps,

Received: April 11, 2023
Accepted: June 6, 2023
Published: June 16, 2023

ACS Publications

© 2023 The Authors. Published by American Chemical Society

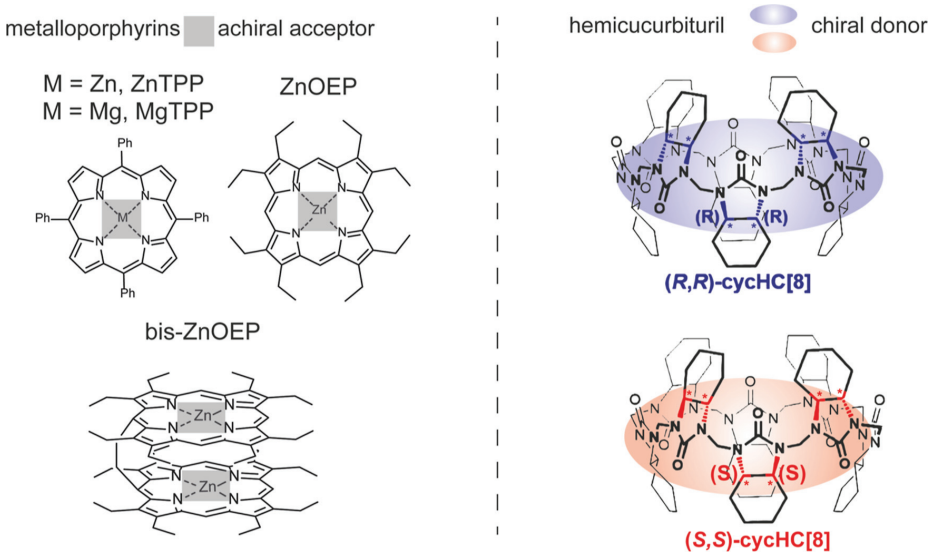

Figure 1. Structures of cycHC[8] enantiomers and metalloporphyrins utilized to produce chiral sensing films.

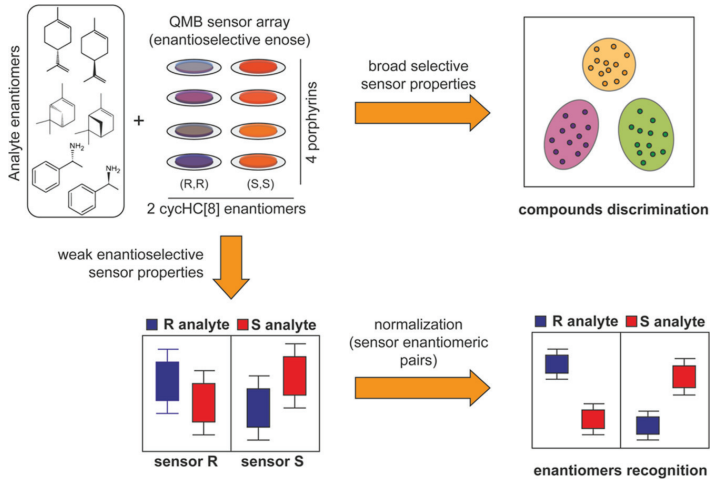

Figure 2. Schematic representation of the proposed enantioselective electronic nose. Different metalloporphyrins allow compound discrimination, whereas chiral induction by hemicucurbituril macrocycles permits recognition of the enantiomers after an ad hoc normalization.

the low yield, and the scarce versatility of chiral receptor structures, hindering the widespread diffusion of these receptors in sensorial platforms.

Here, we explore a novel approach to the development of reliable sensor arrays capable of both molecular discrimination and chiral recognition. The first obstacle related to the preparation of chiral receptors is faced by adopting a supramolecular approach as a facile route for the deposition of chiral films. In this way, we exploited the coordination of achiral metalloporphyrins with two enantiomers of cyclohexanohemicucurbit[8]uril {(*R*,*R*)-and (*S*,*S*)-cycHC-[8]}[6,7] as chiral effectors. Inducing chirality through supramolecular interactions has the great benefit of being less laborious from a synthetic point of view since it is possible to use forming units that are relatively easy to prepare and design according to the application.

In this context, we have combined the binding properties of metalloporphyrins, which have widely been used for the realization of molecular receptors in chemical sensors[8−27] with the facile preparation of enantiomerically pure form of cycHC[8] as chiral macrocyclic effectors.[6,28] Hemicucurbiturils can bind electron-rich species inside[29,30] the cavity and electron-deficient species outside their ring.[31,32] We exploit the latter property to promote the interaction with the metal ions coordinated to several porphyrins to realize chiral hybrid adducts in the solid state. In this way, we have designed solid-state sensors where a chiral block, cycHC, induces chirality in different metalloporphyrins, which in turn act as receptors. The

https://doi.org/10.1021/acsami.3c05177
ACS Appl. Mater. Interfaces 2023, 15, 30674−30683

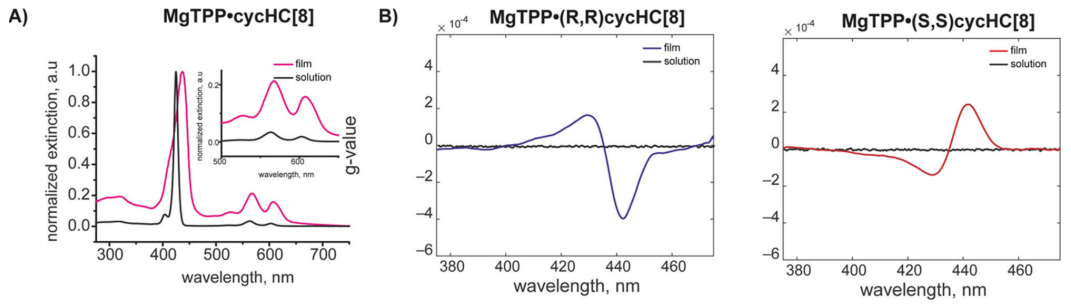

Figure 3. (A) UV−vis spectra of 1:2 mix of chiral cycHC[8] and MgTPP porphyrin in CH_2Cl_2 solution and on spin-coated glass slides. (B) ECD spectra of their enantiomeric adducts on spin-coated glass and solution.

variations in porphyrin structures allow the production of a set of receptors with overlapping and complementary sensitivity patterns versus different volatile organic compound (VOC) classes.

At the same time, mirrored chiral effectors in adducts allow sensors to be selective toward the handedness of analytes; although the selectivity toward the enantiomeric pairs is only partial, even a small difference can be successfully exploited for enantiorecognition, hence mimicking the differential absorption of polarized light utilized in the circular dichroism spectroscopy. This approach is schematically represented in Figures 1 and 2, and it will be detailed in the following Results and Discussion section. Because the achiral porphyrin is a unit responsible for the enantiorecognition properties of films, variations on the substituents and coordinated metal ion of the porphyrin allow to easily produce a large set of chiral sensors, significantly reducing the synthetic effort, with a wide library of metalloporphyrins available.

To the best of our knowledge, this approach has not been reported in the literature yet, and it could represent a breakthrough in the realization of chiral sensor arrays. In this work, we have successfully tested this approach for the chiral recognition of enantiomeric pairs of some model analytes.

2. EXPERIMENTAL DETAILS

2.1. Materials and Methods. Reagents and solvents were purchased from Sigma-Aldrich, Merck, or Carlo Erba and were used as received. Metalloporphyrins and hemicucurbit[8]uril units were prepared following literature procedures.[6,33] (*R*)-(+)-Limonene (97% purity), (*S*)-(−)-limonene (96% purity), (+)-α-pinene (98% purity), (−)-α-pinene (98% purity), (*R*)-(+)-α-methylbenzylamine (98% purity), and (*S*)-(−)-α-methylbenzylamine (98% purity) were commercially available from Sigma-Aldrich. Solvents used for spectroscopic measurements were of spectroscopic grade. UV−vis spectra were measured with a Cary 100 spectrophotometer. CD spectra were obtained on a JASCO J-1500 spectrophotometer, equipped with a thermostated cell holder set at 298 K, and purged with ultrapure nitrogen gas. Linear dichroism contribution (LD) has been found to be <0.0004 DOD units in all of the cases examined.

2.2. Preparation of Solid Films on Glass for Circular Dichroism Studies. Films on glasses were obtained by drop-casting dichloromethane solutions of the adducts. For this purpose, 0.4 mM metalloporphyrins (Figure 1) were dissolved in a 0.2 mM solution of either (*R*,*R*) or (*S*,*S*)-cycHC[8] in CH_2Cl_2. Films on glass were obtained either by drop-casting 50 μL of solutions or by the spin coating technique by repeatedly dropping 10 μL of solution at 1500 rpm.

2.3. Quartz Microbalances. Quartz microbalances (QMBs) are piezogravimetric devices that may act as mass transducers since a load produces a decrease in their resonance frequency linearly correlated to mass increment in the case of small perturbations.[34] The QMBs utilized are AT-cut quartzes oscillating at the first-harmonic frequency of approximately 20 MHz (KVG GmbH). The quartz diameter is 9.0 mm coated by 5.0 mm gold electrodes of diameter on both faces. Such quartzes have a theoretical mass sensitivity of about 7.20 Hz/ng with a minimum reliable frequency measurement of 0.1 Hz.[35]

Sensing films were deposited onto the QMB electrodes by drop-casting the solution in CH_2Cl_2. A 5 μL drop was cast onto the gold electrode waiting for the solvent evaporation. Casting was iterated up to reach at least 15 kHz of material for each side of QMB.

The experimental setup for sensor measurements is depicted in Figure S1. Sensors were allocated in an airtight chamber with a gas inlet and outlet. Each QMB was connected to an electronic oscillator circuit, and in-house designed electronics allowed the measurement of oscillation frequencies of up to 12 piezogravimetric elements. Sensor responses were measured by exposing the systems to different concentrations of saturated vapors of (*R*)- and (*S*)-limonene, (*R*)- and (*S*)-2-phenylethylamine, and (1*R*,5*R*)- and (1*S*,5*S*)-2-pinene enantiomers diluted in a pure nitrogen gas carrier. Saturated vapors were obtained by bubbling pure nitrogen gas in the liquid samples. At 25 °C, the concentrations of saturated vapors of limonene, 2-pinene, and 1-phenylethylamine are 1980,[36] 5822,[37] and 657 ppm,[38] respectively. Flux and vapor dilutions were governed by a system of mass flow controllers (MKS). The total flux at the inlet of the sensor cell was always kept constant at 200 standard cubic centimeters per minute. The temperature of the whole system (liquid sample, gases, and sensors) was always kept at 25 °C, and ambient humidity was maintained at around 10% for the whole experiment.

The sensor array was exposed to each concentration four times, and a random order was used for each sequence replica. Each measurement consisted of a gas exposure (5 min) followed by exposure to the carrier gas (20 min). In the measurement sequence, the enantiomers are alternately delivered at the same concentration to reduce time influence in the responses. Sensor signals were totally reversible.

3. RESULTS AND DISCUSSION

3.1. Spectroscopic Characterization. First, the metalloporphyrin·cycHC adducts have been investigated in solution phase and as solid-state films. The possibility of transferring the chiral information from enantiopure cycHC[*n*] (*n* = 6, 8) to achiral Zn-porphyrin derivatives was previously demonstrated in nonpolar solvents, exploiting the favorable interactions between the electron-deficient porphyrin Zn^{2+} ion and the electron-rich carbonyl oxygen on the outer surface of cycHCs ($Zn^{2+}\cdots O{=}C$).

In the case of ZnTPP·(*R*,*R*)-cycHC[8], crystallographic data showed a complex structure where one molecule of cycHC[8] is bound to two porphyrins, packed in a manner that each

https://doi.org/10.1021/acsami.3c05177
ACS Appl. Mater. Interfaces 2023, 15, 30674−30683

ZnTPP is separated from another porphyrin by cycHC[8]. This creates a chiral environment next to all porphyrins in the crystal.[31]

On the other hand, bis-ZnOEP has demonstrated outstanding chirality sensing properties for amines and alcohols due to the induction of characteristic electronic circular dichroism (ECD) signals.[39] Chirality induction in bis-ZnOEP was also observed by complexation with cycHC[*n*]s.[32] Based on stoichiometry in the crystal structures obtained in the case of ZnTPP, we combined cycHC[8] enantiomers with different metalloporphyrin derivatives (Figure 1) in a 1:2 molar ratio to produce chiral films where the planar configuration of porphyrin derivatives combined with the oxophilicity of Mg and Zn metal ions promote coordination and, consequently, chiral induction.

Chiral films were obtained via deposition of the complexes' solution onto glass slides using drop-casting or spin coating techniques without denoting any relevant difference in optical and chiroptical properties depending on the deposition technique employed. Thus, spin-coated films have been utilized for characterization since the films appeared to be more uniform, avoiding the presence of clusters or coffee-rings phenomena due to solvent volatility.

UV−vis spectra show broadening and bathochromic shift (see Table S1) of the Soret band of all metalloporphyrins•cycHC[8] films as compared with the corresponding spectra in CH_2Cl_2 solution (Figure 3A). Q bands were also red-shifted, suggesting the formation of various porphyrin aggregates in the films as a natural consequence of solvent evaporation. Please note that in the case of aggregation, as in films, the B-band of porphyrins (400−450 nm) decreases in intensity much more than the Q-bands (500−650 nm). Since absorbances are normalized between 0 and 1, the lowering of the main band produces an apparent increase of other bands (as appearing in the inset in Figures 3A and S2).

Concerning the CD characterization, in CH_2Cl_2, the solutions of adducts utilized to prepare sensing layers do not show any ECD features in the visible range. For example, in solution, we can observe ECD signal for the complexes of metalloporphyrin and cycHC[8] with a high excess of cycHC[8], which is necessary due to the micromolar concentration limitation of porphyrins in these measurements.[31] In our case, the porphyrin/cycHC ratio is 2:1. Conversely, in the case of solid films, this limited amount of HC is sufficient to induce chirality once the solvent evaporates. CD spectroscopy discloses the emergence of dichroic bands in all films that contain hemicucurbituril-porphyrin adducts, showing Cotton effects of the opposite sign in the case of antipodal cycHC[8] (Figures 3B and S2). Since HCs are not absorptive in the visible range, the appearance of CD signal in this range is only due to the chirality induction in metalloporphyrins. All UV−vis and ECD spectral features for the eight systems investigated, both in solution and solid-state, are summarized in Table S1. From a chemical sensor point of view, producing chiral films without a high excess of the hemicucurbituril inducers enables the possibility of simply modulating the chemical sensitivity by structural changes only in metalloporphyrins, which possess a high synthetic versatility. As previously mentioned, the possibility of effortlessly producing sensors with different sensitivity patterns is the fulcrum for recognizing different compounds or mixtures in typical enoses. Furthermore, we observed that the CD features manifest on different quartz substrates and deposition methods, proving this approach to be much more robust than films produced with chiral porphyrins, where, for example, solvent, substrate, and deposition techniques strongly influence the possibility of having supramolecular chiral films.[40]

In detail, the presence of either (*S*,*S*) or (*R*,*R*)-cycHC[8] produces the (+/−) or (−/+) bisignate ECD features in the corresponding porphyrin absorption region (Figure 3B). The ECD patterns of films made by two enantiomers may not be perfectly mirrored due to local inhomogeneities that may alter the spectral profiles. Indeed, the ECD signals in anisotropic solid-state samples (including thin films) depend not only upon the differential absorbance of circularly polarized light but also on other film local properties, such as the presence of LD or birefringence contributions. Thus, distinct ECD profiles may be obtained after the formation of films by spin coating or drop-casting due to metastable or kinetically entrapped species after solvent evaporation.[41] Last, in the case of bis-ZnOEP adducts, the ECD pattern is more complex, likely due to the presence of anti-syn conformations of bis-porphyrins in equilibrium with each other and oppositely oriented inter- and intramolecular exciton couplings of corresponding porphyrin electronic transitions in the solid state.[33] Also, in the UV−vis spectra of this adduct film, the broadening of the Soret band derives from the superimposition of the absorptions of both conformations, which are difficult to distinguish due to the close energy position of the corresponding electronic transitions. Perhaps, it can only be seen as some shoulders (if any).

3.2. Sensor Measurements. Subsequently, the films were deposited onto QMBs, and the sensors were exposed to three pairs of enantiomerically pure vapors, as reported in Figure S1. Two achiral sensors based on ZnTPP and bis-ZnOEP films were included as references in the sensor array. VOC concentrations tested are listed in Table S2. Remarkably, use of gravimetric sensors permits estimating and dosing the sensing materials deposited onto the surface, guaranteeing a high reproducibility of the sensors. As reported below, the possibility of obtaining comparable (*R*,*R*)- and (*S*,*S*)-sensor pairs will be crucial for data normalization. Deposition details are reported in Table S3. We selected two terpenes and one chiral amine as representative examples of chiral analytes, which are commercially available in both enantiomeric forms. Limonene has been a very useful model compound in our previous tests, and thanks to its linear structure, it can easily diffuse inside the porphyrin aggregates.[18] Conversely, 2-pinene has a reduced capacity of π-interactions due to its single double bond, and it is bulkier than limonene due to the dimethylmethylene bridge, making the adsorption of this compound to be confined only to the superficial film sites.[42,43] Finally, the planar aromatic 1-phenylethylamine combines $\pi-\pi$ interactions with additional NH_2-coordination to the metal center that may foster the absorption into the film. Figures S3−S5 report the characteristic curves of the sensors to limonene, 1-phenylethylamine, and 2-pinene, respectively. In the case of limonene, almost all chiral sensors show a significantly different response to the two enantiomers. Interestingly, all Zn-porphyrins•(*R*,*R*)-cycHC[8] films show a preference for (*R*)-limonene, whereas MgTPP•(*R*,*R*)-cycHC[8] has an opposite behavior, likely due to the difference in the coordination ability of Zn- and Mg-porphyrins. Specular effects were observed in the case of films based on the (*S*,*S*)-cycHC[8] counterpart. At the same time, as expected, achiral films, namely ZnTPP and bis-ZnOEP, do not display any statistically relevant enantior-

https://doi.org/10.1021/acsami.3c05177
ACS Appl. Mater. Interfaces 2023, 15, 30674−30683

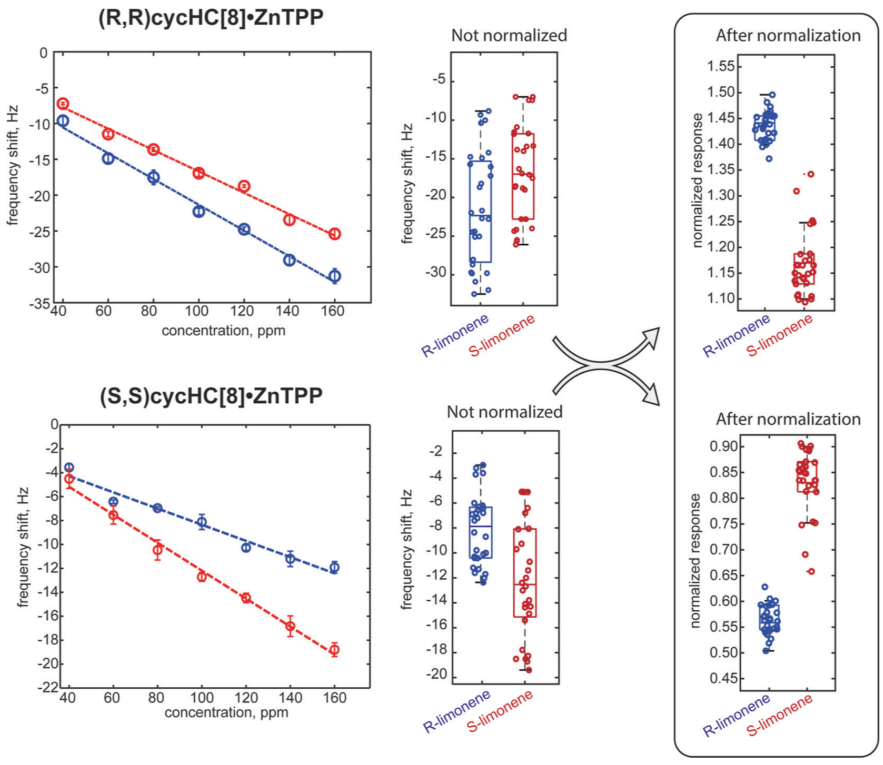

Figure 4. Examples of responses and data distributions of compounds tested with and without normalization involving enantiomeric pair of sensors. Responses of cycHC[8]·ZnTPP sensors toward limonene.

ecognition ability. Albeit the overall sensing mechanism is complicated and will be deeply investigated/modeled in future works, this outcome empirically suggests that the chiral recognition mechanism is based on the interaction of a chiral guest with porphyrins, while the role of cycHC is just to induce chirality in the macrocycle. The lack of enantioselectivity of cycHC toward tested chiral compounds enforces this hypothesis (see Supporting Information, Figures S6−S8). Moreover, pure hemicucurbituril films showed a strong water sensitivity, which notably reduced the enantioselectivity in comparison to that observed in all films produced with adducts of porphyrins−cycHC (see Supporting Information). In the case of 2-pinene (Figure S9), all sensors show a poor response without showing enantioselectivity. This outcome agrees with the previous experiments where the diffusion of analytes into the film emerged as a guiding condition for having enantioselectivity with porphyrins on QMBs.[23] Thus, pinene enantiomers are essentially adsorbed into the superficial portion of the sensing layers, as highlighted by the low sensitivity of all films to these vapors. From the characteristic curves of 1-phenylethylamine, the differences between the responses to the (*R*,*R*)- and (*S*,*S*)-enantiomers appear to be evident only in the sensors based on ZnOEP and bis-ZnOEP, and this separation increases at higher concentrations. As an example, Figures 4 and 5 report the responses of two enantiomeric pairs of sensors based on ZnTPP and ZnOEP toward limonene and 1-phenylethylamine enantiomers. The responses vs concentrations curves evidence a separation between the responses of the two enantiomers regression curves (left plot in each panel). This means that if we consider a fixed concentration, the samples of two enantiomers produce different sensor responses. However, when changes in the sample concentration are considered, it is evident that the same value of sensor response can be produced by a higher concentration of the analyte to which the sensor is less sensitive or by a lower concentration of the analyte to which the sensor is most sensitive. Thus, the variation in sample concentration produces an overlap between the responses of the same sensor to both enantiomers. As a consequence, when we consider the distributions of sensor responses to both enantiomers of the analyte, the boxplots evidence that the mean values of distributions are different, but the dispersion of data due to the concentration makes recognizing one of the two enantiomers impossible. This is visualized in the boxplots reported in Figures 4, 5, and S10.

It is worthy of note that concentration is often ignored or overlooked in recognition tasks. However, it has a central role since a relatively wide range may considerably hinder the possibility of distinguishing two different analytes. To overcome this fundamental problem in enantiomer recognition, we propose a novel normalization protocol to assess the chiral nature of analytes, disregarding their concentration even in the case of broad chemical selectivity and low enantioselectivity.

3.3. Virtual Racemic Sensor Normalization. In the case of mass sensors such as QMBs, the response arises from both

https://doi.org/10.1021/acsami.3c05177
ACS Appl. Mater. Interfaces 2023, 15, 30674−30683

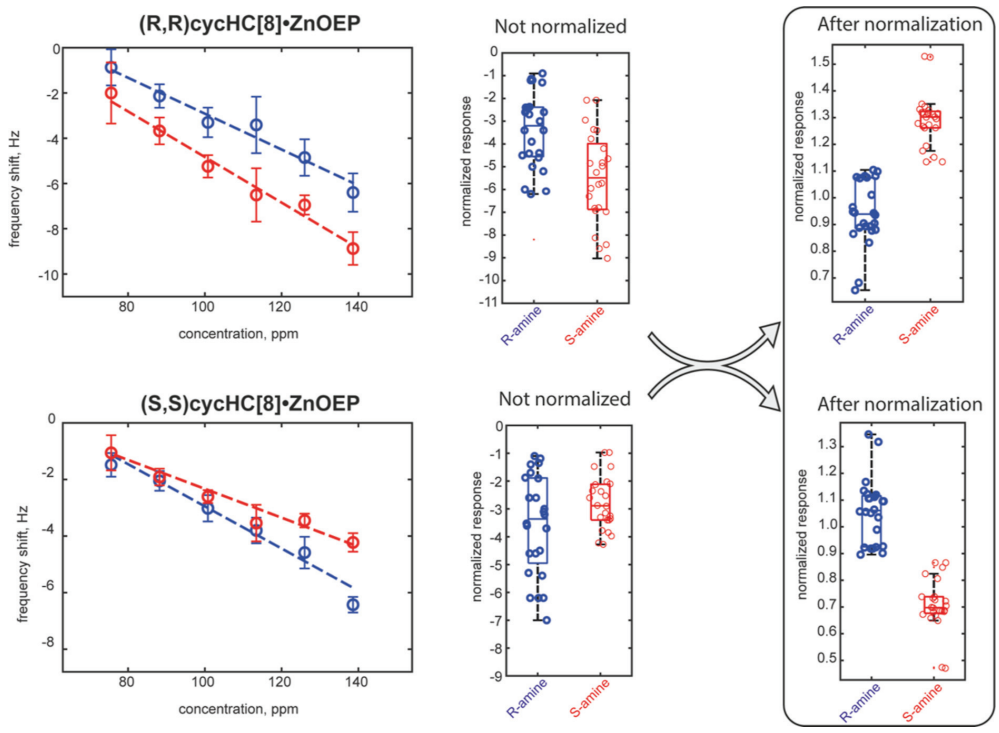

Figure 5. Examples of responses and data distributions of compounds tested with and without normalization involving enantiomeric pair of sensors. Responses of cycHC[8]·ZnOEP sensors toward 1-phenylethylamine.

enantioselective and non-enantioselective interactions. At the same time, each pair of receptor enantiomers is supposed to respond similarly only to the non-enantioselective interactions.

A common technique to recognize two enantiomers of the same compound involves measuring the circular dichroism. Indeed, an active optical enantiomer absorbs slightly different clockwise and anticlockwise circularly polarized light and vice versa for the other enantiomer. The difference in absorbance due to the chirality of enantiomers is even three-four orders of magnitude lower than the total absorbance of the medium, and ad hoc measure units, such as theta, are utilized to indicate the chiral nature of compounds. The ellipticity, termed θ, is calculated as

$$\tan(\theta) = (E_R - E_L)/(E_R + E_L) \quad (1)$$

where E_R and E_L are the magnitudes of the electric field vectors of the R- and L-circularly polarized light. Similarly, here we proposed a normalization based on the interaction of an enantiomer of a chiral analyte with the two enantiomers of a receptor rather than with the two polarizations of light. Indeed, the two enantiomers of a receptor molecule may reveal the chiral nature of an analyte if they have specular patterns of selectivity toward it. Mathematically, the proposed normalization rejects this common component of the responses in the sensor enantiomer pairs since they are likely due to non-enantioselective contribution.

Looking at the denominator of eq 1, we notice the sum of ER and EL. Here we propose, to the best of our knowledge for the first time, a normalization using as the denominator the mean of adduct enantiomer responses, $(R_{RR} + R_{SS})/2$, which we name as virtual racemic sensor reference. As racemic mixtures are 50:50 mixtures of both enantiomers, here we consider the racemic sensor references as a virtual sensor whose response is a 50:50 mixture of the magnitude of responses provided by the two sensor enantiomers. For each of the four metalloporphyrins, a virtual racemic sensor, $\overline{R}_{rac}$, is created by averaging the response of (*R*,*R*)-cycHC[8] and (*S*,*S*)-cycHC[8] based films, R_R and R_S, respectively.

$$\overline{R}_{rac} = (R_R + R_S)/2 \quad (2)$$

Normalized responses R_{Rn} and R_{Sn} can be calculated as follows

$$R_{Rn} = R_R/\overline{R}_{rac} \quad (3)$$

$$R_{Sn} = R_S/\overline{R}_{rac} \quad (4)$$

It is worth noting that quantification secured by QMB allows almost completely compensating for the differences in the amount of sensing material spotted for both enantiomers of each receptor, ensuring almost perfect virtual racemic sensors, which are able to compensate for the dispersion of samples due to concentration changes almost entirely. The Supporting Information reports full details and mathematical demonstration of the normalization proposed here (Paragraph 4 in the Supporting Information).

Figures 4 and 5 show two examples of the data distributions obtained with the proposed normalization, whereas all normalized data are shown in Figure S13. From the above-

https://doi.org/10.1021/acsami.3c05177
ACS Appl. Mater. Interfaces 2023, 15, 30674−30683

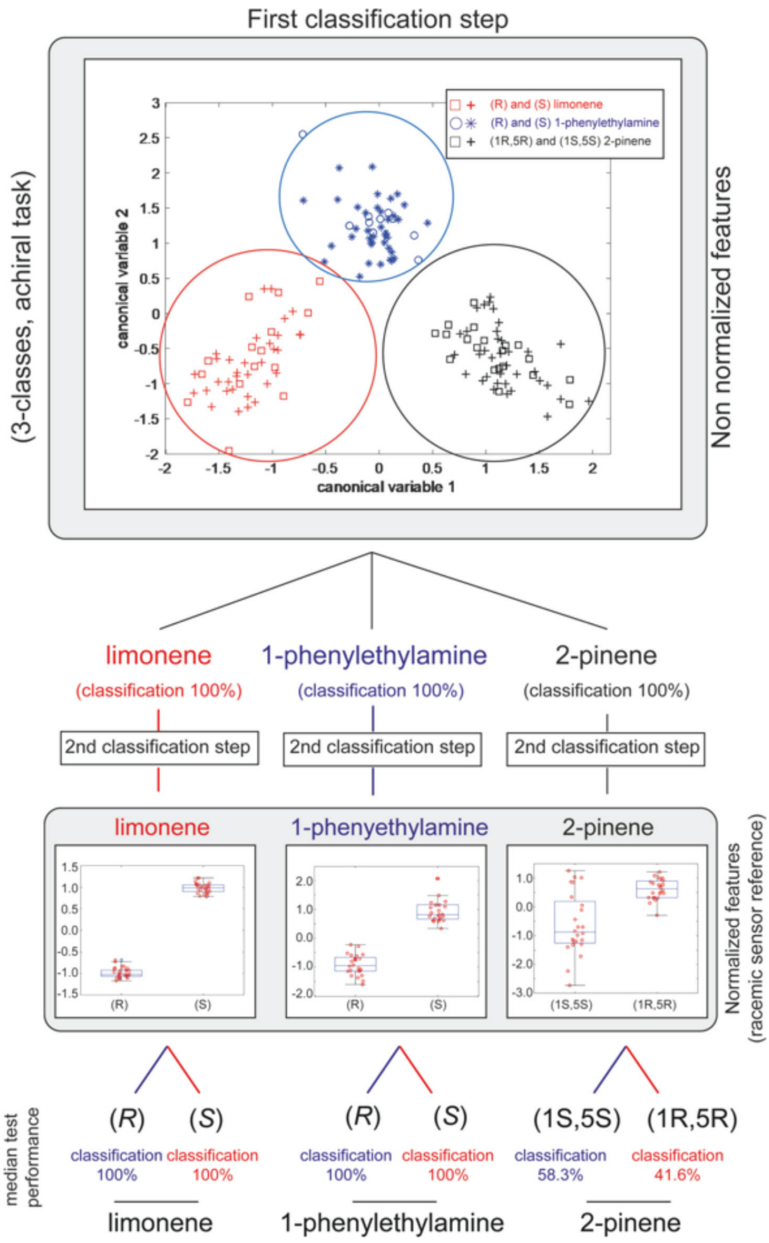

Figure 6. Classification protocol utilizes two steps to recognize the chemical and chiral nature of volatile compounds. The first model utilizes all features without normalization as in typical enoses. The second step utilizes only normalized features by using the virtual racemic reference introduced here. Median classification accuracies over 100 runs are reported in the figure. Overall classification results are reported in the Supporting Information. During each run, a Matlab algorithm generated new training and test datasets. Training and testing sets do not share samples with the same concentration.

mentioned figures, it is possible to observe that a clear separation for limonene enantiomers occurs in all normalized sensors, whereas ZnOEP derivatives almost perfectly recognize amine enantiomers. Remarkably, the expected specularity between the enantiomeric receptors is enhanced after the normalization process since it may compensate for fluctuations from non-chiral sources, such as ancillary variation in concentrations or environmental conditions that may occur in single samples. This first outcome demonstrates the possibility of correctly estimating even minor differences in

https://doi.org/10.1021/acsami.3c05177
ACS Appl. Mater. Interfaces 2023, 15, 30674−30683

sensing responses in the films based on antipodal receptors to improve the recognition of enantiomers. Calculations of normalization effects and benefits on data coming from enantiomeric pair of sensors is reported in paragraph 4 of the Supporting Information, where theoretical and experimental outcomes have been compared.

It is worth noting that we also tested a general normalization method based on one of the two achiral sensors in the array as a reference to normalize the chiral sensor response $\overline{R}$ with respect to concentration as follows

$$\overline{R} = \frac{R}{R_{ref}} \tag{5}$$

where R and R_{ref} are the responses to a sample of chiral and achiral sensors, respectively. Indeed, the use of ZnTPP and bis-ZnOEP sensors as references improves the separation between enantiomer distributions (see Figures S14 and S15); the distributions still present a partial overlapping. The main issue with this generic normalization is the sensitivity subsisting between sensors and the reference, which only partially compensates for the concentration trend (e.g., correlations are reported in Table S4).

3.4. Sample Classification. To combine classic and novel multivariate gas recognition approaches, we performed classification by utilizing a two-step protocol (as reported in Figure 6). Initially, compounds were considered disregarding their chirality, obtaining a three-class task to recognize limonene, 1-phenylethylamine, and 2-pinene. Here, the classification is made by using the non-normalized features of the ten sensors. The first step plot in Figure 6 reports the projection of sensor data in the plane of the first two canonical variables obtained by utilizing non-normalized data. Notably, the three compounds (limonene, 2-pinene, and 1-phenylethylamine) are well separated. However, any separation among enantiomers does not appear evident. In other words, canonical variables of non-normalized responses well represent the distribution and separation of data without considering the chiral identity of compounds.

Once a sample is assigned to a specific class, the second model further assigns it to one of the two enantiomeric classes by using, in this case, the normalized responses of chiral sensors. Panels in Figure 6 show how the distributions of enantiomers can be separated when normalized data are utilized in the case of limonene and 1-phenylethylamine.

In Figure 6, the median classification rates of different cases and steps are reported. Performance was evaluated considering 100 randomly generated training and test subsets from the overall data. The performance of the proposed approach was tested in a challenging scenario where concentrations included in the test were not included in the training and vice versa. In this case, the concentrations appearing in the test and training dataset were randomly selected before each of the 100 runs.

Summaries of the concentrations selected and the number of samples are reported in Table S5. The linear discrimination analysis model was built on training data and applied to test ones. The accuracies for the two steps and different scenarios are reported in Figure S16. Results show that the system acts as a "classic" enose, recognizing the three classes of compounds with a perfect score in almost all cases and as an enantioselective array since it can recognize the chiral identity of limonene and 1-phenylethylamine with high accuracy, disregarding the concentrations. Notably, the normalization allows an accurate classification even if the test is considered to be non-measurable or has out-of-range concentrations with respect to the training. Indeed, in the limonene and amines cases, the model sporadically fails to predict one sample during the test phase only when training and test include completely different ranges of concentrations (see the Supporting Information for concentrations considered).

A last consideration should concern the limit of detection of an enantiomer. In principle, once a compound is correctly recognized, this approach requires that only one of the two sensors detects an enantiomer to assess its chiral nature. In the case of sensor arrays and pure known compounds, the enantiodiscrimination limit can then be estimated considering the lowest LOD for the target compound among the sensors in the array. It is worth noting that this estimation of the detection limit assumes that the sensor array correctly recognizes the target compound among the others in the model and that the enantiomers are actually separated after normalization with the virtual racemic sensor. In this context, the proposed approach potentially has LODs in the order of ten ppm for limonene and phenylethylamine enantiomers.

4. CONCLUSIONS

In analogy with biological systems, the results showed that using sensor arrays with the proper bivariate and multivariate analysis techniques improved the classification performances in terms of enantioselectivity, allowing the recognition of samples of limonene and 1-phenylethylamine without using highly selective sensors. The benefits are even more evident if we consider the possibility of easily obtaining films based on the receptors by mixing chiral hemicucurbituril and metalloporphyrin components. At the same time, this procedure allows tuning the chemical sensitivity by changing the porphyrin scaffold. Finally, QMB permits estimating the material cast on electrodes, validating the concept of a virtual racemic reference. These results are surely promising to extend the concept and application of electronic noses (and tongues) to enantiomer analytes, whose recognition is of great importance in medical, agrochemical, and environmental applications.

■ ASSOCIATED CONTENT

Supporting Information

The Supporting Information is available free of charge at https://pubs.acs.org/doi/10.1021/acsami.3c05177.

Additional experimental details, materials characterization, methods, pictures of experimental setup, QMB measurements, and data analysis (PDF)

■ AUTHOR INFORMATION

Corresponding Author

Roberto Paolesse − *Department of Chemical Science and Technologies, University of Rome Tor Vergata, 00133 Rome, Italy*; orcid.org/0000-0002-2380-1404; Email: roberto.paolesse@uniroma2.it

Authors

Gabriele Magna − *Department of Chemical Science and Technologies, University of Rome Tor Vergata, 00133 Rome, Italy*

Marko Šakarašvili − *Department of Chemistry and Biotechnology, School of Science, Tallinn University of Technology, 12618 Tallinn, Harju Maakon, Estonia*

Manuela Stefanelli − *Department of Chemical Science and Technologies, University of Rome Tor Vergata, 00133 Rome, Italy;* orcid.org/0000-0001-8563-8043
Gabriele Giancane − *Department of Cultural Heritage, University of Salento, I-73100 Lecce, Italy;* orcid.org/0000-0001-5089-5429
Simona Bettini − *Department of Biological and Environmental Sciences and Technologies, DISTEBA, University of Salento, I-73100 Lecce, Italy;* orcid.org/0000-0002-5506-5413
Ludovico Valli − *Department of Biological and Environmental Sciences and Technologies, DISTEBA, University of Salento, I-73100 Lecce, Italy;* orcid.org/0000-0002-6943-8647
Lukas Ustrnul − *Department of Chemistry and Biotechnology, School of Science, Tallinn University of Technology, 12618 Tallinn, Harju Maakon, Estonia;* orcid.org/0000-0003-4170-2132
Victor Borovkov − *Department of Chemistry and Biotechnology, School of Science, Tallinn University of Technology, 12618 Tallinn, Harju Maakon, Estonia;* orcid.org/0000-0001-7898-0457
Riina Aav − *Department of Chemistry and Biotechnology, School of Science, Tallinn University of Technology, 12618 Tallinn, Harju Maakon, Estonia;* orcid.org/0000-0001-6571-7596
Donato Monti − *Department of Chemistry, Sapienza University of Rome, I-00185 Rome, Italy*
Corrado Di Natale − *Department of Electronic Engineering, University of Rome Tor Vergata, 00133 Rome, Italy;* orcid.org/0000-0002-0543-4348

Complete contact information is available at: https://pubs.acs.org/10.1021/acsami.3c05177

Author Contributions

All authors have given approval to the final version of the manuscript.

Notes

The authors declare no competing financial interest.

■ ACKNOWLEDGMENTS

Financial support from EU (Horizon2020 FET-OPEN project 828779 INITIO) and Estonian Research Council grant PRG399 is gratefully acknowledged.

■ ABBREVIATIONS

ZnOEP, zinc octaethylporphyrin
ZnTPP, zinc tetraphenylporphyrin
MgTPP, magnesium tetraphenylporphyrin
cycHC[8], cyclohexanohemicucurbit[8]uril
UV−vis, ultraviolet−visible spectroscopy
ECD, electronic circular dichroism
QMB, quartz microbalance

■ REFERENCES

(1) Shen, J.; Okamoto, Y. Efficient Separation of Enantiomers Using Stereoregular Chiral Polymers. *Chem. Rev.* **2016**, *116*, 1094−1138.
(2) Chen, L. J.; Yang, H. B.; Shionoya, M. Chiral Metallosupramolecular Architectures. *Chem. Soc. Rev.* **2017**, *46*, 2555−2576.
(3) Han, X.; Yuan, C.; Hou, B.; Liu, L.; Li, H.; Liu, Y.; Cui, Y. Chiral Covalent Organic Frameworks: Design, Synthesis and Property. *Chem. Soc. Rev.* **2020**, *49*, 6248−6272.
(4) Manzini, I.; Schild, D.; Di Natale, C. Principles of Odor Coding in Vertebrates and Artificial Chemosensory Systems. *Physiol. Rev.* **2022**, *102*, 61−154.
(5) Röck, F.; Barsan, N.; Weimar, U. Electronic Nose: Current Status and Future Trends. *Chem. Rev.* **2008**, *108*, 705−725.
(6) Prigorchenko, E.; Öeren, M.; Kaabel, S.; Fomitšenko, M.; Reile, I.; Järving, I.; Tamm, T.; Topić, F.; Rissanen, K.; Aav, R. Template-Controlled Synthesis of Chiral Cyclohexylhemicucurbit[8]Uril. *Chem. Commun.* **2015**, *51*, 10921−10924.
(7) Kaabel, S.; Stein, R. S.; Fomitšenko, M.; Järving, I.; Friščić, T.; Aav, R. Size-Control by Anion Templating in Mechanochemical Synthesis of Hemicucurbiturils in the Solid State. *Angew. Chem., Int. Ed.* **2019**, *58*, 6230.
(8) Ishihara, S.; Labuta, J.; van Rossom, W.; Ishikawa, D.; Minami, K.; Hill, J. P.; Ariga, K. Porphyrin-Based Sensor Nanoarchitectonics in Diverse Physical Detection Modes. *Phys. Chem. Chem. Phys.* **2014**, *16*, 9713−9746.
(9) Paolesse, R.; Nardis, S.; Monti, D.; Stefanelli, M.; Di Natale, C. Porphyrinoids for Chemical Sensor Applications. *Chem. Rev.* **2017**, *117*, 2517−2583.
(10) Qi, Z. L.; Cheng, Y. H.; Xu, Z.; Chen, M. L. Recent Advances in Porphyrin-Based Materials for Metal Ions Detection. *Int. J. Mol. Sci.* **2020**, *21*, 5839.
(11) Magna, G.; Nardis, S.; Stefanelli, M.; Monti, D.; Di Natale, C.; Paolesse, R. The Strength in Numbers! Porphyrin Hybrid Nanostructured Materials for Chemical Sensing. *Dalton Trans.* **2021**, *50*, 5724−5731.
(12) Magna, G.; Mandoj, F.; Stefanelli, M.; Pomarico, G.; Monti, D.; Di Natale, C.; Paolesse, R.; Nardis, S. Recent Advances in Chemical Sensors Using Porphyrin-Carbon Nanostructure Hybrid Materials. *Nanomaterials* **2021**, *11*, 997.
(13) Giancane, G.; Valli, L. State of Art in Porphyrin Langmuir-Blodgett Films as Chemical Sensors. *Adv. Colloid Interface Sci.* **2012**, *171−172*, 17−35.
(14) Colombelli, A.; Manera, M. G.; Borovkov, V.; Giancane, G.; Valli, L.; Rella, R. Enhanced sensing properties of cobalt bis-porphyrin derivative thin films by a magneto-plasmonic-opto-chemical sensor. *Sens. Actuators, B* **2017**, *246*, 1039−1048.
(15) Guillén, M. G.; Gámez, F.; Roales, J.; Lopes-Costa, T.; Pinto, S. M. A.; Calvete, M. J. F.; Pereira, M. M.; Pedrosa, J. M. Molecular-Based Selection of Porphyrins Towards the Sensing of Explosives in the Gas Phase. *Sens. Actuators, B* **2018**, *260*, 116−124.
(16) Capan, I.; Tarimci, Ç.; Capan, R. Fabrication of Langmuir−Blodgett Thin Films of Porphyrins and Investigation on Their Gas Sensing Properties. *Sens. Actuators, B* **2010**, *144*, 126−130.
(17) Osica, I.; Imamura, G.; Shiba, K.; Ji, Q.; Shrestha, L. K.; Hill, J. P.; Kurzydłowski, K. J.; Yoshikawa, G.; Ariga, K.; Ariga, K. Highly Networked Capsular Silica-Porphyrin Hybrid Nanostructures as Efficient Materials for Acetone Vapor Sensing. *ACS Appl. Mater. Interfaces* **2017**, *9*, 9945−9954.
(18) Lee, J. S.; Jeong, D. W.; Byun, Y. T. Porphyrin Nanofiber/Single-Walled Carbon Nanotube Nanocomposite-Based Sensors for Monitoring Hydrogen Peroxide Vapor. *Sens. Actuators, B* **2020**, *306*, 127518.
(19) Nardis, S.; Monti, D.; Natale, C. D.; D'Amico, A.; Siciliano, P.; Forleo, A.; Epifani, M.; Taurino, A.; Rella, R.; Paolesse, R. Preparation and Characterization of Cobalt Porphyrin Modified Tin Dioxide Films for Sensor Applications. *Sens. Actuators, B* **2004**, *103*, 339−343.
(20) Xu, H.; Cao, K. D.; Ding, H. B.; Zhong, Q. F.; Gu, H. C.; Xie, Z. Y.; Zhao, Y. J.; Gu, Z. Z. Spherical Porphyrin Sensor Array Based on Encoded Colloidal Crystal Beads for VOC Vapor Detection. *ACS Appl. Mater. Interfaces* **2012**, *4*, 6752−6757.
(21) Avossa, J.; Paolesse, R.; Di Natale, C.; Zampetti, E.; Bertoni, G.; De Cesare, F.; Scarascia-Mugnozza, G.; Macagnano, A. Electrospinning of Polystyrene/Polyhydroxybutyrate Nanofibers Doped with Porphyrin and Graphene for Chemiresistor Gas Sensors. *Nanomaterials* **2019**, *9*, 280.
(22) Castillero, P.; Roales, J.; Lopes-Costa, T.; Sánchez-Valencia, J. R.; Barranco, A.; González-Elipe, A. R.; Pedrosa, J. M. Optical Gas

Sensing of Ammonia and Amines Based on Protonated Porphyrin/TiO_2 Composite Thin Films. *Sensors* **2016**, *17*, 24.
(23) Stefanelli, M.; Magna, G.; Zurlo, F.; Caso, F. M.; Di Bartolomeo, E.; Antonaroli, S.; Venanzi, M.; Paolesse, R.; Di Natale, C.; Monti, D. Chiral Selectivity of Porphyrin−ZnO Nanoparticle Conjugates. *ACS Appl. Mater. Interfaces* **2019**, *11*, 12077−12087.
(24) Esteves, C. H. A.; Iglesias, B. A.; Li, R. W. C.; Ogawa, T.; Araki, K.; Gruber, J. New Composite Porphyrin-Conductive Polymer Gas Sensors for Application in Electronic Noses. *Sens. Actuators, B* **2014**, *193*, 136−141.
(25) Leray, I.; Vernières, M. C.; Bied-Charreton, C. Porphyrins as Probe Molecules in the Detection of Gaseous Pollutants: Detection of Benzene Using Cationic Porphyrins in Polymer Films. *Sens. Actuators, B* **1999**, *54*, 243−251.
(26) Lin, H.; Cheng, X.; Yin, M. J.; Bao, Z.; Wei, X.; Gu, B. Flexible Porphyrin Doped Polymer Optical Fibers for Rapid and Remote Detection of Trace DNT Vapor. *Analyst* **2020**, *145*, 5307−5313.
(27) Yuvaraja, S.; Surya, S. G.; Chernikova, V.; Vijjapu, M. T.; Shekhah, O.; Bhatt, P. M.; Chandra, S.; Eddaoudi, M.; Salama, K. N. Realization of an Ultrasensitive and Highly Selective OFET NO_2 Sensor: the Synergistic Combination of PDVT-10 Polymer and Porphyrin−MOF. *ACS Appl. Mater. Interfaces* **2020**, *12*, 18748−18760.
(28) Aav, R.; Shmatova, E.; Reile, I.; Borissova, M.; Topić, F.; Rissanen, K. New Chiral Cyclohexylhemicucurbit[6]uril. *Org. Lett.* **2013**, *15*, 3786−3789.
(29) Kaabel, S.; Adamson, J.; Topić, F.; Kiesilä, A.; Kalenius, E.; Öeren, M.; Reimund, M.; Prigorchenko, E.; Lõokene, A.; Reich, H. J.; Rissanen, K.; Aav, R. Chiral Hemicucurbit[8]Uril as an Anion Receptor: Selectivity to Size, Shape and Charge Distribution. *Chem. Sci.* **2017**, *8*, 2184−2190.
(30) Shalima, T.; Mishra, K. A.; Kaabel, S.; Ustrnul, L.; Bartkova, S.; Tõnsuaadu, K.; Heinmaa, I.; Aav, R. Cyclohexanohemicucurbit[8]uril Inclusion Complexes With Heterocycles and Selective Extraction of Sulfur Compounds From Water. *Front. Chem.* **2021**, *9*, 786746.
(31) Ustrnul, L.; Kaabel, S.; Burankova, T.; Martõnova, J.; Adamson, J.; Konrad, N.; Burk, P.; Borovkov, V.; Aav, R. Supramolecular Chirogenesis in Zinc Porphyrins by Enantiopure Hemicucurbit[N]-Urils (n = 6, 8). *Chem. Commun.* **2019**, *55*, 14434−14437.
(32) Šakarašvili, M.; Ustrnul, L.; Suut, E.; Nallaparaju, J. V.; Mishra, K. A.; Konrad, N.; Adamson, J.; Borovkov, V.; Aav, R. Self-Assembly of Chiral Cyclohexanohemicucurbit[n]urils with Bis(Zn Porphyrin): Size, Shape, and Time-Dependent Binding. *Molecules* **2022**, *27*, 937.
(33) Borovkov, V. V.; Lintuluoto, J. M.; Inoue, Y. Synthesis of Zn-Mn-and Fe-Containing Mono- and Heterometallated Ethanediyl-Bridged Porphyrin Dimers. *Helv. Chim. Acta* **1999**, *82*, 919−934.
(34) Ballantine, D. S.; White, R. M.; Martin, S. J.; Ricco, A. J.; Zellers, E. T.; Frye, G. C.; Wohl-tjen, H. *Acoustic Wave Sensors: Theory, Design and Physico-Chemical Applications*; Academic Press: San Diego, 1996.
(35) Magna, G.; Belugina, R.; Mandoj, F.; Catini, A.; Legin, A. V.; Paolesse, R.; Di Natale, C. Experimental Determination of the Mass Sensitivity of Quartz Microbalances Coated by an Optical Dye. *Sens. Actuators, B* **2020**, *320*, 128373.
(36) Espinosa Díaz, M. A.; Guetachew, T.; Landy, P.; Jose, J.; Voilley, A. Experimental and Estimated Saturated Vapour Pressures of Aroma Compounds. *Fluid Phase Equilib.* **1999**, *157*, 257−270.
(37) Hawkins, J. E.; Armstrong, G. T. Physical and Thermodynamic Properties of Terpenes.[1] III. The Vapor Pressures of α-Pinene and β-Pinene[2]. *J. Am. Chem. Soc.* **1954**, *76*, 3756−3758.
(38) Available online: https://www.sigmaaldrich.com/IT/it/product/aldrich/726583 (accessed June 21, 2022).
(39) Borovkov, V. V.; Hembury, G. A.; Inoue, Y. Origin, Control, and Application of Supramolecular Chirogenesis in Bisporphyrin-Based Systems. *Acc. Chem. Res.* **2004**, *35*, 449−459.
(40) Magna, G.; Traini, T.; Naitana, M. L.; Bussetti, G.; Domenici, F.; Paradossi, G.; Venanzi, M.; Di Natale, C.; Paolesse, R.; Monti, D.; Stefanelli, M. Seeding Chiral Ensembles of Prolinated Porphyrin Derivatives on Glass Surface: Simple and Rapid Access to Chiral Porphyrin Films. *Front. Chem.* **2022**, *9*, 1198.
(41) Albano, G.; Pescitelli, G.; Di Bari, L. Chiroptical Properties in Thin Films of π-Conjugated Systems. *Chem. Rev.* **2020**, *120*, 10145−10243.
(42) Fang, Y.; Lakey, P. S. J.; Riahi, S.; McDonald, A. T.; Shrestha, M.; Tobias, D. J.; Shiraiwa, M.; Grassian, V. H. A Molecular Picture of Surface Interactions of Organic Compounds on Prevalent Indoor Surfaces: Limonene Adsorption on SiO_2. *Chem. Sci.* **2019**, *10*, 2906−2914.
(43) Hale, S. E.; Endo, S.; Arp, H. P. H.; Zimmerman, A. R.; Cornelissen, G. Sorption of the monoterpenes α-pinene and limonene to carbonaceous geosorbents including biochar. *Chemosphere* **2015**, *119*, 881−888.

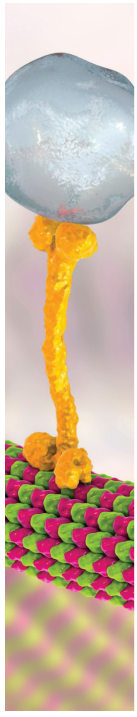
CAS BIOFINDER DISCOVERY PLATFORM™
BRIDGE BIOLOGY AND CHEMISTRY FOR FASTER ANSWERS
Analyze target relationships, compound effects, and disease pathways
Explore the platform
CAS
A division of the American Chemical Society

Author's other publications and conference presentations

Other publications

1. Deniss Klauson, Marko Šakarašvili, Natalja Pronina, Marina Krichevskaya, Erki Kärber, Valdek Mikli. Aqueous photocatalytic degradation of selected micropollutants by Pd-modified titanium dioxide in three photoreactor types. *Environmental Technology*, **2017**, *38*(7), 860–871

Conference presentations

1. Šakarašvili, M.; Ustrnul, L.; Mägi, A.; Aav, R. Reorganization of chiral Zn porphyrin-cyclohexanohemicucurbit[*n*]uril (n=6, 8) complexes in polymer matrix and as thin films. The International Symposium on Macrocyclic and Supramolecular Chemistry (ISMSC), Kyoto, Japan, **2025**, May 25–30 (Poster)
2. Šakarašvili, M.; Ustrnul, L.; Magna, G.; Konrad, N.; Borovkov, V.; Truong, K.-N.; Kuroda, R.; Paolesse, R.; Rissanen, K.; Aav, R. Porphyrin-hemicucurbit[8]uril complexes for chiral sensing. The International Symposium on Macrocyclic and Supramolecular Chemistry (ISMSC), Reykjavik, Iceland. **2023**, June 25-29 (Poster)
3. Šakarašvili, M.; Ustrnul, L.; Borovkov, V.; Aav, R. Chirogenic interaction of chiral cyclohexanohemicucurbit[n]urils with bis(Zn-porphyrin). International Conference on Porphyrins and Phthalocyanines (ICPP-12), Madrid, Spain, **2022**, July 10-15 (Poster)
4. Šakarašvili, M.; Ustrnul, L.; Magna, G.; Konrad, N.; Borovkov, V.; Truong, K.-N.; Paolesse, R.; Rissanen, K.; Aav, R. Porphyrin-based complexes with induced chirality for sensor development. Materials Research Meeting 2021, Yokohama, **2021** December 13-16 (Online flash poster presentation)

Supervised theses

2024, Ander Mägi, B. Sc. *Zn-porphyrin and cyclohexanohemicucurbit[n]uril based chiral sensor materials* (Tallinn University of Technology, Department of Chemistry and Biotechnology)

Curriculum vitae

Personal data

Name: Marko Šakarašvili
Date of birth: 10.06.1992
Place of birth: Tallinn
Citizenship: Estonian

Contact data

E-mail: marko.sakarasvili@taltech.ee

Education

2020–2026	Tallinn University of Technology, PhD
2016–2020	Tallinn University of Technology, MSC
2011–2015	Tallinn University of Technology, BSC
1999–2011	Tallinn Technical Gymnasium, secondary education

Language competence

Estonian	Fluent
English	Fluent
Georgian	Conversational
Russian	Basic

Professional employment

2017–2025	Ordior Eesti OÜ (laboratory equipment sales representative)
2024–2025	Estonian Business and Innovation Agency (evaluating projects as external expert)

Elulookirjeldus

Isikuandmed

Nimi: Marko Šakarašvili
Sünniaeg: 10.06.1992
Sünnikoht: Tallinn
Kodakondsus: Eesti

Kontaktandmed

E-post: marko.sakarasvili@taltech.ee

Hariduskäik

2020–2026	Tallinna Tehnikaülikool, PhD
2016–2020	Tallinna Tehnikaülikool, MSC
2011–2015	Tallinna Tehnikaülikool, BSC
1999–2011	Tallinna Tehnikagümnaasium, keskharidus

Keelteoskus

Eesti Keel	emakeel
Inglise keel	kõrgtase
Gruusia keel	hea
Vene keel	keskpärane

Teenistuskäik

2017–2025	Ordior Eesti OÜ (laboritarvete müügiesindaja)
2024–2025	Ettevõtluse ja Innovatsiooni Sihtasutus (projektide hindaja välise eksperdina)

ISSN 2585-6901 (PDF)
ISBN 978-9916-80-538-1 (PDF)